

Dissertation  
submitted to the  
Combined Faculties of the Natural Sciences and  
Mathematics  
of the Ruperto-Carola-University of Heidelberg,  
Germany  
for the degree of  
Doctor of Natural Sciences

Put forward by

Dipl. Phys. Daniel Jürgen Seifried  
Born in: Aschaffenburg, Germany

Oral examination: 19.12.2012



# Magnetic fields during the early phase of massive star formation

Referees: Prof. Dr. Robi Banerjee  
Prof. Dr. Henrik Beuther



*Für meine Eltern*



## Zusammenfassung

Das Ziel dieser Arbeit ist es, mit Hilfe numerischer Simulationen unser Verständnis von der Entstehung massereicher Sterne in Anwesenheit von Magnetfeldern zu verbessern. Dabei konzentriere ich mich insbesondere auf protostellare Akkretionsraten, die zeitliche Entwicklung und die Eigenschaften von protostellaren Scheiben und der damit verbundenen Ausflüsse sowie die Wechselwirkung von Turbulenz und Magnetfeldern und deren Auswirkung auf die Entstehung von protostellaren Scheiben. In einer systematischen Parameterstudie zeige ich, dass sich die Akkretionsraten über einen weiten Bereich von Anfangsbedingungen nur geringfügig ändern. Des Weiteren demonstriere ich, dass sich beim Fehlen von Turbulenz für starke anfängliche Magnetfelder keine Keplerschen Scheiben ausbilden können, was auf die Abbremsung der Rotation durch die Magnetfelder zurückzuführen ist. Dieses Ergebnis scheint im Widerspruch zu Beobachtungen zu stehen. Die Morphologie der Ausflüsse, die stark von den Anfangsbedingungen abhängt, kann letztendlich auf die Struktur der zugrunde liegenden Scheibe zurückgeführt werden. Wohl-kollimierte Ausflüsse mit hohen Ausflussgeschwindigkeiten entwickeln sich nur, wenn eine Keplersche protostellare Scheibe vorliegt, anderenfalls entwickeln sich langsam ausdehnende, sphärische Ausflüsse. Weiterhin analysiere ich den Ausflussmechanismus mit einem analytischen Kriterium, das im Rahmen dieser Arbeit entwickelt wurde. Sobald supersonische Turbulenz in den Simulationen berücksichtigt wird, bilden sich, im Gegensatz zu den Simulationen ohne Turbulenz, Keplersche protostellare Scheiben aus. Dieses Ergebnis steht im Einklang mit Beobachtungen von sehr jungen protostellaren Objekten.

## Abstract

The goal of this work is to improve our current understanding of the formation process of massive stars in the presence of magnetic fields by means of numerical simulations. In particular, I focus on protostellar accretion rates, the evolution and the properties of protostellar discs and their associated outflows, and the interplay of turbulence and magnetic fields and its impact on protostellar disc formation. In a systematic parameter study I show that the accretion rates are remarkably constant over a wide range of initial conditions. Furthermore, I show that in the absence of turbulence for strong initial magnetic fields only sub-Keplerian discs can form which is attributed to the strong magnetic braking effect. This result seems to be in contrast to observational results. The morphology of the outflows, which shows a strong dependence on the initial conditions, can ultimately be linked to the structure of the underlying disc. Well-collimated outflows with high outflows velocities only develop if a Keplerian protostellar disc is present, otherwise slowly expanding, sphere-like outflows develop. Furthermore, I analyse the driving mechanism of outflows with an analytical criterion derived in the course of this work. When including supersonic, turbulent motions in the simulations, Keplerian protostellar discs form in contrast to the non-turbulent simulations. This result is in agreement with observations of early-type protostellar objects.



# Contents

<b>1. Introduction</b>	<b>1</b>
1.1. Motivation . . . . .	1
1.2. The formation of stars . . . . .	2
1.3. Magnetic fields and star formation . . . . .	3
1.4. Interstellar Turbulence . . . . .	4
1.5. Objectives of this work . . . . .	4
<b>2. Star formation theory</b>	<b>7</b>
2.1. Initial conditions of star formation . . . . .	7
2.1.1. Magnetic fields . . . . .	8
2.1.2. Turbulence . . . . .	11
2.1.3. Summary of the initial conditions . . . . .	12
2.2. The star formation process . . . . .	12
2.2.1. Theoretical models of massive star formation . . . . .	13
2.2.2. Discs and outflows . . . . .	16
2.2.3. The initial mass function . . . . .	18
<b>3. Magnetohydrodynamics</b>	<b>21</b>
3.1. The magnetohydrodynamical equations . . . . .	21
3.1.1. Mass conservation . . . . .	21
3.1.2. Momentum equation . . . . .	22
3.1.3. Energy conservation and equation of state . . . . .	22
3.1.4. The induction equation . . . . .	23
3.1.5. Magnetohydrodynamical waves . . . . .	23
3.1.6. Non-ideal MHD effects . . . . .	24
3.2. The mass-to-flux ratio . . . . .	25
3.3. Magnetic braking . . . . .	26
3.3.1. Aligned rotator . . . . .	26
3.3.2. Perpendicular rotator . . . . .	28
3.4. Summary . . . . .	29
<b>4. The magnetohydrodynamical wind theory</b>	<b>31</b>
4.1. Centrifugally driven jets . . . . .	31
4.2. Magnetic tower flows . . . . .	36
4.3. Summary . . . . .	37

<b>5. Numerical methods and initial conditions</b>	<b>39</b>
5.1. Numerical methods . . . . .	39
5.1.1. Grid refinement and sink particles . . . . .	39
5.1.2. Gas cooling . . . . .	41
5.2. Initial conditions . . . . .	43
<b>6. Disc formation and protostellar accretion</b>	<b>49</b>
6.1. Introduction . . . . .	49
6.2. Results . . . . .	51
6.2.1. The initial collapse phase . . . . .	51
6.2.2. Global disc properties . . . . .	53
6.2.3. Velocity structure . . . . .	59
6.2.4. Torques . . . . .	62
6.2.5. Accretion rates . . . . .	64
6.2.6. Disc fragmentation . . . . .	68
6.3. Discussion . . . . .	72
6.3.1. Numerical caveats . . . . .	72
6.3.2. Disc formation . . . . .	73
6.3.3. Accretion rates . . . . .	76
6.4. Conclusion . . . . .	78
<b>7. The formation of outflows</b>	<b>81</b>
7.1. Introduction . . . . .	81
7.2. A generalised wind theory . . . . .	83
7.3. Results . . . . .	86
7.3.1. Weak field run 26-4 . . . . .	87
7.3.2. Strong field run 5.2-4 . . . . .	95
7.3.3. Long term evolution and jet stability . . . . .	99
7.3.4. The influence of the initial conditions . . . . .	102
7.3.5. The ejection-accretion ratio . . . . .	106
7.4. Discussion . . . . .	108
7.4.1. The launching mechanism . . . . .	108
7.4.2. The evolution and impact of outflows . . . . .	110
7.4.3. Comparison to observations . . . . .	111
7.4.4. The evolution of outflow collimation . . . . .	112
7.5. Conclusion . . . . .	113
<b>8. Disc formation in turbulent cloud cores</b>	<b>117</b>
8.1. Introduction . . . . .	117
8.2. Initial conditions and numerical methods . . . . .	119
8.3. Results . . . . .	121
8.4. Discussion . . . . .	129
8.4.1. Dependence on the initial conditions . . . . .	129
8.4.2. Mass-to-flux ratio . . . . .	130

8.4.3. The reduced magnetic braking efficiency . . . . .	130
8.4.4. Early vs. late stage disc formation . . . . .	132
8.5. Conclusion . . . . .	133
<b>9. Summary and Outlook</b>	<b>135</b>
9.1. Summary . . . . .	135
9.1.1. Disc formation and protostellar accretion rates . . . . .	135
9.1.2. Outflow formation . . . . .	136
9.1.3. Turbulent disc formation . . . . .	136
9.2. Outlook . . . . .	137
9.2.1. Turbulent disc formation for a wider mass range . . . . .	137
9.2.2. Protostellar outflows in turbulent cores . . . . .	137
9.2.3. Subgrid models for protostellar feedback . . . . .	138
<b>A. Appendix</b>	<b>139</b>
A.1. A resolution study for run 26-4 . . . . .	139
<b>Bibliography</b>	<b>145</b>



# 1. Introduction

## 1.1. Motivation

Stars have played and still play a crucial role in the evolution of the present universe. Firstly, by burning hydrogen via nuclear fusion in their interior, stars produce heavier elements and thus were responsible for the chemical enrichment of the primordial gas, which initially only consisted of hydrogen, helium, and traces of lithium. The fusion products are dispersed to the ambient gas by stellar winds and supernova explosions. Secondly, stars heat the interstellar as well as the intergalactic medium by the radiation produced during the fusion reaction, which strongly affects the global thermodynamical properties of the gas. And thirdly, stars inject large amounts of kinetic energy into the interstellar medium (ISM): during their birth phase in form of molecular outflows and jets, during their lifetime in form of stellar winds and – for stars more massive than  $\sim 8 M_{\odot}$  – in form of extremely energetic<sup>1</sup> supernova explosions at the end of their life. Beside effects like the differential rotation of the galaxy and gravitational instabilities, these are the processes which determine the dynamical properties of the ISM (e.g. Mac Low & Klessen, 2004; Elmegreen & Scalo, 2004).

All aforementioned feedback processes occurring during the entire lifetime of a star strongly affect the ISM. However, as the formation of stars takes place in the ISM, these processes also significantly influence the formation mechanism itself. As the formation mechanism of stars in turn determines e.g. the mass distribution of stars, thus directly affecting the feedback processes of stars during their lifetime, there exists a closed circle of the birth, life and death of stars.

In particular the feedback processes of massive stars are very important. Stars are usually denoted as massive if their final mass is above  $\sim 8 M_{\odot}$ . In general the feedback of massive stars is up to several orders of magnitude stronger than that for low-mass stars. For example only massive stars can produce very heavy metals up to iron. Furthermore, as the luminosity of a star roughly scales with the fourth power of its mass, the heating effect of massive stars on the ISM is much more pronounced (see e.g. Zinnecker & Yorke, 2007). Moreover, only massive stars end their lives with a supernova explosion and are therefore much more important for the kinetic energy budget of ISM than low-mass stars. Supernovae are also the only known way to produce elements heavier than iron.

As mentioned already before, there is a mutual influence of the different phases of a star's life. This in turn requires a detailed understanding of each individual phase, i.e. the formation, main lifetime and death of stars, to be able to derive a complete picture of stellar evolution and the influence of stars on the evolution of galaxies. However, despite

---

<sup>1</sup>The typical kinetic energy for a type II core collapse supernova is of the order of  $10^{51}$  erg.

the above mentioned importance of massive stars, in particular their formation process is far from being completely understood and still highly debated in the literature (see e.g. the review by Zinnecker & Yorke, 2007, and Chapter 2 of this work). There are several reasons for the lack of a comprehensive theory of massive star formation. To begin with, massive star formation – as well as low-mass star formation – takes place in the densest parts of the ISM. Therefore, the actual initial conditions of star formation as well as the physical important processes are hard to observe since they are often hidden from the observer by the surrounding gas. Moreover, massive stars – in contrast to low-mass stars – usually form in dense stellar clusters, which makes it hard to entangle the effects from surrounding protostars and the formation process itself. Furthermore, with a distance of about 440 pc (e.g. Hirota et al., 2007) the Orion nebular, the nearest massive star forming region, is about 3 times further away than the nearest low-mass star forming regions, e.g. the  $\rho$  Ophiuchi cloud with a distance of  $\sim 130$  pc (e.g. Wilking et al., 2008). Finally, since massive stars occur more rarely than low-mass stars and since their formation times of  $10^5 - 10^6$  yr are relatively short compared to that of low-mass stars (in general  $> 10^6$  yr, e.g. McKee & Ostriker, 2007), they are less often observed than low-mass stars. For all these reasons research on massive star formation has also to rely on theoretical and numerical work, which is what will be the main focus of this work.

## 1.2. The formation of stars

In the following I give a short and very general overview of the star formation process. For a more detailed discussion I refer the reader to Chapter 2.

Stars observed today are formed during the gravitational collapse of the interstellar gas in galaxies. Due to its own gravity the gas contracts and reaches higher and higher densities. At some point the gas will eventually get dense and hot enough to start burning hydrogen – a star is born. The average rate in our own galaxy with which interstellar gas is transformed into stars is of the order of  $1 M_{\odot} \text{ yr}^{-1}$  (e.g. Robitaille & Whitney, 2010, and references therein). Although at first view this collapse process seems to be relatively simply, a closer look reveals the difficulties in analysing this process. The star formation process covers about 10 orders of magnitude in size from giant molecular clouds with sizes of up to 100 pc down to stellar radii of the order of  $10^6$  km, about 13 orders of magnitude for characteristic timescales from the dynamical timescale of molecular clouds ( $10^6$  yr) down to timescales of chemical reactions and radiative processes of the order of minutes or seconds. The density even covers about 20 orders of magnitude from particle densities of the diffuse ISM of  $10^2 - 10^3 \text{ cm}^{-3}$  up to protostellar densities of the order  $10^{22} \text{ cm}^{-3}$ . Furthermore, all the different physical aspects like gravitational interaction, radiative processes, chemical reactions, turbulence, and magnetic field effects have to be taken into account simultaneously when trying to completely describe the formation process of stars. Hence, the development of a comprehensive star formation theory is extremely challenging. For this reason, work done on this topic usually restricts itself to a limited dynamical or spatial range and certain physical aspects. It is therefore not surprising

that to date a complete star formation theory from molecular clouds down to the final star does not exist, yet.

### 1.3. Magnetic fields and star formation

In this work I restrict myself to the process of massive star formation. Since observations of magnetic fields in star forming regions usually reveal relatively high field strengths (see Section 2.1), its influence on the star formation process is expected to be significant. This is why I will particularly focus on the role magnetic fields play in the formation process of massive stars, a topic which has received attention only recently. Magnetic fields are found to be ubiquitous in our galaxy, other galaxies and even in the intergalactic medium. The origin of galactic magnetic fields, however, is not yet completely understood (see Grasso & Rubinstein, 2001; Widrow, 2002, for a general overview). One possibility is the amplification of an extremely weak, initial magnetic field with a strength as low as  $10^{-30}$  G by the dynamo effect. In this mechanism the magnetic field lines are stretched, twisted and folded by turbulent motions in the primordial gas resulting in a significant increase of the field strength up to strengths observed nowadays, which are in general of the order of  $10^{-6}$  G or even larger. Another reason for the observed magnetic field strength might be primordial magnetic fields formed in the earliest phase of the universe with strengths of the order  $10^{-10}$  G. In this scenario the primordial magnetic field is amplified by the compression of the field due the collapse of the gas during the formation of protogalaxies resulting in the observed field strengths.

Observations of the magnetic field structure in galaxies in general reveal two different components, a well-ordered, large-scale component and a fluctuating, small-scale component. The well-ordered, large-scale magnetic field in our galaxy has a mean strength of about  $6 \mu\text{G}$ , whereas in other galaxies typically values of  $10 - 15 \mu\text{G}$  are found (see e.g. the recent review by Beck, 2012). The ordered field is usually found in the interarm region, i.e. between the spiral arms, oriented parallel to the adjacent spiral arms thus revealing a spiral structure. This spiral structure is thought to be generated by compression at the inner edge of the spiral arm, by shear motions between the spiral arms or by a mean-field dynamo. The rather randomly oriented, small-scale magnetic field in the spiral arms themselves is in general significantly stronger than the large-scale field. The actual strength, however, can vary significantly between individual clouds and embedded cores. Polarisation measurements show that the magnetic field is unordered on scales of a few 100 pc, i.e. on the scale of giant molecular clouds which points to the fact that the random orientation is a product of the turbulent motions typical for star formation activity.

Interestingly, the energy density of the average magnetic field in our galaxy is in approximate equipartition with the cosmic ray energy density and the energy of small-scale turbulent motions. This already indicates that the magnetic field should have a significant influence on the star formation process, both on the global galactic scale but also on the small scale of individual stars. Indeed, the importance of magnetic fields on small scales is demonstrated by the emergence of large ( $\sim 1$  pc) outflows ejected by magnetic

forces from protostellar discs around the forming stars (e.g. Arce et al., 2007, but see also Chapter 2). Such protostellar discs are the birth places of planetary systems like our own around the Sun. Moreover, the protostellar discs and their associated outflows are basic keystones of the current star formation theory at least for low-mass stars. For high-mass stars the picture of an accretion disc driven formation process is still highly debated in the literature (see Chapter 2 for a detailed discussion) although recent observations of outflows and discs around massive protostars point to such a formation mechanism. Hence, one of the main objectives of this work is to test the accretion disc mediated high-mass stars formation scenario with numerical simulations.

## 1.4. Interstellar Turbulence

As stars are born out of the interstellar gas, the properties of the ISM, of which one is its dynamical state, are of particular importance for the star formation process. Observations show that the ISM is in a highly turbulent state (e.g. Larson, 1981, but see also Chapter 2) with kinetic energy injection from the differential galactic rotation, gravitational instabilities and stellar feedback processes (e.g. Mac Low & Klessen, 2004; Elmegreen & Scalo, 2004). During the formation phase of stars in particular molecular outflows inject large amounts of kinetic energy in the surrounding medium thus also affecting the global turbulent energy content. To what extent this kind of energy injection is important for the star formation process – compared to other sources – is still a matter of debate (e.g. Banerjee et al., 2007; Nakamura & Li, 2007). There is no doubt, however, that turbulence itself has a significant impact on the star formation process. Furthermore, the interplay between magnetic fields and turbulence is an extremely complex and highly non-linear problem, which is why in general this can be solved only by means of numerical simulations. Hence, exploring the interaction of turbulent motions and magnetic fields in massive star forming regions will be one of the goals of this work.

## 1.5. Objectives of this work

The goal of this work is to improve our understanding of the influence of magnetic fields, rotation, and turbulence on the collapse of massive, gravitationally unstable cloud cores and the subsequent formation of massive protostars. This is done by means of numerical simulations with a particular focus on

- protostellar accretion rates,
- the structure and properties of protostellar discs,
- the driving mechanism and morphology of molecular outflows, and
- the combined effect of turbulence and magnetic fields on protostellar disc formation.

The above listed topics will be covered in the different parts of this thesis. In Chapter 2 I will firstly give a brief overview of the observational and theoretical basics of star formation focussing on the high-mass star formation process. In the following two Chapters 3 and 4 I introduce the equations of magnetohydrodynamics and discuss the magnetohydrodynamical wind theory. The numerical methods and initial conditions used in my simulations are described in detail in Chapter 5. The combined influence of magnetic fields and rotation on protostellar disc properties and accretion rates is studied in Chapter 6. This analysis is extended to the molecular outflows driven by the protostellar discs in Chapter 7. The effect of turbulence on protostellar disc formation is studied in detail in Chapter 8 before I summarise the main results of my work in Chapter 9.



## 2. Star formation theory

In this chapter I will review our current understanding of the star formation process. I will discuss the conditions present in molecular cloud cores, which are the birth places of stars, in particular focussing on the sites of potential high-mass star formation. Thereafter, a brief overview of the star formation process, concentrating on current models of massive star formation as well as on the role discs and outflows play in the formation process, will be given. For a more extensive review on star formation in general as well as on massive star formation I also refer to the recent reviews of McKee & Ostriker (2007) and Zinnecker & Yorke (2007), respectively.

### 2.1. Initial conditions of star formation

Stars form in the densest parts of the interstellar medium (ISM) namely in molecular clouds. In these giant ( $\sim 10 - 100$  pc) and massive ( $10^4 - 10^6 M_{\odot}$ ) objects in turn, only the densest parts are sites of star formation. The densest condensations in molecular clouds are called molecular cloud cores, which are embedded in somewhat less dense but larger objects called clumps. Following Williams et al. (2000), in this work we use the term *clumps* for condensations which form clusters of stars whereas the term *core* is used for condensations which form single protostars or a small number of gravitationally bound protostars<sup>1</sup>. Clumps have typical masses of  $50 - 500 M_{\odot}$  and sizes of  $0.3 - 3$  pc whereas the somewhat smaller cores have masses and sizes of  $0.5 - 5 M_{\odot}$  and  $0.03 - 0.2$  pc, respectively (see e.g. Bergin & Tafalla, 2007, for an extensive review). Hence, in this terminology cores are the birth places of low-mass stars.

High-mass star formation is believed to take place in Infrared Dark Clouds (IRDCs) (e.g. Egan et al., 1998; Rathborne et al., 2006; Beuther & Sridharan, 2007; Peretto & Fuller, 2010; Tackenberg et al., 2012; Miettinen, 2012b; Beuther et al., 2012) embedded in giant molecular clouds. These objects are seen in absorption against the mid-infrared background radiation. This is due to fact that these clouds are opaque in the infrared and block out the infrared background radiation making them infrared dark compared to their surroundings. IRDCs have masses of a few 100 up to about  $10\,000 M_{\odot}$  and sizes of  $0.5$  pc up to a few pc. The densities and temperatures are in the range of  $10^2 - 10^4 \text{ cm}^{-3}$  and  $10 - 20$  K, respectively. In general IRDCs do not have a spherical shape but rather reveal a filamentary structure which points to a gravoturbulent formation mechanism in larger scale molecular clouds (e.g Mac Low & Klessen, 2004). Furthermore, IRDCs often do not yet harbour young protostellar objects, which

---

<sup>1</sup>Here we note that the terminology for *clumps* and *cores* is not universal throughout the literature. In particular for massive star formation the differentiation is not unambiguous.

would be seen in the near- to mid-infrared. Hence, IRDCs are believed to represent the earliest stage, i.e. the initial conditions of massive star formation. As mentioned before, the IRDCs reveal a filamentary substructure. Along these filaments overdense condensations, so-called High-Mass Starless Cores (HMSCs), exist (e.g. Schneider et al., 2012), which represent the first stage in the formation process of massive stars. Beuther et al. (2007) define three subsequent stages of massive star formation:

- High-Mass Cores harbouring accreting low/intermediate-mass protostar(s) destined to become high-mass star(s)
- High-Mass Protostellar Objects (HMPOs) with masses  $\gtrsim 8 M_{\odot}$
- Final Stars

In this work we aim to simulate the evolution of a HMSC towards a High-Mass Core harbouring accreting low/intermediate-mass protostars. A number of observations have revealed the characteristic properties of such massive cores (e.g. Beuther et al., 2002b; Sridharan et al., 2005; Rathborne et al., 2006; Zhang et al., 2009; Peretto & Fuller, 2010; Wilcock et al., 2011; Beuther et al., 2012; Tackenberg et al., 2012, but see also Beuther et al. (2007) for a recent review) and here we summarise the main results. Typical masses of high-mass cores range from about  $50 M_{\odot}$  up to  $1000 M_{\odot}$  with sizes of the order of  $0.1 - 0.5$  pc. The mean density of the cores lies around  $10^5 \text{ cm}^{-3}$  with peak densities as high as a few  $10^6 \text{ cm}^{-3}$ . Typical temperatures of HMSCs are of the order of  $10 - 20$  K. The density of massive cores typically declines outwards following a power-law profile

$$\rho \propto r^{-p}, \tag{2.1}$$

where the exponent  $p$  is found to lie around 1.5 (Beuther et al., 2002b; Pirogov et al., 2003; Pirogov, 2009).

Significant velocity gradients along a preferred direction are measured frequently in massive cores. These velocity gradients are usually interpreted as a uniform rotation of the cloud core along an axis perpendicular to the gradient (see Fig. 2.1 for an example). Based on the velocity gradient one can infer the amount of rotational energy present. Together with the mass of the core one can estimate the ratio of rotational to gravitational energy  $\beta_{\text{rot}}$ . Typical values from observations are found to range from  $10^{-4}$  up to 1.4 with a mean around 0.01 (e.g. Goodman et al., 1993; Pirogov et al., 2003; Csengeri et al., 2011). Hence, for the core itself rotation seems to play a rather insignificant role. However, due to angular momentum conservation during the collapse the importance of core rotation increases significantly in the further evolution. For this reason, one of the main goals of this work will be to explore the effect of initial core rotation on the formation of (massive) protostars in detail.

### 2.1.1. Magnetic fields

The ISM as a whole is found to be strongly magnetised. Typical magnetic field strengths for the atomic ISM are of the order of  $6 \mu\text{G}$  (e.g. Heiles & Troland, 2005; Beck, 2012,

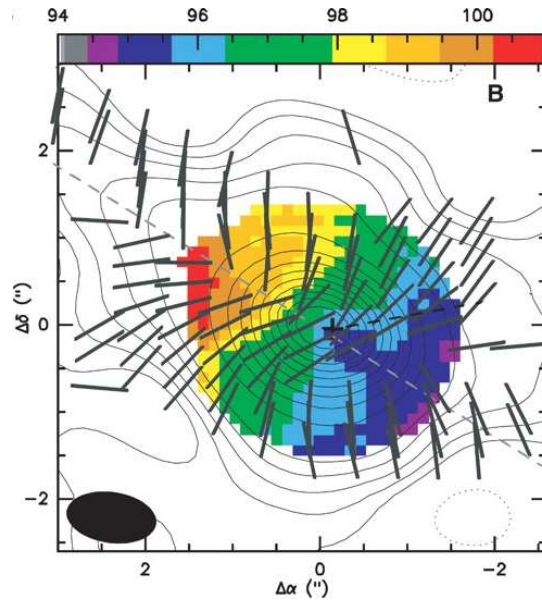


**Figure 2.1.:** Contour map of the  $879 \mu\text{m}$  dust emission superposed on the colour image of the flux weighted velocity map of the  $\text{CH}_3\text{OH } 14_7\text{-}15_6$  line for the massive star forming region G31.41+0.31. Black thick bars indicate the direction of the magnetic field. The line emission (colour scale) reveals a clear velocity gradient along the grey dashed line usually interpreted as core rotation. The magnetic field shows an hourglass-shaped structure. (From Girart et al. 2009, *Science*, 324, 1408. Reprinted with permission from AAAS.)

and references therein). The strength of the magnetic field in the diffuse ISM is usually measured by Faraday rotation or synchrotron observations. In contrast, for the dense, molecular phase, in which stars form and which we are interested in, magnetic field measurements are in general done by Zeeman splitting and the Chandrasekhar-Fermi method (see Heiles & Crutcher, 2005, for an overview). With the Zeeman effect, i.e. the splitting of hyperfine-structure lines, the line-of-sight magnetic field strength  $B_{\text{los}}$  can be measured. The Chandrasekhar-Fermi method (Chandrasekhar & Fermi, 1953) is an indirect method to determine the magnetic field strength in the plane of sky  $B_{\text{pos}}$ . Firstly, by measuring the polarisation of light emitted from dust or molecular line transitions, the morphology of the plane of sky magnetic field can be determined. In a second step the plane-of-sky field strength can be estimated by comparing the fluctuations of  $B_{\text{pos}}$  to the velocity dispersion. The physical motivation for this is that velocity fluctuations will produce random magnetic field fluctuations, which are the stronger the weaker the uniform field  $B_{\text{pos}}$  is.

In particular in the last decade there has been major progress in measuring the magnetic field strength in IRDCs and embedded high-mass cores (Crutcher, 1999; Lai et al., 2001; Curran & Chrysostomou, 2007; Falgarone et al., 2008; Girart et al., 2009; Tang et al., 2009; Beuther et al., 2010; Crutcher et al., 2010; Koch et al., 2012). All these authors typically find magnetic field strengths of the order of a few  $100 \mu\text{G}$  up

to a few mG in massive cloud cores with masses ranging from  $\sim 100 M_{\odot}$  to  $\sim 1000 M_{\odot}$ . Interestingly, whereas for the diffuse ISM with particle densities  $n < 10^3 \text{ cm}^{-3}$  the magnetic field strength is more or less constant with values around  $6 \mu\text{G}$  (e.g. Heiles & Troland, 2005), for densities  $> 10^3 \text{ cm}^{-3}$  the magnetic field strength increases as  $B \propto n^{0.65}$  (Crutcher et al., 2010). This suggests that molecular clouds/IRDCs preferentially form by accumulation of mass along magnetic field lines. As soon as the gas has reached a critical mass, the gas begins to contract also perpendicular to the magnetic field resulting in the observed scaling property. This also explains the general observable trend that magnetic fields are stronger in more massive and thus more dense cloud cores (see above) than in low-mass cores ( $\sim 1 M_{\odot}$ ) with typical field strengths of the order of  $10 - 30 \mu\text{G}$  (e.g. Kirk et al., 2006)

Similar to  $\beta_{\text{rot}}$ , which compares the rotational energy to the gravitational energy, it is common to express the magnetic field strength in a way to estimate its importance compared to gravity. This is usually done in terms of the mass-to-flux ratio  $\frac{M}{\Phi}$  where  $M$  is the mass of the core and  $\Phi$  the amount of magnetic flux through the core. The mass-to-flux ratio for an oblate ellipsoid is usually expressed in units of its critical mass-to-flux ratio (Mouschovias & Spitzer, 1976, but see Section 3.2 for details)

$$\left(\frac{M}{\Phi}\right)_{\text{crit}} = \frac{0.13}{\sqrt{G}}, \quad (2.2)$$

where  $G$  is the gravitational constant. This value is denoted as critical as a cloud core with a mass-to-flux ratio lower than this value will be prevented from gravitational collapse by magnetic forces. Here we note that from now on during the whole course of this work we will denote the normalised, dimensionless mass-to-flux ratio

$$\mu = \frac{M}{\Phi} / \left(\frac{M}{\Phi}\right)_{\text{crit}} \quad (2.3)$$

simply as the *mass-to-flux ratio*, keeping in mind that we actually mean the normalised value. A cloud core with a value of  $\mu > 1$  is denoted as supercritical since here the gravitational force is sufficiently strong to overcome the magnetic force and to induce a gravitational collapse. In contrast, when  $\mu < 1$  the core is denoted as subcritical.

When the mass, size, and magnetic field strength of a molecular cloud core are known, it is straightforward to determine the mass-to-flux ratio  $\mu$  of the core. Observations of high-mass cloud cores usually report mass-to-flux ratios which are only slightly supercritical with values of  $\mu \lesssim 5$  (Crutcher, 1999; Lai et al., 2001; Curran & Chrysostomou, 2007; Falgarone et al., 2008; Girart et al., 2009; Tang et al., 2009; Beuther et al., 2010; Crutcher et al., 2010; Koch et al., 2012). Hence, the magnetic field can be expected to have a significant influence on the collapse of the cloud core and the subsequent star formation process although it cannot completely prevent the collapse. From the numerical side, however, the influence of magnetic fields on the formation process of massive stars is explored only poorly. For this reason, one of the main objectives of this work is to examine the effect of magnetic fields in detail, in particular in combination with an overall core rotation as observed frequently (Goodman et al., 1993; Pirogov et al., 2003; Csengeri et al., 2011).

Cloud core observations usually reveal a well-ordered magnetic field structure on scales of the core. This suggests that the field is relatively strong and that it has a significant impact in the formation of the core (e.g. Curran & Chrysostomou, 2007; Beuther et al., 2010). Moreover, some of the massive cores reveal a magnetic field line morphology which resembles an hourglass shape (e.g. Girart et al., 2009; Tang et al., 2009; Koch et al., 2012). This peculiar shape is generated when an initially uniform magnetic field is dragged inwards due to the inflow of the gas perpendicular to the field lines. Furthermore, the overall orientation of the magnetic field and the rotation axis are often found to be aligned (see Fig. 2.1 for an example).

### 2.1.2. Turbulence

The theory of turbulence in an incompressible fluid was developed by Kolmogorov (1941) and an extensive review of this topic can be found in the textbook by Frisch (1995). For the ISM, however, the assumption of incompressibility is not valid anymore, which significantly complicates the treatment. Indeed, no closed description for compressible turbulence exists so far. Nevertheless, extensive work has been done to study the nature of turbulence in the ISM. For a complete overview of the work done so far, which would be by far beyond the scope of this work, we refer the reader to the seminal reviews by Mac Low & Klessen (2004) and Elmegreen & Scalo (2004). In this section we particularly focus on turbulence in massive star forming sites, i.e. molecular clouds, IRDCs and massive cores.

The ISM as a whole, i.e. the diffuse, atomic and the dense, molecular part are found to be highly turbulent revealing supersonic motions. The turbulent motions are injected by different processes like the differential rotation of the galaxy, supernova explosions, large-scale gravitational instabilities in spiral arms, and – on smaller scales – stellar winds around massive stars or outflows from protostars (see Mac Low & Klessen, 2004; Elmegreen & Scalo, 2004, for a detailed overview of the different processes).

The turbulent properties of molecular clouds were studied in detail for the first time by Larson (1981), who found that the velocity dispersion  $\sigma$  of clouds scales with the cloud size  $l$  as

$$\sigma \propto l^{0.38} \quad (2.4)$$

over almost three orders of magnitude in size. In subsequent, more accurate observations a scaling exponent of around 0.5 was established (e.g. Solomon et al., 1987). Furthermore, the turbulent motions in molecular clouds were found to be highly supersonic with Mach numbers ranging from  $\sim 5$  up to  $\sim 20$ .

Molecular clouds contain IRDCs which are thought to be the birth places of massive stars. These IRDCs reveal filamentary structures, which points to a formation mechanism of IRDCs and their embedded massive cores via an interplay of gravity and turbulence, called gravoturbulent fragmentation (Mac Low & Klessen, 2004). And indeed, a number of molecular line observations of IRDCs and their substructures, i.e. massive cores reveal significantly broadened line widths much broader than the usual thermal line broadening. This shows that supersonic or – in the case of

cores – at least transonic, turbulent motions are present in those structures down to scales of  $\sim 0.1$  pc (Caselli & Myers, 1995; Di Francesco et al., 2001; Zhang et al., 2009; Sadavoy et al., 2012; Miettinen, 2012a,b; Fontani et al., 2012). Typical non-thermal line widths  $\sigma_{\text{turb}}$  found in IRDCs and massive cores are in the range of  $\text{km s}^{-1}$ , which corresponds to turbulent Mach numbers of  $\sim 1$  up to  $\sim 5$ . The simultaneous measurement of the magnetic field strength allows for the determination of whether the observed turbulent velocity fluctuations are in the sub-, trans- or super-Alfvénic range. Typically, observations of star forming regions reveal turbulent motions in the trans-Alfvénic range (Crutcher, 1999; Falgarone et al., 2008), i.e. turbulent magnetic Mach numbers of the order of

$$M_A = \frac{\sigma_{\text{turb}}}{v_A} \sim 1, \quad (2.5)$$

where  $v_A$  is the Alfvénic velocity (see Eq. 3.12). Hence, magnetic and turbulent energies in molecular clouds and their substructures can in general be considered to be in approximate equipartition.

### 2.1.3. Summary of the initial conditions

So far we have presented a short overview of where and under what conditions stars and in particular massive stars form. Here we briefly summarise the main points. Massive star formation typically takes place in infrared-dark clouds (IRDCs), in which high-mass starless cores (HMSCs) are embedded. Each of these HMSCs is thought to form a single or at most a few massive stars. These massive cores have typical masses of  $50 - 1000 M_{\odot}$ , sizes of a few  $0.1$  pc, temperatures of  $10 - 20$  K, and densities between  $10^5 - 10^6 \text{ cm}^{-3}$ . Additionally, the cores are often found to rotate and are in general magnetised with mass-to-flux ratios  $\lesssim 5$ . Furthermore, turbulent motions in the cores are found to be supersonic and trans-Alfvénic.

## 2.2. The star formation process

In this section we briefly review our current understanding of the star formation process in particular focussing on the theory of massive star formation (for comprehensive reviews see McKee & Ostriker, 2007; Zinnecker & Yorke, 2007). We start with a very general theory of star formation developed by Larson (1969) which – even after 40 years of ongoing research – in general still holds for the case of low-mass stars. As discussed before, stars form in dense and gravitationally bound molecular cloud cores. In the first phase of star formation the cloud core collapses in nearly free-fall, i.e. the typical timescale of this phase is the free-fall time

$$\tau_{\text{ff}} = \sqrt{\frac{3\pi}{32G\rho}}, \quad (2.6)$$

where  $G$  is the gravitational constant and  $\rho$  the density of the core. During this first phase the protostellar collapse proceeds in an almost isothermal manner with  $T \sim 10$  K.

This is due to the fact that at these densities the gas in the core is in general optically thin. Hence, the thermal energy gained by the compression of the gas can be radiated away very efficiently by molecular line and dust emission keeping the gas temperature approximately constant. The isothermal collapse proceeds until a central density of the order of  $10^{-13} \text{ g cm}^{-3}$  is reached. At this density the gas gets increasingly optically thick, which prevents the compression heat being radiated away efficiently. Hence the gas starts to become adiabatic, which results in an increasing temperature in the centre. This thermal pressure gradient slows down the collapse bringing it almost to a halt with a nearly hydrostatic equilibrium in the centre. This central, hydrostatic object is called the *first core* and has a typical extension of  $\sim 5 \text{ AU}$ , a density of  $10^{-13} \text{ g cm}^{-3}$ , and a mass of  $\sim 0.05 M_{\odot}$ . In the following the first core keeps accreting gas from its surroundings which results in an ongoing, slow contraction and heating of the core. Once the core has reached a temperature of 2000 K, the molecular hydrogen starts to dissociate. This endothermal reaction uses up the energy released by compression of the gas thus leading to a slower increase of the central temperature. Therefore, the central region becomes gravitationally unstable again, resulting in a second dynamical collapse. This second collapse proceeds until most of the hydrogen molecules are dissociated. At this point a small core in hydrostatic equilibrium forms which is called the *second core*. This second core has a typical central density and temperature of  $10^{-2} \text{ g cm}^{-3}$  and  $10^4 \text{ K}$ , respectively, and can be considered as the progenitor of the final star though with a much lower mass ( $\sim 10^{-3} M_{\odot}$ ).

### 2.2.1. Theoretical models of massive star formation

The picture of star formation sketched in the previous paragraph holds for the formation of low-mass stars. In general low-mass star formation is characterised by formation times shorter than the Kelvin-Helmholtz time  $(GM_*^2/R_*)/L_*$ , where  $M_*$ ,  $R_*$  and  $L_*$  are the mass, radius and luminosity of the star, respectively. This means that a low-mass star has assembled its final mass already before it starts burning hydrogen. For a high-mass protostar this is vice versa, i.e. due to its relatively short Kelvin-Helmholtz time a massive protostar undergoes hydrogen burning already during its formation, which leads to powerful radiation emission. Kahn (1974) and Wolfire & Cassinelli (1987) showed that in the case of a spherically symmetric collapse accretion rates of the order of  $10^{-3} M_{\odot} \text{ yr}^{-1}$  are required to overcome the radiation pressure and to guarantee ongoing accretion onto the protostar. This problem can be alleviated if accretion occurs along a preferred direction, e.g. through an accretion disc, which channels the radiation flux towards the low-density regions in the polar directions created by the outflows (Yorke & Sonnhalter, 2002). Observations of high-mass star-forming regions usually indicate accretion rates of the order of  $10^{-4} - 10^{-3} M_{\odot} \text{ yr}^{-1}$  (e.g. Beuther et al., 2002a,c, 2003; Beltrán et al., 2006) thus high enough to overcome the radiation pressure. Given these accretion rates typical formation times of massive stars are of the order of  $10^5 - 10^6 \text{ yr}$  (see e.g. Section 4.3.1 in McKee & Ostriker, 2007, and references therein). In the following we present different concepts which describe the origin of massive stars and which are highly discussed in recent literature.

### **Monolithic collapse model**

In the monolithic collapse model (McKee & Tan, 2002, 2003) the formation of massive stars takes place in turbulent, gravitationally bound cores. The turbulent motions are considered to be self-similar on all scales and are treated as an additional turbulent pressure which supports the core against rapid gravitational collapse. The core is therefore in an approximate virial equilibrium. Each core is expected to collapse to one or at most a few protostellar objects with accretion rates – enhanced by supersonic turbulence – of the order of  $10^{-3} M_{\odot} \text{ yr}^{-1}$ , i.e. high enough to overcome the effects of radiation pressure.

The model nicely explains the correspondence between the core mass function and the initial (stellar) mass function (Testi & Sargent, 1998) since each core more or less forms only one star with a star formation efficiency  $\epsilon_{\text{core}}$  of the order of 0.5. When rotation is included it also allows for discs and outflows frequently observed around high-mass protostars (see Section 2.2.2). Hence, the monolithic collapse model can be considered as an extrapolation of the low-mass star formation theory with increased accretion rates due to supersonic turbulence.

However, there are some weak points in this model. First of all, the model requires that the mass of the turbulence-supported, quasi-equilibrium core has to be pre-assembled already before the collapse sets in. In a highly turbulent molecular cloud, however, it is not clear how this can be achieved. Secondly, there is a timescale problem arising from the collapse of cores with different densities and masses (Clark et al., 2007). Thirdly, it was criticised that turbulent massive cores would fragment and form many low-mass stars rather than a single high-mass star (Dobbs et al., 2005). However, it was shown that radiative heating from the protostars heats up the core thus suppressing further fragmentation and promoting the formation of a few massive stars (Krumholz et al., 2007, 2010).

### **Competitive accretion**

In the alternative competitive accretion model (Bonnell et al., 1997, 2001) stars form in a clustered environment. Since many stars are present in a small region, they have to compete with each other for the available gas. The ability to accrete strongly depends on the position in the cluster and the protostellar mass. A protostar in the centre of the cluster will have a higher accretion rate than one in the outskirts as on average gas is flowing towards the centre due to its deeper gravitational potential. Similarly a protostar with a high mass affects the gas in its immediate surroundings out to greater distances than a low-mass protostar thus also increasing its ability to accrete gas from the common gas reservoir. Both effects lead to the fact that already massive stars keep on gaining mass with accretion rates higher than lower mass stars, which results in a stellar mass distribution similar to the initial mass function. Hence, one of the main differences to the monolithic collapse model is that in competitive accretion the mass of a star is gathered during the star formation process whereas in the monolithic collapse it is gathered already before star formation sets in.

One point of criticism is that the numerical simulations used to study this model usually have a turbulent energy  $E_{\text{turb}}$  significantly smaller than the gravitational energy  $E_{\text{pot}}$ , while observations suggest a ratio of  $E_{\text{turb}}/E_{\text{pot}} \simeq 1$ . Another objection is that the typical accretion rates found in these simulations are significantly smaller than that expected in the monolithic collapse model and therefore might not be high enough to overcome the radiation pressure which would cause the accretion to halt.

### **Stellar collisions**

A third and somewhat exotic model of massive star formation was suggested by Bonnell et al. (1998). The authors suggested that massive stars could form via stellar collisions. However, stellar densities of  $\sim 10^8$  stars  $\text{pc}^{-3}$  are required for this, which is by far greater than any stellar density observed in our Galaxy (e.g. Baumgardt & Klessen, 2011). Furthermore, the mass loss of such dense star cluster must be finely tuned to reach observed stellar densities and to leave the cluster marginally bound. Finally, it is difficult to explain how this model can account for the discs and outflows frequently observed around massive protostars. Hence, this model is considered as being rather exotic, nevertheless stellar collisions might occasionally occur under extreme condition as present in the densest young cluster.

### **Fragmentation-induced starvation**

A fourth model of massive star formation was recently suggested by Peters et al. (2010a,b). In this model the gas flow directed to the centre of the core is shielded by protostars surrounding the central part. These protostars, which have been formed during subsequent fragmentation of the core, accrete the infalling gas before it can reach the protostars in the centre. Hence, the central objects, which are usually the most massive objects as they have formed first, starve out of material they normally could accrete if no surrounding protostars were present. This behaviour, which is opposite to the effect of competitive accretion, was also detected in other, recent simulations of massive star formation (Peters et al., 2011; Girichidis et al., 2011, 2012).

### **Summary of the massive star formation process**

In this section we have introduced four different models of massive star formation. The monolithic collapse model and the competitive accretion model are the best studied models so far while stellar collisions nowadays are considered as rather unlikely. Though partly describing opposite effects, this does not mean that the different models are exclusive of each other. Which mode of star formation dominates in nature is not yet answered by observations, however, most likely it is some combination of the different models discussed above where the importance of each mode strongly depends on the actual conditions.

### 2.2.2. Discs and outflows

In the theory of star formation discussed so far we have neglected the effect of rotation and magnetic fields. However, as already pointed out in Section 2.1, star forming clumps/cores usually reveal some amount of rotational energy as well as relatively strong magnetic fields. On core scales the amount of rotational energy found is rather small ( $\beta_{\text{rot}} \sim 0.01$ ). However, due to the conservation of angular momentum during the collapse the rotation speed increases until the gas hits the centrifugal barrier, i.e. a rotational supported accretion disc builds up, in which the protostars form. As the discs are strongly magnetised, they can eject large amounts of gas up to a few pc into the surrounding medium (see Section 4 for a detailed discussion of the launching mechanism). These large-scale, so-called molecular outflows usually reveal a bipolar shape along the rotation axis of the disc (see for example Fig 2.2). This picture was confirmed in numerous simulations of low-mass star formation (e.g. Allen et al., 2003; Banerjee & Pudritz, 2006; Price & Bate, 2007; Mellon & Li, 2008; Hennebelle & Fromang, 2008; Hennebelle & Teyssier, 2008; Hennebelle & Ciardi, 2009; Duffin & Pudritz, 2009; Machida et al., 2011; Price et al., 2012). In the following we will briefly mention the actually observed properties of discs and outflows around both low- and high-mass protostars focussing on the earliest stage of protostellar evolution, i.e. the Class 0 stage.

Over the last decades, there has been a large number of observations of discs and outflows around young low-mass protostars (due to the large number of possible citations we rather refer to seminal reviews on this topic like Arce et al., 2007; Klein et al., 2007; McKee & Ostriker, 2007; Williams & Cieza, 2011, including numerous important references). Typical observed sizes of protostellar discs reach up to a few 100 AU, total disc masses range from  $10^{-3} - 10^{-1} M_{\odot}$  with an average around  $0.005 M_{\odot}$ . The outflows driven by the protostellar discs are significantly larger than the discs themselves reaching typical sizes of  $0.1 - 1$  pc. Outflow velocities range from about  $10 \text{ km s}^{-1}$  up to a few  $100 \text{ km s}^{-1}$  and derived dynamical ages<sup>2</sup> for Class 0 objects from a few  $10^3$  yr to a few  $10^4$  yrs. Typical mass and momentum outflow rates are of the order of  $10^{-7} - 10^{-6} M_{\odot} \text{ yr}^{-1}$  and  $10^{-5} M_{\odot} \text{ km s}^{-1} \text{ yr}^{-1}$ , respectively. Outflows from low-mass protostars are usually highly collimated with collimation factors, i.e. the ratio of the length to the width, ranging from 3 to  $> 20$ . To summarise, the picture of low-mass star formation via disc accretion and associated outflows is a broadly confirmed theory widely accepted among astrophysicists.

In the case of massive star formation the question whether massive protostars form in accretion discs just as their low-mass counterparts was discussed controversially for a long time. However, in the last years there has been an increasing number of observations of discs around high-mass protostellar objects. These observations show that there seem to exist two types of discs (see Cesaroni et al., 2007, for a recent review). The first one are so-called toroids which are large-scale ( $\sim 10\,000$  AU) discs with masses in excess of

---

<sup>2</sup>The dynamical age of an outflow is defined as the size of the outflow divided by the characteristic outflow speed.

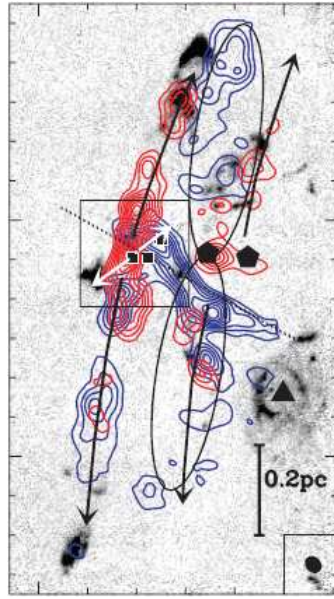


**Figure 2.2.:** CO emission (contours) overlaid on the grey-scale H<sub>2</sub> emission in the massive star forming region IRAS 05358+3543. The ellipses and arrows present the presumable positions of molecular outflows. (Credit: Beuther et al. 2002a, A&A, 387, 931. Reproduced with permission © ESO)

10 M<sub>⊙</sub> and in general more massive than the central protostellar object. These toroids are usually not rotationally supported, i.e. sub-Keplerian discs with very high infall rates of up to 10<sup>-2</sup> M<sub>⊙</sub> yr<sup>-1</sup>. The other kind of discs are rotationally supported discs with masses of the order of 0.1 – 10 M<sub>⊙</sub> and thus usually less massive than the central object. Typical sizes of the rotationally supported discs range from a few 100 AU up to a few 1000 AU (e.g. Fuller et al., 2001; Shepherd et al., 2001; Fernández-López et al., 2011; Preibisch et al., 2011).

Outflows observed around high-mass protostars are in general much more powerful than those from low-mass protostars. Typical mass and momentum outflow rates are of the order of 10<sup>-5</sup> – 10<sup>-3</sup> M<sub>⊙</sub> yr<sup>-1</sup> and 10<sup>-4</sup> – 10<sup>-2</sup> M<sub>⊙</sub> km s<sup>-1</sup> yr<sup>-1</sup>, respectively (e.g. Beuther et al., 2002c; Zhang et al., 2005; Shi et al., 2010; Wang et al., 2011; Ren et al., 2011). Sizes (0.1 – 1 pc) and characteristic velocities (10 – 1000 km s<sup>-1</sup>) of the massive outflows on the other hand are similar to those around low-mass objects thus having dynamical ages up to a few 10<sup>4</sup> yr, which corresponds to the protostar still being in the Class 0 stage. In general, observations show that outflows around high-mass protostars are less collimated than their low-mass counterparts with collimation factors around 2 (e.g. Ridge & Moore, 2001; Wu et al., 2004). However, also significantly better collimated outflows with collimation factors as high as 10 have been found (Beuther et al., 2002a, 2004, but see also Fig. 2.2). Interestingly there seems to be a correlation between outflow age and collimation showing that young outflows (≲ 10<sup>4</sup> yr) seem to be stronger collimated than older outflows. Based on this observation, Beuther & Shepherd (2005)

suggest an evolutionary scenario in which in the earliest stage well-collimated, magnetically driven outflows form. Later on, due to the increasing luminosity of the protostar and the build-up of HII-regions, the outflows get progressively less collimated over time. Interestingly, massive outflows are often observed to consist of two different velocity components, a fast, well-collimated inner component, and a low-velocity, wide-angle, outer component in which the former is embedded (e.g. Beuther et al., 2004; Ren et al., 2011). Such two components are also frequently observed around low-mass objects (see Bachiller, 1996, for an overview).

To summarise, in the last years there has been an increasing number of observations of discs and outflows around massive protostars indicating that massive stars indeed form via disc accretion similarly to low-mass stars with disc sizes/masses and outflow rates significantly above those of low-mass objects. However, radiation effects coming into play at higher masses, i.e. later stages, will significantly influence the formation process in that stage.

### 2.2.3. The initial mass function

One particularly interesting property of the star formation process is the distribution of the initial stellar masses. This mass distribution reveals a surprisingly uniform shape in many different star forming regions in the present day universe and is usually described by the *initial mass function* (IMF),  $\phi(m)$ . The first determination of the IMF in the solar neighbourhood was done by Salpeter (1955), who showed that the number of stars with masses in the range  $m$  to  $m + dm$  is approximately given by

$$\phi(m)dm \propto m^{-2.35} dm. \quad (2.7)$$

However, newer observations have shown that the approximation by a single power-law is too simple. A frequently used parametrisation of the IMF is given by a broken power-law (Kroupa, 2001)

$$\phi(m) \propto \begin{cases} m^{-0.3} & \text{for } 0.01 M_{\odot} \leq m < 0.08 M_{\odot} \\ m^{-1.3} & \text{for } 0.08 M_{\odot} \leq m < 0.5 M_{\odot} \\ m^{-2.3} & \text{for } 0.5 M_{\odot} \leq m. \end{cases} \quad (2.8)$$

An alternative description of the IMF below  $\sim 1 M_{\odot}$  is given by Miller & Scalo (1979), who approximated  $\phi$  by a log-normal distribution

$$\phi(\log m) \propto \exp\left(-\log\left(\frac{m}{m_c}\right)^2 / 2\sigma^2\right) \quad (2.9)$$

with typical values of  $m_c \simeq 0.2 M_{\odot}$  and  $\sigma \simeq 0.55$  (Chabrier, 2005). Here, the IMF is given in the logarithmic representation, i.e.  $\phi(\log m)$  gives the number of stars per logarithmic mass interval<sup>3</sup>. Above  $1 M_{\odot}$  the IMF is again given by Eq. 2.8.

---

<sup>3</sup>We note that in the logarithmic representation the absolute values of the exponents given in Eq. 2.8 are smaller by 1.

We note that the distribution of the core masses (CMF) reveals a shape qualitatively similar to the IMF (see e.g. the review by Ward-Thompson et al., 2007), which points to a direct correlation between the CMF and the IMF. However, the nature of this correlation as well as the actual functional form of the IMF are still highly debated (e.g. Bastian et al., 2010). Several models have been developed in the past to explain the particular shape of the IMF and its connection to the CMF. However, as a detailed discussion of the IMF and its origin would be beyond the scope of this work, we refer the reader to the recent review of Bastian et al. (2010). Finally, we note that in this work we will not consider the effect of magnetic fields on the shape of the IMF for two reasons. Firstly, we do not follow the simulations to the end of the star formation process and secondly, only a couple of protostars form in our simulations, which makes reliable conclusions about the IMF impossible.



## 3. Magnetohydrodynamics

In this chapter I briefly describe the fundamental magnetohydrodynamical (MHD) equations which govern the evolution of an astrophysical fluid under the influence of magnetic fields and self gravity. A more detailed consideration of the equations of MHD and their derivation can be found in standard text books (e.g Shu, 1992; Padmanabhan, 2000). I will also discuss two very general effects of the magnetic field in the formation process of stars, namely the stabilisation against gravitational induced collapse and the removal of angular momentum.

### 3.1. The magnetohydrodynamical equations

Conservation laws play an important role in fluid dynamics just like they do in other fields of physics. Based on the conservation of mass, momentum and energy three fundamental equations can be derived for a magnetised (astrophysical) fluid corresponding to the three first moments of the Boltzmann equation. Two further equations governing the evolution of the magnetic field and an equation of state are necessary to close this system of equations. For the case of ideal MHD we assume that the conductivity of the fluid is extremely high, ideally infinity, and that the gas and the magnetic field are coupled perfectly to each other. In the following we briefly discuss the equations of MHD. We note that all equations are given in the Eulerian frame. This is a fixed frame of reference (laboratory frame) in which at all points in space the physical quantities are defined. In contrast to that, in the Lagrangian frame of reference not considered here, the motion of individual fluid elements is followed, i.e. a frame comoving with the fluid particle is considered.

#### 3.1.1. Mass conservation

The conservation of mass is described by the *continuity equation*

$$\frac{\partial \rho}{\partial t} + \nabla(\rho \mathbf{v}) = 0, \quad (3.1)$$

where  $\rho$  is the gas density and  $\mathbf{v}$  the velocity of the fluid element. The continuity equation shows that the mass within a given volume can only be changed by a mass flux through its surface. If different chemical species would be considered, a source term would appear on the right hand side of Eq. 3.1. An astrophysical example would be the formation or dissociation of molecular hydrogen. Since here no chemical processes are considered, Eq. 3.1 remains valid for the course of this work.

### 3.1.2. Momentum equation

The conservation of momentum under the influence of gravity and magnetic fields is described by the *equation of motion*

$$\frac{\partial(\rho v_i)}{\partial t} + \frac{\partial(\rho v_i v_k)}{\partial x_k} = -\frac{\partial P}{\partial x_i} - \rho \frac{\partial \Phi}{\partial x_i} - \frac{1}{8\pi} \frac{\partial B_k^2}{\partial x_i} + \frac{1}{4\pi} B_k \frac{\partial B_i}{\partial x_k} \quad (3.2)$$

for the  $i$ -th component of the momentum. Here  $B$  is the magnetic field strength and  $P$  the thermal pressure. The gravitational potential  $\Phi$  is determined by Poisson's equation

$$\Delta \Phi = 4\pi G \rho, \quad (3.3)$$

where  $\Delta$  is the Laplace operator and  $G$  the gravitational constant. In vector notation Eq. 3.2 reads

$$\frac{\partial \mathbf{v}}{\partial t} + (\mathbf{v} \nabla) \mathbf{v} = -\frac{1}{\rho} \nabla P - \nabla \Phi - \frac{1}{\rho} \frac{\nabla B^2}{8\pi} + \frac{1}{\rho} \frac{(\mathbf{B} \nabla) \mathbf{B}}{4\pi}. \quad (3.4)$$

The second to last term on the right hand side of this equation shows that there is a contribution to the acceleration of gas due to the gradient in the magnetic pressure. This part of the Lorentz force acts to spread out the magnetic field lines into a more uniform configuration. The last term in Eq. 3.4 describes the magnetic tension, which tries to stretch out curved field lines in analogy to a bent rubber band.

### 3.1.3. Energy conservation and equation of state

The conservation of energy can be formulated in vector notation as follows:

$$\frac{\partial}{\partial t} e + \nabla \cdot \left( \mathbf{v} \left( \rho e + P + \frac{B^2}{8\pi} \right) - \frac{1}{4\pi} (\mathbf{v} \mathbf{B}) \mathbf{B} \right) = -\rho \mathbf{v} \nabla \Phi. \quad (3.5)$$

Here  $e$  is the total energy density of the fluid element, i.e. the sum of kinetic and thermal energy density  $e_{\text{int}}$

$$e = \rho \frac{v^2}{2} + e_{\text{int}}. \quad (3.6)$$

The relation between the gas pressure and the thermal energy density is described by the equation of state

$$P = (\gamma - 1) e_{\text{int}}, \quad (3.7)$$

where  $\gamma$  is the adiabatic exponent, which is set to  $5/3$  throughout this work. The temperature can be calculated from the pressure via

$$P = \frac{\rho k_B T}{\mu_{\text{mol}} m_p}, \quad (3.8)$$

where  $k_B$  is the Boltzmann constant,  $m_p$  the proton mass, and  $\mu_{\text{mol}}$  the mean molecular weight of the molecules of the gas. Throughout this work we use  $\mu_{\text{mol}} = 2.3$  for the mean molecular weight, which is a reasonable value for molecular hydrogen gas in present day star forming regions.

### 3.1.4. The induction equation

The above set of equations can be completed by further equations governing the evolution of the magnetic field. The first equation is the induction equation, which can be derived from Maxwell's equations:

$$\frac{\partial \mathbf{B}}{\partial t} = \nabla \times (\mathbf{v} \times \mathbf{B}). \quad (3.9)$$

The induction equation describes the transport of magnetic flux with the gas under ideal MHD conditions. In addition to that, one has to obey the constraint for the divergence of the magnetic field

$$\nabla \cdot \mathbf{B} = 0. \quad (3.10)$$

With the equations 3.1 – 3.10 we now have a closed set of equations which in principle could be solved. However, due to the complexity of the equations an analytical solution is possible only under very specialised circumstances. In general, however, only a numerical solution, as done in the simulations presented in this work, is possible.

### 3.1.5. Magnetohydrodynamical waves

In analogy to the sound speed

$$c_s = \sqrt{\frac{k_B T}{\mu_{\text{mol}} m_p}} \quad (3.11)$$

for a fluid without any magnetic fields, one can derive the speed with which small perturbations in a resting magnetised medium will propagate by linearising the magnetohydrodynamical equations. As the magnetic field imprints a preferred direction on the fluid, the propagation speed of the magnetohydrodynamical waves depends on its direction, e.g. parallel or perpendicular to the field lines. As the detailed derivation of the magnetohydrodynamical waves is discussed in detail in numerous textbooks (see, e.g. Shu, 1992; Padmanabhan, 2000), in the following we only present the main results.

There exist three different magnetohydrodynamical waves in a magnetised fluid. The first one is the so-called Alfvén wave which has a propagation speed of

$$v_A = \frac{B}{\sqrt{4\pi\rho}}, \quad (3.12)$$

where  $B$  is the strength of the local magnetic field. The Alfvén wave can be considered as a transversal wave in which a perturbation  $\delta B$  perpendicular to the original magnetic field  $B$  is transported along the direction of the field line. One can imagine the Alfvén wave as a wave on a string where the restoring force is provided by the magnetic tension.

The two remaining waves are more complex in nature and represent a mixture of acoustic waves and purely magnetic waves. For the fast magnetic wave the propagation speed is

$$v_{A,\text{fast}} = \left( \frac{c_s^2 + v_A^2}{2} + \sqrt{\left( \frac{c_s^2 + v_A^2}{2} \right)^2 - c_s^2 v_A^2 \cos^2 \psi} \right)^{1/2}, \quad (3.13)$$

where  $\psi$  is the angle between the propagation direction and the magnetic field and  $v_A$  the Alfvén velocity. Hence the speed of the fast magnetic wave, which sometimes is also called the magnetosonic wave, ranges from  $\max(c_s, v_A)$  for  $\psi = 0$  up to  $\sqrt{c_s^2 + v_A^2}$  for  $\psi = \pi/2$ .

The other wave not discussed so far is the slow magnetic wave, which propagates with a speed of

$$v_{A,\text{slow}} = \left( \frac{c_s^2 + v_A^2}{2} - \sqrt{\left( \frac{c_s^2 + v_A^2}{2} \right)^2 - c_s^2 v_A^2 \cos^2 \psi} \right)^{1/2}. \quad (3.14)$$

Hence, the slow magnetic wave travels with  $\min(c_s, v_A)$  parallel to the magnetic field whereas the transversal propagation is suppressed.

### 3.1.6. Non-ideal MHD effects

So far we have considered the behaviour of a fluid under the assumption of ideal MHD, i.e. the conductivity is infinite and the gas and the magnetic field are coupled perfectly to each other. When relaxing these conditions, one obtains two non-ideal MHD effects: Ohmic dissipation in the case of a finite conductivity and ambipolar diffusion in the case of an imperfect gas-field coupling.

We first consider the case that the conductivity  $\sigma$  of the fluid is finite. When deducing the induction equation (Eq. 3.9) from Maxwell's equations under the condition that  $\sigma$  remains finite, the induction equation now reads

$$\frac{\partial \mathbf{B}}{\partial t} = \nabla \times (\mathbf{v} \times \mathbf{B}) - \nabla \times \left( \frac{c^2}{4\pi\sigma} (\nabla \times \mathbf{B}) \right). \quad (3.15)$$

It can be easily seen that Eq. 3.15 reduces to Eq. 3.9 in the case of an infinitely high  $\sigma$ . On the other hand, when assuming that  $\sigma$  is finite and spatially constant, the last term in Eq. 3.15 reduces to  $\frac{c^2}{4\pi\sigma} \nabla^2 \mathbf{B}$ . Hence, in this case when setting  $\mathbf{v} = 0$ , Eq. 3.15 resembles a diffusion equation for the magnetic field with a diffusion coefficient  $D = c^2/4\pi\sigma$ . By comparing the two terms on the right hand side of Eq. 3.15 one can estimate the relative importance of the advection (1. term) to the diffusion (2. term) for the magnetic field. For typical astrophysical fluids it was shown that Ohmic dissipation, i.e. the second term, starts to get important for densities above  $10^{-12} \text{ g cm}^{-3}$  (Nakano et al., 2002).

The second non-ideal MHD effect to consider is ambipolar diffusion. Strictly spoken the magnetic field has no direct influence on the neutral molecules and dust grains in the ISM but only acts on the charged ions, which for typical astrophysical fluid account for a fraction of about  $10^{-6} - 10^{-4}$  of all particles. However, the ions transfer the force exerted by the magnetic field to the neutrals by the friction force, i.e. by collisions between charged and neutral particles. For ideal MHD the coupling between ions and neutrals is considered to be very efficient so that there is no relative motion between both constituents, i.e. the collision frequency is (almost) infinitely high so that the magnetic field more or less directly acts on the uncharged particles. However, if

the coupling between ions and neutrals decreases, the influence of the magnetic field on the bulk of material, i.e. the neutral part, decreases as well as. Hence, the ions, and thus also the magnetic field, can develop a relative velocity with respect to the bulk of material. In the induction equation the effect of ambipolar diffusion manifests itself as (e.g. Brandenburg & Zweibel, 1994)

$$\frac{\partial \mathbf{B}}{\partial t} = \nabla \times (\mathbf{v} \times \mathbf{B}) + \nabla \times \left[ \frac{((\nabla \times \mathbf{B}) \cdot \mathbf{B})}{4\pi\gamma_{\text{AD}}\rho_i\rho_n} \mathbf{B} - \frac{B^2}{4\pi\gamma_{\text{AD}}\rho_i\rho_n} (\nabla \times \mathbf{B}) \right], \quad (3.16)$$

where  $\rho_i$  and  $\rho_n$  are the densities of the charged and neutral particles, respectively, and  $\gamma_{\text{AD}}$  the collisional coupling constant. The term

$$\eta_{\text{AD}} = \frac{B^2}{4\pi\gamma_{\text{AD}}\rho_i\rho_n} \quad (3.17)$$

is the ambipolar diffusivity. As can be seen, ambipolar diffusion does *not only* introduce a magnetic diffusion part in the induction equation but also a second term proportional to  $(\nabla \times \mathbf{B}) \cdot \mathbf{B}$ , which has to be taken into account for the correct modelling of ambipolar diffusion. However, just like for Ohmic dissipation, for an infinitely high coupling constant  $\gamma_{\text{AD}}$ , i.e. a perfect coupling between ions and neutrals, Eq. 3.16 reduces to Eq. 3.9.

Although we consider only ideal MHD in the simulations presented in this work, also here magnetic diffusion occurs. Since in the code the equations of MHD are approximated by discretised differential equations, they are accurate only up to a certain order  $n$  in space and time (usually  $n = 2$  for the scheme used in this work), which results in errors of the order of  $n + 1$ . These discretisation errors mimic the existence of diffusive processes. When numerical diffusion applies to the momentum equation (Eq. 3.4), one usually talks about numerical viscosity, whereas when it applies to the magnetic field (Eq. 3.9), it is often called numerical resistivity. Although numerical diffusion is usually reduced to a minimum in standard Eulerian grid codes, it cannot be avoided completely. Hence, also in the simulations presented in this work magnetic diffusion will occur, which in principle allows the gas to slip perpendicular to the magnetic field lines.

## 3.2. The mass-to-flux ratio

Considering an oblate ellipsoid<sup>1</sup> of gas that is threaded by a uniform magnetic field along the minor axis, one can analyse its stability against gravitationally induced collapse by applying the virial theorem (e.g. Spitzer, 1968). As can be shown, there exists a critical mass below which the cloud is stabilised against collapse by the magnetic field

$$M_{\text{crit}} = \frac{c_1}{3\pi} \left( \frac{5}{G} \right)^{1/2} \Phi. \quad (3.18)$$

Here,  $c_1$  is a numerical constant that depends on the given geometry,  $G$  the gravitational constant, and

$$\Phi = \int_A B dA \quad (3.19)$$

---

<sup>1</sup>The initially spherical core becomes oblate due to its contraction mainly along the field lines.

the magnetic flux through the ellipsoid, where  $A$  is the cross section of the core. From numerical calculations Mouschovias & Spitzer (1976) found  $c_1$  to be 0.53. Hence, there is a critical ratio of the mass to the magnetic flux, denoted as the *critical mass-to-flux ratio*, below which the collapse of a gas cloud perpendicular to the magnetic field lines is suppressed. Its numerical value reads

$$\left(\frac{M}{\Phi}\right)_{\text{crit}} = \frac{0.53}{3\pi} \left(\frac{5}{G}\right)^{1/2} = \frac{0.13}{\sqrt{G}}. \quad (3.20)$$

To estimate the dynamical importance of the magnetic field compared to gravity for a given gas cloud, one can calculate its actual mass-to-flux ratio  $M/\Phi$  and compare it to the critical mass-to-flux ratio. Throughout this work we will express the mass-to-flux ratio of a cloud in units of the critical mass-to-flux ratio, i.e.

$$\mu = \frac{M}{\Phi} / \left(\frac{M}{\Phi}\right)_{\text{crit}} = \frac{M}{\Phi} / \frac{0.13}{\sqrt{G}}. \quad (3.21)$$

A cloud with a value of  $\mu > 1$  cannot be stabilised against gravitational collapse by the magnetic field and is therefore denoted as supercritical whereas for  $\mu < 1$  the cloud is stable and is denoted as subcritical.

We note that when normalising the mass and magnetic flux with the cross section of the cloud, one can – at least approximately – rewrite the mass-to-flux ratio as

$$\frac{M}{\Phi} \simeq \frac{\Sigma}{B}, \quad (3.22)$$

where  $\Sigma$  is the column density along any given field line. In this representation it can be seen that for ideal MHD, where gas is allowed to move freely only along magnetic field lines, the mass-to-flux ratio for a given field line can never change. However, in numerical simulations for this to be true one would have to integrate along the entire field line, which in general is difficult to accomplish and therefore usually not done. The fact that  $\Sigma/B$  should not change under ideal MHD conditions is also denoted as *flux freezing* as the magnetic field is perfectly coupled to the gas, in a manner of speaking frozen in the gas. This flux freezing can also directly be inferred from the induction equation (Eq. 3.9).

We again emphasise that from now on whenever mentioning the *mass-to-flux ratio* we always refer to the normalised, dimensionless mass-to-flux ratio (Eq. 3.21) and not to the actual dimensional form  $M/\Phi$ .

## 3.3. Magnetic braking

### 3.3.1. Aligned rotator

By taking the cross product of the momentum equation (Eq. 3.4) with the position vector  $\boldsymbol{x}$ , one can derive the angular momentum equation. From this equation it can be inferred that also the magnetic field can transport angular momentum. In a simplified setup Mouschovias & Paleologou (1980) calculated the typical timescale for the spin

down of a cylindrical gas cloud due to magnetic fields. In the following we will briefly recapitulate their derivation, for a more detailed consideration we refer to the original publication.

We consider a cylindrical gas cloud of radius  $R$ , half-thickness  $Z$  and uniform density  $\rho_c$  threaded by a uniform magnetic field  $\mathbf{B}_c$  parallel to the cylinder axis. The cloud is embedded in a low-density medium with constant density  $\rho_{\text{ext}}$  and a magnetic field equal to the cloud's magnetic field. We assume that the cloud is initially rotating rigidly around the symmetry axis with an angular frequency  $\Omega_c$  whereas the surrounding medium is at rest. We place the centre of the cloud at the origin and set the cylinder axis, i.e. the rotation axis, to the  $z$ -axis. Hence the magnetic field is  $\mathbf{B}_c = (0, 0, B_c)$  and it is advantageous to use the cylindrical polar coordinates  $(r, z, \phi)$ .

Under the afore made assumptions the induction equation in the ambient medium (Eq. 3.9) reduces to

$$\frac{\partial B_\phi(r, z, t)}{\partial t} = r B_c \frac{\partial \Omega(z, t)}{\partial z}, \quad (3.23)$$

where  $\Omega = v_\phi/r$  is the angular velocity of the gas. Here the fact has been used that  $\Omega$  does not depend on  $r$  (as can be shown easily) and that  $B_\phi$  has the functional form  $B_\phi = r f(z, t)$ . In addition, from the  $\phi$  component of the momentum equation (Eq. 3.4) one can infer that

$$\frac{\partial \Omega(z, t)}{\partial t} = \frac{B_c}{4\pi r \rho_{\text{ext}}} \frac{\partial B_\phi(r, z, t)}{\partial z}. \quad (3.24)$$

Combining Eqs. 3.23 and 3.24 we obtain a wave equation for the ambient medium

$$\frac{\partial^2 \Omega(z, t)}{\partial t^2} = v_{\text{A,ext}}^2 \frac{\partial^2 \Omega(z, t)}{\partial z^2}, \quad z > Z. \quad (3.25)$$

Here  $v_{\text{A,ext}}$  is the Alfvénic velocity in the external medium

$$v_{\text{A,ext}} = \frac{B_c}{\sqrt{4\pi \rho_{\text{ext}}}} \quad (3.26)$$

representing the propagation speed of torsional magnetic waves in the ambient medium.

To obtain the equation of motion for the cloud itself, we consider the change of its angular momentum, which is equal to the magnetic torque  $N$  at the surface of the cylinder, i.e.  $I_c \partial \Omega_c(t)/\partial t = N$ . The moment of inertia of the cylinder  $I_c$  per unit area is  $2Z\rho_c r^2$ . The torque of the magnetic field at the surface of the cylinder, which can be derived from the momentum equation, is  $N = 2r B_c B_\phi(r, z, t)/4\pi$ , where the factor 2 is due to the fact that the upper and lower surface of the cylinder have to be taken into account. Hence, the equation of motion becomes

$$\frac{\partial \Omega_c(t)}{\partial t} = \frac{B_c B_\phi(r, z, t)}{4\pi r Z \rho_c} \Big|_{z=Z}. \quad (3.27)$$

Taking the time derivative of this equation and using Eq. 3.23 to eliminate  $B_\phi$ , one obtains the following equation, which is valid at the upper/lower surface of the cylinder:

$$\frac{\partial^2 \Omega_c(t)}{\partial t^2} = \frac{1}{Z} \frac{\rho_{\text{ext}}}{\rho_c} v_{\text{A,ext}}^2 \frac{\partial \Omega(z, t)}{\partial z} \Big|_{z=Z}. \quad (3.28)$$

In combination with Eq. 3.25 we can now describe the evolution of the angular velocity of the cloud and the surrounding medium. With the boundary conditions

$$\Omega(z = \infty, t) = 0, \quad \Omega(Z, t > 0) = \Omega_c(t > 0), \quad \Omega(z, t) = \Omega(-z, t) \quad (3.29)$$

and the following normalisation

$$\tau = \frac{t}{Z/v_{A,\text{ext}}}, \quad \zeta = \frac{z}{Z}, \quad \rho = \frac{\rho_c}{\rho_{\text{ext}}} \quad (3.30)$$

one can rewrite Eqs. 3.25 and 3.28 as

$$\frac{\partial^2 \Omega}{\partial \tau^2} = \frac{\partial^2 \Omega}{\partial \zeta^2}, \quad \zeta > 1 \quad (3.31)$$

$$\frac{\partial^2 \Omega}{\partial \tau^2} = \frac{1}{\rho} \frac{\partial \Omega}{\partial \zeta}, \quad \zeta = 1. \quad (3.32)$$

The solution of this system of differential equations is given by

$$\Omega(\zeta, \tau) = \Omega_c \exp(-(\tau - \zeta + 1)/\rho) \quad \text{if } \tau - \zeta + 1 \geq 0; \quad (3.33)$$

$$= 0 \quad \text{otherwise} \quad (3.34)$$

and is valid for  $\zeta \geq 1$ . Here we have assumed that  $\Omega(\zeta < 1, \tau) = \Omega(\zeta = 1, \tau)$ . The above equation describes the propagation of a wavefront into the ambient medium. The condition  $\tau - \zeta + 1 \geq 0$  simply reflects the fact that no perturbations can be present ahead of the wavefront originating at  $\zeta = 1$  and  $\tau = 0$ .

The angular velocity of the cylinder is now given by evaluating Eq. 3.33 at  $\zeta = 1$  giving

$$\Omega_c(\tau) = \Omega_c \exp(-\tau/\rho). \quad (3.35)$$

Rewriting this in the dimensional form shows that the rotation of the cloud is slowed down in a characteristic timescale of

$$t_{\text{mag},\parallel} = \frac{\rho_c}{\rho_{\text{ext}}} \frac{Z}{v_{A,\text{ext}}}. \quad (3.36)$$

The physical interpretation of this timescale is easy to understand. The term  $Z/v_{A,\text{ext}}$  is the time the Alfvén wave in the external medium needs to travel the distance equal to the half-thickness of the cylinder, which we refer to as the Alfvén crossing time. Hence, the ratio of the cloud to external density times the Alfvén crossing time is exactly the time the wave has to travel to set an amount of the ambient medium in rotation which has the same moment of inertia  $I_{\text{ext}}$  as that of the cloud  $I_c$ .

### 3.3.2. Perpendicular rotator

Next we consider the braking of a cylinder with a magnetic field perpendicular to the rotation axis as derived by Mouschovias & Paleologou (1979). For reasons of clarity

we will constrain our consideration on the main results only. We consider the same cylinder as in the aligned case embedded in the same ambient medium. However, now the magnetic field is perpendicular to the overall rotation, i.e. perpendicular to the symmetry axis of the cylinder. The magnetic field in the ambient medium has initially only a radial<sup>2</sup> component

$$B_r = B_0 \frac{R}{r}, \quad r \geq R \quad (3.37)$$

whereas the toroidal and the  $z$ -component are initially zero everywhere. By a similar approach as for the former case one obtains a similar set of differential equations

$$\frac{\partial^2 \Omega(\xi, \tau)}{\partial \tau^2} = \frac{1}{\xi} \frac{\partial}{\partial \xi} \left[ \frac{\partial \Omega(\xi, \tau)}{\partial \xi} \right], \quad \xi > 1; \quad (3.38)$$

$$\frac{\partial^2 \Omega(\xi, \tau)}{\partial \tau^2} = \frac{2}{\rho} \frac{\partial \Omega(\xi, \tau)}{\partial \xi}, \quad \xi = 1, \quad (3.39)$$

where

$$\tau = \frac{2t}{R/v_{A,0}}, \quad \xi = \left( \frac{r}{R} \right)^2, \quad v_{A,0} = \frac{B_0}{\sqrt{4\pi\rho_{\text{ext}}}}. \quad (3.40)$$

The exact solution of the above problem, however, is very complex and includes Bessel functions, exponential and trigonometric functions (Mouschovias & Paleologou, 1979) which is why we do not consider it in detail here. Nevertheless, one can obtain a characteristic timescale for which the cylinder will be slowed down in the case of a perpendicular magnetic field, which is

$$t_{\text{mag},\perp} = \frac{1}{2} \left[ \left( 1 + \frac{\rho_c}{\rho_{\text{ext}}} \right)^{1/2} - 1 \right] \frac{R}{v_{A,0}}. \quad (3.41)$$

Physically this time can be understood as the time the Alfvén wave needs to travel radially outwards until it has reached a distance where the moment of inertia of the covered external medium is equal to the moment of inertia of the cloud  $I_c$ . For the calculation of this quantity it has to be taken into account that the Alfvén velocity in the ambient medium decreases as  $B_r$  decreases.

In case of a very large value of  $\rho_c/\rho_{\text{ext}}$  and for comparable  $Z$  and  $R$  one can see that  $t_{\text{mag},\perp}$  is roughly a factor of  $(\rho_c/\rho_{\text{ext}})^{1/2}$  smaller than  $t_{\text{mag},\parallel}$  (Eq. 3.36), i.e. in the case of a perpendicular magnetic field magnetic braking is more efficient. The reason for this is that in this case the Alfvén wave travels radially outwards thus gradually affecting regions with larger and larger moments of inertia.

### 3.4. Summary

In the beginning of this chapter we have presented the equations of ideal magnetohydrodynamics governing the evolution of a magnetised (astrophysical) fluid. In the following

---

<sup>2</sup>Here radial means cylindric radial with respect to the orientation of the cylindrical gas cloud.

we list all relevant equations which have to be solved simultaneously for a general magnetohydrodynamical problem:

$$\begin{aligned}
 \frac{\partial \rho}{\partial t} + \nabla(\rho \mathbf{v}) &= 0 \\
 \frac{\partial \mathbf{v}}{\partial t} + (\mathbf{v} \nabla) \mathbf{v} &= -\frac{1}{\rho} \nabla P - \nabla \Phi - \frac{1}{\rho} \frac{\nabla B^2}{8\pi} + \frac{1}{\rho} \frac{(\mathbf{B} \nabla) \mathbf{B}}{4\pi} \\
 \frac{\partial}{\partial t} e + \nabla \left( \mathbf{v} \left( \rho e + P + \frac{B^2}{8\pi} \right) - \frac{1}{4\pi} (\mathbf{v} \mathbf{B}) \mathbf{B} \right) &= -\rho \mathbf{v} \nabla \Phi \\
 e &= \rho \frac{v^2}{2} + e_{\text{int}} \\
 P &= (\gamma - 1) e_{\text{int}} \\
 \Delta \Phi &= 4\pi G \rho \\
 \frac{\partial \mathbf{B}}{\partial t} &= \nabla \times (\mathbf{v} \times \mathbf{B}) \\
 \nabla \mathbf{B} &= 0.
 \end{aligned}$$

We again emphasise that the above equations are valid under the conditions of ideal MHD only. We also briefly discussed non-ideal MHD effects like Ohmic dissipation and ambipolar diffusion and how they enter the induction equation, and the origin of numerical diffusion.

We also presented the different magnetohydrodynamical waves which can occur in a fluid and discussed the stabilising effect of magnetic fields against gravitationally induced collapse introducing the mass-to-flux ratio. We also briefly explained the general mechanism of how magnetic fields can remove angular momentum from a rotating structure. In the following we summarise all relevant quantities:

$$\begin{aligned}
 \text{Alfvén velocity:} & \quad v_A = \frac{B}{\sqrt{4\pi\rho}} \\
 \text{Mass-to-flux ratio:} & \quad \mu = \frac{M}{\Phi} \frac{0.13}{\sqrt{G}} \\
 \text{Magnetic braking time aligned rotator:} & \quad t_{\text{mag},\parallel} = \frac{\rho_c}{\rho_{\text{ext}}} \frac{Z}{v_{A,\text{ext}}} \\
 \text{Magnetic braking time perpendicular rotator:} & \quad t_{\text{mag},\perp} = \frac{1}{2} \left[ \left( 1 + \frac{\rho_c}{\rho_{\text{ext}}} \right)^{1/2} - 1 \right] \frac{R}{v_{A,0}}.
 \end{aligned}$$

## 4. The magnetohydrodynamical wind theory

In the previous chapter we have discussed the equations of magnetohydrodynamics. Due to their complexity these equations can be solved in their generality only numerically. However, before we come to the numerical solution of the MHD equations in the context of massive star formation, we firstly consider two examples relevant for this work where exact analytical solutions exist. As pointed out already before, usually some additional assumptions are required for an analytical solution of the equations of MHD. In what follows these assumptions are

- stationarity and
- axisymmetry.

Stationarity means that the solution is time-independent, hence all terms containing  $\partial/\partial t$  in Eqs. 3.1 – 3.10 can be omitted. Furthermore, the solution is symmetric with respect to a particular axis, here the  $z$ -axis. Hence, all quantities in the MHD equations only depend on two spatial coordinates, the cylindric radial coordinate  $r$  and the  $z$  coordinate. For all the calculations made in the remainder of this chapter one has to keep these assumptions in mind.

### 4.1. Centrifugally driven jets

Firstly, we consider the centrifugal acceleration mechanism describing the ejection and acceleration of gas from a Keplerian disc. The responsible mechanism can directly be inferred from the stationary and axisymmetric MHD equations, which have been analysed by several authors (e.g. Chandrasekhar, 1956; Mestel, 1961). The analysis is done in cylindrical coordinates, i.e.  $r$ ,  $z$  and  $\phi$ . The subscript “pol“ stands for the poloidal component of a vector quantity, i.e. the sum of the  $z$ - and  $r$ - component.

One key aspect of the solution of the stationarity and axisymmetric MHD equations is that it includes four so-called surface functions. These surface functions are constant on each magnetic surface, i.e. along any given magnetic field line. As the derivation of these four constants is longish and does not give any new insights, in the following we only show the final results by listing all four constants:

1. Combining the induction equation (Eq. 3.9), the divergence-free equation (Eq. 3.10) and the continuity equation (Eq. 3.1) reveals that the poloidal velocity is always parallel to the poloidal magnetic field

$$\rho \mathbf{v}_{\text{pol}} = k \mathbf{B}_{\text{pol}}, \quad (4.1)$$

where  $k$ , the so-called *mass loading*, is the first surface function, i.e. it is constant along any given field line. The mass loading represents the ratio of the mass flux to magnetic flux along each field line.

2. The second surface function that can be derived from the three aforementioned equations is the *angular velocity* of the magnetic surface

$$\omega = \frac{v_\phi}{r} - \frac{kB_\phi}{r\rho}, \quad (4.2)$$

where  $v_\phi$  is the rotation speed of the gas. The angular velocity  $\omega$  can be interpreted as the local rotation speed of the magnetic field.

3. Using the equation of motion (Eq. 3.4) yields the third surface function, the *angular momentum invariant*

$$l = rv_\phi - \frac{rB_\phi}{4\pi k}. \quad (4.3)$$

This is the angular momentum per unit mass removed by the outflow where a part of it is carried by the magnetic field.

4. Finally, making use of the energy equation (Eq. 3.5) yields the *energy invariant* along a poloidal field line

$$\epsilon = \frac{1}{2}v^2 + \Phi + h - \frac{r\omega B_\phi}{4\pi k}, \quad (4.4)$$

where  $h$  is the enthalpy. This equation is also called the Bernoulli equation. For the sake of simplicity, in the following analysis the effect of the thermal pressure is considered to be negligible, i.e. the enthalpy  $h$  is omitted.

The above results can now be applied to a situation adapted to star formation (e.g. Blandford & Payne, 1982; Pelletier & Pudritz, 1992; Spruit, 1996). For this purpose a thin disc in the midplane, i.e.  $z = 0$  threaded by a poloidal magnetic field is considered. This disc is rotating with the Keplerian velocity  $v_\phi = \sqrt{\frac{GM}{r}}$  around a point mass of mass  $M$ . As we consider a rotating system, it is helpful to go to a frame corotating with the magnetic field, i.e. rotating with the angular velocity  $\omega$ . This can be done by modifying the Bernoulli equation (Eq. 4.4) as follows:

$$\epsilon' = \epsilon - l\omega = \frac{1}{2}v_{\text{pol}}^2 + \frac{1}{2}(v_\phi - r\omega)^2 + \Phi_{\text{cg}}, \quad (4.5)$$

where  $\Phi_{\text{cg}}$  is the centrifugal-gravitational potential

$$\Phi_{\text{cg}}(r, z, \omega) = -\frac{GM}{\sqrt{r^2 + z^2}} - \frac{1}{2}\omega^2 r^2. \quad (4.6)$$

As can be seen,  $\epsilon'$  is also a constant along any field line since it was derived by the combination of three surface functions. When comparing Eq. 4.5 to Eq. 4.4 it can be

seen that all magnetic field terms have vanished. This is due to the fact that in the rotating frame the gas flow is strictly parallel to the magnetic field and therefore the Lorentz force vanishes. Nevertheless, Eqs. 4.4 and 4.5 are equivalent despite their very different appearance.

Considering Eq. 4.2 one can put further constraints on the value of  $\omega$ . Due to symmetry arguments  $B_\phi$  has to be zero in the midplane. Hence, the angular velocity of the magnetic surface  $\omega$  at radius  $r_0$  and  $z = 0$  has to be equal to the gas rotation frequency in the midplane<sup>1</sup>, i.e.

$$\omega = \frac{v_\phi(r_0, z = 0)}{r_0} = \sqrt{\frac{GM}{r_0^3}}. \quad (4.7)$$

This means that in the midplane the magnetic field and the gas are rotating with the same angular frequency as expected from the conditions of ideal MHD.

For the further consideration it is now assumed that the magnetic field is strong enough to retain a purely poloidal structure, i.e. it performs a rigid rotation which guarantees that  $B_\phi$  remains zero. Hence, also above the midplane each fluid element is forced to corotate with the magnetic field like a bead on a wire. The rotation velocity is therefore  $v_\phi = r\omega$ , where  $\omega$  is the rotation frequency of the magnetic field line threading the fluid element. Hence, Eq. 4.5 reduces to

$$\epsilon' = \frac{1}{2}v_{\text{pol}}^2 + \Phi_{\text{cg}}. \quad (4.8)$$

It can now be seen that the change of the poloidal gas velocity  $v_{\text{pol}}$  only depends on the behaviour of  $\Phi_{\text{cg}}$  along a given field line. This is due to the fact that the gas can move freely only along the magnetic field lines. To analyse for which magnetic field configuration an outflow can be launched, in Fig. 4.1 the line where  $\Phi_{\text{cg}}$  is equal to the value at  $(r = r_0, z = 0)$ ,  $\Phi_{\text{cg}}(r_0, 0) = \sqrt{\frac{GM}{r_0^3}}$  is shown. It can be inferred from Eq. 4.8 that, if the magnetic field line through the point  $(r = r_0, z = 0)$  connects to a point where  $\Phi_{\text{cg}}$  is larger than  $\sqrt{\frac{GM}{r_0^3}}$ , this would cause  $v_{\text{pol}}$  to drop and hence the gas to fall back on the disc. From Fig. 4.1 it can be seen that this happens if the inclination is too small, i.e. the magnetic field lines are almost perpendicular to the disc. Hence, a minimum inclination of the field lines with respect to the  $z$ -axis is required so that they reach to a region where  $\Phi_{\text{cg}} < \Phi_{\text{cg}}(r_0, 0)$ . In this case  $v_{\text{pol}}$  will increase, i.e. an outflow will be launched.

One can show that to first order in  $r$  and close to the point  $(r = r_0, z = 0)$  the plotted line in Fig. 4.1 can be parametrised as

$$z = \pm\sqrt{3}(r - 1), \quad (4.9)$$

hence the gradient at  $(r = r_0, z = 0)$  is  $\sqrt{3}$ . This means that magnetic field lines require an inclination larger than

$$\alpha_{\text{min}} = 90^\circ - \text{atan}(\sqrt{3}) = 30^\circ \quad (4.10)$$

---

<sup>1</sup>Recall that the disc is rotating Keplerian.

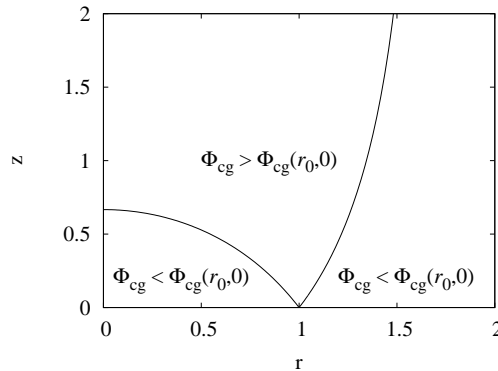


**Figure 4.1.:** Contour where  $\Phi_{cg} = \Phi_{cg}(r_0, 0) = \sqrt{\frac{GM}{r_0^3}}$ . An outflow can be launched if the field line starting from  $(r_0, 0)$  reaches to the right part where  $\Phi_{cg} < \Phi_{cg}(r_0, 0)$ . The units are chosen such that  $r_0 = 1$ .

for outflow launching, i.e. it will reach to the region right of the separating line in Fig. 4.1<sup>2</sup>. This 30°-condition (Blandford & Payne, 1982) is one of the key results of the centrifugal wind theory and will be applied later on when analysing the simulation results to determine the underlying outflow launching mechanism. To rephrase the above results in other words one could say that, if the projection of the centrifugal force along the poloidal magnetic field line exceeds the projected gravitational force, which happens at a magnetic field line inclination larger than 30°, the gas will get accelerated out- and upwards.

Two important points should be kept in mind whenever using the 30°-criterion: firstly, it was derived for Keplerian disc rotation and is therefore only applicable when the underlying disc is rotating with the Keplerian velocity. Secondly, the criterion is only valid at the surface of the disc, i.e. only slightly above the midplane. It is therefore not of use when studying the outflow driving mechanism further above the disc.

Two further important predictions are made by the above described centrifugal wind theory: the first is the maximum achievable outflow velocity, which is directly linked to the rotation speed in the disc via (Michel, 1969; Pelletier & Pudritz, 1992)

$$v_{\text{out,max}} \simeq \sqrt{2} v_{\text{kep}}(r_0) \frac{r_A}{r_0}. \quad (4.11)$$

Here,  $v_{\text{kep}}(r_0)$  is the Keplerian velocity at the footpoint of the magnetic field lines and  $r_A$  the cylindrical radius where the outflow velocity exceeds the Alfvénic velocity  $v_A$  (Eq. 3.12). Beyond this point the assumption of a purely poloidal magnetic field breaks down and the centrifugal acceleration mechanism as described above does not work anymore. From detailed theoretical analysis it is found that the ratio of  $\frac{r_A}{r_0}$  usually is of the order of  $\sim 3$ . Hence, the maximum outflow velocity is in general a factor of a few higher than the maximum rotation velocity of the underlying disc.

<sup>2</sup>We note that an inclination towards the  $z$ -axis will not result in an outflow since in this case at some point the magnetic field lines would inevitably enter again the region where  $\Phi_{cg} > \Phi_{cg}(r_0, 0)$ .

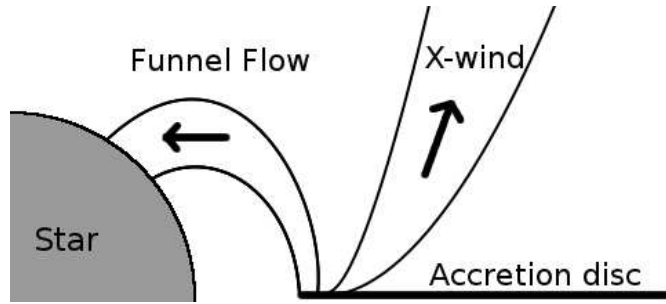


**Figure 4.2.:** Sketch of the magnetic field line structure for an X-wind. The wind is driven along the open field lines while accretion onto the star occurs along the closed field lines.

A further key result of the above theory is the relation between the mass loss rate in the outflow  $\dot{M}_{\text{out}}$  and the mass accretion rate  $\dot{M}_{\text{acc}}$  (e.g. Pudritz & Norman, 1986; Pelletier & Pudritz, 1992). Under the assumption that the inwards transport of angular momentum by the infall of gas is balanced by the extraction of angular momentum through the magnetic field, one can find the approximate relation

$$\frac{\dot{M}_{\text{out}}}{\dot{M}_{\text{acc}}} \simeq \left( \frac{r_0}{r_A} \right)^2. \quad (4.12)$$

As the value of  $\frac{r_A}{r_0}$  typically lies around  $\sim 3$ , in centrifugally driven winds the ratio  $\frac{\dot{M}_{\text{out}}}{\dot{M}_{\text{acc}}}$  is in general of the order of 0.1. This demonstrates that even with a moderate mass loss rate a significant amount of angular momentum can be extracted from the protostellar disc.

To summarise, the centrifugal acceleration mechanism relies on a Keplerian disc which is threaded by a poloidal magnetic field. Close to the disc the gas is forced to corotate with the magnetic field which has a negligible toroidal component. Hence, a net centrifugal acceleration overcoming the gravitational force arises, which accelerates the gas upwards along the field lines. The outflow velocity and the outflow mass rate are directly coupled to the rotation velocity in the disc and the mass accretion rate, respectively.

For the sake of completeness we also briefly mention an alternative model of driving an outflow by magnetocentrifugal acceleration, the so-called X-wind model (see Shu et al., 2000, for an extensive review). As we do not consider this kind of wind in our simulations, in the following we only phenomenologically describe the launching mechanism. In contrast to the aforementioned disc wind, here the main driving agent is the magnetic dipole field of a central star surrounded by an accretion disc. The disc does not reach down to the stellar surface but is separated from it by a gap. The inner edge of the disc connects to the star via closed field lines while further out the field lines are opened up (see Fig. 4.2). The disc at the inner edge is rotating with the Keplerian velocity and since the star is connected with this inner part it is forced in corotation with the disc, i.e. the star is rotating more slowly than its breakup speed. When the material accreted through the disc reaches the inner gap a part of it is funnelled along the closed field lines towards the polar caps of the star. The remaining gas – normally a fraction of about

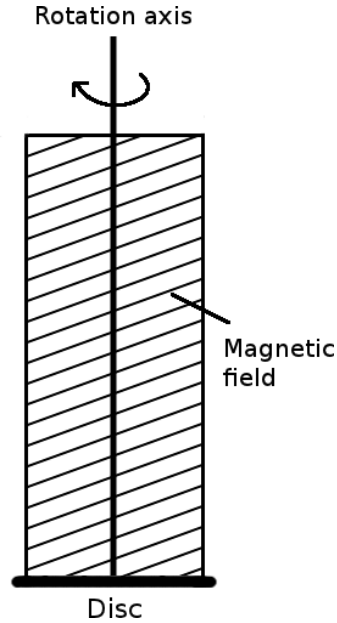


**Figure 4.3.:** Sketch of the magnetic field configuration in an outflow driven by the toroidal magnetic field component.

10 – 30% – is flung outwards along the open field lines by centrifugal acceleration thus forming a jet from the innermost part of the disc. We note that the general mathematical treatment of this mechanism resembles that of the centrifugal disc wind, i.e. one obtains a stationary, axisymmetric solution of the MHD equations from which the properties for the inner field line structure can be inferred.

## 4.2. Magnetic tower flows

In the launching mechanism discussed in the section before, the dominating magnetic field component is the poloidal component as the gas is forced to corotate with the footpoint in the disc where the magnetic field is anchored. At the opposite end also an almost purely toroidal field configuration is able to drive an outflow.

A detailed analysis of the driving mechanism is given by Lynden-Bell (1996, 2003). However, here we only briefly describe the basic mechanism. Considering Fig. 4.3 where the magnetic field configuration in such an outflow is sketched, it can be seen that the outflow is dominated by a strong toroidal magnetic field  $B_\phi$ . This toroidal component is created by the rotation of the underlying disc, which was initially threaded by a purely poloidal magnetic field. At the tip of the outflow a strong gradient in  $B_\phi$  in the vertical direction occurs. Likewise there could be a gradient in  $B_\phi$  over the entire extension of the outflow. However, the crucial point is that, as can be inferred from Eq. 3.4, a gradient in the magnetic field or, to be more precise, in the magnetic pressure  $B^2/8\pi$  exerts an acceleration on the gas. Hence, in the situation displayed in Fig. 4.3 there is a magnetic

force driving the tip of the outflow upwards. Moreover, if the gradient of  $B_\phi$  extends over the entire vertical range of the outflow, there will be a continuous acceleration of the gas over the complete outflow extension. Such a configuration, i.e. an outflow driven by the pressure gradient of the toroidal magnetic field is denoted as a "magnetic tower flow" (Lynden-Bell, 1996, 2003).

In a more sophisticated analysis Lynden-Bell (1996) showed that the vertical growth rate  $\dot{Z}$  of the outflow is proportional to the angular frequency  $\Omega$  of the disc. This can be understood in the way that the faster the disc rotates the faster  $B_\phi$  is build up, which in turn determines the magnetic pressure force and hence the acceleration of the gas.

To summarise, an outflow can be driven by the toroidal magnetic field if there is a decline of  $B_\phi$  along the vertical axis. The driving mechanism of such a magnetic tower flow is in sharp contrast to a centrifugally driven outflow where  $B_\phi$  is in general negligible.

### 4.3. Summary

In this chapter we have discussed three different theories explaining the generation of magnetically driven outflows, namely the magneto-centrifugal acceleration, magnetic tower flows and the X-wind model. The first two models describe two opposite regimes of a magnetically driven disc wind. For a centrifugally driven wind the main driving agent is the poloidal magnetic field whereas the effect of the toroidal field can be considered negligible. In contrast, in a magnetic tower flow a highly wound up field line structure is present where the gas is accelerated by the pressure of the toroidal magnetic field alone. During the course of this work we will derive a theoretical framework for magnetically driven winds which unifies both regimes in one set of equations and allows us to identify the underlying outflow driving mechanism.



## 5. Numerical methods and initial conditions

In this chapter I give an overview of the code used to perform the simulations as well as of the additional specific features implemented in order to study the underlying problem. Furthermore, I in detail describe the initial conditions of the simulations performed and how they compare to recent observations.

### 5.1. Numerical methods

The simulations presented in this work are performed with the astrophysical code FLASH in version 2.5 (Fryxell et al., 2000). The FLASH code is a versatile astrophysical MHD code, which was successfully applied for a great number of astrophysical problems over the last decade. It is designed to solve the magnetohydrodynamical equations on an Eulerian grid. For this purpose the computation domain is divided in cubic subdomains called blocks which consist of  $8^3$  cells. The MHD equations are solved with a scheme that preserves positive states, i.e. density and internal energy, and applies well for astrophysical – in particular highly supersonic – problems (Bouchut et al., 2007, 2010; Waagan, 2009; Waagan et al., 2011). Poisson’s equation (Eq. 3.3) for the gravitational potential is solved with the tree gravity solver implemented by Richard Wünsch<sup>1</sup>. The code is parallelised using the MPI<sup>2</sup> library.

#### 5.1.1. Grid refinement and sink particles

FLASH uses an adaptive mesh refinement (AMR) algorithm based on the PARAMESH library (Olson et al., 1999). The linear spatial resolution between two neighbouring refinement levels differs by a factor of two, i.e. during a refinement process each cubic cell is divided into 8 smaller cells with half the linear size. In order to keep the block structure, always the complete block is refined/derefined. Whether an existing block will be refined or derefined depends basically on two criteria:

- If the second spatial derivative of a chosen variable in a cell is larger/smaller than a certain threshold, the entire block containing this cell will be refined/derefined. For the simulations presented here we have chosen the gas density for the second derivative refinement criterion. This guarantees that the protostellar discs and the

---

<sup>1</sup>Currently there is no publication available describing the implementation and testing of the tree gravity solver in FLASH2.5. However, tests in our working group have revealed good scaling properties as well as the capability to calculate the gravitational potential to high accuracy.

<sup>2</sup>Message Passing Interface

outflows are resolved on the highest level allowing for detailed conclusions about their properties.

- The Jeans length  $\lambda_J = c_s \sqrt{\frac{\pi}{G\rho}}$  for a given cell is resolved by at least 8 grid cells. This is done in order to avoid artificial fragmentation, which would occur if  $\lambda_J$  is resolved by less than 4 grid cells (Truelove et al., 1997).

The combination of both criteria guarantees that the densest parts as well as shocks, e.g. at the tip of the outflows, will be resolved reasonably well.

As the maximum spatial resolution in the simulations is limited and the maximum gas density keeps on increasing during a gravitationally induced collapse, at some point the Jeans length cannot be resolved with more than 8 grid cells anymore. Hence, in order to avoid the violation of this refinement criterion, a sink particle algorithm is applied (Federrath et al., 2010). If the density in a cell exceeds a certain threshold  $\rho_{\text{crit}}$  a sink particle will be formed containing the mass of the cell in excess of  $\rho_{\text{crit}}$ , i.e.

$$\Delta m = (\rho - \rho_{\text{crit}})dV, \quad (5.1)$$

where  $\rho$  is the density of the cell and  $dV$  its volume. The density of the affected cell will be set to  $\rho_{\text{crit}}$ . In addition several further checks have to be fulfilled to prevent the spurious formation of sink particles during the simulation (see Federrath et al., 2010, for details):

- The gas has to converge along all three spatial axes.
- The gravitational potential has a local minimum at this position.
- The gas is Jeans unstable and gravitationally bound.
- The gas is not within one accretion radius  $r_{\text{acc}}$  of an already existing sink particle.

After a sink particle has been formed it can accrete gas from its surrounding cells only if the cells are within a given accretion radius  $r_{\text{acc}}$  (see Section 5.2) and have a density above  $\rho_{\text{crit}}$ , and if the gas is gravitationally bound to the sink particle. In this case the excess mass (Eq. 5.1) is added to the mass of the sink particle and the cell density is set to  $\rho_{\text{crit}}$ . We note that an additional refinement criterion is included which guarantees that the sink particles always reside on the highest refinement level allowed in the simulation.

We mention that while accreting gas and thus changing the density, the magnetic field is not altered during the accretion process. This is done in order to avoid the violation of the divergence-free condition for the magnetic field (Eq. 3.10). Keeping the magnetic field unchanged is motivated also physically by the onset of non-ideal MHD effects like Ohmic dissipation at densities of  $\sim 10^{-12}$  g cm $^{-3}$  (e.g. Nakano et al., 2002, and Section 3.1.6 of this work), which roughly corresponds to the chosen value of  $\rho_{\text{crit}}$  (see Section 5.2). In general, non-ideal MHD effects would allow the gas to slip against the field lines, hence leaving them in the environment of the protostar. We emphasise that in all our

simulations at some point in time the increase of the magnetic field strength within the sink accretion radius ceases due to numerical diffusion. Numerical diffusion effectively allows the magnetic field to partly decouple from the gas motions and to diffuse outwards despite ongoing accretion onto the sink particle.

### 5.1.2. Gas cooling

A key property for the formation process of stars is the thermodynamical behaviour of molecular hydrogen gas. The cooling routine modelling this behaviour was implemented and extensively tested by Banerjee et al. (2004, 2006). Different cooling and heating processes determine how the thermodynamical properties of the gas evolve. These processes are due to line emission of molecules containing also heavier elements than hydrogen like oxygen or carbon. Furthermore, dust particles significantly influence the thermodynamical behaviour of the gas. Molecular hydrogen itself, however, plays only a minor part although it is the most abundant molecule. The reason for this is its symmetric structure without any dipole moment which does not allow for rotation transition and the emission of corresponding photons.

Molecules provide an efficient way of getting rid of excess thermal energy. The energy excess is radiated away by molecular line emission of excited molecules. Neufeld & Kaufman (1993) and Neufeld et al. (1995) provide a detailed calculation of the cooling rate due to molecular line emission of several cooling agents like  $\text{H}_2\text{O}$ ,  $\text{CO}$ ,  $\text{H}_2$ ,  $\text{HCl}$ ,  $\text{O}_2$ ,  $\text{C}$  and  $\text{O}$ . The cooling rates depending on temperature and density are available in a tabulated form, which is read in at the beginning of the simulation. Hence, for any given density and temperature in a cell the corresponding molecular line cooling rate  $\Lambda_{\text{line}}$  can be read off.

Beside molecular line cooling also cooling by the energy exchange between the gas and the dust is modelled. Here basically the thermal energy of the gas is transferred to the dust via collisions. The energy transfer rate for this process is (Goldsmith, 2001)

$$\Lambda_{\text{gd}} = 2 \cdot 10^{-33} \left( \frac{n(\text{H}_2)}{\text{cm}^{-3}} \right)^2 \left( \frac{\Delta T}{\text{K}} \right) \left( \frac{T_{\text{gas}}}{\text{K}} \right)^{1/2} \text{ erg cm}^{-3} \text{ s}^{-1}, \quad (5.2)$$

where  $n(\text{H}_2)$  is the particle density. As can be seen, the energy transfer scales linearly with the temperature difference  $\Delta T = T_{\text{gas}} - T_{\text{dust}}$  between gas and dust.

The dust temperature is assumed to be the equilibrium dust temperature, which is found by solving the equation

$$\Gamma_{\text{cr}} + \Lambda_{\text{gd}} - \Lambda_{\text{dust}} = 0 \quad (5.3)$$

for  $T_{\text{dust}}$ . Eq. 5.3 includes the different heating and cooling processes of dust. The dust is heated by the absorption of cosmic rays with a rate of (Goldsmith, 2001)

$$\Gamma_{\text{cr}} = 3.9 \cdot 10^{-28} \left( \frac{n(\text{H}_2)}{\text{cm}^{-3}} \right) \text{ erg cm}^{-3} \text{ s}^{-1}, \quad (5.4)$$

where a dimensionless cosmic ray shielding parameter of  $10^{-4}$  is assumed. Furthermore, it is heated by the energy transfer from the gas with a rate of  $\Lambda_{\text{gd}}$  (Eq. 5.2). Finally, the

dust cools via thermal emission of the dust grains. The corresponding cooling rate can be expressed in a parametrised form

$$\Lambda_{\text{dust}} = \kappa(n, T_{\text{dust}}) \tilde{\sigma} T_{\text{dust}}^4. \quad (5.5)$$

Here  $\kappa$  is the density and temperature dependent opacity (see Goldsmith, 2001; Semenov et al., 2003, for details) and  $\tilde{\sigma}$  the Stefan-Boltzmann constant  $\sigma$  multiplied by a factor of unity (Goldsmith, 2001)

$$\tilde{\sigma} = 1.209 \sigma. \quad (5.6)$$

Inserting Eqs. 5.2, 5.4 and 5.5 into Eq. 5.3, the latter can be solved for the equilibrium dust temperature. However, due to the complicated functional form of Eq. 5.3, an analytical solution for  $T_{\text{dust}}$  is not possible. Hence, in the code for each cell Eq. 5.3 is solved iteratively with a Newton iteration scheme. With  $T_{\text{dust}}$  known, subsequently the gas cooling rate due to the energy transfer to dust particles  $\Lambda_{\text{gd}}$  can be calculated.

At densities above  $\sim 10^{-13} \text{ g cm}^{-3}$  the gas starts to get optically thick preventing the radiation from efficiently leaving the region where it has been emitted. For this reason we apply a very crude approximation for the diffusion of radiation in the optically thick regime, i.e. when  $\rho > 10^{-13} \text{ g cm}^{-3}$ . Assuming that in an optically thick gas the typical lengthscale for the change of the radiation field is approximately given by the Jeans length  $\lambda_{\text{J}}$ , one can calculate the optical depth  $\tau$  of the gas for a given opacity  $\kappa$

$$\tau \simeq \kappa \cdot \lambda_{\text{J}}. \quad (5.7)$$

For gas above the aforementioned density threshold we assume that the ability of the dust to cool via thermal blackbody radiation is reduced. We model this by replacing the opacity  $\kappa$  in Eq. 5.5 by an effective opacity

$$\kappa_{\text{eff}} = \min(\kappa, 1/\lambda_{\text{J}}). \quad (5.8)$$

Now the modified dust cooling rate  $\Lambda_{\text{dust}}$  is used in Eq. 5.3 to calculate the dust equilibrium temperature  $T_{\text{dust}}$ , which finally enters the gas-dust cooling rate (Eq. 5.2) and thus also affects the cooling ability of the gas. Furthermore, we also reduce the molecular line cooling rate  $\Lambda_{\text{line}}$  by a factor of  $(1 - \tau)$  to account for the effect that in the optically thick regime the radiation due to molecular line emission will be reabsorbed very quickly. To guarantee positivity of the cooling rates, in the correction factor  $(1 - \tau)$  the opacity  $\tau$  (Eq. 5.7) is limited to values between 0 and 1. We note that the above described, somewhat heuristic approximation for the optically thick regime is very crude. However, it was shown that with this description the expected thermodynamical behaviour of molecular gas is reproduced reasonably well (Banerjee et al., 2004, 2006; Banerjee & Pudritz, 2006).

To summarise, the total cooling rate  $\Lambda_{\text{tot}}$  of the gas consist of the molecular line cooling rate  $\Lambda_{\text{line}}$  and of the rate of energy transfer from gas to dust  $\Lambda_{\text{gd}}$ . Both cooling rates are density and temperature dependent. Additional heating terms – except the intrinsic adiabatic heating due to compression of the gas – are not considered here.

We apply the cooling routine described above after each hydrodynamical timestep. After calculating the total cooling rate

$$\Lambda_{\text{tot}} = \Lambda_{\text{line}} + \Lambda_{\text{gd}} \quad (5.9)$$

in each cell, the thermal energy  $e_{\text{int}}$  is changed by

$$\Delta e_{\text{int}} = -(\Lambda_{\text{tot}} \cdot dt). \quad (5.10)$$

Using a subcycling scheme ensures that during one subcycle timestep  $dt_{\text{sub}}$  the relative change of thermal energy of each cell does not exceed 20%, i.e.

$$|\Lambda_{\text{tot}} \cdot dt_{\text{sub}}| \leq 0.2 e_{\text{int}}. \quad (5.11)$$

In case the energy change would be above 20% the subcycling timestep is reduced such that the energy change reduces to 20% and the thermodynamical variables will be updated accordingly. Thereafter an updated cooling rate according to the new gas and dust temperature is calculated and so on. The subcycling continues until the sum of the subcycling timesteps  $dt_{\text{sub}}$  is equal to the global hydrodynamical timestep  $dt$ .

## 5.2. Initial conditions

The aim of this work is to simulate the collapse of massive molecular cloud cores and the subsequent formation of protostellar discs and molecular outflows and to study the influence of magnetic fields and gas motions on these processes. Hence, in this section we will firstly describe the numerical setup used to mimic typical initial conditions for massive star formation as described in detail in Section 2.1. The results of these simulations will be discussed in Chapter 6 and 7. The detailed initial conditions for the simulations including turbulent motions will be described later during this work at the beginning of Chapter 8. However, in the following as well as in Chapter 6 and 7 we omit the influence of turbulence and focus on the effect of magnetic fields and rotation alone. For this purpose we set up a spherical molecular cloud core (in the following simply *core*) with a mass of  $100 M_{\odot}$  and a diameter of 0.25 pc, which is in good agreement with observational findings (see Section 2.1). The core is placed in a cubic simulation domain with a length of 0.75 pc to avoid corruption of the simulation results by boundary effects. The gas surrounding the core has a density 100 times lower than that at the edge of the core which is why one can neglect its dynamical influence on the simulation results. In order to assure pressure equilibrium at the edge of the core, the temperature of 2000 K in the ambient gas is 100 times higher than the initially uniform temperature of 20 K in the core. The density profile of the core declines as

$$\rho \propto r^{-1.5} \quad (5.12)$$

for radii larger than 0.0125 pc, i.e. larger than a tenth of the core radius. Inside this radius the density profile follows a parabolic distribution

$$\rho \propto \left(1 - \left(\frac{r}{r_0}\right)^2\right) \quad (5.13)$$

in order to avoid unphysically high densities in the centre of the core which would arise for an  $r^{-1.5}$ -profile. The density distribution inside 0.0125 pc is chosen such that there is a continuously differentiable transition at  $r = 0.0125$  pc. The density in the centre and at the edge of the core are initially  $2.3 \cdot 10^{-17}$  and  $4.2 \cdot 10^{-19}$  g cm $^{-3}$ , respectively<sup>3</sup>. For a mean molecular weight of  $\mu_{\text{mol}} = 2.3$  adopted in this work, this corresponds to a particle density of  $n = 6.0 \cdot 10^6$  and  $1.1 \cdot 10^5$  cm $^{-3}$ , respectively. The particle densities as well as the exponent of the density profile are in good agreement with observations as discussed in Section 2.1. Here we note that for a purely hydrodynamical situation with initial turbulence, the chosen density profile defines the transition between systems with low degree of fragmentation (for steeper density profiles) and with high susceptibility for fragmentation (for shallower density profiles) as shown by Girichidis et al. (2011).

Calculating the average Jeans mass using a temperature of 20 K and the average density of the core  $\langle \rho \rangle = 8.27 \cdot 10^{-19}$  g cm $^{-3}$  reveals that the core contains about 56 Jeans masses and is therefore highly gravitationally unstable. This fact and the high mass of 100  $M_{\odot}$  show that the considered core is in principle suitable for massive star formation.

Beside the mass distribution, which will not be changed in this work, there are two further crucial parameters affecting the evolution of molecular cloud cores, namely the rotational energy and the magnetic field strength. The first parameter we consider is the magnetic field strength. In the beginning all simulations have a magnetic field which is pointing in the  $z$ -direction only, i.e.  $\mathbf{B} = (0, 0, B_z)$ . Furthermore,  $B_z$  declines outwards with the cylindric radius  $R$  as

$$B_z \propto R^{-0.75} . \quad (5.14)$$

This guarantees that initially in the equatorial plane the ratio of thermal to magnetic pressure  $\beta_{\text{plasma}} = \frac{P}{B^2/8\pi}$  is constant. To guarantee  $\nabla \mathbf{B} = 0$ , which reduces to  $\partial_z B_z = 0$  in our case,  $B_z$  is constant along the  $z$ -direction. The fact that the magnetic field declines with the cylindric radius is a compromise between observations showing an hourglass-shaped field configuration (e.g. Girart et al., 2009; Tang et al., 2009, but see also Fig. 2.1) and a numerically feasible setup. However, by the time the first sink particle forms, in all simulations a self-consistent, hourglass-like field configuration similar to observations has built up. It is therefore expected that the chosen initial magnetic field configuration does not change the results significantly compared to an initially hourglass-shaped configuration.

The second parameter affecting the evolution of molecular cloud cores is the rotation of the core. The cores studied here are initially all rotating rigidly around the  $z$ -axis, i.e. the rotation axis is parallel to the magnetic field. We note that, as neither the density field nor the velocity field have any perturbations at the beginning of the simulations, one can expect a uniform and inward directed collapse to occur.

As mentioned in Section 2.1 the actual values for the strength of the magnetic field and the rotational energy in star forming regions are subject to large variations. To account for this variation, we perform a series of simulations varying the strength of the

---

<sup>3</sup>Hence, the density in the ambient medium is  $4.2 \cdot 10^{-21}$  g cm $^{-3}$ .

Run	$\mu$	$\gamma$	$B$ [ $\mu\text{G}$ ]	$\beta_{\text{rot}}$	$\omega$ [ $10^{-13} \text{s}^{-1}$ ]
26-20	26	$1.13 \cdot 10^{-3}$	132	$2 \cdot 10^{-1}$	7.07
26-4	26	$1.13 \cdot 10^{-3}$	132	$4 \cdot 10^{-2}$	3.16
26-0.4	26	$1.13 \cdot 10^{-3}$	132	$4 \cdot 10^{-3}$	1.00
26-0.04	26	$1.13 \cdot 10^{-3}$	132	$4 \cdot 10^{-4}$	0.316
10-20	10.4	$7.06 \cdot 10^{-3}$	330	$2 \cdot 10^{-1}$	7.07
10-4	10.4	$7.06 \cdot 10^{-3}$	330	$4 \cdot 10^{-2}$	3.16
10-0.4	10.4	$7.06 \cdot 10^{-3}$	330	$4 \cdot 10^{-3}$	1.00
5.2-20	5.2	$2.82 \cdot 10^{-2}$	659	$2 \cdot 10^{-1}$	7.07
5.2-4	5.2	$2.82 \cdot 10^{-2}$	659	$4 \cdot 10^{-2}$	3.16
5.2-0.4	5.2	$2.82 \cdot 10^{-2}$	659	$4 \cdot 10^{-3}$	1.00
2.6-20	2.6	$1.13 \cdot 10^{-1}$	1318	$2 \cdot 10^{-1}$	7.07
2.6-4	2.6	$1.13 \cdot 10^{-1}$	1318	$4 \cdot 10^{-2}$	3.16
inf-0	$\infty$	0	0	0	0

**Table 5.1.:** Performed simulations with normalised initial mass-to-flux-ratio  $\mu$ , ratio of magnetic to gravitational energy  $\gamma$ , magnetic field strength in the centre  $B$ , ratio of rotational to gravitational energy  $\beta_{\text{rot}}$ , and the corresponding angular frequency  $\omega$ . The results of these simulations are discussed in Chapter 6 and 7.

magnetic field and the amount of rotational energy. The strength of the magnetic field is often parametrised with the mass-to-flux ratio  $\mu$  (Eq. 3.21). In the simulations presented in this work  $\mu$  varies from 2.6 for strong fields up to 26 for weak fields. This corresponds to an initial magnetic field strength in the centre of the core ranging from about 100  $\mu\text{G}$  up to  $\sim 1$  mG. The amount of rotational energy is parametrised by the dimensionless ratio of the rotational energy to the gravitational energy,  $\beta_{\text{rot}}$ . In the models presented here  $\beta_{\text{rot}}$  ranges from  $4 \cdot 10^{-3}$  to  $2 \cdot 10^{-1}$  corresponding to rotation frequencies of the order  $10^{-14} - 10^{-13} \text{s}^{-1}$ . In total we have performed 12 simulations with varying initial conditions. The individual simulations and their corresponding initial values are listed in Table 5.1. In the nomenclature of each run the first number gives the mass-to-flux ratio and the second number  $\beta_{\text{rot}}$  multiplied by a factor of 100. For comparative purposes we also performed a simulation with zero magnetic field and zero rotation denoted as run inf-0. We again note that the simulations without turbulence are not listed here.

As already pointed out in Section 2.1, observations of high-mass star-forming regions typically reveal mass-to-flux ratios  $\mu < 5$  and magnetic field strengths between a few 100  $\mu\text{G}$  and a few mG. In this work this range is covered with a number of simulations (runs with  $\mu \lesssim 5.2$  in Table 5.1) but in addition to that we also consider initial configurations with significantly weaker magnetic fields ( $\mu > 10$ ) as found in magnetohydrodynamical simulations (e.g. Padoan et al., 2001; Tilley & Pudritz, 2007). For comparative purposes with the rotational energy in Table 5.1 also the ratio of magnetic to gravitational energy  $\gamma$  is given. The considered rotational energies coincide reasonably well with values from observations ranging from  $10^{-4}$  up to  $\sim 1$  with a mean around 0.01 (e.g. Goodman et al., 1993; Pirogov et al., 2003; Csengeri et al., 2011). We note that both  $\gamma$

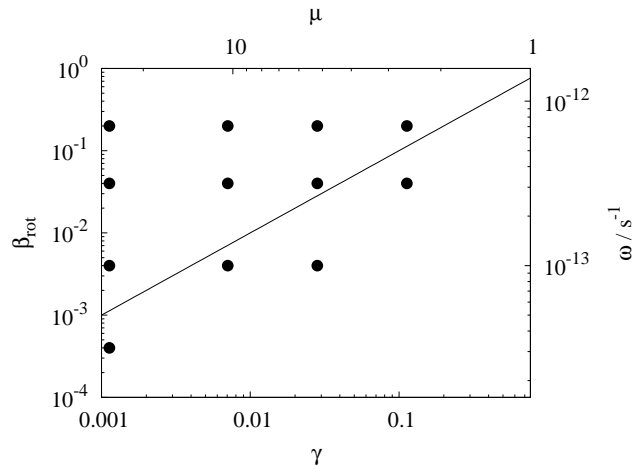


**Figure 5.1.:** Initial values of the 12 simulations performed. The initial rotational ( $\beta_{\text{rot}}$ ) and magnetic energy ( $\gamma$ ) are normalised to the gravitational energy. As can be seen, the starting points bracket the curve where rotational and magnetic energy are equal (black line). The second axes show the corresponding normalised mass-to-flux ratio  $\mu$  and the rotation frequency  $\omega$ .

and  $\beta_{\text{rot}}$  are always smaller than 1 due to the high gravitational energy of the  $100 M_{\odot}$  cores.

The distribution of the initial parameters in the magnetic field - rotation phase space is shown in Fig. 5.1. For comparative purposes, beside the mass-to-flux ratio also the ratio of the magnetic energy to the gravitational energy  $\gamma$  is shown. Here we note that both  $\gamma$  and  $\beta_{\text{rot}}$  are calculated numerically from the initial snapshot of each simulation. In addition the rotation frequency is shown on the second y-axis. It can be seen from Fig. 5.1 that beside the fact that both the magnetic and rotational energies extend over more than two orders of magnitude, the simulations also bracket the line where  $\gamma$  equals  $\beta_{\text{rot}}$ .

Two further rather numerical aspects have to be mentioned in this context as they are directly linked to the setup described above. The first aspect to mention is the used spatial resolution. Initially the cloud core is resolved by a grid with a spacing of 302 AU fulfilling the applied refinement criteria (see Section 5.1.1). During the simulation we allow for 13 levels of refinement resulting in a maximum spatial resolution of

$$dx = 4.7 \text{ AU}. \quad (5.15)$$

With this resolution the gravitational collapse can be followed up to a density of  $\sim 10^{-12} \text{ g cm}^{-3}$  without violating the Jeans length refinement criterion. The resolution is therefore sufficient to resolve the transition around  $10^{-13} \text{ g cm}^{-3}$  where the molecular gas starts to get optically thick and heats up significantly. To guarantee that the Jeans refinement criterion is not violated, sink particles are created if the density exceeds the critical value of

$$\rho_{\text{crit}} = 1.78 \cdot 10^{-12} \text{ g cm}^{-3}. \quad (5.16)$$

The accretion radius of the sink particles is

$$r_{\text{acc}} = 12.6 \text{ AU} \quad (5.17)$$

corresponding to 2.7 grid cells which was found to be a reasonable value<sup>4</sup>.

The second numerical aspect to discuss is related to the launching of an outflow after the formation of the protostellar disc surrounding the sink particle. This outflow will evacuate the regions above and below the disc thus significantly increasing the Alfvénic velocity  $v_A$  (Eq. 3.12) due to the low gas densities. This in turn would significantly reduce the hydrodynamical timestep required for the stability of the numerical solution, which would make the simulations prohibitively costly due to the significantly increased number of timesteps necessary to follow the simulations over a reasonably long time. In order to avoid this, we introduce a minimum density threshold within 67 AU<sup>5</sup> around the simulation centre as soon as the outflow is launched. Within this radius the gas density is kept above a minimum value of  $1 \cdot 10^{-15} \text{ g cm}^{-3}$ . This means that whenever the density in a cell falls below this threshold during one timestep, it is artificially set to the limit of  $1 \cdot 10^{-15} \text{ g cm}^{-3}$ . Hence, one can avoid the hydrodynamical timestep falling to prohibitively small values. The effects of this artificial density threshold will be discussed in detail in Section 6.3.1.

To summarise, we will perform a series of collapse simulations of  $100 M_{\odot}$  cores with varying initial conditions concerning the magnetic field strength and the rotational energy of the core. For this purpose the initial conditions are adapted to recent observations of massive star forming regions. Furthermore, the initial parameters for the magnetic field and the core rotation are chosen in such a way that they cover a wide range in parameter space. Hence, we are able to infer systematical effects of the initial conditions on processes like protostellar disc formation and outflow launching. The results of this analysis will be presented in the following two chapters. We again note that the inclusion of turbulence typically observed in massive star forming cores but not present in this setup will be postponed to Chapter 8.

---

<sup>4</sup>private communication with C. Federrath

<sup>5</sup>This value was found to be reasonable by visually inspecting the simulations.



## 6. Disc formation and protostellar accretion

In Chapter 5 the numerical methods as well as the initial conditions of the simulations I performed are described in detail. In this chapter I will analyse the results of these simulations focussing on the formation of discs and protostellar accretion rates and discuss potential consequences for the formation of massive stars. The evolution and properties of the outflows launched from the protostellar discs will be discussed in Chapter 7. The computational costs of all simulations presented here and in Chapter 7 sum up to about 1 000 000 CPU hours. The results and discussion presented in this chapter have been published in Seifried et al. 2011, MNRAS, 417, 1054.

### 6.1. Introduction

The question of how massive stars form is still a highly debated field of research (e.g. Zinnecker & Yorke, 2007). It is believed that massive star formation takes place in high-mass molecular cloud cores with masses ranging from roughly  $100 M_{\odot}$  up to a few  $1000 M_{\odot}$ . Characteristic for such cores are sizes of few  $0.1 \text{ pc}$  and peak densities up to  $10^6 \text{ cm}^{-3}$  (e.g. Beuther et al., 2007, but see Section 2.1). Furthermore, from observations it is known that the interstellar medium as a whole is magnetised (see Beck, 2012, for a recent overview). Also the star forming cloud cores partly reveal a significant magnetisation. To remind the reader, the importance of the magnetic field can be estimated by the mass-to-flux ratio  $\mu$  normalised to the critical mass-to-flux ratio (Mouschovias & Spitzer, 1976, but see Section 3.2):

$$\mu = \frac{M_{\text{core}}}{\Phi_{\text{core}}} / \left( \frac{M}{\Phi} \right)_{\text{crit}} = \frac{M_{\text{core}}}{\Phi_{\text{core}}} / \frac{0.13}{\sqrt{G}}. \quad (6.1)$$

Observed mass-to-flux ratios in high-mass star forming cores are typically only slightly supercritical with  $\mu \lesssim 5$  (Falgarone et al., 2008; Girart et al., 2009; Beuther et al., 2010; Crutcher et al., 2010) indicating a significant influence of magnetic fields on the star formation process. In magnetohydrodynamical simulations, however, also higher values of  $\mu$  up to  $\sim 20$ , i.e. weaker magnetic fields, are found (e.g. Padoan et al., 2001; Tilley & Pudritz, 2007). Another common feature of star forming cores are their slow rotation velocities. Observed cores have rotational energies normalised to the gravitational energy which scatter around a mean of about 0.01 (Goodman et al., 1993; Pirogov et al., 2003; Csengeri et al., 2011).

In the field of low-mass star formation there is a great number of observations of discs and large-scale outflows which are the basic keystones of the widely accepted disc accretion scenario for low-mass star formation (see, e.g. the reviews by Mac Low & Klessen,

2004; McKee & Ostriker, 2007). A similar formation scenario for massive stars is supported by a growing number of discs and bipolar outflows observed around high-mass protostellar objects (see Beuther & Shepherd, 2005; Cesaroni et al., 2007, for recent reviews). Therefore, it is worthwhile to study the influence of magnetic fields and rotation on the formation of discs and outflows in the context of massive star formation with numerical simulations.

For low-mass star forming regions ( $M_{\text{core}} \sim 1 M_{\odot}$ ), the influence of magnetic fields on the collapse of rotating cloud cores, the subsequent formation and evolution of discs and the launching of outflows has received extensive attention (e.g. Allen et al., 2003; Banerjee & Pudritz, 2006; Price & Bate, 2007; Mellon & Li, 2008; Hennebelle & Fromang, 2008; Hennebelle & Teyssier, 2008; Hennebelle & Ciardi, 2009; Duffin & Pudritz, 2009; Machida et al., 2011; Price et al., 2012). All authors find a more or less significant influence of magnetic fields on the evolution of discs surrounding the protostars. The perhaps most important result of these studies is that for a mass-to-flux ratio of  $\mu \lesssim 10$  the formation of Keplerian discs is largely suppressed. This so-called magnetic braking catastrophe (Allen et al., 2003; Mellon & Li, 2008) turned the traditional angular momentum problem upside down: In highly magnetised cores magnetic braking seems to be so efficient that large-scale Keplerian discs, commonly observed around low-mass protostars, cannot form. Low-mass star formation simulations also reveal a strong impact of magnetic fields on the fragmentation properties of discs. In particular, strong magnetic fields tend to suppress disc fragmentation even in the presence of initial density perturbations (e.g. Hosking & Whitworth, 2004; Machida et al., 2005; Hennebelle & Teyssier, 2008; Duffin & Pudritz, 2009). These results are in contrast with the observational fact that a large fraction of low-mass stars are binaries (e.g. Duquennoy & Mayor, 1991).

The influence of magnetic fields on massive star formation, however, has received attention only recently (Banerjee & Pudritz, 2007; Peters et al., 2011; Hennebelle et al., 2011; Commerçon et al., 2011). Banerjee & Pudritz (2007) study the very early evolution of a protostar, its surrounding disc, and the outflow performing a simulation with extremely high spatial resolution. The protostellar evolution over a timescale of some  $10^4$  yr is examined by Peters et al. (2011), Hennebelle et al. (2011) and Commerçon et al. (2011), the latter two authors focussing on the effect of magnetic fields and turbulence while Peters et al. (2011) study the interplay of magnetic fields and radiation. In this chapter we systematically study the influence of rotation and magnetic fields on the formation and accretion history of massive stars and examine the question under which conditions massive Keplerian discs can form in an already very early stage of protostellar evolution. We perform a series of collapse simulations with different initial rotational and magnetic energies following the protostellar evolution over a few 1000 yr. Rotational and magnetic energies are selected in a way to cover a large range in parameter space in accordance with observations and other numerical simulations (see Fig. 5.1). Thus, we are able to detect systematic dependencies of the results on the initial conditions. Furthermore, the simulations serve as a useful guide to select representative parameter sets for subsequent and more detailed studies.

This chapter is organised as follows. In the next section we present the results of the simulations listed in Table 5.1. Since the simulation setup and the used numerical methods are identical for this chapter and Chapter 7, all information on this can be found in Chapter 5.1 and will not be repeated here. In the result section (Section 6.2) firstly, the time evolution of the protostellar discs is presented for two representative simulations. Next, we analyse the velocity structure and the magnetic properties of the gas in the midplane. Afterwards, the accretion histories of the protostars as well as the effects of disc fragmentation are examined. In Section 6.3 the results are discussed in a broader context and are compared to other numerical and observational studies before we summarise our results in Section 6.4.

## 6.2. Results

In the analysis of the results and in the discussion we will mainly focus on the phase after the first sink particle has formed. However, in the next section we briefly describe the initial collapse phase until the first sink particle forms before we analyse the subsequent evolution of the protostellar discs and the sink particles in detail in the following sections.

### 6.2.1. The initial collapse phase

As pointed out in Section 5.2, the considered cores contain about 56 Jeans masses and are thus highly gravitationally unstable. Hence, one can assume that the initial collapse proceeds almost in free-fall. The typical timescale for the collapse is therefore the free-fall time, which in the current setup is

$$\tau_{\text{ff}} = \sqrt{\frac{3\pi}{32G\rho}} = 13.9\text{kyr} . \quad (6.2)$$

Here we have used the density  $\rho = 2.3 \cdot 10^{-17} \text{ g cm}^{-3}$  in the centre of the core. In Table 6.1 we list the formation time  $t_0$  of the first sink particle for all runs performed. It can be seen that in the magnetised runs  $t_0$  is longer than  $\tau_{\text{ff}}$  by a factor of 1.1 to 1.4 and that also in run inf-0 the collapse time is also somewhat longer than  $\tau_{\text{ff}}$ . For this reason we performed a series of test runs for the setup of run inf-0 where the initial resolution in the centre of the core is increased by a factor of 4, 8 and 16, respectively. The observed collapse times  $t_0$  are then 15.0 kyr, 14.8 kyr and 14.7 kyr, respectively. Hence, there is a slight dependence of  $t_0$  on the initial resolution of the order of a few 100 yr. In general, however,  $t_0$  stays well above  $\tau_{\text{ff}}$  indicating that this is not a numerical effect. A physical reason for the prolonged collapse time is probably the build-up of a strong pressure gradient in the centre of the core counteracting gravity. Furthermore, the free-fall time of 13.9 kyr has to be considered as a lower limit as the maximum density in the centre of the core has been used for its calculation whereas it might be more appropriate to calculate the free-fall time somewhat outside the centre at lower densities. Hence, the somewhat prolonged collapse time  $t_0$  compared to  $\tau_{\text{ff}}$  in run inf-0 is most likely a real effect. In contrast, the unexpected fact that  $t_0$  for run inf-0 is somewhat longer than for

Run	$t_0$ (kyr)	$M_{\text{sink}}$ ( $M_{\odot}$ )	$\dot{M}_{\text{acc}}$ ( $10^{-4} M_{\odot}/\text{yr}$ )	$N_{\text{sinks}}$ yr	$t_{\text{sim}}$
26-20	15.7	1.85(1.14)	3.69	20	5000
26-4	15.2	2.65(2.02)	5.30	12	5000
26-0.4	15.0	3.59	7.18	1	5000
26-0.04	15.0	4.16	8.31	1	5000
10-20	15.8	1.28	3.19	1	4000
10-4	15.3	2.23	5.57	1	4000
10-0.4	15.2	2.98	7.46	1	4000
5.2-20	16.7	1.78	4.45	1	4000
5.2-4	16.2	2.28	5.71	1	4000
5.2-0.4	16.1	2.55	6.37	1	4000
2.6-20	21.3	1.30	4.33	1	3000
2.6-4	20.5	1.48	4.93	1	3000
inf-0	15.1	4.39	8.77	1	5000

**Table 6.1.:** Formation time  $t_0$  of the first sink particle, total mass (the mass in brackets is the mass of the most massive sink if more than one is formed) of all sink particles at the end of each simulation, the corresponding time averaged total accretion rate, the number of sinks created, and the time the simulations have being followed after the first sink particle has formed.

the runs 26-0.4 and 26-0.04 is most like a numerical issue. Turning on a weak magnetic field ( $\mu = 26$ ) in a test run with no rotation results in a slightly shorter collapse time of 15.0 kyr compared to inf-0. This suggest that the somewhat longer  $t_0$  in run inf-0 (compared to the runs 26-0.4 and 26-0.04) is an intrinsic effect of the numerical scheme which we will not follow up further here.

However, in each simulation subset (equal  $\mu$  or  $\beta_{\text{rot}}$ ) there are physically well motivated trends in  $t_0$  recognisable. As can be inferred from Table 6.1, the collapse gets slowed down with an increasing magnetic field strength and an increasing amount of rotational energy as both counteract gravity. Interestingly, the variation of the rotational energy by two orders of magnitude at a fixed magnetic field strength changes  $t_0$  by no more than roughly 0.8 kyr, i.e. by  $\sim 5\%$ . In contrast, increasing the magnetic energy by a factor of 100 for fixed rotational energies prolongs the collapse time by roughly 5 kyr, i.e.  $\sim 30\%$ . However, as all cores are supercritical ( $\mu > 1$ ) and have rotational energies well below the gravitational energy ( $\beta_{\text{rot}} < 1$ ), one cannot expect the collapse time  $t_0$  to be significantly longer than the free-fall time  $\tau_{\text{ff}}$ . In the following sections we will focus on the evolution of the protostellar discs and the sink particles after  $t_0$ . Therefore, from now on all time specifications will refer to the time elapsed since the formation of the first sink particle at  $t_0$ .

### 6.2.2. Global disc properties

In this section we discuss the time evolution of the properties of the protostellar discs found in the simulations. From the last column of Table 6.1 it can be seen that the simulations are followed for several 1000 yr after the first sink particle has formed. The reason that runs with stronger magnetic fields have been simulated less long is due to the increased computational costs in these runs due to higher Alfvénic velocities, which reduce the overall hydrodynamical timestep. However, despite the rather limited time significant trends can be inferred from the simulation results.

Since in total 12 simulations have been performed, we will concentrate on two representative simulations and discuss the time evolution of the discs in these two runs in detail. For this purpose, we consider run 26-4 and run 5.2-4, which have equal initial rotational energies but different magnetic field strengths. To begin with, we compare the properties of the gas in a well-defined region of interest at the midplane of the simulations where the protostellar discs are located. This region is a cylinder with a height of 47 AU above and below the midplane and variable radius. Here we mention that, although this height does not reflect the real disc scale height, we will use it for three reasons. Firstly, this choice allows for a numerically simple calculation of the desired quantities. Furthermore, it guarantees that for different simulations and times identical areas are compared. Finally, it is used as it is hardly possible to determine a well-defined disc scale height as even in a single run the disc height varies in time and radial position. For example, the frequently used approximation of the scale height for thin accretion discs (e.g. Cesaroni et al., 2007)

$$H = \frac{c_s}{\omega} \quad (6.3)$$

varies between a few AU and  $\sim 100$  AU for a single run. Here  $c_s$  is the sound speed (Eq. 3.11). Trying to fit the vertical density distribution above/below the midplane for the simulation data by a Gaussian distribution gives scales height strongly varying with the radial distance from the centre, but nevertheless in rough accordance with the afore made theoretical estimate of 1 – 100 AU. Hence we argue that the choice of 47 AU, located in the middle of this range, is reasonable.

In the following we will denote this region simply as *the disc*. The disc quantities shown in the following are averaged vertically and azimuthally before consideration. First we consider the radial dependence of the column density and of the mass-weighted temperature in the discs in the runs 26-4 and 5.2-4. From the results shown in Fig. 6.1 it can be inferred that in run 26-4 an accretion shock occurs where both, column density and temperature experience a sudden increase. This is also true for run 5.2-4, although here the increase in column density and temperature is somewhat smoother. In both cases, however, the shock front moves outwards as time evolves reaching several 100 AU in radius. In run 26-4 the density profile inside 100 AU is nearly flat with values around a few  $10^{25} \text{ cm}^{-2}$ . This corresponds to average volume densities of  $\sim 10^{-14} \text{ g cm}^{-3}$  and maximum densities  $\gtrsim 10^{-13} \text{ g cm}^{-3}$  in the midplane of the discs. For run 5.2-4 the density profile is declining outwards and seems to decrease slightly over time. In both

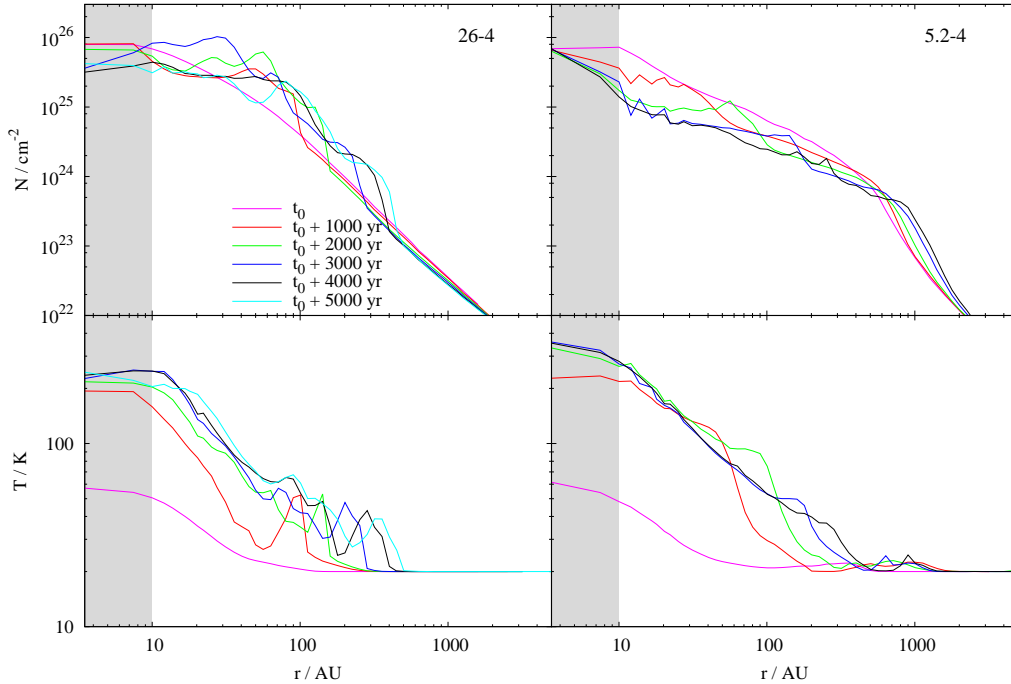


**Figure 6.1.:** Radial profile of the column density (upper panel) and mass-weighted temperature (bottom panel) for run 26-4 (left panel) and run 5.2-4 (right panel) at different times after the formation of the first sink particle at time  $t_0$ . The profiles are calculated by averaging azimuthally and vertically over a disc with a height of 47 AU above and below the midplane. The region below  $r = 10$  AU is subject to resolution effects. Therefore, here and in the following plots we shaded this area to guide the reader’s eye.

cases the mass-weighted temperature in the midplane increases up to a few 100 K, i.e. by about one order of magnitude compared to the surroundings of the discs.

The temperature increase in the inner region is due to the fact that the gas gets optically thick at density around  $10^{-13} \text{ g cm}^{-3}$  (see Banerjee et al., 2006, and Section 5.1.2 for details of the applied cooling function). Therefore, the gas in the disc loses its ability to cool efficiently and cannot fast enough radiate away the thermal energy transferred to it by compression work. This results in temperatures of up to a few 100 K in the inner disc region consistent with observational results (see e.g. the review of Cesaroni et al., 2007, and references therein). Further out in the discs the gas experiences a strong temperature increase due to shock heating. At the accretion shock at a few 100 AU kinetic energy is converted relatively fast into thermal energy. Assuming that the gas gets decelerated by  $\sim 1 \text{ km s}^{-1}$  (see Fig. 6.3 further down) and the corresponding kinetic energy is immediately transformed into thermal energy, this would result in a temperature increase of roughly 90 K. This is in accordance with the observed increase of about 30 K when taking into account that a good fraction of the energy will be radiated away and that the conversion into heat does not happen all at once.

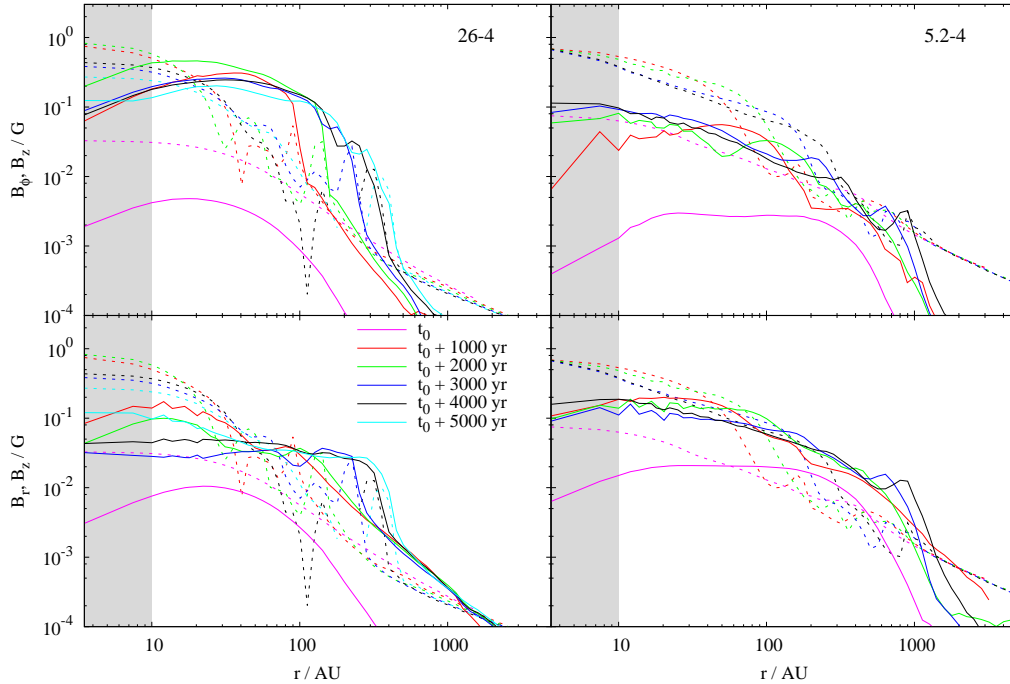


**Figure 6.2.:** Radial profile of the toroidal component (top) and the radial component (bottom) of the magnetic field for run 26-4 (left) and run 5.2-4 (right) at the same times as in Fig. 6.1. For comparative purposes  $B_z$  (dashed lines) is shown in both panels as well. For radii  $\gtrsim 20$  AU in both runs  $B_r$  is comparable in magnitude to  $B_z$  whereas  $B_\phi$  is larger than  $B_z$  for run 26-4 and smaller than or comparable to  $B_z$  for run 5.2-4. At  $r < 20$  AU  $B_z$  is in both cases the dominant component.

Next we show the time evolution of the magnetic properties of the discs in the two runs 26-4 and 5.2-4 in Fig. 6.2. For the calculation of  $B_r$  and  $B_\phi$  the absolute values are used for the averaging procedure as both components have opposite signs above and below the midplane and hence would cancel themselves out. For comparative purposes we plot  $B_z$  (initially the only component in the simulations) and either  $B_\phi$  (top) or  $B_r$  (bottom) in each panel. For the comparison we only consider the radial range above 10 AU as the region further inside is subject to resolution effects. As can be seen, the different components in the disc reach values of up to about 1 G.  $B_z$  is somewhat larger in run 5.2-4 than in run 26-4 due to the five times higher initial field strength in run 5.2-4. In both runs, however, for radii  $\gtrsim 20$  AU  $B_r$  (bottom panel of Fig. 6.2) is of the order of  $B_z$ .  $B_r$  is created by the inwards drag of the magnetic field during the collapse and later during the accretion process. In contrast to  $B_r$ , the toroidal components differ significantly between both runs (see top panel of Fig. 6.2). In run 26-4  $B_\phi$  is the dominant component in the region within the accretion shock being larger than  $B_z$  and  $B_r$  by up to one order of magnitude. This is due to the fast rotation of the disc winding up the poloidal field. In contrast, in the strongly magnetised run 5.2-4,  $B_\phi$  is mostly smaller

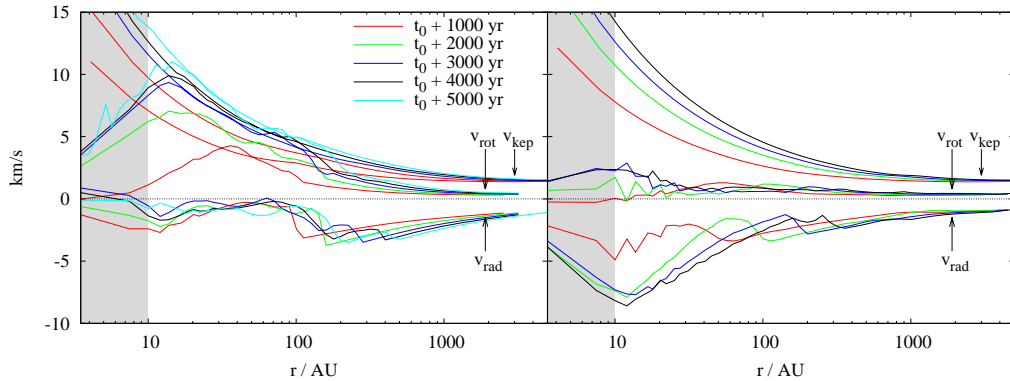


**Figure 6.3.:** Radial profile of the Keplerian velocity  $v_{\text{kep}}$ , rotation velocity  $v_{\text{rot}}$  and radial velocity  $v_{\text{rad}}$  (negative values) for run 26-4 (left) and run 5.2-4 (right). The velocities are averaged in the same way as in Fig. 6.1 and shown for the same snapshots except that of  $t = t_0$ . For run 26-4 a rotationally supported disc builds up while in run 5.2-4 the rotation velocity stays clearly sub-Keplerian all the time with radial infall close to free-fall.

than  $B_z$ , which is attributed to the lower rotation velocity in this case (see Fig. 6.3 and text below). For radii  $< 20$  AU, in both runs  $B_z$  is the dominant component. However, here already numerical effects come into play which in particular might hinder the build-up of the toroidal magnetic field component. We also mention that all components show signs of an accretion shock at a few 100 AU moving outwards with time in accordance with the density and temperature field shown in Fig. 6.1. This is caused by the tight coupling of magnetic fields and matter due to the conditions of ideal MHD. Furthermore, a comparison with the thermal pressure shows that in both runs the magnetic pressure in the region within the accretion shock is larger than or at least equal to the thermal pressure. This implies that the magnetic field most likely plays a significant role in the evolution of the protostellar disc and in the accretion history of the protostars.

Next we analysis the time evolution of the velocity structure in the two discs in run 26-4 and run 5.2-4. For this purpose, in Fig. 6.3 we show the radial dependence of the rotation velocity  $v_{\text{rot}}$ , the radial velocity  $v_{\text{rad}}$ , and the Keplerian velocity  $v_{\text{kep}}$ . The Keplerian velocity is calculated using the total mass, including sink particles, within the sphere of given radius  $r$ . It can be seen that for run 26-4 (left panel) a rotationally supported disc builds up with rotation velocities close to the Keplerian value. The maximum radius, where  $v_{\text{rot}}$  equals  $v_{\text{kep}}$  increases over time reaching about 150 – 200 AU after 5000 yr. At the same time, as expected for a rotationally supported disc, the radial velocity in the inner region nearly drops to zero.

The overall situation changes dramatically when considering run 5.2-4 (right panel). Here, no rotationally supported disc builds up with  $v_{\text{rot}}$  staying significantly below  $v_{\text{kep}}$  all the time. In fact, the absolute value of  $v_{\text{rad}}$  is almost always higher than the rotation velocity and of the order of the free-fall velocity  $v_{\text{ff}} = \sqrt{2}v_{\text{kep}}$ . Nevertheless, as can be seen in the top right panel of Fig. 6.1, a flat disc-like structure with a significantly increased column density builds up. We emphasise that for both cases considering the behaviour

within the central 10 AU is not conclusive since at such small radii the resolution limit is reached.

The dramatically different evolution of the density, magnetic field and velocity structure in the midplane of both runs is also indicated in Fig. 6.4. Here we show the column density integrated over the total disc height of  $2 \cdot 47$  AU, the magnetic field strength and the velocity field along a slice in the midplane for two different times. For run 26-4 (left panel of Fig. 6.4) a well-defined Keplerian disc with more or less sharp boundaries develops, which was already indicated by the jump in the column density in Fig. 6.1. The velocity field within the disc reveals a significant rotational component as already seen in Fig. 6.3. Interestingly, despite the strong fragmentation occurring in the inner 200 AU, the overall disc-like structure is maintained. In contrast, in run 5.2-4 (right panel of Fig. 6.4) there is no evidence for the development of a Keplerian disc and the column density increases more or less smoothly towards the centre with nearly radial infall. In contrast to run 26-4 only one sink particle has formed in the very centre. In the bottom panel of Fig. 6.4 the  $z$ -component of the magnetic field in the midplane is shown. As can be seen, a field strength of up to 1 G is reached with slightly higher values for run 5.2-4. The close coupling of magnetic fields and matter due to the conditions of ideal MHD is especially pronounced in run 26-4 in the left panel of Fig. 6.4. Here the strong increase in the column density at  $r \sim 350$  AU coincides quite well with a jump in  $B_z$ .

The strong coupling of the magnetic field to the gas density is demonstrated even more clearly in Fig. 6.5 where the distribution of  $B_z$  and the total magnetic field strength  $|\mathbf{B}|$  over the whole density range is shown. Apart from local variations, the average of  $B_z$  and  $|\mathbf{B}|$ , calculated in density bins of equal size in log-space, scales roughly as  $\rho^{2/3}$  or slightly weaker over more than 6 order of magnitude in density. This is in accordance with the scaling of a magnetic field in case of a spherical collapse under the conditions of ideal MHD.

As the sink particles keep on accreting and the magnetic field is not altered during the accretion process, over the time a large amount of magnetic flux accumulates in the centre. As in addition to that ideal MHD is considered, the field lines cannot diffuse outwards. This is the cause of the bubble-like features seen in run 5.2-4: Beyond a certain point in time, the magnetic pressure in the centre is strong enough to effectively counteract gravity and starts to push material outwards reducing the magnetic flux in the centre. Indeed, analysing the  $B_z$  component of the magnetic field in the bottom right panel of Fig. 6.4 shows that the outwards moving gas is associated with a strong  $B_z$ . This is also reflected in the radial profile of  $B_z$  which over time decreases slightly in the very centre whereas at larger radii  $B_z$  increases (see right panel of Fig. 6.2). Such a magnetic flux release, which was also observed by Zhao et al. (2011), will probably hamper the formation of rotationally supported discs as the magnetic bubble expands radially outwards and therefore prevents the gas in the disc to rotate around the central objects. However, as it is not one of the main goals of this work to study these features in detail, we will not follow this point much further.

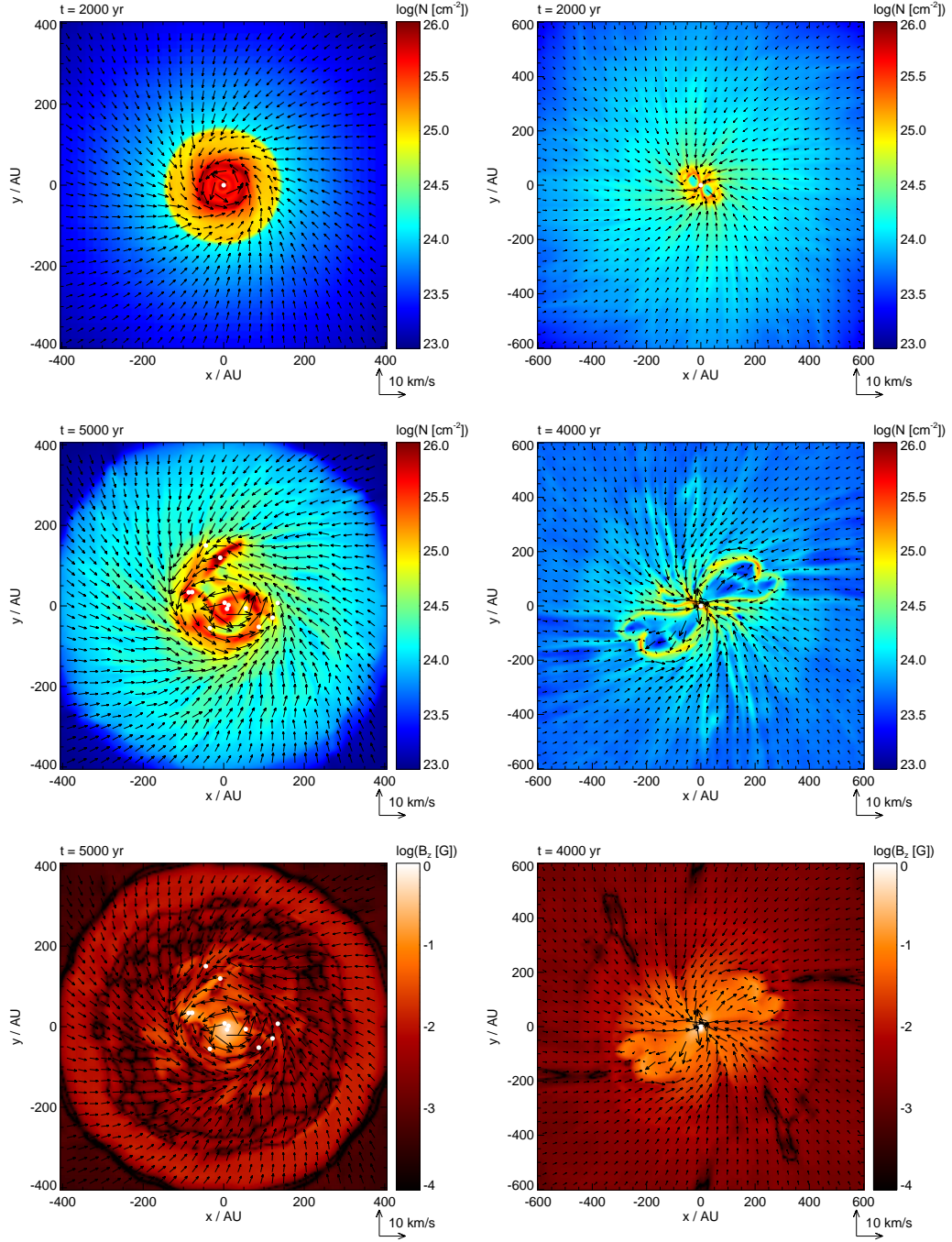


**Figure 6.4.:** Column density of the discs after 2000 yr (top) and at the end of the simulations (middle), i.e. after 5000 yr for run 26-4 (left) and 4000 yr for run 5.2-4 (right). White dots mark the projected positions of the sink particles, black vectors the velocity field in the midplane. In run 26-4 the disc is well defined with its inner region being subject to fragmentation. In contrast, in run 5.2-4 a disc with sub-Keplerian motions forms. Bottom:  $z$ -component of the magnetic field in the midplane for run 26-4 (left) and run 5.2-4 (right) at the end of each simulations. The tight correlation between field strength and matter is due to the conditions of ideal MHD. Note the different spatial scales in the left and right panel.

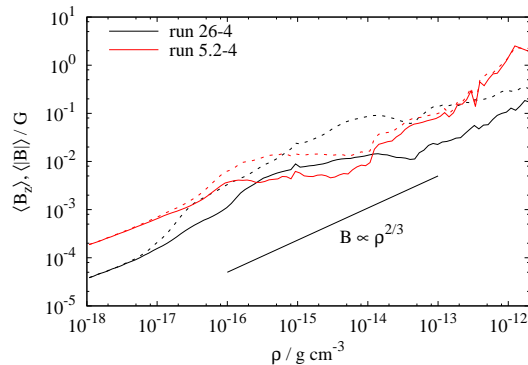


**Figure 6.5.:** Average of  $B_z$  (solid lines) and  $|B|$  (dashed lines) versus density for run 26-4 (black) and run 5.2-4 (red) at the end of each simulation. The average is calculated in density bins of equal size in log-space. The magnetic field is strongly coupled to the gas and scales roughly as  $B \sim \rho^{2/3}$  over more than 6 orders of magnitude in density.

### 6.2.3. Velocity structure

Next, we focus on the effect of the initial conditions on the velocity field in the midplane around the central sink particle. We omit the time evolution of the individual runs as the behaviour of each run is qualitatively similar to one of the two runs shown before and concentrate on the situation at the end of each simulation. As already shown in Section 6.2.2, even small changes in the initial configuration of the core, i.e. a five times stronger initial magnetic field, cause characteristic differences. The effects of core rotation and magnetic field strength on the velocity structure at the end of the simulations can be seen in Fig. 6.6. Beside the radial velocity  $v_{\text{rad}}$  the ratio  $v_{\text{rot}}/v_{\text{kep}}$  is shown as well. Decreasing the initial amount of rotational energy for runs with fixed magnetic field strength (see individual panels of Fig. 6.6) reduces the centrifugal support against gravity resulting in lower values of  $v_{\text{rot}}/v_{\text{kep}}$  and consistently in higher infall velocities. Additionally, the differences for runs with varying  $\beta_{\text{rot}}$  but fixed  $\mu$  seem to decrease when the initial field strength is increased. Furthermore, comparing runs with fixed  $\beta_{\text{rot}}$  but varying field strength (equal colours) shows that the centrifugal support, i.e.  $v_{\text{rot}}/v_{\text{kep}}$  decreases with increasing field strength. This effect is pronounced strongest for high initial rotational energies.

In principle, the simulations can be divided into two sets depending on the initial mass-to-flux-ratio  $\mu$ . In general, for runs with  $\mu \gtrsim 10$  centrifugally supported discs develop whereas for  $\mu < 10$  the formation of Keplerian discs is largely suppressed and only sub-Keplerian discs form at this early stage (see Section 6.3.2 for a detailed comparison with other numerical work). An overview of the observed dependency of disc formation and fragmentation on the initial conditions is given in Fig. 6.7. We note that in the runs 26-0.04 and 10-0.4 the structure formed in the midplane strongly resembles that of centrifugally supported discs. However, as the rotational velocities are – at least at this

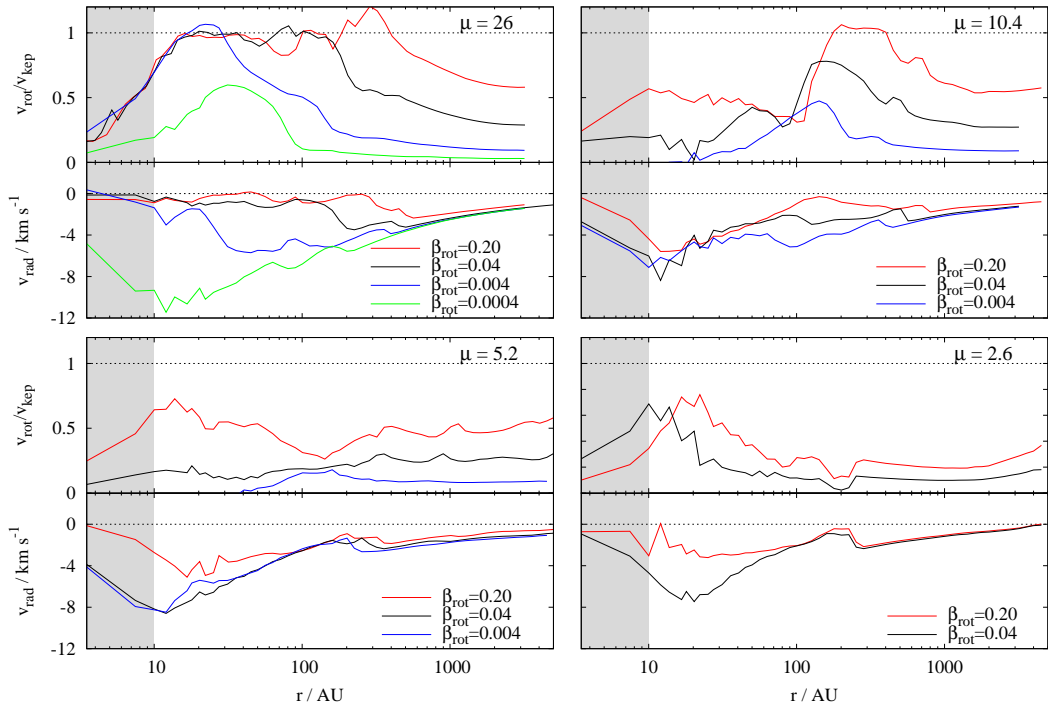


**Figure 6.6.:** Radial profile of the velocity field for the simulations with  $\mu = 26$  (top left), 10.4 (top right), 5.2 (bottom left) and 2.6 (bottom right) at the end of each simulation. For better comparison between the individual simulations the rotation velocity  $v_{\text{rot}}$  is normalised to the Keplerian velocity  $v_{\text{kep}}$ . The plotted quantities are again averaged azimuthally and vertically in a disc with a height of 47 AU. For higher  $\beta_{\text{rot}}$  the ratio  $v_{\text{rot}}/v_{\text{kep}}$  is closer to unity as expected for a Keplerian disc. Only in case of weak magnetic fields (top row) the rotation velocity reaches the Keplerian velocity while it is significantly below  $v_{\text{kep}}$  for strong magnetic fields. As expected, the absolute value of  $v_{\text{rad}}$  increases with decreasing  $v_{\text{rot}}/v_{\text{kep}}$  due to a lower centrifugal support against gravity.

early stage – well below the Keplerian velocity and the radial infall velocities relatively high, we do not denote them as Keplerian discs.

In the following, we qualitatively describe the track of a fluid particle moving along the midplane towards the centre. For all simulations considered in this work, the fluid particle first gets accelerated inwards until a radius of some 100 AU (depending on the specific simulation considered) is reached. At this radius the gas experiences a deceleration, meaning its infall motion decreases. This region can be identified as a so-called magnetic barrier (Mellon & Li, 2008) and is found in all simulations. This kind of barrier is different from a centrifugal barrier as here the rotation velocity is well below the Keplerian velocity which would be necessary to balance gravity. The reason for deceleration at such a magnetic barrier is twofold. Firstly, an outward directed thermal pressure gradient accounts for a part of the deceleration. This can be inferred from the significant increase in density and temperature at the corresponding radius (compare Fig. 6.1).

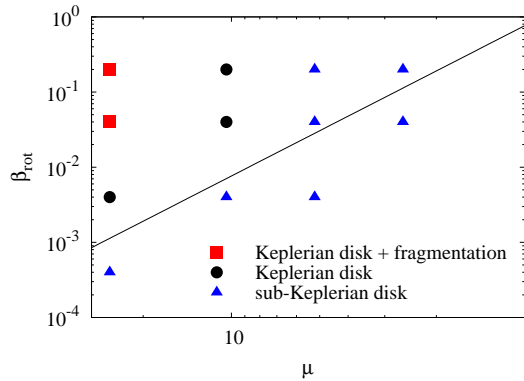


**Figure 6.7.:** Phase diagram of magnetic field and rotational energy showing the results of the simulations concerning the question of disc formation. For  $\mu < 10$  no centrifugally supported discs form (blue triangles) as well as for the slowly rotating cores in the runs 26-0.04 and 10-0.4. For weak magnetic fields Keplerian discs (black circles) form. Two of these discs are subject to fragmentation (red squares). The black solid line shows the curve where rotational and magnetic energy are equal.

Furthermore, the magnetic field itself slows down the infall motion via the combination of an outward directed magnetic pressure gradient and the effect of magnetic tension, which can be inferred from Fig. 6.2. All components of the magnetic field experience a sudden increase in the region of deceleration, thus resulting in outward directed magnetic forces. Both magnetic pressure and magnetic tension increase in strength for smaller  $\mu$  with magnetic tension starting to dominate for low  $\mu$ . For cases with  $\mu < 1$  not considered here, we expect the collapse of the core perpendicular to the field lines to be prevented completely by the Lorentz force as shown by Mouschovias & Spitzer (1976).

For radii within the magnetic barrier the velocity profiles start to differ significantly from each other. For *weak magnetic fields* (top panel of Fig. 6.6) the gas infall speed stays roughly constant. Due to angular momentum conservation the rotation velocity increases, which in consequence leads to another slow down of the infall motion. For the highest rotational energies a centrifugal barrier is encountered bringing the infall completely to halt (see runs 26-20, 26-4 and 10-20). As seen in the top panel of Fig. 6.6, the occurrence and extension of the centrifugal barrier depend strongly on the initial conditions. As an increase in centrifugal support and hence a slowdown of infall gives magnetic braking more time to operate (Mouschovias & Paleologou, 1980), angular momentum can be extracted more efficiently. This is seen in the sudden drop of  $v_{\text{rot}}/v_{\text{kep}}$  for runs with  $\mu = 10.4$  inside the centrifugal barrier causing a loss of centrifugal support and thus again speed-up of the infall motion. This is also the case for runs with *strong magnetic fields*, i.e. low  $\mu$  (bottom panel of Fig. 6.7) where magnetic braking starts to act efficiently on the gas directly after it passes the magnetic barrier so that no centrifugal barrier occurs anymore. We note that the innermost drop of  $v_{\text{rad}}$  ( $r < 10$  AU) without a corresponding increase in  $v_{\text{rot}}/v_{\text{kep}}$  is most likely caused by the limiting effect of numerical resolution as this region is only marginally resolved by about 3 grid cells.

### 6.2.4. Torques

The reason for the effective magnetic braking is shown in Fig. 6.8 where the edge-on view of the runs 26-4 and 5.2-4 at two different times is plotted. As can be seen, due to the collapse of the gas the magnetic field in the midplane has been dragged inwards producing a long magnetic lever arm (Allen et al., 2003) with a large radial component (see also Fig. 6.2). This lever arm connects the outer, slowly rotating region with the inner, fast rotating region, hence significantly enhancing the magnetic braking efficiency. As discussed before, in the case of strong magnetic fields ( $\mu < 10$ ) magnetic braking is so efficient that large centrifugally supported discs do not form at such an early stage. This is known as the magnetic braking catastrophe and was reported previously by several authors for ideal MHD simulations (e.g. Allen et al., 2003; Mellon & Li, 2008; Hennebelle & Fromang, 2008; Hennebelle & Ciardi, 2009). For a better qualitative and quantitative understanding of the magnetic braking effect we calculate the  $z$ -component of the two main torques acting on the disc, i.e. the torque exerted by the infalling gas

$$\tau_{\text{gas}} = - \int dV \nabla \cdot (\rho \mathbf{v} \cdot [\mathbf{r} \times \mathbf{v}]_z) \quad (6.4)$$

and the torque exerted by magnetic fields

$$\tau_{\text{mag}} = \frac{1}{4\pi} \int dV [\mathbf{r} \times ((\nabla \times \mathbf{B}) \times \mathbf{B})]_z. \quad (6.5)$$

For the calculations we integrate over a disc with a height of 47 AU above and below the midplane. Due to the nearly axisymmetric gravitational potential the gravitational torque is smaller than  $\tau_{\text{gas}}$  and  $\tau_{\text{mag}}$  by 2 – 4 orders of magnitude which is why we safely can neglect it in the following analysis.

In Fig. 6.9 the time evolution of  $\tau_{\text{gas}}$  and  $\tau_{\text{mag}}$  is shown for the runs 26-4 and 5.2-4. The torques are averaged azimuthally and plotted against the radius. To allow for a better comparison with  $\tau_{\text{gas}}$  we plot  $-\tau_{\text{mag}}$ . A positive  $\tau$  denotes a flux of angular momentum into the disc while for a negative  $\tau$  angular momentum is removed from it. Hence, in both runs the magnetic field is removing angular momentum from the disc, i.e. slowing down its rotation ( $\tau_{\text{mag}} < 0$ ) whereas the gas exerts a positive torque on the disc. It can be seen that the torques increase steadily with time (except for run 26-4 at 3000 yr). For run 26-4  $\tau_{\text{gas}}$  is almost always larger than the magnetic torque whereas in run 5.2-4  $\tau_{\text{gas}}$  is roughly balanced by  $-\tau_{\text{mag}}$  from the very beginning. These differences show up even more clearly in Fig. 6.10 where the torques at the end of each simulation are shown. Analysing the different panels in Fig. 6.10, it can be seen that at large radii the gas torques are always larger than  $-\tau_{\text{mag}}$ . This implies that the magnetic field has only a small effect on the collapse in the outer parts. In contrast, at smaller radii of a few 100 AU the effect of the magnetic field becomes more and more evident. For runs with a weak magnetic field (top left panel of Fig. 6.10) the torque exerted by the gas is nearly everywhere above the magnetic torque. Thus, there is a net flux of angular momentum into the discs resulting in the observed build-up of centrifugally supported discs. Only for run 26-20  $-\tau_{\text{mag}}$  equals or even exceeds  $\tau_{\text{gas}}$  in the inner region although only on

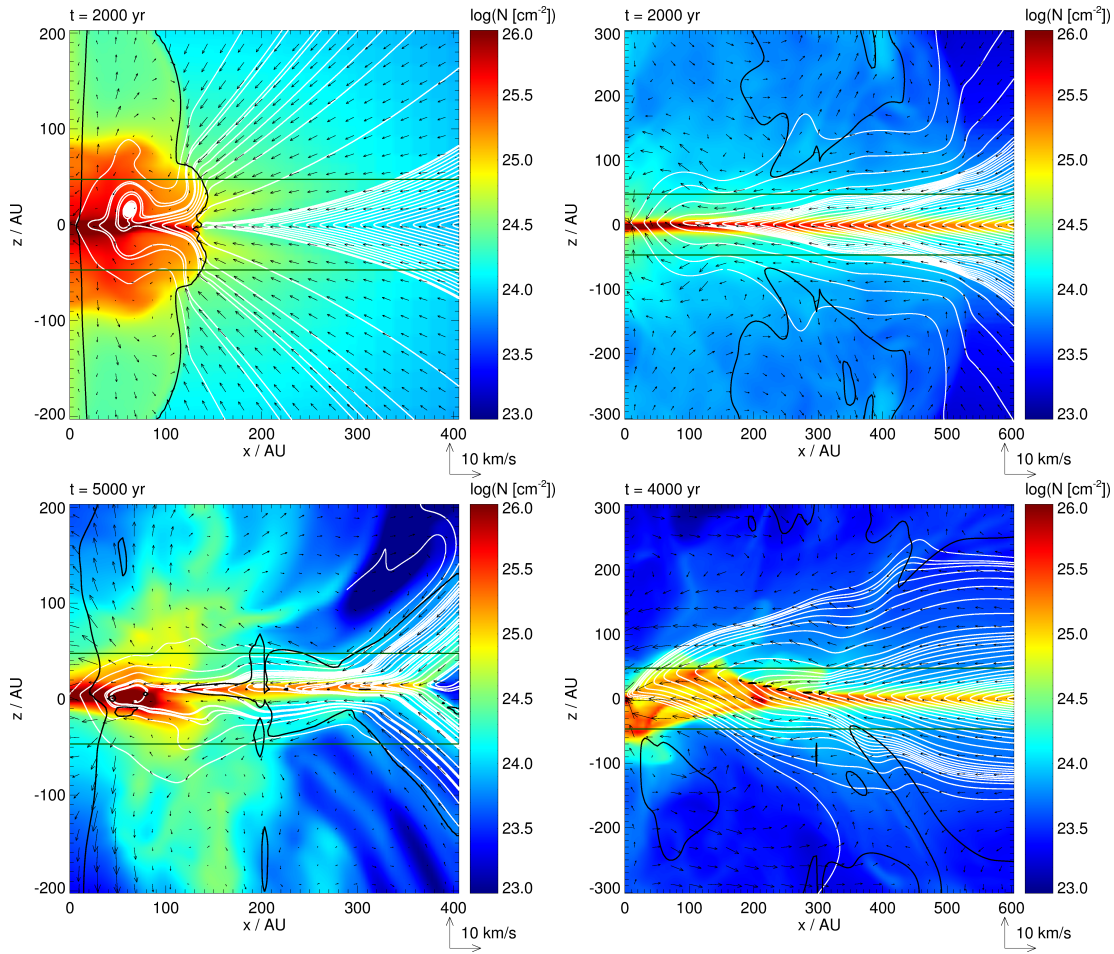


**Figure 6.8.:** Edge-on view of the central region for run 26-4 (left) and run 5.2-4 (right). Superposed on the column density are the velocity field (black vectors) and the magnetic field lines (white lines). Also shown are the regions where the toroidal magnetic field dominates over the poloidal field (black lines) and the region used for calculating disc properties (dark green line). As can be seen, in run 26-4 the greatest part of the inner region is dominated by the toroidal magnetic field whereas in run 5.2-4 only smaller parts further out are dominated by  $B_\phi$  (see also Chapter 7 for a detailed consideration of this result). Note the different spatial scales in the left and right panel.

a low level. This is due to the large Keplerian disc, which has already formed in this run having only very small infall velocities and thus a low  $\tau_{\text{gas}}$ . The sharp jump of  $\tau_{\text{gas}}$  around  $r = 300$  AU in this run is caused by the accretion shock at the edge of the disc where  $v_{\text{rad}}$  drops to zero (see top left panel of Fig. 6.6). When lowering  $\mu$ , i.e. increasing the field strength, the magnetic torque approaches  $\tau_{\text{gas}}$ . In particular for the runs with  $\mu = 5.2$  and  $2.6$   $-\tau_{\text{mag}}$  is very close to  $\tau_{\text{gas}}$  (bottom panel of Fig. 6.10). This indicates that an equilibrium between  $\tau_{\text{gas}}$  and  $\tau_{\text{mag}}$  is reached where as much angular momentum is removed by magnetic braking as it is added due to the gas infall. Hence, in the case

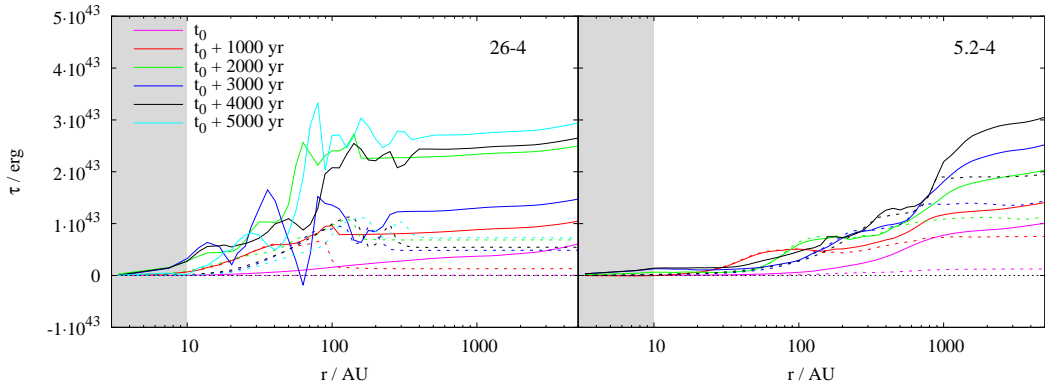


**Figure 6.9.:** Gas torque (solid lines) and magnetic field torque (dashed lines) exerted on the disc for run 26-4 (left) and run 5.2-4 (right). The torques are averaged azimuthally and shown at the same times as in Fig. 6.3. As  $\tau_{\text{gas}}$  is negative, we plot  $-\tau_{\text{gas}}$  for better comparison.

of strong magnetic fields the net angular momentum flux is roughly zero preventing Keplerian discs from forming.

To summarise, centrifugally supported discs at very early stages only form in simulations with  $\mu \gtrsim 10$  (see Fig. 6.7 for an overview). In these cases magnetic braking is too weak to remove angular momentum at the same rate as it is transported inwards by gas motions so that Keplerian discs are able to form.

### 6.2.5. Accretion rates

Closely related to the velocity structure of the matter around the sink particles is the accretion onto the particles themselves. The general behaviour of the accretion rate with varying initial conditions can be inferred from Table 6.1 where we list the totally accreted masses and the corresponding time averaged accretion rates. Additionally, in Fig. 6.11 the accretion rates of all runs are plotted against the initial mass-to-flux ratio. Up to  $\sim 4 M_{\odot}$  are accreted during the simulations resulting in time averaged accretion rates of a few  $10^{-4} M_{\odot} \text{ yr}^{-1}$ . Interestingly, the accretion rates do not vary by more than a factor of about 3 between the different simulations. This is remarkable, considering the large range in parameter space covered by the initial conditions (see Fig. 5.1). For each set of simulations with equal  $\mu$  there is also a rough correspondence between the accretion rate and the infall velocity shown in Fig. 6.6. As expected, higher infall motions result in higher accretion rates.

For a more detailed analysis of the accretion rates, we consider their time evolution in Fig. 6.12. We mention that for the runs 26-20 and 26-4, where more than one sink particle is formed, both the total accretion rate on all sink particles (solid lines) and the accretion rate of the first particle formed (dashed lines) are shown. A more detailed analysis of the accretion history in the case of fragmentation will be carried out in Section 6.2.6. As can be seen in Fig. 6.12, for all runs without further fragmentation there seems to be a slight decrease in the accretion rates over time. Numerical studies (e.g. Klessen,

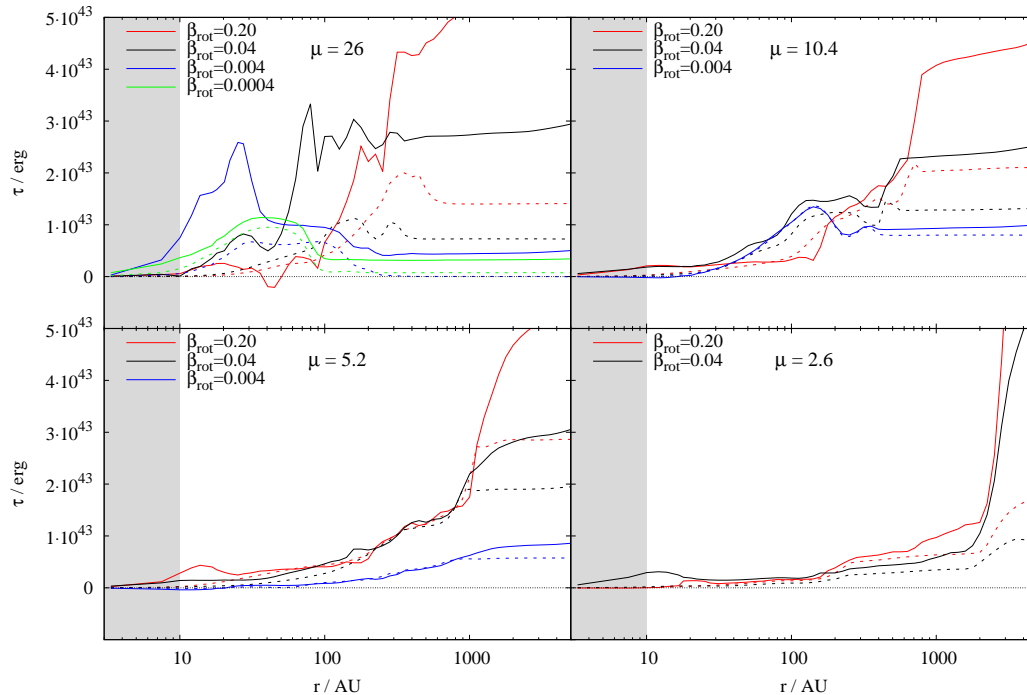


**Figure 6.10.:** Gas torque (solid lines) and magnetic field torque (dashed lines) exerted on the disc for runs with  $\mu = 26$  (top left), 10.4 (top right), 5.2 (bottom left) and 2.6 (bottom right) at the end of each simulation. As  $\tau_{\text{gas}}$  is negative, we plot  $-\tau_{\text{gas}}$  for better comparison. For high magnetic field strengths the magnetic torque roughly balances the gas torque resulting in the suppression of the formation of Keplerian discs.

2001; Schmeja & Klessen, 2004) as well as observational results (see Andre et al., 2000, for an overview) indicate that there is indeed a decline in the accretion rate by orders of magnitude, although timescales for this decline are typically of the order of several  $10^4$  yr and are therefore much longer than in our study. Another typical feature of the accretion rates shown in Fig. 6.12 are the fast variations within a factor of about 2 around the mean value. This fast variations are caused by moderate density perturbations developing in the midplane. Each time a perturbation moves through the centre, it causes the accretion to vary around its mean. The variations are generally rather small (with a few exceptions in the runs 26-20, 26-4 and 26-0.4) and would probably be smoothed out in time by viscous effects in the inner disc not resolved here. However, we cannot exclude that the varying accretion rates would influence the protostellar evolution as proposed by stellar evolution models (e.g. Wuchterl & Klessen, 2001; Baraffe & Chabrier, 2010). For the runs 26-20 and 26-4 where further sink particles are formed the total accretion rate shows no signs of a decrease. In contrast, an increase of the total accretion rates seems to occur as soon as fragmentation sets in. The accretion onto the first sink particle formed (dashed lines), however, seems to decrease from this point on (see also Section 6.2.6).

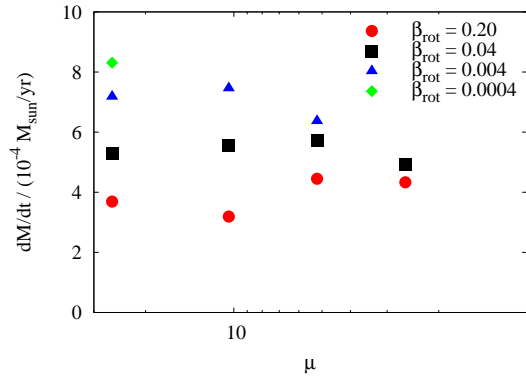


**Figure 6.11.:** Mean accretion rates of the different simulations plotted against the initial mass-to-flux-ratio  $\mu$ . Equal symbols denote equal initial rotational energies. The accretion rates seem to converge with decreasing  $\mu$ .

The only simulations where the accretion rates decrease significantly over time are the runs with  $\mu = 2.6$  showing a sharp drop after roughly 2500 yr. This is caused by the occurrence of magnetically driven bubbles in the midplane as shown exemplarily in the right panel of Fig. 6.4. In the other runs, however, the accretion rates seem to decrease only slightly showing no sign that the magnetically driven outflow, which is launched from the protostellar disc shortly after the formation of the protostar, can significantly reduce mass accretion over time. Similar results in related work on magnetic fields in massive star formation are found by Peters et al. (2011) and Hennebelle et al. (2011) as well. This is due to the fact the mass accretion through the disc is nearly unaffected by the shut-off of gas infall from below or above the disc due to the outflow. This is demonstrated in Fig. 6.8, clearly showing the ongoing accretion through the midplane. In order to analyse to what extent the combined effect of magnetic fields and rotation influences mass accretion, we performed the reference calculation inf-0 with no magnetic field and zero rotation. In this run the sink particle accretes  $4.39 M_{\odot}$  within the first 5000 yr corresponding to a time averaged accretion rate of  $8.77 \cdot 10^{-4} M_{\odot} \text{ yr}^{-1}$ . Hence, the accretion rates in runs with magnetic fields and rotation are reduced to a level of about 35% – 95% of this value (see Table 6.1).

As can be inferred from Table 6.1 and from Fig. 6.11, there are some systematic trends in the time averaged accretion rates with varying initial conditions, although the overall variation is not very large ( $\lesssim 3$ ). Increasing the overall rotational support against gravity, i.e.  $\beta_{\text{rot}}$ , for fixed  $\mu$  results in lower accretion rates. This is in agreement with the increase in  $v_{\text{rot}}/v_{\text{kep}}$  and the decrease in  $v_{\text{rad}}$  in the surrounding disc as shown in Fig. 6.6. As already observed for the velocity structure in the midplane, the differences in the accretion rates for runs with different  $\beta_{\text{rot}}$  but fixed  $\mu$  decrease with increasing magnetic field strength as can be seen in Fig. 6.11. As shown before, this is due to the efficient magnetic braking removing angular momentum at roughly the same rate as it is transported inwards. As a consequence, the accretion rates are roughly independent of the initial amount of angular momentum. An even further increase in the field strength

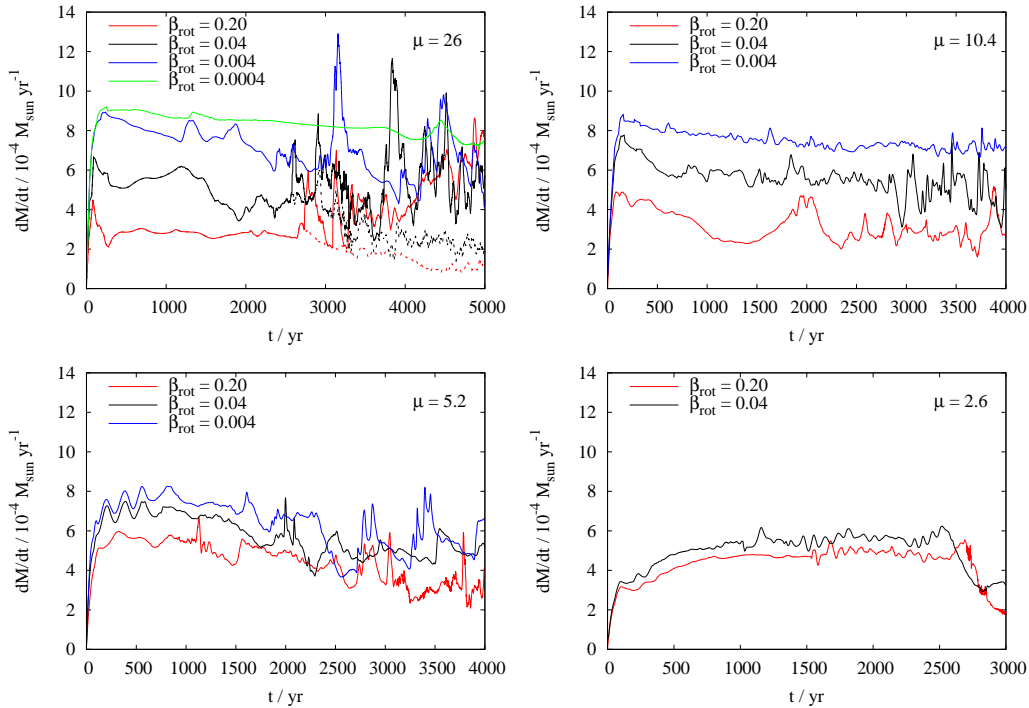


**Figure 6.12.:** Total accretion rates of all runs performed with  $\mu = 26$  (top left), 10.4 (top right), 5.2 (bottom left) and 2.6 (bottom right). For the runs 26-20 and 26-4 also the accretion rate of the first sink particle formed is shown (dashed lines). As expected, the accretion rates decrease with increasing initial rotational energy for a given magnetic field strength. The differences in the accretion rates for runs with fixed  $\mu$  but varying  $\beta_{\text{rot}}$  decrease with increasing magnetic field strength.

would probably result in even lower accretion rates than the  $4 - 5 \cdot 10^{-4} M_{\odot} \text{ yr}^{-1}$  observed for  $\mu = 2.6$  due to stronger magnetic forces counteracting gravity.

The accretion rates for varying  $\mu$  but fixed  $\beta_{\text{rot}}$  show an interesting and less clear behaviour. For high initial rotational energies, i.e.  $\beta_{\text{rot}} = 0.20$  and  $0.04$ , respectively, the accretion rates are roughly constant or even show a slight increase with decreasing  $\mu$  until  $\mu = 5.2$  and then drop for the case with  $\mu = 2.6$ . For  $\beta_{\text{rot}} = 0.004$  the accretion rate increases from  $\mu = 26$  to  $\mu = 10.4$  and start to decline at  $\mu = 5.2$  already. We attribute this behaviour to two competing effects of the magnetic field. On the one hand, magnetic fields act to enhance accretion onto the protostar by magnetic braking reducing the centrifugal support against gravity. Hence, the effect of magnetic braking alone would cause increasing accretion rates with decreasing  $\mu$  as it is indeed observed for low field strengths. The second effect influencing the accretion rates is the Lorentz force, i.e. the combination of magnetic pressure and magnetic tension, induced by strongly bent field lines (see Fig. 6.8). Magnetic pressure and magnetic tension counteract gravity by exerting an outward directed force on the gas resulting in reduced accretion rates. The

strength of this effect increases with the field strength thus tending to lower the accretion rates for low values of  $\mu$  which is indeed observed in Fig 6.11.

The combination of both effects – magnetic braking enhancing accretion and the Lorentz force counteracting accretion – results in the observed non-linear behaviour of the accretion rates: By increasing the magnetic field strength at a given  $\beta_{\text{rot}}$  up to a certain critical value an equilibrium between the torques acting on the disc is reached where the removal of angular momentum by magnetic braking balances its inwards transport (see Fig. 6.10). Up to this value, an increase in the field strength is associated with increasing or at least constant accretion rates as observed in our simulations. Further increase in the field strength beyond this point cannot enhance the magnetic braking efficiency anymore. In fact, now the increase of the magnetic field strength (decrease, if  $\mu$  is considered) leads to declining accretion rates due to the growing strength of the Lorentz force counteracting gravity, in accordance with our findings of declining accretion rates for strong fields with  $\mu \lesssim 5$ . The exact value of  $\mu$ , where this turnover occurs, depends on the initial amount of rotational energy and decreases with increasing  $\beta_{\text{rot}}$ .

### 6.2.6. Disc fragmentation

As mentioned earlier, the runs 26-20 and 26-4 show rapid fragmentation of the protostellar disc after the first protostar has formed. Due to a high amount of rotational energy and a weak magnetic field, magnetic braking can only remove a small amount of angular momentum leading to the formation of Keplerian discs with considerable extensions of a few 100 AU (see top left panel of Fig. 6.6 for comparison). As the mass load onto these discs exceeds their capability to transport material inwards by gravitational, viscous or magnetic torques, the discs become unstable and fragment (e.g. Kratter et al., 2010). In the simulations presented here, this happens  $\sim 2500$  yr after the formation of the first sink particle. At the end of the simulations, i.e. after 5000 yr there are 12 sink particles in run 26-4 and 20 in run 26-20. All other simulations show no fragmentation so far although some of them form a Keplerian disc (see Fig. 6.7).

The accretion histories for run 26-20 and run 26-4 are shown in Fig. 6.13. Run 26-20 (left panel) exhibits a very symmetric disc fragmentation forming pairs of protostars at roughly the same time and opposite positions (as seen from the centre). Even in their further mass evolution each pair develops very similar as can be seen from the left panel of Fig. 6.13 where the lines of each pair are nearly indistinguishable. For run 26-4 (right panel) only the evolution of the second and third sink particle is symmetric, while at later times there is no pairwise formation of sink particles anymore due to an asymmetric evolution of the disc. We note that in both runs only the first sink particle created has reached a mass above  $1 M_{\odot}$  so far whereas all other particles have masses of at most  $\sim 0.1 M_{\odot}$ . For comparative purposes, in Fig. 6.13 we also plot the totally accreted mass of all sinks formed. As can be seen, in both runs more than 60% of the total mass is accreted onto the first sink particle.

After about 2500 yr, i.e. after the creation of further sink particles, there occurs a slight but nevertheless noticeable decrease in the accretion onto the first sink particle

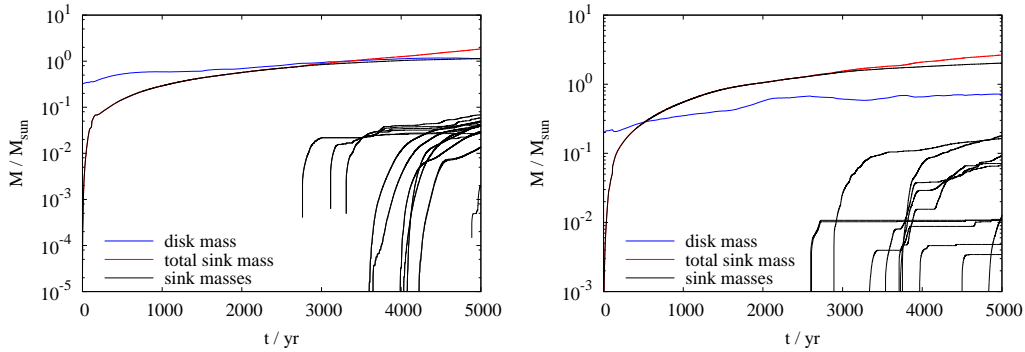


**Figure 6.13.:** Accretion history of run 26-20 (left) and run 26-4 (right). The red lines show the total mass of all sink particles. The formation of sink particles in run 26-20 occurs pairwise (except the first one) and also the further evolution of each pair is nearly indistinguishable except at the very end so that in the beginning each line represents two particles. Also shown is the time evolution of the disc mass, which is of the order of or somewhat below the totally accreted mass.

(see the dashed lines in the top left panel of Fig. 6.12). This fragmentation-induced starvation (Peters et al., 2010a,b) is caused by the surrounding sink particles soaking up the infalling material. This behaviour was also observed recently in related work on massive star formation (Peters et al., 2011; Girichidis et al., 2011, 2012). However, in these cases the starvation effect for the first sink particle, partly with a complete shut-off of the accretion flow, is much more pronounced than in our case where the accretion rates decrease by a factor of  $\sim 2$  only. The reason for this difference is probably the longer physical time simulated by these authors.

Beside the sink masses, in Fig. 6.13 also the disc masses are shown. For the mass determination we define the disc as follows: Firstly, we determine the maximum cylindrical radius  $r_{\max}$  where the gas falls below a density of  $5 \cdot 10^{-15} \text{ g cm}^{-3}$ . This density threshold was found to reasonably agree with the density at the accretion shock seen in Fig. 6.1. The disc mass is then defined as the total mass of gas within a cylinder with a height of 47 AU above and below the midplane and a radius of  $r_{\max}$  around the centre. As can be seen, at the end of the simulations the disc masses are of the order of  $1 M_{\odot}$  and therefore somewhat below the totally accreted sink masses.

Next, we study the stability of the discs against gravitationally induced perturbations. Disc stability is described by the Toomre parameter (Toomre, 1964) defined as

$$Q = \frac{\kappa c_s}{\pi \Sigma G} \quad (6.6)$$

with the epicyclic frequency  $\kappa$ , sound speed  $c_s$ , surface density  $\Sigma$ , and gravitational constant  $G$ . Discs are prone to gravitationally induced fragmentation if  $Q$  is lower than 1. As magnetic fields are present in the discs, one can define the magnetic Toomre

parameter (Kim & Ostriker, 2001)

$$Q_M = \frac{\kappa (c_s^2 + v_A^2)^{1/2}}{\pi \Sigma G}, \quad (6.7)$$

where  $v_A$  is the Alfvénic velocity (Eq. 3.12) taking into account all components of the magnetic field. In the following, we analyse the stability of the discs in the runs 26-20, 10-20, 5.2-20 and 26-0.4 as these simulations cover a wide range of initial conditions. In particular, we concentrate on the stabilising effect of the magnetic field by comparing  $Q_M$  and  $Q$ .

In Fig. 6.14 the face-on view of the discs at the end of each simulation as well as the radial dependence of the Toomre parameters are plotted.  $Q$  and  $Q_M$  are calculated numerically by the azimuthally averaged values of  $c_s$ ,  $v_A$ ,  $\kappa$ , and  $\Sigma$  and are shown for several times. For the disc in run 26-20 (top left) we also show the situation after 4000 yr, which corresponds to the time when the ring at 200 AU starts to fragment. It can be seen that by then the hydrodynamical Toomre parameter  $Q$  drops below 1 around 200 AU and 400 AU. However, only around 200 AU a fragmented ring is observed in the top-on view of the disc, which agrees with the magnetic Toomre parameter  $Q_M$  dropping to  $\sim 1$  only at this position (at 4000 yr). After 5000 yr  $Q_M$  has increased again as a good fraction of the gas has already been accreted by the sink particles. We note that we have neglected the contribution of secondary sink particle to the column density. However, their only effect would be to lower  $Q$  and  $Q_M$  in regions which are already unstable and fragmenting but not outside it and therefore they would not change the results qualitatively.

However, of more interest are the cases where no fragmentation has occurred. In run 10-20 (top right) no fragmentation has occurred in agreement with a value for  $Q$  of  $\sim 1$  except around 500 AU where it is lower. However, at this particular position as well as everywhere else  $Q_M$  is above 1. This indicates that around 500 AU the magnetic pressure contributes to the stability of the disc just as around  $r = 400$  AU in run 26-20. For the sub-Keplerian discs found in run 5.2-20 and 26-0.4 (bottom panel of Fig. 6.14) the hydrodynamical Toomre parameter is below 1 over a wide range indicating instability. However, no fragmentation occurs as can be seen in the top-on views. In contrast to  $Q$  the magnetic Toomre parameter  $Q_M$  is in general above 1, which fits better to the observed behaviour indicating that the magnetic field is responsible for stabilising the disc. However, it is not clear to what extent the Toomre analysis, originally derived for rotationally supported discs without infall motions, is applicable for strongly sub-Keplerian discs with significant infall motions as presented here. We also note that discs were found to be stable against fragmentation even for  $Q < 1$ . Kratter et al. (2010), analysing the stability of discs under purely hydrodynamical conditions, find stable discs with  $Q$  being locally smaller than 1. The authors attribute this to the fact that  $Q = 1$  indicates instability of axisymmetric perturbations in infinitely thin discs (Toomre, 1964). For thick discs, as it is the case in our simulations, they argue that the instability criterion is expected to be somewhat relaxed (Goldreich & Lynden-Bell, 1965). Hence, even in cases where  $Q$  is smaller than 1 and no fragmentation occurs,

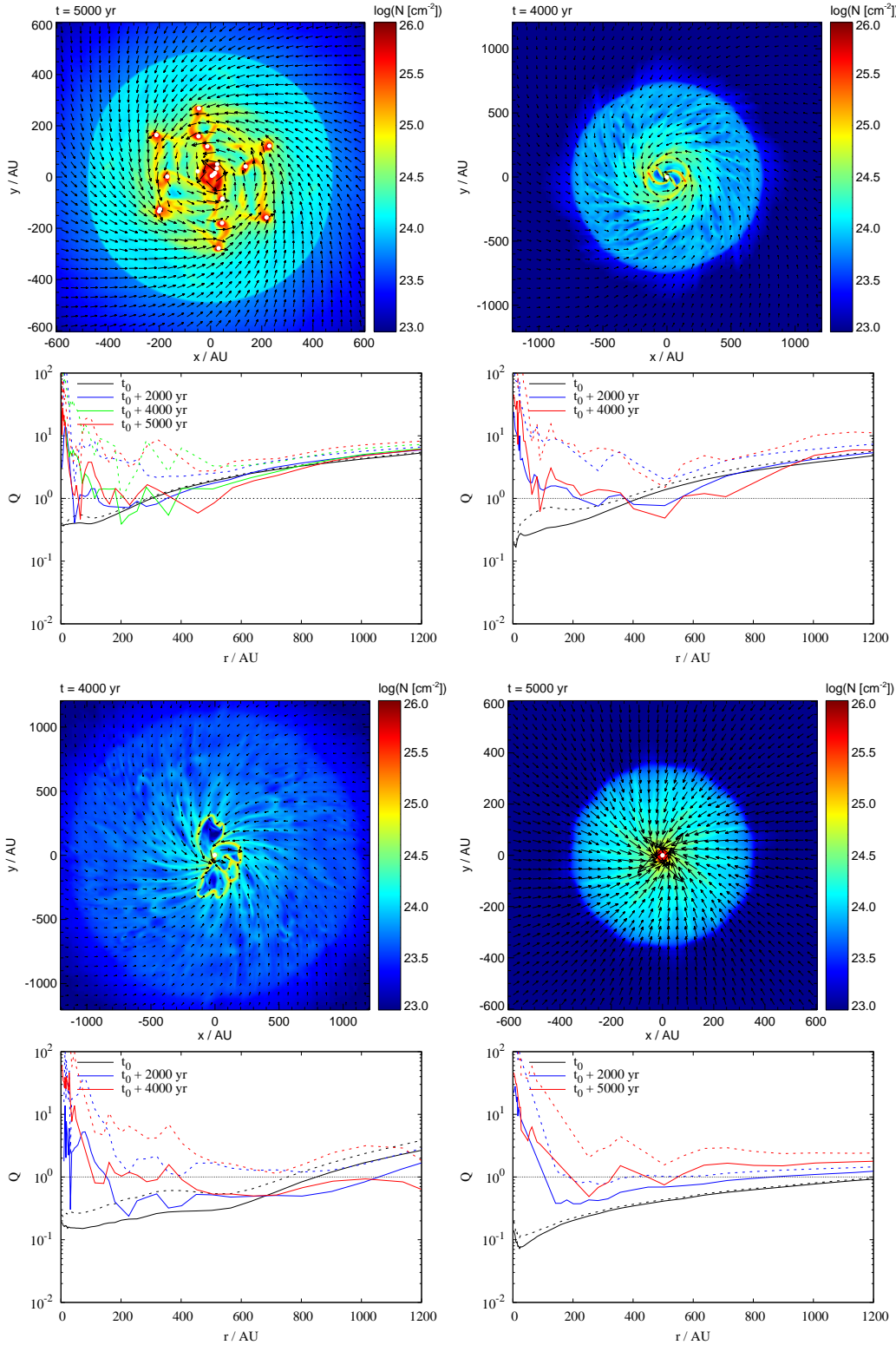


**Figure 6.14.:** Column density of the disc in the runs 26-20, 10-20, 5.2-20 and 26-0.4 (from top left to bottom right) at the end of each simulation. Below each column density plot the Toomre parameter  $Q$  (solid lines) and magnetic Toomre parameter  $Q_M$  (dashed lines) for  $t = 0$  yr, 2000 yr and 4000 yr (for runs 10-20 and 5.2-20) and 5000 yr (for runs 26-20 and 26-0.4) plotted against the radius are shown. The hydrodynamical Toomre parameter  $Q$  is of the order of 1 or – in particular for the sub-Keplerian discs in the bottom panel – slightly below 1 whereas  $Q_M$  is almost everywhere above 1.

stability could be given due to the thermal pressure alone without the magnetic pressure being needed.

To summarise, the Keplerian discs, also those in the other runs not shown here, are in parts reasonably well described by the hydrodynamical Toomre parameter  $Q$ . However, there is some indication that the magnetic pressure is required to stabilise the disc against fragmentation. For sub-Keplerian the suppression of fragmentation seems to be even more a consequence of the magnetic field. However, in this case the Toomre analysis might be misleading due to the sub-Keplerian nature of the discs and the strong infall motions not considered in the derivation of the Toomre criterion. We mention that we expect fragmentation to occur also for other runs with low magnetic field strengths ( $\mu \geq 10$ ) if the evolution of the discs would be followed further. This assumption is supported by the fact that the discs show a continuing growth due to ongoing infall and are only marginally stable ( $Q \simeq 1$ ).

## 6.3. Discussion

### 6.3.1. Numerical caveats

The simulations considered so far were run with a maximum resolution of 4.7 AU. In order to test the resolution dependency of our results we performed two more simulations with the same initial setup as in run 26-4 but with a resolution varied by a factor of 4 in either direction. A detailed comparison of the results is shown in the appendix A. The results of the resolution study suggest that the spatial resolution of 4.7 AU used in the simulations presented in this work is sufficient to properly follow the dynamical evolution of the protostellar discs and of the accretion rates.

As mentioned in Section 5.2, a minimum density threshold of  $1 \cdot 10^{-15} \text{ g cm}^{-3}$  in the central 67 AU is applied after the formation of the first sink particle. The exact amount of mass added artificially over the whole simulation time depends on the individual simulation but never exceeds a few  $10^{-2} M_{\odot}$  corresponding to a mass rate of  $10^{-6} - 10^{-5} M_{\odot} \text{ yr}^{-1}$ , which is significantly below the observed accretion rates of a few  $10^{-4} M_{\odot} \text{ yr}^{-1}$ . Hence, we suppose that the dynamical influence of the density threshold is negligible. Therefore its application seems to be appropriate in order to avoid very small hydrodynamical timesteps which in turn would significantly increase the computational costs for the simulations.

It is not clear to what extent our results are affected by the chosen density profile  $\rho(r) \propto r^{-1.5}$ . Girichidis et al. (2011) find that concerning fragmentation properties their results strongly depend on the initial density profile which they attribute to the varying relative importance of turbulence compared to gravity. As we do not include turbulent motions in our simulations, our results should depend less on the density profile than in the work of Girichidis et al. (2011), in particular with regard to the accretion rates, which also vary only rather moderately in the work of Girichidis et al. (2011). Hence, considering protostellar disc formation and accretion rates, we expect our results to be representative for  $100 M_{\odot}$  cores with the given rotational and magnetic energies.

### 6.3.2. Disc formation

As demonstrated in Fig. 6.7, a transition from early-type, large-scale Keplerian discs to sub-Keplerian discs occurs around a normalised initial mass-to-flux ratio  $\mu$  of  $\sim 10$  independent of the initial amount of rotational energy. This is in good accordance with a couple of papers studying the evolution of low-mass magnetised discs. While Hennebelle & Fromang (2008) and Hennebelle & Ciardi (2009) find a value for  $\mu$  between 5 – 10, below which Keplerian disc formation is suppressed, Allen et al. (2003) and Mellon & Li (2008) find no Keplerian discs for  $\mu$  up to at least 10. Duffin & Pudritz (2009) studying the possible fragmentation of magnetised discs with an initial  $\mu = 3.5$  find sub-Keplerian rotation profiles as well in agreement with the results mentioned before. Although all these simulations apply to low-mass star formation with core masses around  $1 M_{\odot}$ , the observed maximum value of  $\mu$  for which the formation of large-scale Keplerian discs is suppressed agrees remarkably well with our finding of  $5 < \mu < 10$ .

For the sub-Keplerian discs observed in our simulations the infall velocities are in general significantly larger than the rotation speed, i.e.  $|v_{\text{rot}}/v_{\text{rad}}| < 1$ , and close to free-fall (see right panel of Fig. 6.3 and Fig. 6.6). This is attributed to the highly gravitationally unstable configuration of the cores containing about 56 Jeans masses and the lack of rotational support due to the very efficient magnetic braking. Hence, the cores cannot be stabilised against gravitational collapse by thermal pressure alone in contrast to low-mass cores containing only  $\sim 1$  Jeans mass. Indeed, for highly magnetised low-mass cores with sub-Keplerian disc rotation the infall velocities are significantly smaller than in our case and usually even smaller than the rotation velocities (e.g Hennebelle & Fromang, 2008; Duffin & Pudritz, 2009).

For  $\mu \gtrsim 10$  we find large-scale Keplerian discs in our simulations. Although this value of  $\mu$  is lower than usually measured in molecular cloud cores (Falgarone et al., 2008; Girart et al., 2009; Beuther et al., 2010), the result concerning disc formation is in agreement with an increasing number of observations of rotationally supported discs in massive star forming regions made in recent years (see Cesaroni et al., 2007, and references therein). As an example, discs with sizes of a few 100 AU to 1000 AU and masses between 0.1 and about  $10 M_{\odot}$  have been observed (Fuller et al., 2001; Shepherd et al., 2001; Chini et al., 2004; Fernández-López et al., 2011; Preibisch et al., 2011). These discs are similar in size to the discs obtained in our runs with weak magnetic fields and also show Keplerian-like rotation profiles. In addition, our disc masses of  $\sim 1 M_{\odot}$  calculated in run 26-20 and run 26-4 (see Fig. 6.13) lie well in the mass range spanned by these observations. However, the protostars observed by the authors mentioned before have masses around 5 –  $10 M_{\odot}$  and are therefore a factor of a few more massive than our most massive sink particles. We attributed this to the fact that the observed disc/star-systems are in a somewhat later evolutionary stage than our systems. Nevertheless, the fact that the disc masses in our simulations are somewhat lower than the mass of the protostar(s) fits well in the general trend observed by the authors mentioned before.

In contrast, for  $\mu < 10$  sub-Keplerian discs are observed in our simulations. Again, we mention that our simulations end a few 1000 yr after sink particle formation, thus in a very early phase. An observer looking at such a system from edge-on will observe

a flattened structure similar to a Keplerian disc but without the typical signatures of rotation (see right panel of Fig. 6.8). Indeed, there is a growing number of observations of such flattened structures reported in literature (see Cesaroni et al., 2007, and references therein), although these observations often refer to more massive structures and more evolved protostellar objects than present in our simulations. Due to the insufficient centrifugal support, these structures are not in equilibrium and show considerable radial infall motions, in accordance with our findings (compare bottom panel of Fig. 6.6).

The reason for the lack of centrifugal support in such sub-Keplerian discs is the strong magnetic torque acting on the midplane (see Fig. 6.10). Angular momentum is removed by magnetic braking at roughly the same rate as it is provided by the infalling gas. The angular momentum removed from the midplane is partly deposited in the outflow and partly in regions further out which are connected to the inner parts by the magnetic lever arm (Allen et al., 2003) created through the equatorial pinching of the magnetic field (see Fig. 6.8). A possible way to reduce the magnetic braking efficiency would be the inclusion of non-ideal MHD effects like ohmic dissipation or ambipolar diffusion in the simulations. However, recent numerical work including ambipolar diffusion (Mellon & Li, 2009; Duffin & Pudritz, 2009), ohmic dissipation (Dapp & Basu, 2010; Dapp et al., 2012) and also both effects (Li et al., 2011) show that even in the case of non-ideal MHD it is not possible to form Keplerian discs in such early stages. In fact, the aforementioned authors find that the formation of rotationally supported discs in the case of strong magnetic fields is suppressed down to scales well below our resolution limit of roughly 10 AU unless a strongly enhanced resistivity – when including Ohmic dissipation – is used (Krasnopolsky et al., 2010). Including the Hall effect can result in the formation of large-scale Keplerian discs (Krasnopolsky et al., 2011). The authors claim, however, that a Hall coefficient about one order of magnitude larger than expected under realistic conditions would be required. Hence, at the evolutionary stage considered in this work, we cannot expect to form a proper, large-scale Keplerian disc even by including the effects of ambipolar diffusion, Ohmic dissipation or the Hall effect in our calculations.

In the case of turbulent, strongly magnetised low-mass cores, Santos-Lima et al. (2012) have reported the formation of 100 AU scale, Keplerian discs, which they attribute to the effect of turbulent reconnection (Lazarian & Vishniac, 1999). However, as we have not included turbulence in the simulations presented so far, we will postpone this particular topic to Chapter 8 where we focus on the effect of turbulent motions on the formation of protostellar discs.

The question now arises how Keplerian discs on 100 AU scale can form if the non-turbulent cores have mass-to-flux ratios  $\mu \lesssim 5$ . As seen from the previous discussion, protostellar discs are frequently observed around massive protostars. Furthermore, even if no clear indications of discs are found, in general the observation of well-collimated outflows requires the presence of an underlying disc (e.g. Beuther et al., 2002c; Zhang et al., 2005). Hence, protostellar discs should be rather common around massive protostars. However, this seems to be in contradiction with our simulation results, in particular as observed star forming regions usually have mass-to-flux ratios which are only slightly super-

critical with  $\mu \lesssim 5$  (e.g. Falgarone et al., 2008; Girart et al., 2009; Beuther et al., 2010). Following the long term evolution of highly magnetised low-mass cores, Machida et al. (2011) find large-scale Keplerian discs occurring after roughly  $10^5$  yr. The authors argue that in their case magnetic braking only redistributes the angular momentum within the collapsing cores but does not completely remove it. Additionally, they find that the outflows are too weak to ultimately remove a significant fraction of mass and angular momentum from the cores. Thus, most of the core’s mass and angular momentum finally fall onto the midplane resulting in a large-scale Keplerian disc even for high magnetic field strengths. However, we note that the authors might underestimate the total amount of mass and angular momentum transferred into the interstellar medium since only low-velocity outflows are modelled in their simulations. Considering high-velocity jets and radiation-driven outflows, the amount of material ejected into the interstellar medium could be considerably larger, thus impeding the formation of large Keplerian discs. For massive stars we expect this to be even more severe as here radiation-driven outflows are even more powerful and will be able to eject angular momentum – deposited in the envelope by magnetic effects – at even higher rates than low-mass protostellar outflows (e.g. Arce et al., 2007).

At the same time outflows also provide a possible solution of the disc formation problem by diluting the envelope in which the magnetic field lines are anchored (see also Section 6.2.2 in Mellon & Li, 2008). As the magnetic braking timescale (Eq. 3.36)

$$t_{\text{mag},\parallel} = \frac{\rho_{\text{c}}}{\rho_{\text{ext}}} \frac{Z}{v_{\text{A,ext}}} \propto \rho_{\text{ext}}^{-1/2} \quad (6.8)$$

increases with decreasing envelope density<sup>1</sup>, this allows large-scale, centrifugally supported discs to form in particular at later stages not considered in this work when most of the envelope has been blown away by powerful outflows. This would agree with the fact that most of the observed disc/star-systems (see Cesaroni et al., 2007, and references therein) are in a later evolutionary stage than our systems. However, these observations could also be biased by the fact that massive Class 0 objects are more difficult to detect. For example, observations of low-mass Class 0 objects indicate that for the majority of the objects discs are present from the very early stages on (Jørgensen et al., 2009; Enoch et al., 2009, 2011). On the other hand, the picture of a successive growth of centrifugally supported discs during the evolution into Class I / II is supported from the theoretical side by Dapp & Basu (2010) and Dapp et al. (2012). Therefore, we expect large-scale Keplerian discs to form in our runs if the evolution would be followed over a much longer time, thus relaxing the problem of catastrophic magnetic braking.

In summary, our simulations suggest that in non-turbulent cloud cores Keplerian discs do not form around massive protostars in the very early stage except for unusually weak magnetic fields. Nevertheless, we expect that centrifugally supported discs will build up during the subsequent evolution of the collapsing cores.

Another point not mentioned explicitly so far is the fact that disc fragmentation seems to be suppressed for stronger magnetic fields which was also ob-

<sup>1</sup>Here the scaling of  $v_{\text{A,ext}} \propto \rho_{\text{ext}}^{-1/2}$  (see Eq. 3.12) was taken into account.

served by other authors. For low-mass cores it was shown that fragmentation can be suppressed by strong initial magnetic fields even if initial density perturbations are present (Hosking & Whitworth, 2004; Machida et al., 2005; Hennebelle & Teyssier, 2008; Duffin & Pudritz, 2009). Similar results are found for turbulent high-mass cores by Commerçon et al. (2011). Such a fragmentation inhibition in high-mass cores as observed in our work and by Commerçon et al. (2011) raises the question of how massive binaries can form. Even in the simulations where disc fragmentation occurs we do not see indications for massive binaries so far but rather a single massive protostar with a couple of low-mass companions (compare Fig. 6.13). Of course, these findings could be a consequence of the early stage the simulations end. Nevertheless, our results indicate that massive binaries possibly form in later evolutionary stages and that the initial mass ratio should be far from unity with the more massive star sitting in the centre. Observations, however, reveal that a significant fraction of massive binaries consists of stars with nearly equal masses (e.g Mason et al., 1998; Pinsonneault & Stanek, 2006). This apparent contradiction could be resolved by the work of Artymowicz & Lubow (1996) and Bate & Bonnell (1997). By simulating circumbinary discs these authors find that the masses of binary components, even when unequal in the beginning, tend to equal as accretion within the disc occurs preferentially onto the lower-mass companion. Also different binary formation scenarios like disc-assisted captures of a second protostar (Moeckel & Bally, 2007) might be at work.

### 6.3.3. Accretion rates

A prominent feature in run 5.2-4 are the bubble-like structures occurring around the centre of the disc (see right panel of Fig. 6.4). These features also occur in other runs with strong initial magnetic fields and are independently observed by Zhao et al. (2011). These bubbles are a consequence of our assumption of ideal MHD and provide a possibility to release magnetic flux from the centre. For runs with  $\mu = 2.6$  the bubbles show a significant influence on the accretion rates (bottom right panel of Fig. 6.12) reducing the accretion after 2500 yr. However, for runs with  $\mu = 5.2$  the influence of such bubbles seems to be rather limited as we cannot detect any significant changes in the accretion rates (see bottom left panel of Fig. 6.12). We therefore conclude that the accretion rates are reliable for runs with  $\mu$  down to  $\sim 5$  and – up to 2500 yr – even for the both runs with  $\mu = 2.6$ . A possible solution to avoid the formation of bubbles like features could be the inclusion of the effects of non-ideal MHD such as ambipolar diffusion or ohmic dissipation as done in recent work (Duffin & Pudritz, 2009; Mellon & Li, 2009; Dapp & Basu, 2010; Dapp et al., 2012). However, Nakano et al. (2002) argue that ohmic dissipation starts to act efficiently at particle densities above  $10^{-12} \text{ cm}^{-3}$ , which is well above the typical densities found in our discs. Hence, ohmic dissipation is not expected to be capable of significantly reducing the magnetic flux in the centre. Ambipolar diffusion, however, starts to act at lower densities (Duffin & Pudritz, 2009) and thus might be able to reduce the field strength in the centre before magnetically driven bubbles can occur.

As shown in Fig. 6.11, the accretion rates of the different runs vary only by a factor of  $\sim 3$ , which is attributed to the two competing effects of the magnetic field namely

magnetic braking and the Lorentz force. Adopting accretion rates of a few  $10^{-4} M_{\odot} \text{ yr}^{-1}$  as observed in our simulations, stars of about  $30 M_{\odot}$  would form within some  $10^4$  yr up to a few  $10^5$  yr roughly independent of the initial conditions. However, this only holds if the accretion rates stay roughly constant over the entire formation process, which might be an oversimplification as indicated by the slight decrease of the accretion rates on individual sink particles seen in Fig. 6.12 (see also Klessen, 2001; Schmeja & Klessen, 2004). A possible way to significantly change accretion rates would be to vary the initial density profile and mass of the molecular cloud core, parameters which are not explored in this work in order to limit the computational costs (see e.g. Girichidis et al., 2011). Fragmentation seems to increase the total accretion rate (top left panel of Fig. 6.12) whereas it decreases the accretion onto the first (and innermost) sink particle (see also Peters et al., 2010a,b, 2011; Girichidis et al., 2011, 2012)

Our observed accretion rates agree well with accretion rates from a number of massive star formation simulations. To begin with, our accretion rates match those necessary to overcome the radiation pressure as deduced from 1-dimensional calculations (Kahn, 1974; Wolfire & Cassinelli, 1987). Radiation-hydrodynamical collapse simulations in 2 dimensions (Yorke & Sonnhalter, 2002; Kuiper et al., 2010) and 3 dimensions (Krumholz et al., 2007, 2009; Kuiper et al., 2011) with similar core masses reveal accretion rates of a few  $10^{-4} M_{\odot} \text{ yr}^{-1}$  up to  $10^{-3} M_{\odot} \text{ yr}^{-1}$  very similar to ours. Peters et al. (2010a,b, 2011) simulating the long term evolution of HII-regions around massive protostars find similar accretion rates as well. This suggests that in our simulations accretion would continue even if the effect of radiation would be included. Girichidis et al. (2011) studying the effect of different initial conditions on massive star formation find accretion rates around  $10^{-3} M_{\odot} \text{ yr}^{-1}$ , somewhat higher than ours possibly caused by the omission of rotation or magnetic fields counteracting gravity and thus mass accretion. Similar accretion rates were also found in earlier work by Banerjee & Pudritz (2007) studying the very early evolution of a collapsed cloud core under the influence of magnetic fields and rotation using a significantly higher resolution than in our work. Hennebelle et al. (2011) observe accretion rates of the order of  $10^{-5} - 10^{-4} M_{\odot} \text{ yr}^{-1}$  somewhat smaller than ours, which we attribute to the larger core size of  $\sim 1$  pc used in their setup.

Furthermore, our accretion rates agree reasonably well with theoretical estimates as well as with observational results. Calculating the accretion rates with the formula given in the theoretical work of McKee & Tan (2003) adapted to our setup, we find a value of about  $3 \cdot 10^{-4} M_{\odot} \text{ yr}^{-1}$  very similar to the actually observed accretion rates. Observational results for accretion rates in massive star forming regions are hard to obtain and are often calculated only indirectly via observed outflow mass rates. Nevertheless, results from several high-mass star forming regions indicate accretion rates of the order of  $10^{-4} - 10^{-3} M_{\odot} \text{ yr}^{-1}$  (e.g. Beuther et al., 2002a,c, 2003; Beltrán et al., 2006) again in good accordance with our results.

## 6.4. Conclusion

We have studied the collapse of massive molecular cloud cores with varying initial rotational and magnetic energies. The cores are supercritical with mass-to-flux ratios between 2.6 and 26 and have rotational energies well below the gravitational energy. Containing about 56 Jeans masses the cores are highly gravitationally unstable and hence are presumable sites of massive star formation. We focussed our discussion on the formation of protostellar discs and on protostellar accretion as measured by sink particles. We find that disc properties are highly sensitive to the initial magnetic field strength whereas protostellar accretion rates are only marginally influenced by varying initial conditions. In the following we summarise our main findings.

1. For normalised mass-to-flux ratios  $\mu$  below 10 the formation of centrifugally supported discs is completely suppressed. Instead, for  $\mu < 10$  sub-Keplerian discs are formed with almost no rotational support and radial infall velocities close to free-fall. In contrast, for weak magnetic fields ( $\mu \gtrsim 10$ ) well-defined Keplerian discs with sizes of a few 100 AU build up over time. The finding of a critical value of  $\mu$  around 10 for Keplerian disc formation agrees well with several studies of collapsing low-mass cores.
2. Sub-Keplerian rotation for strong magnetic fields ( $\mu \lesssim 10$ ) is caused by magnetic braking. Analysing the torques acting on the midplane we find that angular momentum is removed due to magnetic braking at roughly the same rate as it is transported inwards due to the gas infall thereby preventing Keplerian discs from forming.
3. Observed accretion rates are of the order of a few  $10^{-4} M_{\odot} \text{ yr}^{-1}$  varying only within a factor of  $\sim 3$  between the individual runs. This variation is remarkably small considering the large differences in the initial conditions varying over more than two orders of magnitude in parameter space. We attribute this to two competing effects of the magnetic field. Increasing the magnetic field strength results in an increased accretion rate due to an enhanced magnetic braking efficiency lowering centrifugal support. Above a certain field strength, however, a further increase leads to declining accretion rates due to the effect of magnetic pressure and tension. This results in rather moderate changes in the accretion rates for different initial conditions. Furthermore, accretion rates for different amounts of angular momentum seem to converge with increasing field strength due to the effect of magnetic braking.
4. For the majority of the simulations disc fragmentation does not occur. Analysing the discs shows that in parts they are described reasonably well with the classical Toomre parameter  $Q$ , i.e. thermal pressure can stabilise the discs. However, there is some indication, in particular for sub-Keplerian discs, that the magnetic pressure is required to stabilise the discs. In two simulations, which are subject

to fragmentation, neither thermal nor magnetic pressure can stabilise the discs. Accordingly, both  $Q$  and  $Q_M$  are below 1.

5. In the two runs with disc fragmentation more than 10 sink particles are formed during the first 5000 yr. Among these sinks only the first one created reaches a mass above  $1 M_\odot$  thus containing more than 60% of the totally accreted mass. All other particles have masses of at most  $0.1 M_\odot$ . The discs formed in both runs reach masses around  $1 M_\odot$  somewhat below the totally accreted sink particle masses.
6. The outflows launched from the protostellar discs are not capable of significantly reducing mass accretion over time. Compared to a run with zero magnetic field and zero rotation, mass accretion is reduced to a level of 35% – 95%.
7. Radial profiles of column density and temperature exhibit accretion shock features moving outwards as time evolves. The shocks occur when the infalling gas hits either centrifugal or magnetic barriers thus strongly decreasing the infall speed.

A growing number of observations of discs and bipolar outflows around high-mass protostars (see Beuther & Shepherd, 2005; Cesaroni et al., 2007, for recent reviews) support a high-mass star formation scenario via disc accretion. On the other hand, observations also reveal that prestellar cores with masses ranging from  $2 - 2000 M_\odot$  are usually only slightly supercritical with  $\mu \lesssim 5$  (Falgarone et al., 2008; Girart et al., 2009; Beuther et al., 2010). Together with our numerical results this suggest that there should be no Keplerian discs in the very early stages of typical high-mass star forming regions but rather flattened, strongly sub-Keplerian structures. This apparent dichotomy has an important impact on the formation of discs around massive stars. To enable the observed presence of centrifugally supported discs in later stages, effects in the later evolution of the system are required reducing the efficiency of magnetic braking. We discussed possible effects in the context of massive star formation like outflows and non-ideal MHD leading to a successive growth of discs in the later evolution.

So far, the influence of turbulent initial conditions as indicated by observations (e.g. Caselli & Myers, 1995) is completely neglected in our setup. The effect of turbulent motions, in particular on the formation of protostellar discs will be studied in detail in Chapter 8 of this work. For further simulations not performed in the course of this work it would be also interesting to study the effect of ambipolar diffusion, which is expected to act efficiently in the high density regime of protostellar discs. For this purpose, the existing set of simulations serves as a useful guide to select representative simulations to be repeated with increased resolution and additional physics. After having studied in detail the influence of the initial conditions on accretion rates and disc formation, in the next chapter we will discuss the formation and properties of protostellar outflows.



## 7. The formation of outflows

In the previous chapter I studied the effect of the initial conditions on protostellar accretion rates and the formation of protostellar discs for a series of simulations. In this chapter I will analyse the effect of varying initial conditions on the formation and evolution of molecular outflows for the same simulations. The numerical methods and the setup of the simulations are described in detail in Chapter 5 and will therefore not be repeated here. The results and the discussion presented in the following have been published in Seifried et al., 2012b, MNRAS, 422, 347.

### 7.1. Introduction

The formation of massive stars and the evolution of associated protostellar outflows is still a highly debated question (e.g. Beuther & Shepherd, 2005; Zinnecker & Yorke, 2007). It is believed that massive stars form in high-mass molecular cloud cores with masses ranging from about  $100 M_{\odot}$  up to a few  $1000 M_{\odot}$ . Such cores have characteristic sizes of a few  $0.1 \text{ pc}$  and peak densities of up to  $10^6 \text{ cm}^{-3}$  (e.g. Beuther et al., 2007). A crucial ingredient for the formation of outflows is the magnetic field in the cloud cores. Its dynamical importance can be estimated by the mass-to-flux ratio  $\mu$  normalised to the critical mass-to-flux ratio (Mouschovias & Spitzer, 1976, but see Section 3.2). For high-mass star forming cores the observed mass-to-flux ratio is typically slightly supercritical with  $\mu \gtrsim 5$  (Falgarone et al., 2008; Girart et al., 2009; Beuther et al., 2010; Crutcher et al., 2010) indicating a significant influence of magnetic fields on the star formation process. In large-scale turbulence simulations, however, also higher values of  $\mu$  up to 20, i.e. weaker magnetic fields, have been found (e.g. Padoan et al., 2001; Tilley & Pudritz, 2007). In combination with the observed overall slow rotation of cores (Goodman et al., 1993; Pirogov et al., 2003) all necessary ingredients for the formation of protostellar outflows are present. Indeed, there is a growing number of observations of outflows around massive protostellar objects (see Beuther et al., 2002c; Zhang et al., 2005, for recent compilations). The generation of such massive outflows, in particular their underlying driving mechanism and their properties will be the focus of our interest here.

For low-mass star formation ( $M_{\text{core}} \sim 1 M_{\odot}$ ), the generation, evolution and properties of protostellar outflows have been studied in great detail over the last years (e.g. Allen et al., 2003; Banerjee & Pudritz, 2006; Mellon & Li, 2008; Machida et al., 2008; Hennebelle & Fromang, 2008; Hennebelle & Ciardi, 2009; Commerçon et al., 2010; Tomida et al., 2010; Duffin & Pudritz, 2009; Price et al., 2012). Despite the intensive research in this field there is still no consensus about which exact mechanism drives

the outflows except the fact that all outflows are magnetically driven. Different results can be found in literature about whether the outflow is driven by centrifugal acceleration (Blandford & Payne, 1982; Pudritz & Norman, 1986; Pelletier & Pudritz, 1992) or by the pressure of the toroidal magnetic field (Lynden-Bell, 1996, 2003, but see Chapter 4 for an overview of both models). A possible reason for this might be the different methods used to analyse the outflows. In this work we seek to clarify this problem by deriving a fully self-consistent, generalised criterion from magnetohydrodynamical (MHD) wind theory to determine the underlying driving mechanism. The criterion is applicable in the same way to low- and high-mass protostellar objects.

Numerical studies on the influence of magnetic fields in massive star forming regions have received attention only recently. The formation of a protostar and the associated outflow in a magnetised high-mass core was studied for the first time by Banerjee & Pudritz (2007) using a very high spatial resolution. The interplay of magnetically driven outflows and ionising radiation is analysed by Peters et al. (2011), who find a sphere-like outflow morphology. In this context we also mention the work of Vaidya et al. (2011), who study the effect of outflow decollimation due to radiation forces, but at much later times than presented here. Examining the influence of initial turbulence, an aspect not considered in this chapter, Hennebelle et al. (2011) and Commerçon et al. (2011) find that strong magnetic fields reduce the number of fragments formed during the collapse. A similar trend was also reported in the Section 6.2.6 in this work but for the present simulations without turbulence. A second crucial result of the previous chapter that will be of particular importance in the following is the fact that for simulations with strong magnetic fields ( $\mu < 10$ ) only sub-Keplerian protostellar discs can form due to the very efficient magnetic braking (see Section 6.2.3 and in particular Fig. 6.7).

In the present chapter, we systematically analyse the influence of the rotational and magnetic energy on protostellar outflows. We focus on the underlying launching mechanism and how the initial conditions affect global outflow properties like mass, momentum and the morphology. In particular, we are able to examine how the development of a two-velocity-component outflow or a sphere-like outflow (Peters et al., 2011) depends on the initial configuration. For this purpose we use the same simulations as in Chapter 6. We note that the initial conditions are selected in a way to cover a large parameter space in accordance with observations and numerical simulations. With the generalised outflow criterion derived in this work we will show that magneto-centrifugally driven outflows consist of two different regimes described by the MHD wind theory. In the first regime close to the disc and the rotation axis, acceleration is dominated by the centrifugal force, i.e. gas gets flung outwards along the poloidal magnetic field lines, whereas in the second regime further away from the disc  $B_\phi$  starts to dominate the acceleration. Furthermore, we will also show that despite large morphological differences all outflows observed in this work are launched by centrifugal acceleration and that the differences in collimation are mainly caused by varying hoop stresses.

The chapter is organised as follows. In Section 7.2 we derive the generalised criterion to determine the outflow driving mechanism. The results of our simulations (see Table 5.1)

are presented in Section 7.3. Firstly, two representative simulations are discussed in detail also testing the newly developed outflow criterion. Next, we analyse the long term evolution and stability of the outflows before the effect of varying initial conditions on the outflow properties are examined. In Section 7.4 the results are discussed in a broader context and are compared to theoretical, numerical and observational studies before we conclude in Section 7.5.

## 7.2. A generalised wind theory

In Chapter 4 we have presented the two classical MHD wind theories explaining the launching and driving of molecular outflows. In the centrifugal acceleration picture (Section 4.1) the gas is flung out- and upwards along poloidal magnetic field lines when the field lines are inclined strongly enough so that the centrifugal force exceeds gravity. In contrast in a magnetic tower flow (Section 4.2) the acceleration of the gas is due to a gradient in the toroidal magnetic field  $B_\phi$ . However, as can be seen later in the result section, in outflows there are not only regimes where the magnetic field structure is dominated either by the poloidal or the toroidal magnetic field so that neither of the two mechanisms described before can exclusively be responsible for the outflow driving.

In order to properly analyse the outflow driving mechanism, in the following we develop a criterion which is more general and therefore has less restrictions to the magnetic field structure. The advantage of this criterion is that it is directly applicable to the simulation data and that it can distinguish between a centrifugally driven outflow and an outflow driven by the pressure gradient of the toroidal magnetic field. Moreover, in contrast to the  $30^\circ$ -condition derived in the centrifugal wind theory, the criterion presented in the following can be applied to the entire outflow structure as well as situations with sub-Keplerian discs.

Like the centrifugal wind theory the new criterion is based on the axisymmetric, stationary MHD equations. The key points used for its derivation are again the four surface constants listed in the Eqs. 4.1 – 4.4. For the sake of simplicity we neglect the enthalpy  $h$  in Eq. 4.4. Making use of the Eqs. 4.1 and 4.2 one can rewrite Eq. 4.4 as follows:

$$\epsilon = \frac{1}{2}v_{\text{pol}}^2 + \frac{1}{2}v_\phi^2 + \Phi - \frac{v_\phi}{v_{\text{pol}}} \frac{1}{4\pi} \frac{B_\phi B_{\text{pol}}}{\rho} + \frac{1}{4\pi} \frac{B_\phi^2}{\rho}. \quad (7.1)$$

As can be seen, the energy invariant  $\epsilon$  is now expressed in variables which can all directly be inferred from the simulations data. The last term on the right hand side of Eq. 7.1 containing  $B_\phi^2$  describes the influence of the toroidal magnetic field on the dynamics of outflows. It states that in magnetic wind theory, beside the poloidal magnetic field flinging material outwards, also the toroidal magnetic field can contribute to the acceleration of gas (see also Spruit, 1996, for a detailed discussion). Magnetocentrifugal acceleration in an outflow therefore has two regimes: a centrifugally dominated and a  $B_\phi$  (magnetic pressure) dominated regime. In the following we will use *centrifugal acceleration* when describing regions in which gas is accelerated mainly by flinging gas outwards along the poloidal field lines as described in detail in Section 4.1. In contrast, *magneto-centrifugal*

*acceleration* describes a situation where both centrifugal acceleration and acceleration due to  $B_\phi$  are at work. The magnetic tower described in Section 4.2 is the extreme case of magneto-centrifugal acceleration where the gas acceleration is more or less exclusively due to the effect of  $B_\phi$ .

Whether gas gets accelerated or not, i.e. whether  $v_{\text{pol}}$  increases or decreases, depends on the behaviour of the terms on the right hand side of Eq. 7.1. As  $\epsilon$  in total is constant along each poloidal magnetic field line, the general condition for gas acceleration is therefore

$$\partial_{\text{pol}} \left( \frac{1}{2} v_\phi^2 + \Phi - \frac{v_\phi}{v_{\text{pol}}} \frac{1}{4\pi} \frac{B_\phi B_{\text{pol}}}{\rho} + \frac{1}{4\pi} \frac{B_\phi^2}{\rho} \right) < 0. \quad (7.2)$$

Here  $\partial_{\text{pol}}$  denotes the spatial derivative along a given poloidal magnetic field line. Given that the above criterion is fulfilled, the term  $1/2v_{\text{pol}}^2$  in Eq. 7.1 increases along the poloidal field line, i.e. an outflow is launched. This criterion is universal and can be applied to the entire outflow structure. It traces all regions where gas gets accelerated outwards including those regions dominated by the effect of  $B_\phi$ . In addition, it only contains variables which are directly accessible from the simulations, which makes it very handy for our purpose. During the course of this work we sometimes will refer to this criterion as the *general criterion*.

However, this criterion alone is not too helpful as it traces the entire region where gas gets accelerated, which – in principle – could also be inferred from the simulation data directly. The main goal in this section, however, is to find a criterion which allows to distinguish between centrifugal and  $B_\phi$  dominated acceleration. Therefore the centrifugal wind theory presented in Section 4.1 has to be modified such that is applicable to the entire outflow structure as well as situations where sub-Keplerian discs are present.

The basis of the following analysis is just like in Section 4.1 the assumption that the magnetic field is strong enough to retain a purely poloidal structure, i.e.  $B_\phi = 0$ , which would cause the gas to rigidly corotate with the magnetic field. Therefore, the rotation frequency of the gas  $\Omega$  can be set to the rotation frequency of the magnetic field,

$$\Omega = \frac{v_\phi}{r} = \omega. \quad (7.3)$$

Hence, like in the centrifugal wind theory the basis for our further consideration is Eq. 4.8

$$\epsilon' = \frac{1}{2} v_{\text{pol}}^2 + \Phi_{\text{cg}}.$$

Then the question of whether gas can get accelerated reduces to the question of how

$$\Phi_{\text{cg}}(r, z, \omega) = -\frac{GM}{\sqrt{r^2 + z^2}} - \frac{1}{2} \omega^2 r^2.$$

changes along a given magnetic field line. If  $\Phi_{\text{cg}}$  decreases along the field line,  $v_{\text{pol}}$  increases, i.e. the gas gets accelerated and vice versa. To remind the reader, the 30°-condition in the centrifugal wind theory was derived by setting  $\omega$  to the Keplerian value at the footpoint of the magnetic field line in the disc. This will not be done here to guarantee the more general nature of the desired criterion.

The problem in a numerical simulation is that for an arbitrarily chosen point  $(r_*, z_*)$  somewhere above the disc it is often not possible to determine the footpoint in the disc where the magnetic field line passing through  $(r_*, z_*)$  is anchored. Therefore, in the expression for  $\Phi_{\text{cg}}$  it is not possible to set  $\omega = \Omega_0$  where  $\Omega_0$  would be the angular frequency at the (unknown) footpoint of the field line in the disc. However, under the afore made assumption that the gas and the magnetic field corotate, this problem can be circumvented. The angular frequency of the magnetic surface  $\omega$  is simply replaced by the local angular frequency of the gas, i.e.

$$\omega_* := \frac{v_{\phi,*}}{r_*} \quad (7.4)$$

which is known from the simulation data. Hence, at any given point  $(r_*, z_*)$  one can calculate the value of the centrifugal-gravitational potential

$$\Phi_{\text{cg},*} := \Phi_{\text{cg}}(r_*, z_*) = -\frac{GM}{\sqrt{r_*^2 + z_*^2}} - \frac{1}{2}v_{\phi,*}^2. \quad (7.5)$$

By solving the equation

$$\Phi_{\text{cg}}(r, z, \omega_*) = -\frac{GM}{\sqrt{r^2 + z^2}} - \frac{1}{2}\omega_*^2 r^2 = \Phi_{\text{cg},*} \quad (7.6)$$

for  $z$  under the assumption that the gas would rotate everywhere with  $\omega_* = v_{\phi,*}/r_*$ , one obtains the shape of an isocontour

$$z(r, \omega_*, \Phi_{\text{cg},*}) = -\frac{\sqrt{-r^6\omega_*^4 - 4r^4\omega_*^2\Phi_{\text{cg},*} - 4r^2\Phi_{\text{cg},*}^2 + 4G^2M^2}}{r^2\omega_*^2 + 2\Phi_{\text{cg},*}}. \quad (7.7)$$

Along this isocontour – which of course passes through the point  $(r_*, z_*) - \Phi_{\text{cg}}(r, z, \omega_*)$  remains constant with a value of  $\Phi_{\text{cg},*}$  as defined in Eq. 7.5. The contour therefore divides the area in regions where the centrifugal potential is smaller/larger than the centrifugal potential at  $(r_*, z_*)$ . According to Eq. 4.8 and under the assumption that the gas is rotating rigidly with the magnetic field, it can be seen that, if the magnetic field line through  $(r_*, z_*)$  reaches to the region where  $\Phi_{\text{cg}}$  is smaller than  $\Phi_{\text{cg},*}$ , the gas will be accelerated and vice versa. This can be tested by comparing the slope of the isocontour (Eq. 7.7) with that of the magnetic field line ( $B_z/B_r$ ) at  $(r_*, z_*)$ . Hence, taking the derivative of Eq. 7.7 with respect to  $r$  and comparing it to the ratio  $B_z/B_r$  yields the desired criterion. For centrifugal acceleration to work at an arbitrarily chosen point the criterion therefore is

$$\frac{r}{z} \frac{1}{GM} \left( \frac{v_{\phi}^2}{r^2} (r^2 + z^2)^{3/2} - GM \right) / \left( \frac{B_z}{B_r} \right) > 1. \quad (7.8)$$

For the sake of simplicity the  $*$  symbol was omitted in the above formula and  $\Phi_{\text{cg}}$  was replaced with the right hand side of Eq. 7.5. It is important to note that every quantity in Eq. 7.8 has to be taken at the point considered, i.e. at  $(r, z)$ .

The above criterion was derived by setting  $B_\phi = 0$  and assuming rigid corotation of the magnetic field and the gas, i.e. the gas is flung out- and upwards along the poloidal field lines. In summary, the criterion in Eq. 7.8 traces centrifugally accelerated gas which is why we will call it the *centrifugal criterion* in the following. When analysing simulation data, regions of outflowing gas not traced by the centrifugal criterion should be fit by the general outflow criterion (Eq. 7.2), which also takes into account the acceleration by the toroidal magnetic field  $B_\phi$ . Hence, by comparing the results of both criteria we are able to distinguish between regions dominated by centrifugal acceleration and those by acceleration due to  $B_\phi$ .

Finally we note that Eq. 7.1 nicely demonstrates that a classification into centrifugally driven outflows on the one hand and magnetic tower flows on the other might be an oversimplification. In reality there is a coexistence of centrifugal acceleration and acceleration due to the pressure gradient of  $B_\phi$  both contained in Eq. 7.1. We will refer to this several times in the course of this work.

### 7.3. Results

In this section, we present the results of our collapse simulations focussing on the evolution and the launching mechanism of outflows. The evolution of the protostellar discs and the accretion properties of the protostars were studied in detail in Chapter 6. We limit our consideration to the phase after the first sink particle has formed to study the time evolution of the outflow and its underlying launching mechanism in detail. In the following, all times refer to the time elapsed since the formation of the first sink particle.

Before going into the details, it is of interest to give some rough estimate of the maximum outflow velocities which can be obtained in our simulations. According to Eq. 4.11, with sink masses of up to  $M_{\max} \sim 4 M_\odot$  (Table 7.1) and a minimum spatial resolution element of  $dx = 4.7$  AU, the maximum reachable rotation velocities and thus also the outflow velocities

$$v_{\text{out,max}} \sim v_{\text{rot,max}} \sim v_{\text{kep,max}} = \sqrt{\frac{GM_{\max}}{dx}} \quad (7.9)$$

are limited to about  $10 \text{ km s}^{-1}$ .

In general, the outflows are launched shortly after the creation of the first sink particle as soon as a protostellar disc builds up. In each simulation the outflow evolves over time and shows no signs of re-collapse until the end of the simulation. However, outflow morphologies and global properties like mass or momentum (see Table 7.1) differ significantly between the individual runs. Hence, in the following we select two representative simulations with equal initial rotational energies but different magnetic field strengths to study the properties and the launching mechanism of the outflows in detail.

Run	$M_{\text{out}}$ ( $M_{\odot}$ )	$P_{\text{out}}$ ( $M_{\odot} \text{ km s}^{-1}$ )	$L$ (AU)	$M_{\text{sink}}$ ( $M_{\odot}$ )	$t_{\text{sim}}$ (yr)	$\dot{M}_{\text{out}}$ ( $10^{-4} M_{\odot} \text{ yr}^{-1}$ )	$\dot{P}_{\text{out}}$ ( $10^{-4} M_{\odot} \text{ km s}^{-1} \text{ yr}^{-1}$ )
26-20	0.509	0.337	707	1.85	5000	1.02	0.673
26-4	0.853	2.37	3215	2.65	5000	1.71	4.74
26-0.4	0.526	2.23	3720	3.59	5000	1.05	4.46
26-0.04	0.080	0.202	856	4.16	5000	0.16	0.404
10-20	1.09	1.02	1240	1.28	4000	2.73	2.54
10-4	0.603	0.585	669	2.23	4000	1.51	1.46
10-0.4	0.164	0.177	445	2.98	4000	0.41	0.442
5.2-20	0.875	1.70	2110	1.78	4000	2.19	4.25
5.2-4	0.656	0.715	1128	2.28	4000	1.64	1.79
5.2-0.4	0.537	0.586	1100	2.55	4000	1.34	1.46
2.6-20	0.116	0.281	1942	1.30	3000	0.39	0.938
2.6-4	0.095	0.215	1455	1.48	3000	0.32	0.717

**Table 7.1.:** Listed are the mass, momentum and extension of the outflows, the total sink particle mass at the end of each simulation, the time the runs have being followed after the first sink particle has formed, and the time averaged mass and momentum outflow rates.

### 7.3.1. Weak field run 26-4

#### General properties

We start our consideration with run 26-4 which has a weak initial magnetic field ( $\mu = 26$ ) and a moderate rotational energy ( $\beta_{\text{rot}} = 0.04$ ). In Fig. 7.1 we show the density, the poloidal velocity field and the outflow velocity

$$v_{z,\text{out}} = v_z \cdot \frac{z}{|z|} \quad (7.10)$$

of the outflow in a slice along the  $z$ -axis at two different times. It can be seen that initially the outflow expands rather slowly into the surrounding medium as within the first 2000 yr it has reached a height of  $\sim 250$  AU only. After 2000 yr the growth rate increases and reaches a roughly constant value of about  $1 \text{ AU yr}^{-1} \simeq 4.7 \text{ km s}^{-1}$ . We will discuss this behaviour in detail at the end of Section 7.3.1. Fig. 7.1 also shows that a bow shock at the tip of the outflow develops extending down to the edge of the centrifugally supported disc. As indicated by the velocity vectors, most of the gas within the bow shock is directed vertically outwards with velocities up to  $15 \text{ km s}^{-1}$ , in agreement with the estimate made before. This velocity corresponds to highly supersonic motions of Mach numbers up to  $\sim 55$  using a temperature of 20 K as present in the undisturbed, ambient medium and Mach numbers of about 15 – 20 with respect to temperatures of a few 100 K in the outflow itself. The outflow morphology at 2000 yr and 5000 yr reveals a self-similar appearance. In particular the collimation factor of the outflow, i.e. the ratio of the length to the width of one outflow lobe, settles around a value of  $\sim 4$ . We especially mention the very turbulent structure seen in the outflow

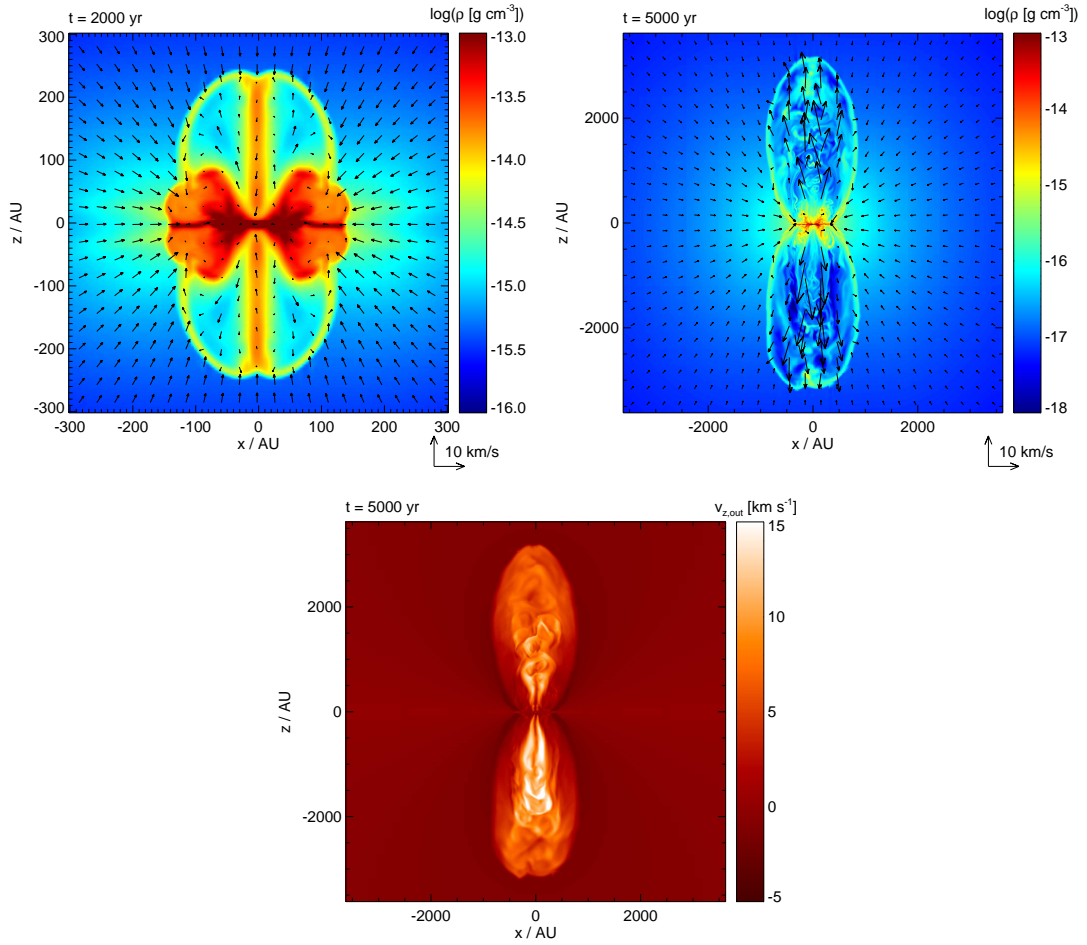


**Figure 7.1.:** Slice along the  $z$ -axis in the weak-field run 26-4, at 2000 yr (for the density field only) and 5000 yr after the formation of the first sink particle. The two top panels show the density field and the poloidal velocity vectors (black arrows). Note the different spatial scales between the left and right panel. The outflow velocity ( $v_{z,\text{out}}$ , bottom panel) and the density field after 5000 yr show a very turbulent structure caused by internal shocks.

after 5000 yr in both the density and the velocity field. Several internal shock fronts and instabilities have occurred in the outflow although no perturbations are included in the initial conditions. This turbulent structure is a consequence of instabilities and not of episodic ejection events. We checked this by visually inspecting the time evolution of the outflow, finding that continuous ejection occurs over the entire time range. Furthermore, a highly time variable ejection rate would also require significant variations in the mass accretion rate (e.g. Pudritz & Norman, 1986, but see also Eq. 4.12), which is clearly not the case (see Fig. 6.12). A turbulent structure as observed here was recently also reported by Staff et al. (2010) for jet simulations. The energy in the shocks dissipates and heats up the jet possibly resulting in optical forbidden line emission (Staff et al.,

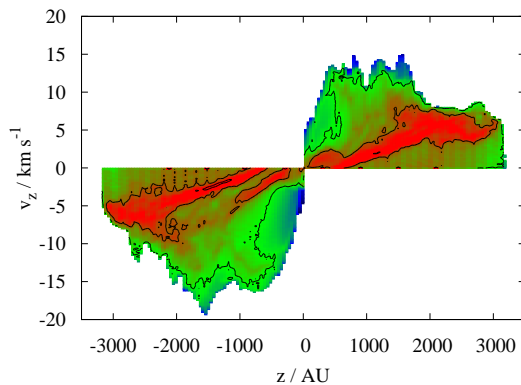


**Figure 7.2.:** Position-velocity diagram for the weak-field run 26-4 after 5000 yr. The contours have a logarithmic spacing. The bulk velocity increases with distance. The maximum velocity shows several clear peaks which are attributed to internal shock fronts.

2010). Interestingly, despite the turbulent structure the outflow keeps expanding with constant speed. Another interesting fact is that the gas is continuously ejected from the disc over the whole 5000 yr although the protostellar disc starts to fragment around  $t \simeq 2500$  yr and has formed 11 further fragments by then (compare Fig. 6.13). Hence, fragmentation does not necessarily terminate the driving of outflows, a fact which is also observed in run 26-20.

To study the outflow structure in more detail, we show the position-velocity (PV) diagram of the outflow at 5000 yr in Fig. 7.2. The PV diagram is frequently used by observers to study the velocity structure of outflows (e.g. Lada & Fich, 1996; Beltrán et al., 2011). For the diagram shown here we only take into account outflowing gas. As indicated by the contours, the velocity of the bulk of outflowing material increases with distance from the midplane. Such a “Hubble Law” is frequently observed for outflows around low- as well as high-mass protostellar objects (e.g. Lada & Fich, 1996; Arce & Goodman, 2001; Beuther et al., 2003; Wang et al., 2011; Ren et al., 2011; Beltrán et al., 2011). The maximum outflow velocity saturates around  $15 \text{ km s}^{-1}$  showing several distinct peaks which we attribute to the internal shocks in the outflow (see bottom panel of Fig. 7.1). Above a distance of about 2000 AU, however, the maximum velocity experiences a significant drop from about 15 to  $10 \text{ km s}^{-1}$ . At the same time the “Hubble law” describing the evolution of the bulk velocity truncates and the bulk velocity saturates at a value of  $\sim 5 \text{ km s}^{-1}$ . We attribute this to a strong internal shock front and the very turbulent structure at these distances, which reduce the maximum outflow velocity and prevent an efficient overall acceleration although local gas acceleration is still possible. The position where this happens gradually moves outwards in time whereas the bulk velocity above this point remains almost constant with a value of  $\sim 5 \text{ km s}^{-1}$ .

In Fig. 7.3 we show radial profiles of the density and outflow velocity at different vertical positions. Both quantities are averaged azimuthally before plotting. As can be seen, below 2000 AU the highest velocities occur close to the symmetry axis of the jet. In particular the velocity profile at  $z = 500$  AU shows a very well-confined, fast velocity

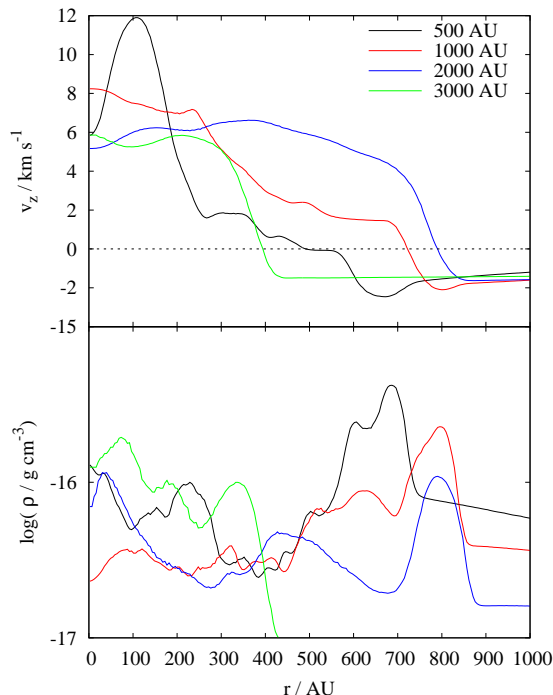


**Figure 7.3.:** Radial profiles of the outflow velocity (top) and the density (bottom) at different vertical positions for the weak-field run 26-4 after 5000 yr. The quantities are averaged azimuthally before plotting. For  $z < 2000$  AU the outflow velocity increases towards the  $z$ -axis whereas at larger distances it has an almost flat radial profile. The density profiles are rather flat showing only small variations and a prominent jump associated with the bow shock.

component with a rather sharp drop-off at a radius of 150 – 200 AU. This two velocity components, the fast, central as well as the slower, enclosing component are also seen in the PV diagram (Fig. 7.2) in particular in the region between  $z = 0$  and  $-1000$  AU where two "Hubble laws" seem to be present. The good collimation of the fast jet component is most likely due to the strong hoop stress exerted by the toroidal magnetic field. Such two-velocity-component outflows with a well-collimated, fast component close to the axis of the outflow and a wider spread, slower component are frequently observed around low-mass protostars (see e.g. Bachiller, 1996, for a review) and also around massive protostars (e.g. Beuther et al., 2004; Ren et al., 2011). Furthermore, they are also observed in jet simulations (e.g. Staff et al., 2010).

We note that the decrease of  $v_{z,\text{out}}$  close to  $r = 0$  at  $z = 500$  AU (black line in the top panel of Fig. 7.3) is most likely a numerical issue as gas very close to the  $z$ -axis cannot get accelerated properly due to the limited resolution. Above  $z = 2000$  AU the velocity profile is more or less smooth over the whole radial range. In accordance with the PV diagram (Fig. 7.2) for those distances no velocities higher than  $\sim 6 \text{ km s}^{-1}$  occur. The density profiles (bottom panel of Fig. 7.3) show a relatively flat shape at all distances with variations of about half an order of magnitude and possibly a slight increase towards

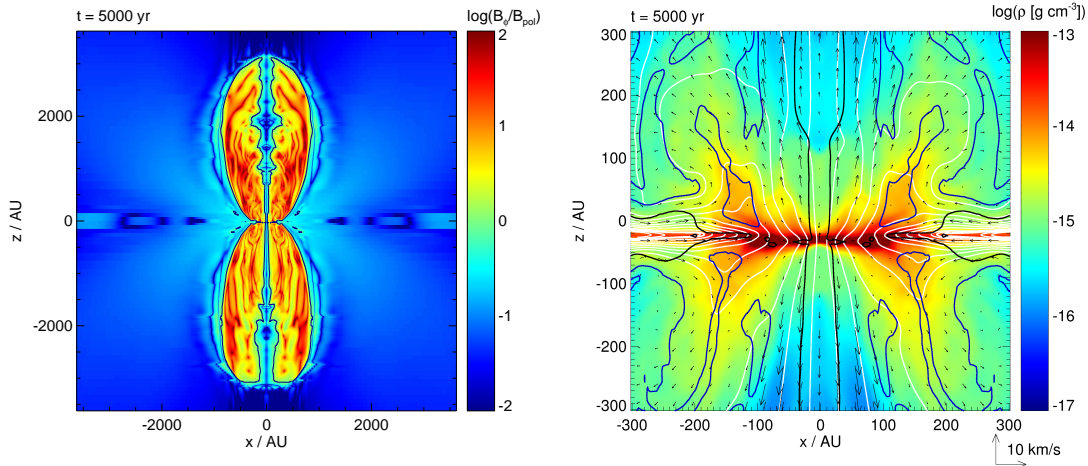


**Figure 7.4.:** Magnetic field structure of the weak-field run 26-4 after 5000 yr in a slice along the  $z$ -axis. All quantities are averaged azimuthally. Left: Ratio of the toroidal to poloidal magnetic field. Black contours give the transition from the toroidally to the poloidally dominated region. Almost the whole outflow area is dominated by  $B_\phi$ . Right: Density field in the inner region. Also shown are the poloidal magnetic field lines (white lines), the velocity field (black arrows) and the contours where  $B_\phi/B_{\text{pol}} = 1, 10$  (black and dark blue lines, respectively). Almost everywhere the poloidal magnetic field has inclination larger than  $30^\circ$  with respect to the  $z$ -axis suitable for centrifugal acceleration.

the  $z$ -axis. At the outer edge the density experiences a strong increase due to the bow shock confining the outflow. By carefully comparing with the top panel of Fig. 7.3, it can be seen that the material in the bow shock partly reveals infall velocities.

### Launching mechanism

Next, we analyse the underlying launching mechanism of the outflow in the weak field case 26-4. Once again, in order to smooth out local perturbations, which inevitably would occur in an arbitrarily chosen slice along the  $z$ -axis, the quantities shown in the following are averaged azimuthally. Firstly, the relative importance of the toroidal ( $B_\phi$ ) and poloidal magnetic field ( $B_{\text{pol}}$ ) for the total magnetic energy content in the outflow is studied. This is done in the left panel of Fig. 7.4 where the value of  $B_\phi/B_{\text{pol}}$  in a slice along the  $z$ -axis is shown. As can be seen, almost the complete outflow region is dominated by  $B_\phi$ . The toroidal component is created by the rotation of the protostellar disc in which the initially purely poloidal magnetic field is anchored.  $B_\phi$  reaches values larger than  $B_{\text{pol}}$  by up to 2 orders of magnitude. Hence,  $B_\phi$  should have a crucial effect on the evolution of the outflow. Depending on the position, the absolute values of  $B_\phi$  and  $B_{\text{pol}}$  vary between  $\sim 0.01$  G and  $\sim 1$  G.

As mentioned in Section 4.2, outflows driven by the pressure gradient of the toroidal magnetic field are often denoted as magnetic tower flows (Lynden-Bell, 1996, 2003). The fact that the outflow region is mainly dominated by  $B_\phi$  suggests that the outflow is

such a magnetic tower flow. However, a closer inspection reveals that the region close to the symmetry axis, where the highest velocities occur (see bottom panel of Fig. 7.1), is either only weakly dominated by the toroidal magnetic field or even dominated by  $B_{\text{pol}}$ , i.e.  $B_{\phi}/B_{\text{pol}} \leq 10$ . We emphasise that even a field configuration which is dominated by  $B_{\phi}$  does not contradict the centrifugal acceleration mechanism. Blandford & Payne (1982) find values of  $B_{\phi}/B_{\text{pol}}$  up to  $\sim 10$  (see their Fig. 4) in the acceleration region in agreement with our findings. Therefore, we assume that the outflow is driven by centrifugal acceleration although there is certainly a contribution to the acceleration by  $B_{\phi}$  as well. In the following we will quantitatively confirm this assumption.

To do so, in the right panel of Fig. 7.4 we analyse the magnetic field structure in detail concentrating on the inner region where the jet is launched. The poloidal magnetic field lines are overplotted on the density field. In addition, we show the poloidal velocity field and the contours where  $B_{\phi}/B_{\text{pol}} = 1, 10$  respectively. As can be seen, the field lines just above/below the disc are strongly inclined against the  $z$ -axis. Except for the innermost part the inclination angle is everywhere above  $30^{\circ}$ , which is required to launch cold gas from the disc by centrifugal acceleration (Blandford & Payne, 1982). Here we emphasise that an inclination angle smaller than  $30^{\circ}$  does not necessarily mean that centrifugal launching is impossible. The  $30^{\circ}$ -condition is valid only for a cold gas, i.e. if thermal pressure can be neglected<sup>1</sup>. As soon as a thermal pressure gradient is present aiding to accelerate the gas upwards, even inclination angles below  $30^{\circ}$  are sufficient for jet launching. As there is clearly a pressure increase towards the centre in the disc, the innermost region is suitable for centrifugal acceleration as well even though the inclination is below  $30^{\circ}$ . Furthermore, as pointed out before, in the inner region where the actual acceleration takes place the magnetic field is not or only weakly dominated by  $B_{\phi}$  in agreement with the findings of Blandford & Payne (1982). In contrast, for a magnetic tower flow (Lynden-Bell, 2003) one would expect a much more wound up structure with a clearly dominating toroidal magnetic field component. However, we note that the toroidal magnetic pressure also contributes to the acceleration of the gas as implied in the MHD wind theory (see Eq. 7.2). As argued before, the launching from the disc itself, however, is most likely due to centrifugal acceleration.

To further support the conclusion of a centrifugally driven wind, we apply the two criteria derived in Section 7.2 (see Eqs. 7.2 and 7.8) to the simulation data at 5000 yr. In contrast to the Blandford & Payne criterion, we can in general determine the driving mechanism of the outflow away from the disc surface. The results are shown in Fig. 7.5, where the regions where the two criteria are fulfilled are shaded grey. As can be seen, within about 800 AU above/below the disc there is a continuous region close to the  $z$ -axis where centrifugally dominated acceleration is possible (left panel). Also at larger heights centrifugal acceleration partly works, in particular close to the symmetry axis of the jet. The grey shaded region around the  $z$ -axis in the upper left panel of Fig. 7.5 agrees very well with the region where the highest outflow velocities are detected. Hence, despite the strong assumptions like stationarity, axis-symmetry and corotation used to derive the criterion given in Eq. 7.8, it works reasonably well. In particular, it is applicable to

---

<sup>1</sup>Remember that we omitted the term  $h$  in Eq. 4.4 for the derivation of the  $30^{\circ}$ -condition.

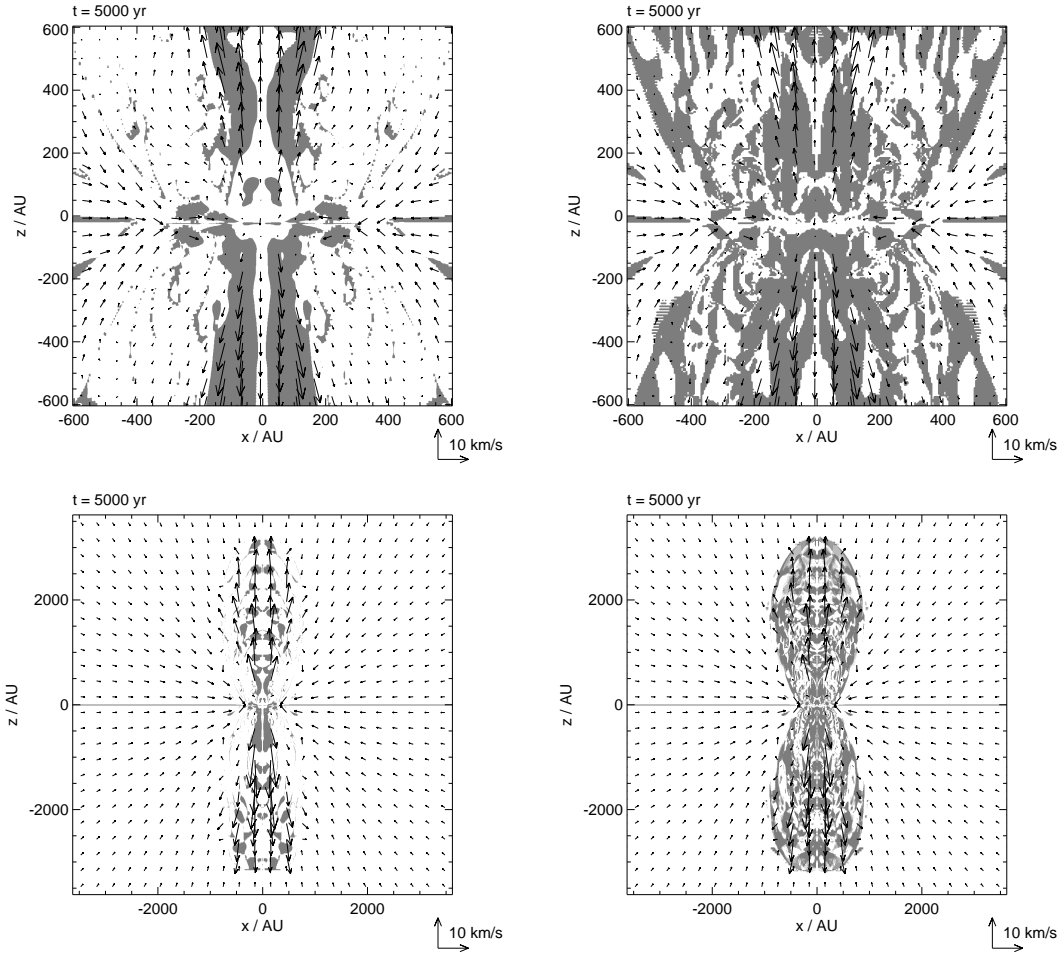


**Figure 7.5.:** Slice along the  $z$ -axis in the weak-field run 26-4 after 5000 yr for two different scales. Gray shaded areas show the regions where the criteria derived in Section 7.2 are fulfilled (Eq. 7.8 in the left panel and Eq. 7.2 in the right panel). The left panels show that centrifugal acceleration works mainly close to the  $z$ -axis up to a height of about 800 AU, which agrees very well with the region where the highest velocities are found. The general criterion is more volume filling and traces also regions in the outer parts.

regions far from the disc surface in contrast to the  $30^\circ$ -criterion of Blandford & Payne (1982). We therefore draw the following conclusions: The assumption of corotation is reasonably well fulfilled in the inner part of the outflow ( $|z| \leq 800$  AU) despite the partly significant toroidal magnetic field (see Fig. 7.4). Hence, the central jet can be considered as centrifugally driven, i.e. gas gets flung out- and upwards along the poloidal magnetic field lines. The result also demonstrates that the ratio of  $B_\phi$  to  $B_{\text{pol}}$  and the  $30^\circ$ -condition – apart from the disc surface – are not sufficient to unambiguously determine the driving mechanism above/below the disc.

Taking into account the effect of  $B_\phi$  in the most general expression of magneto-centrifugal driving (Eq. 7.2) gives a markedly different result (see right panel of Fig. 7.5). The grey shaded area is now much more volume filling, in particular in the outer parts of the outflow with radii  $\gtrsim 200$  AU where outflowing gas is present as well. As purely centrifugal dominated acceleration does not work in this region, here we expect  $B_\phi$  to be mainly responsible for the outflow driving. The results in the upper panel of Fig. 7.5 nicely demonstrate the capability of our criterion to distinguish between the different driving mechanisms, which was the reason for its derivation. An increasing importance of  $B_\phi$  for the driving can also be seen in the upper parts of the outflow ( $|z| \geq 800$  AU). Here the situation is less suitable for pure centrifugal acceleration (bottom left panel of Fig. 7.5) but in general magneto-centrifugal acceleration is still possible in great parts (bottom right panel). This is why we argue that  $B_\phi$  must contribute significantly to the outflow dynamics at great heights.

We note that even the general criterion given in Eq. 7.2 is not fulfilled everywhere in outflow structure. This is due to the fact that the gas indeed does not get accelerated everywhere, e.g. in the shock regions. Another possible reason is the azimuthal averaging process. However, the very different results given by the two criteria, in particular in the upper panel of Fig. 7.5, strongly indicate that the two distinct outflow regions are real.

Although the gas in the outflow experiences several internal shocks (see Fig. 7.1), the bulk velocity steadily increases within about 2000 AU (Fig. 7.2). This can be explained by the fact that acceleration is possible over almost the entire extension of the outflow (bottom right panel of Fig. 7.5). After experiencing a shock which decreases the outflow speed, the gas gets reaccelerated again by centrifugal acceleration and/or the toroidal magnetic field pressure. This happens repeatedly over the whole outflow extension thereby successively increasing the bulk velocity. This situation markedly differs from episodic jet ejection, which also would produce internal shock fronts. Therefore, the knotty structure often observed in protostellar jets is not necessarily a consequence of several outflow ejection events but can also result from a continuously fed jet where gas repeatedly shocks and reaccelerates (see also Staff et al., 2010).

As already seen in the right panel of Fig. 7.4 the magnetic field lines get straightened very quickly above and below the disc. We attribute this to the hoop stress produced by the toroidal magnetic field collimating the outflowing gas and therefore also the magnetic field lines. Nevertheless, the gas still gets accelerated centrifugally despite the almost vertical direction of the magnetic field lines (Fig. 7.5). Furthermore, as shown in Fig. 7.4, the largest part of the outflow is dominated by the toroidal magnetic field component. Therefore it is not surprising that over its complete extension the outflow as a whole stays well-collimated.

As shown in the previous section, the expansion speed is not constant over time but experiences a relatively sharp increase after about 2000 yr (compare Fig. 7.1). We attribute this to a change in the underlying driving mechanism of the outflow. Indeed, analysing the outflow with our criterion given in Eq. 7.8 shows that within the first 2000 yr purely centrifugal acceleration is not possible indicating that in the beginning the outflow is mainly driven by the toroidal magnetic pressure. The expansion speed in this phase

is almost the same in the vertical and horizontal direction (see top panel of Fig. 7.1) with the outer edge of the bubble coinciding with the position of the accretion shock at the disc edge. It is only in this initial stage when we call the outflow a magnetic tower flow (Lynden-Bell, 1996, 2003). In contrast to the situation at 5000 yr in this transient phase there is no acceleration of gas from the disc. In fact, the gas is accelerated only at the tip of the outflow. Therefore the situation differs significantly from the later stages. After  $\sim 2000$  yr a fast, well-collimated outflow component, the centrifugal driven jet develops in the region close to the  $z$ -axis. The launching of the jet coincides with the build-up of a well-defined, extended ( $\sim 100$  AU) Keplerian disc whereas prior to that disc rotation is mostly sub-Keplerian (see red line in Fig. 6.3).

In summary, besides the magnetic field line structure the application of the criterion derived in this work strongly indicates that the outflow in run 26-4 is mainly driven centrifugally at  $|z| \leq 800$  AU while the dynamics of  $B_\phi$  gets more important at large radii and larger heights where the flow is magneto-centrifugally driven.

### 7.3.2. Strong field run 5.2-4

#### General properties

Next, we describe global properties of the outflow generated in run 5.2-4, which has a 5 times stronger initial magnetic field than run 26-4, i.e.  $\mu = 5.2$ , but the same amount of rotational energy ( $\beta_{\text{rot}} = 0.04$ ). The outflow shown in Fig. 7.6 reveals significant differences compared to the outflow in run 26-4 (compare Fig. 7.1). Whereas the latter is well collimated with a collimation factor of  $\sim 4$ , the former has a rather sphere-like morphology expanding with roughly the same speed in all directions, therefore also maintaining a self-similar morphology for all times. The outflow velocities reach values of up to  $5 \text{ km s}^{-1}$ , about a factor of 2 – 3 lower than in run 26-4. The expansion speed of the outflow is almost constant over time with a value of  $0.28 \text{ AU yr}^{-1} \simeq 1.3 \text{ km s}^{-1}$ . This is noticeably smaller than the expansion speed of  $1 \text{ AU yr}^{-1}$  observed in run 26-4. Consequently also the bow shock structure in run 5.2-4 is less pronounced.

A closer inspection of the outflow presented in Fig. 7.6 reveals that in particular close to the symmetry axis and the centre of the bubble gas is still falling inwards even at late times. Gas with outward directed motions occurs mainly in the outer wings. The outflow direction in the inner part is almost radial and gets collimated at relatively large radii of  $\sim 500$  AU. This is remarkably different to the situation in run 26-4 where almost all the gas within the outflow area is moving outwards and preferentially parallel to the  $z$ -axis. A consequence of the complicated velocity structure observed in Fig. 7.6 is the complex density structure showing several shock-like features in the bubble. We remind the reader that the flattened structure in the midplane is a strongly sub-Keplerian disc with significant infall motions (see Section 6.2.2). The sub-Keplerian rotation is a consequence of the strong initial magnetic field decelerating the rotation of the initial core via the magnetic braking mechanism (see Section 3.3).

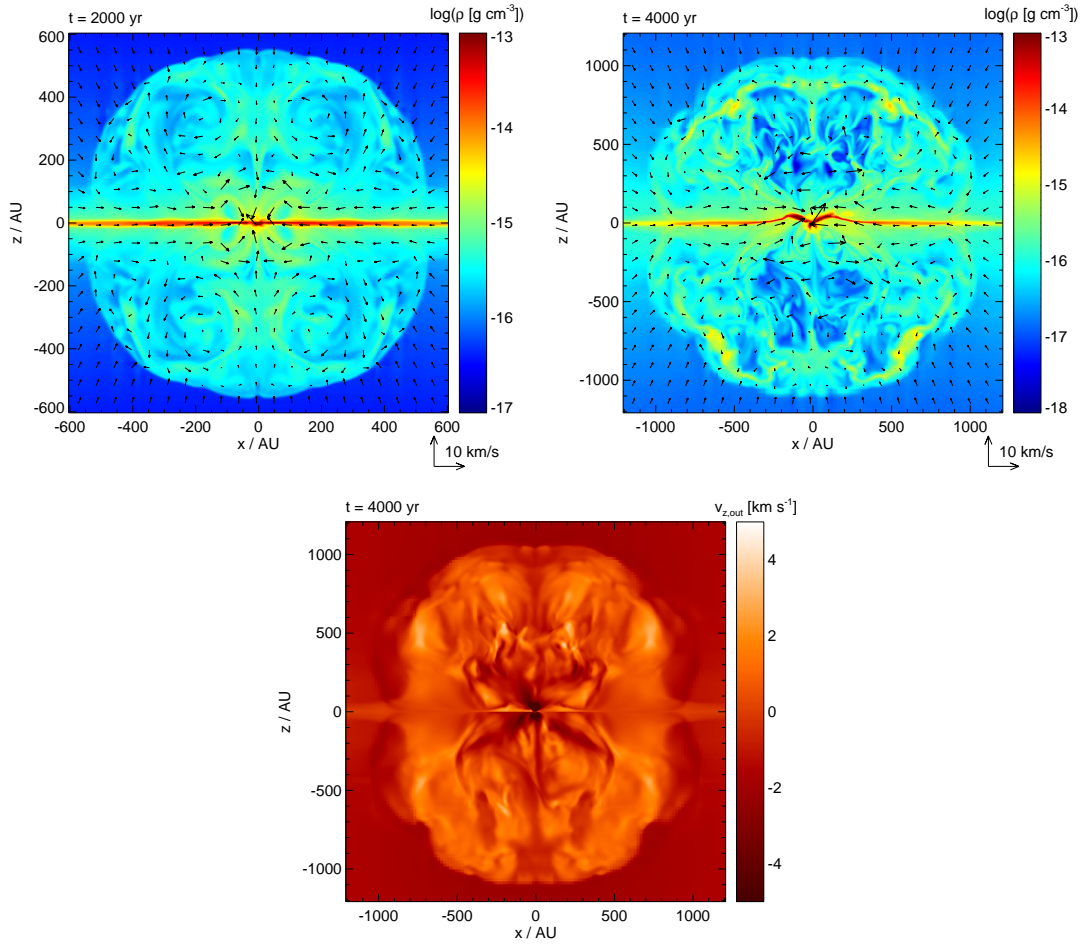


**Figure 7.6.:** Same as in Fig. 7.1 but for the strong-field run 5.2-4. The outflow is poorly collimated and has significantly lower outflow velocities than the outflow in run 26-4.

### Launching mechanism

The different morphologies of the outflows in run 5.2-4 and run 26-4 raise the question whether the underlying launching mechanisms differ. Firstly, we examine the relative importance of the toroidal and poloidal magnetic field components in the left panel of Fig. 7.7. Here again – as in Section 7.3.1 – all quantities like velocity, magnetic field and density are averaged azimuthally before being plotted in order to smooth out local variations which might complicate the analysis. As can be seen, a great part of the outflow bubble is dominated by  $B_{\text{pol}}$  in contrast to the outflow in run 26-4 (see Fig. 7.4). Interestingly, the regions where  $B_{\phi}$  dominates are usually associated with relatively fast outflowing gas. In contrast, the regions which are dominated by  $B_{\text{pol}}$  have only slow outflow velocities ( $\lesssim 1$  km s $^{-1}$ ) or even infall motions. The fact that outflowing gas

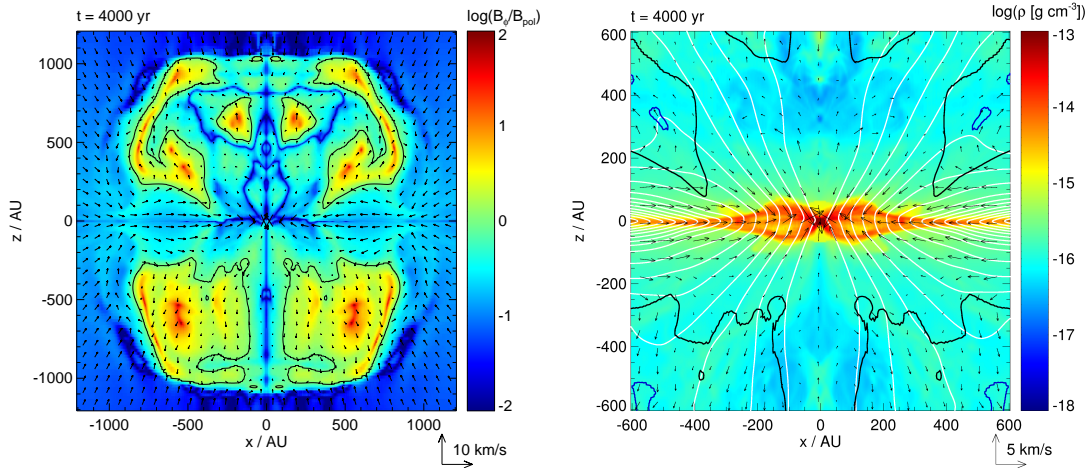


**Figure 7.7.:** Same as in Fig. 7.4 but for the strong-field run 5.2-4. Left: Additionally the poloidal velocity field (black vectors) is shown. Only parts of the outflow bubble, mainly associated with outflowing gas, are dominated by  $B_\phi$ . Right: The strong inclination of the poloidal magnetic field lines is caused by the inwards drag of infalling gas in the disc.

seems to be associated with a strong toroidal magnetic field, i.e.  $B_\phi/B_{\text{pol}} > 1$ , suggests that the outflow might be driven by the pressure gradient of  $B_\phi$ .

In the right panel of Fig. 7.7 the magnetic field line structure in the inner region is considered in more detail. The poloidal field lines have a strongly pronounced hourglass-shaped configuration with a strong radial component. This is caused by the rapid gas infall in the disc which continuously drags the field lines inwards. Although the poloidal field line structure seems suitable for centrifugal acceleration, i.e. the magnetic field lines are inclined by more than  $30^\circ$  with respect to the  $z$ -axis, only in parts of the region outflowing gas is present, in particular in regions more than 200 AU above/below the disc. Hence, the  $30^\circ$ -criterion does not work in this case.

The failure of the Blandford & Payne criterion is not surprising as it was derived for Keplerian disc rotation only and therefore does not apply for strongly sub-Keplerian discs as it is the case here. The physical reason for centrifugal acceleration to fail in the inner region are the slow rotation velocities. Hence, the centrifugal force is reduced significantly and close to the protostar and to the disc it cannot overcome gravity. Consequently gas cannot get flung outwards along the poloidal magnetic field lines. Only at larger radii, where the gravitational force is sufficiently reduced, does centrifugal acceleration work. This fits with the observation that the bulk of outflowing material indeed emerges from radii  $\gtrsim 300$  AU (see Fig. 7.7).

Our centrifugal launching criterion (Eq. 7.8) does not require an underlying Keplerian disc. Hence, we also can apply it in this case. We show the result in the left panel of Fig. 7.8 whereas the right panel shows the result of applying the general outflow criterion (Eq. 7.2). For comparative purposes we also show the regions where gas feels a real, radial

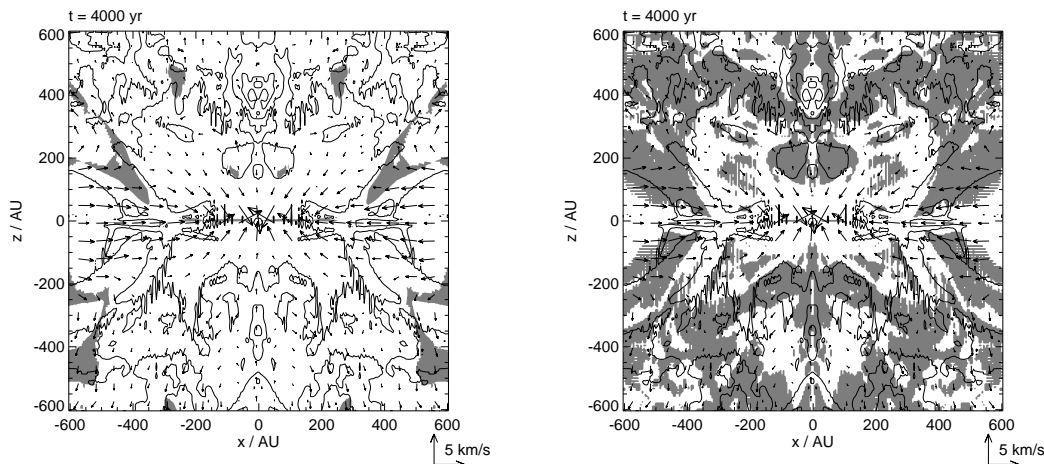


**Figure 7.8.:** Same as in Fig. 7.5 but for the strong-field run 5.2-4 and after 4000 yr. The black contours enclose the regions where gas feels a real acceleration. Left: Centrifugal acceleration is possible only in a small part of the outflow. Right: The general outflow criterion fits the regions of gas acceleration very well.

outward directed acceleration (enclosed by black lines)

$$a_r = \frac{d\mathbf{v}}{dt} \cdot \mathbf{e}_r \simeq \left( \frac{d\mathbf{v}}{dx_i} \frac{dx_i}{dt} \right) \cdot \mathbf{e}_r = \left( \frac{d\mathbf{v}}{dx_i} v_i \right) \cdot \mathbf{e}_r > 0, \quad (7.11)$$

where the time derivative is approximated by spatial derivatives. As already observed in Fig. 7.7, regions of acceleration can be found at radii  $\gtrsim 300$  AU but also closer to the  $z$ -axis and significantly above/below the disc. Purely centrifugal acceleration, however, only works in the outer regions (grey shaded areas in left panel of Fig. 7.8). In the upper outflow lobe the grey shaded region fits the outer region of acceleration reasonably well. Although in the lower outflow lobe the agreement is rather poor, it shows that in case of sub-Keplerian disc rotation the criterion clearly works better than the  $30^\circ$ -criterion, which would predict outflowing gas everywhere. Furthermore, the results suggest that the bulk of outflowing material, which emerges from radii  $\gtrsim 300$  AU, is launched centrifugally also in the case of sub-Keplerian disc rotation.

However, in particular in the lower outflow lobe and close the  $z$ -axis, the predicted regions of purely centrifugal acceleration hardly match the regions of real acceleration. Hence, as in the weak field case 26-4, we suppose that in these regions the toroidal magnetic field strongly influences the outflow dynamics. Indeed, analysing the outflow with the general criterion taking into account  $B_\phi$  shows that now the grey shaded regions fit the regions of real acceleration much better, in particular close to the  $z$ -axis (right panel of Fig. 7.8). Naturally, the agreement is not perfect, which is probably due to the azimuthal averaging process and due to the fact that the outflow is not stationary as assumed for the derivation of the criterion. Nevertheless, it agrees remarkably well, demonstrating the importance of  $B_\phi$ . Hence, we tentatively suggest that in run 5.2-4 its

influence on the driving is even more pronounced than in run 26-4 where the fast gas is mainly driven centrifugally.

Next, we consider the reason for the poor collimation of the outflow. Outflow collimation is due to the hoop stress produced by  $B_\phi$ . Furthermore, we again note that the disc has strongly sub-Keplerian rotation due to very efficient magnetic braking (see Chapter 6). As magnetic braking basically transfers a part of the rotational energy of the disc into energy of the toroidal magnetic field, one could naively expect  $B_\phi$  in the outflow to be relatively strong and hence the outflow to be well collimated. However, as already indicated in Fig. 7.7,  $B_\phi$  is larger than  $B_{\text{pol}}$  only in parts of the outflow suggesting a rather moderate toroidal field strength. Indeed, comparing the absolute energy content  $E_{\text{mag},\phi}$  stored in the toroidal magnetic field of the outflow in the strong-field run 5.2-4 with that in the weak-field run 26-4 after 4000 yr, reveals that  $E_{\text{mag},\phi}$  is more than 3 times larger in the latter. The reason for this is that in run 5.2-4 a significant fraction of the angular momentum is removed by magnetic braking already *before* the gas falls onto the disc. Indeed, the disc in run 5.2-4 has a 2 times lower specific angular momentum

$$l_{\text{disc}} = \frac{L_{\text{disc}}}{M_{\text{disc}}} \quad (7.12)$$

than the disc in run 26-4. Therefore, there is less rotational energy left for being transferred into  $E_{\text{mag},\phi}$ . Consequently,  $B_\phi$  in the outflow and therefore also the hoop stress responsible for collimation are significantly weaker. As at the same time the poloidal magnetic field is relatively strong in run 5.2-4, the collimation of the flow (and the poloidal field lines) gets even more difficult thus resulting in the poorly collimated, sphere-like outflow.

Peters et al. (2011), studying the interplay of ionising radiation and magnetic fields, find a similar sphere-like outflow structure existing over a timescale of several  $10^4$  yr. The authors simulated a  $1000 M_\odot$  core with a resolution of 98 AU and a weaker initial magnetic field ( $\mu = 14$ ) than in our run 5.2-4. Due to the fragmentation of the disc as well as the effects of the emerging HII region no well-defined Keplerian disc builds up in their simulation. As argued above, this and the resulting weaker  $B_\phi$  lead to the development of a poorly collimated outflow. Hence, despite different initial conditions the similarities between the outflows observed by Peters et al. (2011) and in this work are not surprising.

To summarise, due to magnetic braking the gas in the disc in run 5.2-4 is rotating relatively slowly (sub-Keplerian). Therefore,  $B_\phi$  generated by rotation is weak resulting in a poorly collimated outflow.

### 7.3.3. Long term evolution and jet stability

Due to computational cost reasons we cannot follow the outflow evolution over more than a few  $10^3$  yr. Nevertheless, we can try to estimate whether these outflows will persist over time or fall back due to the gravitational attraction of the central object and the ram pressure of the infalling gas. For this purpose we compare the outflow velocity  $v_{z,\text{out}}$

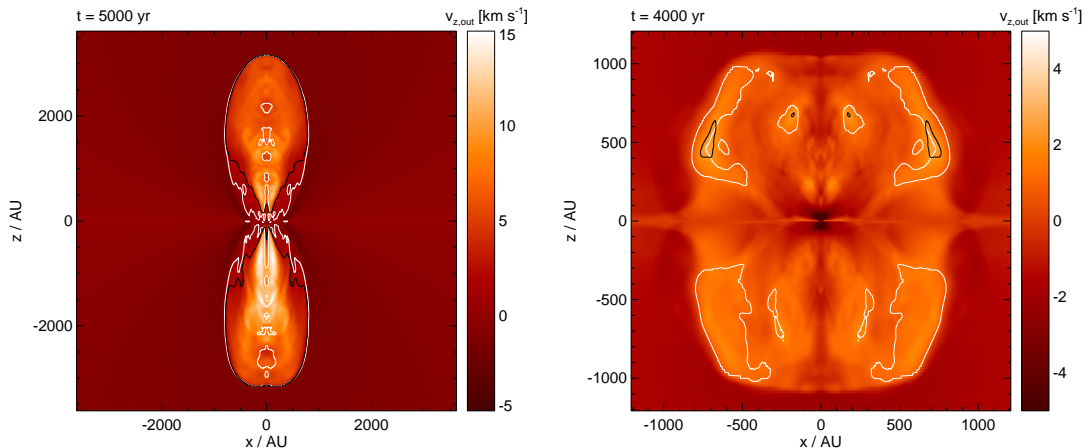


**Figure 7.9.:** Slice along the  $z$ -axis for the weak-field run 26-4 after 5000 yr (left) and the strong-field run 5.2-4 after 4000 yr (right). The outflow velocity  $v_{z,\text{out}}$  is overlaid by the contours where  $v_{z,\text{out}}$  equals the escape velocity  $v_{\text{esc}}$  (black line) and the poloidal fast magnetosonic velocity  $v_{A,\text{fast}}$  (white line). For the weak magnetic field case 26-4 (left),  $v_{z,\text{out}}$  is almost everywhere higher than  $v_{\text{esc}}$  and  $v_{A,\text{fast}}$ . In contrast, for run 5.2-4 in most parts  $v_{z,\text{out}}$  is smaller than  $v_{\text{esc}}$ , and exceeds  $v_{A,\text{fast}}$  only in parts of the outflow. Note the three times larger spatial scale in the left panel and the different colour scaling.

with two basic velocities. The first one to compare with is the escape velocity

$$v_{\text{esc}} = \sqrt{\frac{2GM_{\text{sd}}}{r}}, \quad (7.13)$$

where  $M_{\text{sd}}$  is the mass of the star + disc system and  $r$  the spherical radius. For the outflow to escape the gravitational potential of the central object  $v_{z,\text{out}}$  has to exceed  $v_{\text{esc}}$ . In order to take into account the effect of thermal and magnetic pressure in the surrounding gas which also might slow down the outflow, we furthermore compare the outflow velocity to the maximum poloidal component of the fast magnetosonic velocity (Eq. 3.13)

$$v_{A,\text{fast}} \simeq \sqrt{v_{A,\text{pol}}^2 + c_s^2}. \quad (7.14)$$

In Fig. 7.9 we show the azimuthal average of the outflow velocity  $v_{z,\text{out}}$  and the contours where  $v_{z,\text{out}}$  equals the two velocities mentioned above in a slice along the  $z$ -axis for run 26-4 (left panel) and run 5.2-4 (right panel).

We first concentrate on run 26-4. As already seen in Fig. 7.3, below 2000 AU the highest velocities occur close to the  $z$ -axis. Furthermore, it can be seen that the outflow velocity exceeds the escape velocity and also the fast magnetosonic velocity in most parts of the outflow. In Fig. 7.10 we plot the ratio of  $v_{z,\text{out}}$  to  $v_{\text{esc}}$ , the poloidal Alfvénic velocity  $v_{A,\text{pol}} = \frac{B_{\text{pol}}}{\sqrt{4\pi\rho}}$  and  $v_A$  (Eq. 3.12) for run 26-4 along a vertical line at a radius of 100 AU and 300 AU. As before the quantities are averaged azimuthally. The outflow velocity

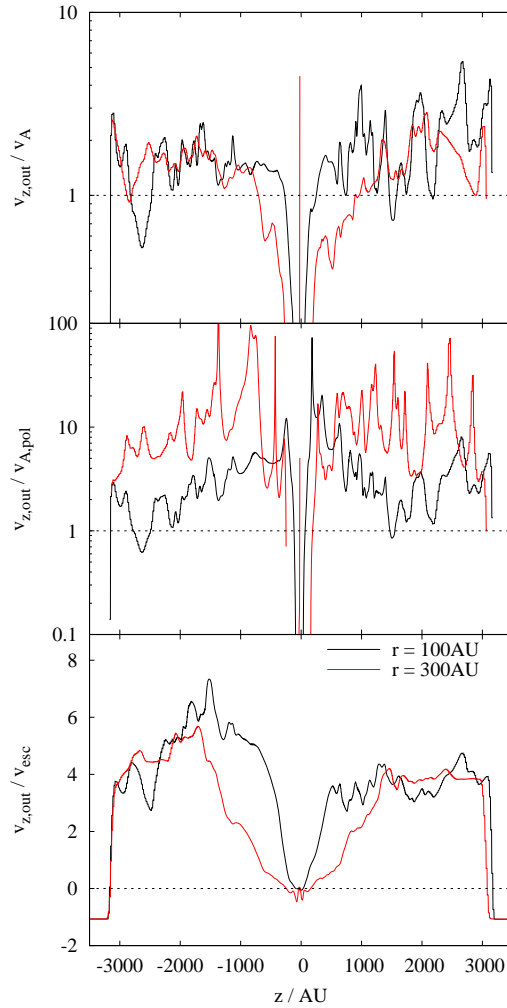


**Figure 7.10.:** Ratio of  $v_{z,\text{out}}$  to the Alfvénic speed  $v_A$  (top), to the poloidal Alfvénic speed  $v_{A,\text{pol}}$  (middle) and to the escape speed  $v_{\text{esc}}$  (bottom) for run 26-4 along a vertical line at a radius of 100 AU (black line) and 300 AU (red line). The outflow velocity is significantly higher than  $v_{\text{esc}}$  and  $v_{A,\text{pol}}$  whereas it is comparable to  $v_A$ , probably indicating a self-regulated outflow speed.

exceeds the escape speed by up to one order of magnitude (bottom panel of Fig. 7.10) and the poloidal Alfvénic velocity even by up to two orders of magnitude although the average ratio is 5 – 10 (middle panel of Fig. 7.10). We attribute the higher value of  $v_{z,\text{out}}/v_{A,\text{pol}}$  at a radius of 300 AU to somewhat lower values of  $v_{A,\text{pol}}$  in this region. The absolute outflow velocity, however, decreases with increasing radius as already seen in Fig. 7.3 and 7.9. Interestingly, over the entire outflow extension the gas velocity is comparable to or only slightly larger than  $v_A$  (top panel of Fig. 7.10). This possibly points to some kind of self-regulation in the outflow where the gas speed is held in the trans-Alfvénic range by internal shocks: Once the gas reaches a significantly super-Alfvénic

speed, the flow cannot be stabilised anymore leading to instabilities and shocks, which in turn reduce the velocity to trans-Alfvénic speeds (see also Ouyed et al., 2003). Beyond the shock the gas gets reaccelerated by magneto-centrifugal forces (Section 7.3.1) until it shocks again. Interestingly, the gas speed is comparable to  $v_A$  and not to  $v_{A,\text{pol}}$ , i.e.  $B_\phi$  has to be taken into account. This indicates that  $B_{\text{pol}}$  is not the main agent stabilising the flow although it certainly contributes (Ray, 1981). Indeed, Appl & Camenzind (1992) show that jets with a toroidal magnetic field are even more stable than jets with a purely poloidal field. In our case we therefore suppose that the stability of the jet is significantly enhanced by  $B_\phi$ . Despite ongoing fragmentation of the protostellar disc (see Section 6.2.6 for details), the driving of the outflow seems not to decline over time. As furthermore  $v_{z,\text{out}}$  is significantly larger than  $v_{\text{esc}}$  and  $v_{A,\text{fast}}$ , it can be expected that the outflow in run 26-4 will escape the gravitational potential of the central star/disc-system and finally will leave the core even when taking into account the ram pressure of the infalling gas.

Considering run 5.2-4 in the right panel of Fig. 7.9 reveals a markedly different situation. Comparing  $v_{z,\text{out}}$  to  $v_{A,\text{fast}}$  shows that the gas is moving super-Alfvénic only in parts of the outer wings of the outflow. Furthermore, a comparison with  $v_{\text{esc}}$  shows that the outflowing gas is moving almost everywhere with velocities below the escape velocity. In general,  $v_{z,\text{out}}$  exceeds  $v_{\text{esc}}$  and  $v_{A,\text{fast}}$  by a factor of at most 2. Therefore, when taking into account the additional deceleration of the outflow by the ram pressure of the infalling material, it might be possible that the outflow will re-collapse to the star/disc-system.

To summarise, the outflows of the two simulations presented so far do not only differ in their morphology and their kinematics but possibly also in their longer term evolution. The well-collimated outflow is likely to overcome the gravitational potential of the central protostar and leave the core whereas the sphere-like, slowly expanding outflow might only be a short-lived, transient feature in the very early phase of massive star formation possibly recollapsing again.

#### 7.3.4. The influence of the initial conditions

So far only the outflows in the runs 26-4 and 5.2-4 have been considered in detail. We have chosen these particular runs as they give representative examples for the outflows observed in the other simulations. The remaining outflows reveal qualitative similarities to one of the two outflows presented before. One of the main results of the previous sections is that the different morphologies can be attributed to the different velocity structure in the discs resulting in different radial positions where the outflows are launched and variations in the strength of the hoop stress, i.e.  $B_\phi$ , responsible for outflow collimation. To further confirm this picture, in the following we consider the complete set of simulations and connect the outflow properties to the properties of the protostellar disc.

We start with the remaining weakly magnetised runs. The outflows in the runs 26-20, 26-0.4 and 26-0.04 show similar morphologies as the outflow in run 26-4. They are reasonably well-collimated with collimation factors between 2 in run 26-20 and  $\sim 4.5$  in run 26-0.4 and have outflow velocities preferentially parallel to the  $z$ -axis. Interestingly,

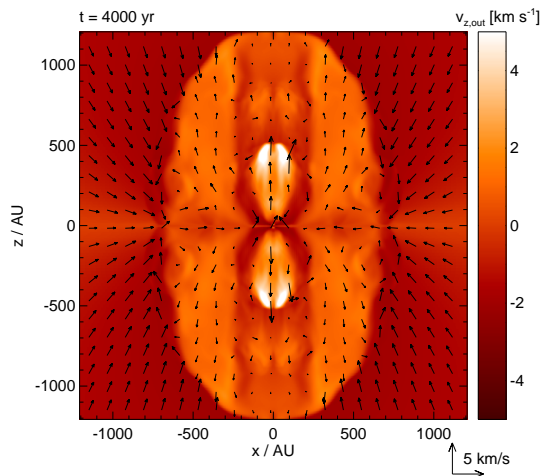


**Figure 7.11.:** Slice along the  $z$ -axis in run 10-20 after 4000 yr showing the outflow velocity. Two distinct outflow components are clearly visible, the inner, well-collimated, fast jet and the outer, low-velocity outflow.

in the runs 10-20 and 5.2-20, whose outflows are rather poorly collimated, a fast and well-collimated jet close to the  $z$ -axis develops after about 2500 yr embedded in the slowly expanding, poorly collimated outflow. Similar applies to run 26-20 with the difference that by the end of the simulation the initial, slowly expanding, poorly collimated outflow is overtaken by the faster, more collimated jet. For demonstrative purposes, in Fig. 7.11 we show the situation in run 10-20 after 4000 yr. We mention that similar outflows consisting of two distinct components, an outer, slowly expanding and an inner, fast component have recently also been observed in low-mass star formation simulations (Banerjee & Pudritz, 2006; Machida et al., 2008; Hennebelle & Fromang, 2008; Tomida et al., 2010; Duffin & Pudritz, 2009).

Analysing the magnetic field line structure in the runs 26-20, 26-0.4, 26-0.04, 10-20 and 5.2-20 reveals situations similar to that in run 26-4. In the inner region close to the symmetry axis of the jet where the gas gets accelerated, the magnetic field is only weakly dominated by the toroidal field component or not at all, i.e.  $B_\phi/B_{\text{pol}} \lesssim 10$ . Furthermore, the field lines at the disc surface are inclined by more than  $30^\circ$  with respect to the vertical axis. As the discs rotate with Keplerian velocities just like in run 26-4 or as in the runs 5.2-20 and 26-0.04 with at least about half the Keplerian speed, we therefore suppose that the gas gets launched from the discs by centrifugal acceleration. Applying our centrifugal outflow criterion (Eq. 7.8) for these runs shows that above the disc the region where purely centrifugal acceleration works is not as extended as in run 26-4. However, also in these cases the region of centrifugal acceleration is in general near the  $z$ -axis. With the general criterion for magneto-centrifugal acceleration (Eq. 7.2), however, we can fit the entire outflow regions by far better. Hence, considering the jets as purely centrifugally driven might not be an appropriate choice too far from the disc. The evidence shows that the pressure gradient of the toroidal magnetic field significantly

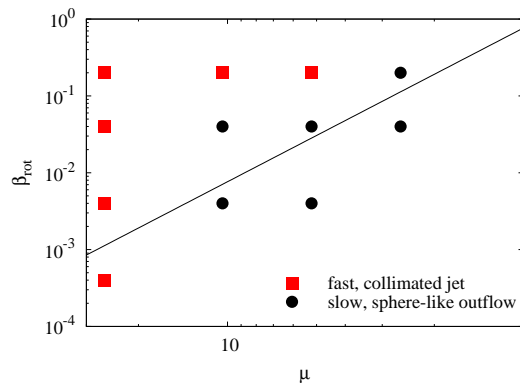


**Figure 7.12.:** Phase diagram of magnetic field and rotational energy (see Table 5.1) showing the results of the simulations concerning the question of jet formation. For runs with a weak magnetic field ( $\mu = 26$ ) or high rotational energies well-collimated, centrifugally driven jets develop (red squares). In contrast, for the remaining runs only slowly expanding, poorly collimated outflows are generated (black circles).

contributes to the gas acceleration although, as pointed out before, the launching from the disc itself is most likely to due to centrifugal acceleration. Comparing the results of both criteria also suggest that the dynamics of the outer, slowly expanding outflows in the runs 26-20, 10-20 and 5.2-20 are mainly determined by  $B_\phi$ .

All remaining runs show poorly collimated, low-velocity outflows with outflowing gas emerging almost radially at radii  $\gtrsim 100$  AU and gas infall close to the  $z$ -axis. Furthermore, the magnetic field line properties in the centre are similar to run 5.2-4 and the protostellar discs driving the outflows are all clearly sub-Keplerian. Moreover, applying the outflow criteria derived in Section 7.2 gives very similar results as for run 5.2-4. Therefore we conclude that in these runs the outflow driving mechanism is very similar to that in run 5.2-4, i.e. gas is launched centrifugally from the disc at large radii ( $r \gtrsim 100$  AU) with support by  $B_\phi$ . At larger distances  $B_\phi$  is mainly responsible for the further acceleration (see Section 7.3.2). To remind the reader, the poor collimation is a consequence of the large launching radii and of the weak toroidal magnetic field in the outflow. The larger launching radii are a result of the fact that close to the centre gravity is too strong to be overcome by the weak centrifugal force.

In Fig. 7.12 we show the dependence of the outflow morphology on the initial conditions. It can be seen that only for the runs with weak magnetic fields ( $\mu \geq 26$ ) or high rotational energies ( $\beta_{\text{rot}} = 0.20$ ) do well-collimated jets occur. Moreover, all runs with clearly sub-Keplerian discs have poorly collimated outflows (see Fig. 6.7). This clearly demonstrates that for a collimated, high-velocity jet to form a disc with (almost) Keplerian rotation is necessary. In contrast, if the disc is rotating clearly sub-Keplerian, both outflow speed and collimation decrease significantly.

Next, we consider the influence of the initial conditions on global outflow properties like mass and momentum. The results for each simulation are listed in Table 7.1. For the calculation of the outflow mass and momentum we only take into account gas more

than 47 AU above/below the midplane. By doing so, we avoid the outflow quantities to be affected by material in the protostellar disc. For the momentum we only consider the  $z$ -component. The outflow masses are of the order of  $0.1 - 1 M_{\odot}$  thus significantly lower than the sink masses (see also Section 7.3.5 below). The momenta of the outflows are of the order of  $0.1 - 1 M_{\odot} \text{ km s}^{-1}$ , which in combination with the outflows masses gives average velocities of a few  $\text{km s}^{-1}$ , thus lower than typically found in observations (e.g. Beuther et al., 2002c, but see also Section 7.4.3 for a detailed discussion).

In general, for a fixed magnetic field strength both centrifugal and  $B_{\phi}$  dominated acceleration predict that the power of the outflow should increase with the rotation speed of the protostellar disc. Hence, for larger amounts of initial rotational energy and thus faster disc rotation, the outflow mass and momentum are expected to be higher as well. Indeed, comparing runs with equal  $\mu$  in Table 7.1 reveals that except for run 26-20 the outflows are in general more powerful for higher  $\beta_{\text{rot}}$ . We suppose that in run 26-20 the generation of the outflow might be slightly delayed as the material falling onto the disc has a high excess of angular momentum, which has to be removed before moving further inwards. Therefore, the accretion rate and consequently also the outflow rates  $\dot{M}_{\text{out}}$  and  $\dot{P}_{\text{out}}$  are lower (see also Section 7.3.5).

Interestingly, there is no clear trend recognizable in  $\dot{M}_{\text{out}}$  and  $\dot{P}_{\text{out}}$  when considering simulations with fixed  $\beta_{\text{rot}}$  but varying  $\mu$  (see Table 7.1). In general, for runs with  $\mu \geq 5.2$  there are variations in  $\dot{M}_{\text{out}}$  and  $\dot{P}_{\text{out}}$  within about one order of magnitude. For strong magnetic fields ( $\mu = 2.6$ ), however, there seems to be a rapid decline in outflow power. Naively, it could be expected that the power of the outflows would increase with magnetic field strength. This is not the case since for stronger magnetic fields disc rotation gets more and more sub-Keplerian (see Section 6.2.3 for a detailed discussion). This results in a weaker centrifugal acceleration and a weaker toroidal magnetic field responsible for further accelerating the outflow. Therefore, for both driving mechanisms – centrifugal acceleration and the magnetic tower flow – the outflow power is expected to decrease for strongly sub-Keplerian discs in agreement with our observations. We emphasise that, as the outflow morphologies differ significantly between the individual simulations with equal  $\beta_{\text{rot}}$  but varying  $\mu$ , the results of such a comparison have to be taken with care.

In summary, we find that the generation of a fast ( $v_{z,\text{out}} \simeq 10 \text{ km s}^{-1}$ ), well-collimated jet depends on the build-up of a Keplerian disc. In these jets the gas is most likely launched centrifugally from the disc. Somewhat above/below the disc, however, we expect the toroidal magnetic field to come into play contributing significantly to the acceleration of the gas. In contrast, for sub-Keplerian discs slowly expanding, sphere-like outflows develop, in which the gas is launched centrifugally from the disc as well although at larger radii. Here as well  $B_{\phi}$  plays an important role in accelerating the outflow at larger distances. Although the outflow morphologies are very different, global properties like mass and momentum vary only within a factor of 10 showing a decrease towards high magnetic field strengths.

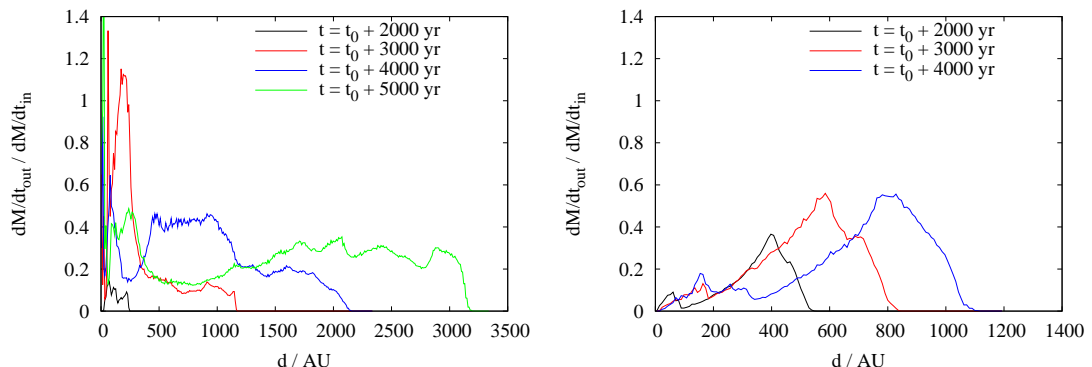


**Figure 7.13.:** Ratio of the mass outflow rate over infall rate in the weak-field run 26-4 (left) and the strong-field run 5.2-4 (right) as a function of the distance from the centre. The values in both runs agree with theoretical estimates and other numerical work.

### 7.3.5. The ejection-accretion ratio

Next, we compare the mass outflow rates  $\dot{M}_{\text{out}}$  with the mass infall rates  $\dot{M}_{\text{in}}$ . To begin with, we limit our consideration to the fiducial runs 26-4 and 5.2-4. In Fig. 7.13 we show the ratio of outflow to infall rate  $\dot{M}_{\text{out}}/\dot{M}_{\text{in}}$  as a function of the distance  $d$  from the centre for different times. The outflow and infall rates are computed on the surface of a cylinder of radius  $d$  and height  $2d$  centred around the midpoint of the simulation domain<sup>2</sup>. In run 26-4  $\dot{M}_{\text{out}}/\dot{M}_{\text{in}}$  is not constant over the outflow extension but varies between 0.1 and 0.4 for  $d > 500$  AU. We attribute these variations to the internal shocks occurring in the outflow (compare Fig. 7.1 or 7.9). Although being somewhat higher, in general the observed range roughly agrees with theoretical estimates of  $\sim 0.1$  obtained for the centrifugal acceleration mechanism (Pudritz & Norman, 1986; Pelletier & Pudritz, 1992, but see also Eq. 4.12). The high value of  $\dot{M}_{\text{out}}/\dot{M}_{\text{in}}$  at  $d < 500$  AU is due to the circulation flow in the outer parts of the outflow ( $r \simeq 200 - 300$  AU, see right panel of Fig. 7.4). As the outflow speed of this material is not sufficient to escape the gravitational potential, it falls back to the disc thus not contributing to the outflow rate at larger distances. The shape of  $\dot{M}_{\text{out}}/\dot{M}_{\text{in}}$  in run 5.2-4 is qualitatively very different from that in run 26-4. The ratio seems to saturate around a value of  $\sim 0.1$  for late times and small distances ( $d \leq 400$  AU) in agreement with theoretical estimates. For larger distances, however,  $\dot{M}_{\text{out}}/\dot{M}_{\text{in}}$  increases and reaches values of up to 0.6 pointing to the fact that part of the outflowing material is entrained and does not stem from the disc. However, also for this run the measured  $\dot{M}_{\text{out}}/\dot{M}_{\text{in}}$  is in reasonable agreement with theoretical predictions for centrifugal acceleration even though partly somewhat higher.

Next, we consider  $\dot{M}_{\text{out}}/\dot{M}_{\text{in}}$  for the whole set of simulations performed. To avoid the problem that even for an individual outflow this ratio is not constant in time and position, we follow a simpler approach than before. For this purpose we approximate  $\dot{M}_{\text{out}}/\dot{M}_{\text{in}}$

<sup>2</sup>We have chosen a cylinder instead of a sphere to lower numerical errors when computing the flux through the surface.

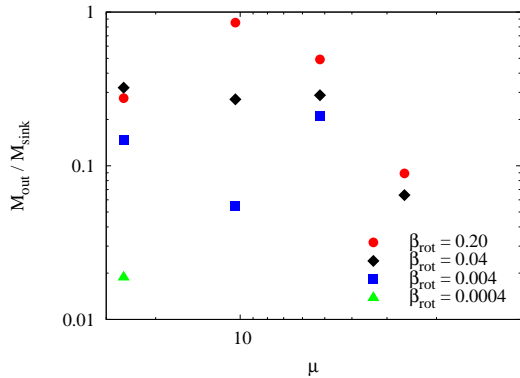


**Figure 7.14.:** Ratio of outflow mass to sink mass at the end of each simulation as a function of  $\mu$  (see Table 5.1). Equal symbols denote equal initial rotational energies. The calculated values scatter around a mean of  $\sim 0.3$  in rough agreement with theoretical estimates.

by the ratio of the total outflow mass to the total mass accreted onto the sink particles (see Table 7.1). The result is shown in Fig. 7.14. Excluding one exemption (run 10-20) the ratios are all smaller than 0.5. The values have a mean of  $\sim 0.3$ , which agrees very well with other numerical work (Tomisaka, 1998, 2002; Hennebelle & Fromang, 2008; Duffin & Pudritz, 2009) and which is only slightly higher than analytical estimates of  $\sim 0.1$ . However, the scatter of the individual values is significant ranging from about 0.02 in run 26-0.04 up to 0.9 in run 10-20. Interestingly, run 26-20 has a value of  $\dot{M}_{\text{out}}/\dot{M}_{\text{in}}$  around 0.3 in accordance with the other runs although the absolute values in this simulation are very small (see Table 7.1). This confirms the explanation given in Section 7.3.4 that in run 26-20 the entire outflow ejection process is delayed due to the high excess of angular momentum which causes lower accretion rates and in turn also lower outflow rates. Furthermore,  $\dot{M}_{\text{out}}/\dot{M}_{\text{in}}$  is in general higher for higher  $\beta_{\text{rot}}$ . As discussed in Section 7.3.4, this is a consequence of the fact that the outflow power increases with  $\beta_{\text{rot}}$  whereas at the same time the accretion rates decrease due to an enhanced centrifugal support. For varying  $\mu$ , however, there is no clear trend in  $\dot{M}_{\text{out}}/\dot{M}_{\text{in}}$  recognizable except a possible drop-off for the highly magnetised runs with  $\mu = 2.6$ , which was already observed in Section 7.3.4 for the absolute outflow quantities.

Although the derived values of  $\dot{M}_{\text{out}}/\dot{M}_{\text{in}}$  are in general somewhat higher than analytical predictions, they agree reasonably well with observational results ranging from about 0.1 to 0.3 (Richer et al., 2000; Beuther et al., 2002c; Klaassen et al., 2011). Furthermore, a ratio of  $\sim 0.3$  is often used to estimate accretion rates of massive protostar from observed outflow mass rates (Beuther et al., 2002a,c, 2003, 2004; Zhang et al., 2005). As we have shown this value fits reasonably well over a wide range of initial conditions. Hence, we suppose that accretion rates derived that way seem to be reliable within a factor of a few.

## 7.4. Discussion

### 7.4.1. The launching mechanism

Our analysis presented in the Sections 7.3.1 and 7.3.2 suggests that in all simulations the gas is launched from the disc by centrifugal acceleration (Blandford & Payne, 1982). At larger distances above/below the disc the pressure of the toroidal magnetic field significantly contributes to the acceleration of the gas. Although Lynden-Bell (1996, 2003) describe outflows whose dynamics are determined by the toroidal magnetic field, we emphasise that our outflows are for the most parts (in time and space) not such so-called magnetic tower flows. In fact, the effect of  $B_\phi$  is also implicitly contained in the MHD wind theory as shown in Section 7.2 (see Eq. 7.2). Therefore, it is more appropriate to consider our outflows in the framework of MHD wind theory as it contains both centrifugal acceleration and magnetic pressure effects. In such a magneto-centrifugally driven wind the gas is ejected from the disc surface and then gets accelerated towards larger heights. In contrast, in a magnetic tower (Lynden-Bell, 1996, 2003) gas gets accelerated only at the tip of the outflow – there is no sustained mass loss coming from the disc. Tower flows are transient phases that arise only in the earliest stages of outflows.

For simulations with weak initial magnetic fields or high rotational energies the situation is as follows: Shortly after the formation of the first sink particle a sub-Keplerian disc builds up driving a slow ( $\sim 1 \text{ km s}^{-1}$ ) outflow whose driving is probably dominated by the magnetic pressure. As soon as a well-defined, large-scale Keplerian disc develops, in the inner region a fast ( $\sim 10 \text{ km s}^{-1}$ ), well-collimated jet is launched by centrifugal acceleration. At larger heights and radii  $\gtrsim 200 \text{ AU}$ , however,  $B_\phi$  significantly contributes to the acceleration. An outer, slowly expanding outflow component is still clearly visible at the end of the simulations 26-20, 10-20 and 5.2-20 (see Fig. 7.11). Such outflows consisting of two components, an outer, slowly expanding and an inner, fast component have also been observed in low-mass star formation and jet simulations (Banerjee & Pudritz, 2006; Machida et al., 2008; Hennebelle & Fromang, 2008; Duffin & Pudritz, 2009; Tomida et al., 2010; Staff et al., 2010) as well as observations (e.g. Bachiller, 1996; Beuther et al., 2004; Ren et al., 2011). For runs with strong magnetic fields, the protostellar discs are sub-Keplerian all the time due to strong magnetic braking. Therefore, during the time covered by our simulations no fast, central jet component develops and only a slowly expanding, poorly collimated bubble is present. The gas seems to be mainly launched centrifugally although the toroidal magnetic field has most likely a large impact on the driving of the outflow already close to the disc.

We tried to clarify the situation by applying the criteria derived in Section 7.2 which only depend local quantities and the protostellar mass. In general, using the criteria for the present simulations indicates that they are applicable despite the constraints like axis-symmetry, stationarity and corotation assumed for its derivation. We show that for strongly sub-Keplerian discs the centrifugal criterion (Eq. 7.8) acceptably fits the region where the outflow gets launched (see left panel of Fig. 7.8) in contrast to the  $30^\circ$ -criterion (Blandford & Payne, 1982), which fails when analysing the sub-Keplerian cases. Together with the results from run 26-4 this demonstrates that simply considering

the inclination of the magnetic field with respect to the  $z$ -axis is not necessarily sufficient to determine the driving mechanism nor the region where the outflow gets launched: On the one hand even for inclination angles smaller than  $30^\circ$  the outflow can be driven centrifugally (see Fig. 7.4 and 7.5) whereas on the other hand there are situations where purely centrifugal acceleration does not work despite inclination angles larger than  $30^\circ$  (see Fig. 7.7 and 7.8).

Again, we emphasise that in all runs the mechanism responsible for outflow launching is centrifugal acceleration. Only at larger heights do the effects of the toroidal magnetic field come into play. The situation is therefore not such that the outflow is either driven centrifugally or by the toroidal magnetic pressure. Such a classification often found in literature is an oversimplification not describing the situation appropriately as both processes play an important role. We have shown that there is a continuous transition, from centrifugal dominated acceleration to acceleration dominated by  $B_\phi$ . These two regimes are both implied in the solution of the stationary MHD equations presented in Section 7.2 (see also Section 4.1 of Spruit, 1996). The different outflow morphologies mainly result from the varying strength of  $B_\phi$  responsible for collimation since for clearly sub-Keplerian discs  $B_\phi$  is too weak to properly collimate the outflows.

As mentioned before, several authors have simulated outflows consisting of two different components. However, their conclusions as which component is driven by which mechanism partly contradict each other. On the one hand, some authors (Banerjee & Pudritz, 2006; Duffin & Pudritz, 2009) claim that the outer, larger scale outflow is driven by the magnetic pressure (Lynden-Bell, 1996, 2003) whereas the inner, fast outflow embedded in the first one is considered as a centrifugally driven jet (Blandford & Payne, 1982). On the other hand, Machida et al. (2008) and Tomida et al. (2010) find the situation to be exactly vice versa. All authors argue on the basis of an analysis of the field line structure such as the ratio of  $B_\phi$  to  $B_{\text{pol}}$  or the field line inclination with respect to the protostellar disc. As we argued above, this kind of consideration alone can be misleading, which might have caused the contradictory results. Hence, it would be interesting to apply the criterion derived in this work to confirm the results in an independent way. This was recently done by Duffin et al. (2012) in simulations of low-mass cores. The results support our interpretation that the outer outflow component is magnetic pressure driven, and the inner component centrifugally driven. Furthermore, this demonstrates the applicability of our criterion in equal measure to low-mass and high-mass protostellar outflows without any further restrictions.

Studying the influence of the initial magnetic field strength on the formation of outflows around low-mass stars, Hennebelle & Fromang (2008) find striking similarities to our results, i.e. a well-collimated, fast outflow component embedded in a slowly expanding component for weak magnetic fields and a poorly collimated outflow for strong fields. Their interpretation of a centrifugally driven wind for the latter component and a magnetic tower flow for the former component, however, is in opposition to our interpretation. Hence, it would be interesting to apply our criterion derived here to test their conclusion in a different way. Differences might also result from the fact that Hennebelle & Fromang (2008) consider a low-mass core, which is less gravitationally unstable. Therefore, in par-

ticular in the strongly magnetised case the disc seem to be less sub-Keplerian possibly leading to different results.

In general, concerning outflow morphology our results agree remarkably well with those of low-mass star formation simulations even over the wide range of initial conditions covered in our work. However, the good agreement between our and the low-mass case results could not be expected a priori as in contrast to low-mass cores the cores presented here are highly gravitationally unstable (about 56 Jeans masses). Therefore the dynamics and timescales of the whole system differ significantly from low-mass cores. Another difference, though not covered here, is the influence of initial turbulence and radiative feedback of the protostars. However, as we are still in a very early evolutionary stage, we suppose that the effect of radiation is still rather limited. In contrast, the influence of turbulence, which we will examine in Chapter 8, is expected to be significant (see also Hennebelle et al., 2011).

#### **7.4.2. The evolution and impact of outflows**

For typical massive star forming regions the observed mass-to-flux ratios are usually only slightly supercritical, i.e.  $\mu \lesssim 5$  (Falgarone et al., 2008; Girart et al., 2009; Beuther et al., 2010). Based on the results obtained in this work, the question arises how well-collimated, fast outflows frequently observed around high-mass protostellar objects can form (e.g. Beuther et al., 2002c, 2004; Beltrán et al., 2011). As we have shown, the formation of such outflows is linked to the build-up of Keplerian discs. Therefore the question reduces to how the magnetic braking efficiency can be reduced allowing Keplerian discs to form. A possible solution is provided by the poorly collimated outflows themselves evacuating the region above and below the disc therefore significantly reducing the magnetic braking efficiency due to the enhanced magnetic braking timescale (Eq. 3.36). Furthermore, Hennebelle & Ciardi (2009) and Ciardi & Hennebelle (2010) showed that a misalignment between the rotation axis and the initial magnetic field can reduce the magnetic braking efficiency. Simulations including non-ideal MHD effects like ambipolar diffusion (Mellon & Li, 2009; Duffin & Pudritz, 2009) or ohmic dissipation (Dapp & Basu, 2010; Dapp et al., 2012; Li et al., 2011) show that these effects can – if at all – reduce the magnetic braking efficiency only in later stages. All these possibilities point to a successive build-up of Keplerian discs during the protostellar evolution towards Class I/II objects, hence allowing the generation of well-collimated, high-velocity jets for typically magnetised cores in later stages only (see also Section 6.3.2 for a more detailed discussion). The role turbulence plays in the formation of Keplerian discs, possibly also in earlier stages, will be studied extensively in the next chapter.

As shown in Fig. 7.2, the position-velocity (PV) diagram for run 26-4 shows a typical "Hubble law"-like behaviour also seen in observations (e.g. Lada & Fich, 1996; Beltrán et al., 2011). Such a behaviour is a natural outcome of several wind models like the jet-driven bow shock model or the wind-driven shell model (see Cabrit et al., 1997, for an overview). However, the comparison between our results and those models is not straightforward as in those wind models the velocity increase with distance is only an apparent and no real acceleration. This apparent acceleration is a consequence of the

inclination of the outflow with respect to the plane of the sky and the fact that mainly gas swept up in the bow shock and not inside the outflow lobe contributes to the observable emission. In contrast, in our case the observed acceleration is real and is mainly due to the gas inside the bow shock structure whereas the material in the shock itself has mainly negative velocities (compare Fig. 7.3). Hence, an observed increase of the bulk velocity with distance in outflows can also be real and not only due to a projection effect.

However, an interesting point made by those wind models is the fact that the outflows partly consist of gas entrained from the ambient medium. We tested this statement by implementing a passive mass scalar in run 26-4 which reveals an outflow morphology similar to that assumed in the wind models. This mass scalar is set to 1 within a disc with a height of 75 AU above and below the midplane and gets advected with the gas. Hence, we can test how much of the gas in the outflow stems from this disc and how much from the ambient medium. The analysis shows that by the end of the simulation about 92% of the gas mass in the outflow stems from this disc. Hence, most of the gas gets accelerated from the bottom of the outflow up to the tip and only a small part is entrained from the ambient medium. A possible explanation might be the high infall velocities, which are a result of the highly gravitationally unstable configuration. We suggest that the gas hitting the bow shock it is mainly deflected sideways and gets channelled downwards along the shock rather than getting stuck and being entrained with the outflow. The situation might change if the core is less gravitationally unstable and the infall velocities are smaller. We tentatively suppose that in this case it is more likely that the gas gets entrained by the outflow.

Yorke & Sonnhalter (2002) and Krumholz et al. (2005) suppose that outflows create low-density regions along the polar direction, which aid the formation of massive stars by channelling the radiation outwards, therefore diminishing the radiation pressure and allowing accretion to proceed. As seen in the right panel of Fig. 7.4, the material ejected from the disc indeed carves a low-density region in the polar direction. It would be interesting to see whether the density decrease in our simulations is sufficient to allow radiation produced by the protostar to escape efficiently as recently seen in radiation-hydrodynamical simulations by Cunningham et al. (2011). Furthermore it would be of interest to see to what extent the radiation pressure would decollimate the outflow as found recently by Vaidya et al. (2011) on the basis of 2-dimensional jet simulations.

### 7.4.3. Comparison to observations

In Table 7.1 we have listed the mass and momentum outflow rates of all runs performed. The calculated mass-loss rates vary between  $1.6 \cdot 10^{-5}$  and  $2.7 \cdot 10^{-4} M_{\odot} \text{ yr}^{-1}$ . Although at the lower end this is in agreement with typically observed mass loss rates in high-mass star forming regions ranging from  $10^{-5}$  up to a few  $10^{-3} M_{\odot} \text{ yr}^{-1}$  (e.g. Beuther et al., 2002c; Zhang et al., 2005; Wang et al., 2011; Ren et al., 2011). Like our simulations these observations refer to the very early stage of massive star formation although the calculated dynamical timescales are of the order of a few  $10^3$  up to a few  $10^4$  yr, thus typically somewhat longer than ours. However, since for a large fraction of

the observed systems no signs of HII-regions have been detected, the outflows are most likely still magneto-centrifugally driven and not radiation driven winds which is why our mass-loss rates compare reasonably well.

The calculated momentum outflow rates in our models range from  $4.0 \cdot 10^{-5}$  to  $4.7 \cdot 10^{-4} M_{\odot} \text{ km s}^{-1} \text{ yr}^{-1}$ . This is at the lower end usually reported by observations of massive protostellar outflows finding  $\dot{P}_{\text{out}}$  of the order of  $10^{-4}$  to  $10^{-2} M_{\odot} \text{ km s}^{-1} \text{ yr}^{-1}$  (e.g. Beuther et al., 2002c; Zhang et al., 2005; Shi et al., 2010; Wang et al., 2011). However, as the outflow velocity in centrifugally driven jets is coupled to the rotation velocity (Michel, 1969; Pelletier & Pudritz, 1992, and Eq. 4.11), the maximum outflow velocities which can be reached in our simulations are of the order of  $10 \text{ km s}^{-1}$  (see Eq. 7.9), about one order of magnitude lower than typically observed. Therefore, the lower values of  $\dot{P}_{\text{out}}$  in our runs are not surprising. However, we expect our momentum outflow rates to increase and to become comparable to observations if we run the simulations over comparable timescales of a few  $10^4 \text{ yr}$  and with a higher resolution, which would allow for faster outflow material arising from deeper in the gravitational potential.

Observational results on outflow morphologies are still somewhat ambiguous. On the one hand, outflows around massive protostars are usually found to be less collimated than their low-mass counterparts revealing collimation factors of the order of  $1 - 2$  (e.g. Ridge & Moore, 2001; Wu et al., 2004). On the other hand, Beuther et al. (2002a, 2004) also find highly collimated, massive outflows with collimation factors as high as 10. Based on this, Beuther & Shepherd (2005) propose an evolutionary scenario in which well-collimated, magnetically driven outflows occur in the very early phase of massive star formation. In its further evolution the outflows get progressively less collimated due to the build-up of HII-regions. According to this, early-stage outflows as presented here should all be more or less well collimated. Obviously this is not the case since only runs with a weak magnetic field ( $\mu = 26$ ) reveal well-collimated outflows with collimation factors up to 4.5. Therefore, our results suggest that the collimation not only depends on the evolutionary stage but also on the initial conditions of the molecular cloud core, in particular on the magnetic field strength.

#### 7.4.4. The evolution of outflow collimation

Our results suggest that during the very early stages ( $10^3 - 10^4 \text{ yr}$ ) outflows in typically magnetised, massive cores ( $\mu \lesssim 5$ ) should rather be poorly collimated with collimation factors of  $1 - 2$  instead of  $5 - 10$ . This agrees with a number of observations of outflows around young massive protostellar objects (e.g. Ridge & Moore, 2001; Torrelles et al., 2003; Wu et al., 2004; Sollins et al., 2004; Surcis et al., 2011). Therefore, we suggest that in the earliest stage, i.e. even before the scenario described by Beuther & Shepherd (2005) applies, outflows are indeed rather poorly collimated except in case of an unusually weak magnetic field. In their further evolution, however, the collimation will increase quickly due to the development of a fast, central jet component coupled to the build-up of a Keplerian disc. Such a behaviour can in particular be seen in the runs 26-20, 10-20 and 5.2-20. Hence we suggest that, beside tracing later stages as proposed

by Beuther & Shepherd (2005), poorly collimated outflows around massive protostars could also trace the very early stage of massive star formation. Hence, one might have to be careful when trying to infer the actual stage of protostellar evolution from the collimation of the outflow.

To confirm such an evolutionary scenario as proposed here, observations of the earliest stage of massive star formation would be necessary in combination with magnetic field measurements. Unfortunately, to date such observations are difficult to obtain and therefore rather rare. However, there is an interesting observation which supports the picture of very early stage, poorly collimated outflows successively collimating over time. Observing two spatially adjacent, massive protostars in the star forming region W75N, Torrelles et al. (2003) and Surcis et al. (2011) find the younger of the two having a spherical outflow whereas the more evolved protostar has a well-collimated outflow. Due to the close proximity to each other, the authors expect the environmental conditions to be very similar and hence not to cause the morphological differences. Therefore, the authors conclude that the differences are rather a consequence of different evolutionary stages and that the younger, poorly collimated outflow is possibly only a transient feature. This interpretation fits perfectly into our above described evolutionary scenario in which after some time a poorly collimated outflow gets overtaken by a well-collimated jet.

## 7.5. Conclusion

We have studied the collapse of massive molecular cloud cores with varying initial rotational and magnetic energies. The mass-to-flux ratio of the magnetically supercritical cores ranges from 2.6 up to 26. The cores have rotational energies well below the gravitational energy and contain about 56 Jeans masses. Hence, they are highly gravitationally unstable and possible sites of massive star formation. In this chapter we focussed on the launching mechanism and the properties of outflows in the earliest protostellar stage. Furthermore, based on the stationary, axisymmetric MHD equations we derived a generalised criterion to determine the launching mechanism of the outflows. The criterion is applicable to the entire outflow region and to situations with sub-Keplerian disc rotation. In the following we summarise our main findings.

1. We showed that our outflow criterion (Eqs. 7.2 and 7.8) can successfully separate the different driving mechanisms and that it works over the entire extension of the outflows. We discuss an example where the outflow is centrifugally driven up to a height of about 800 AU thereby demonstrating that considering only the ratio of  $B_\phi$  to  $B_{\text{pol}}$  is not sufficient to determine the driving mechanism. Furthermore, we successfully apply the criterion to runs with clearly sub-Keplerian protostellar discs where the frequently used  $30^\circ$ -criterion for the inclination of magnetic field lines fails.
2. The morphology and dynamics of the outflows critically depend on the magnetic field strength: well-collimated, high-velocity jets for runs with weak magnetic fields

( $\mu \geq 26$ ) or high rotational energies ( $\beta_{\text{rot}} = 0.20$ ) and poorly collimated, slowly expanding outflows for runs with strong fields. The development of fast jets is coupled to the build-up of Keplerian discs. In none of the strongly magnetised runs with clearly sub-Keplerian disc rotation a well-collimated jet is observed.

3. In all runs centrifugal acceleration is responsible for launching the gas from the discs. With increasing distance from the disc the pressure gradient of the toroidal magnetic field progressively contributes to the further acceleration of the gas. For runs with sub-Keplerian discs the outflows are centrifugally dominated only at large radii ( $\gtrsim 100$  AU) where gravity is sufficiently reduced to be overcome by the centrifugal force. In these outflows  $B_\phi$  seems to play a more important role in the driving than in the fast jets.
4. The morphological differences of the outflows are mainly due to the varying strength of the hoop stress responsible for outflow collimation. For sub-Keplerian discs the generation of  $B_\phi$  happens more slowly so that their corresponding outflows are less collimated.
5. We show that an outflow can be maintained despite the fragmentation of the protostellar disc. Furthermore, knotty outflow structures can also be produced in continuously fed jets by gas repeatedly experiencing shocks and reacceleration even far from the disc. For such outflows the toroidal magnetic field seems to contribute significantly to the overall stability.
6. The observed mass and momentum outflow rates are of the order of  $10^{-4} M_\odot \text{ yr}^{-1}$  and  $10^{-4} M_\odot \text{ km s}^{-1} \text{ yr}^{-1}$ , respectively, thus in reasonable agreement with observational results. The mass ejection-accretion ratios scatter around a mean of 0.3 in agreement with both theoretical estimates and observational results.
7. Based on the results of the strongly magnetised simulations ( $\mu \lesssim 5$ ), we suggest an evolutionary scenario where a poorly collimated outflow is typical for the very early stage of massive star formation. Over time the outflow collimation will increase due to the development of a well-collimated, fast jet overtaking the slowly expanding outflow. This picture is also supported by observations. Furthermore, analysing the sphere-like, slowly expanding outflows suggest that they are possibly only transient features, which might re-collapse during their further evolution.

We showed that a simple approach such as the value of  $B_\phi/B_{\text{pol}}$  or the inclination of magnetic field lines is not sufficient to determine the launching mechanism of outflows. This could be the reason for the partly conflicting results found in literature. We therefore strongly suggest to use a self-consistent criterion which is applicable to the entire outflow region as well as sub-Keplerian discs frequently found in numerical simulations (e.g. Mellon & Li, 2008; Hennebelle & Fromang, 2008; Duffin & Pudritz, 2009, and Chapter 6). Moreover, we emphasise that a separation in purely centrifugally or purely magnetic pressure driven winds is probably an oversimplification not describing the situation appropriately. We showed that magneto-centrifugal acceleration has two

regimes, a centrifugally dominated and a  $B_\phi$  dominated one and that within a realistic outflow there is a continuous transition from one regime to the other.

A growing number of observations of discs and well-collimated, bipolar outflows around high-mass protostars (see Beuther & Shepherd, 2005; Cesaroni et al., 2007, for recent reviews) support a high-mass star formation scenario via disc accretion similar to low-mass star formation. On the other hand, observations also show that prestellar cores with masses ranging from 2 – 2000  $M_\odot$  are usually only slightly supercritical with  $\mu \lesssim 5$  (Falgarone et al., 2008; Girart et al., 2009; Beuther et al., 2010). Together with our numerical results this suggest that typically there should be no well-collimated jets in the very early stages of high-mass star formation but rather sphere-like, slowly expanding outflow structures. As discussed in this chapter, the question of how well-collimated jets are generated breaks down to the problem of how Keplerian discs can be formed in highly magnetised cores. For this to happen, effects that reduce the efficiency of magnetic braking are required. In the later evolution of the system, the initial, slowly expanding outflows as well as non-ideal MHD effects could accomplish this, resulting in a successive growth of discs and the development of well-collimated jets over time. In the next chapter we will discuss in detail the role turbulence plays in the formation of protostellar discs and present a simple way how to form Keplerian discs from the very beginning on.



## 8. Disc formation in turbulent cloud cores

In the previous two chapters I have shown that there exists a problem in forming Keplerian protostellar discs and well-collimated outflows in typically magnetised ( $\mu \lesssim 5$ ) molecular cloud cores. In this chapter I will add a main ingredient of massive star formation, namely supersonic turbulence, to the simulations. So far turbulence has been neglected in this work to be able to explicitly study the influence of rotation and magnetisation without any interaction from turbulent motions. In the following I will study the influence of turbulence on the formation process of massive stars for a selected subset of the simulations presented before. The results and the discussion presented in this chapter have been published in Seifried et al. 2012a, MNRAS, 423, L40.

### 8.1. Introduction

In recent years a great number of simulations have been performed that investigate the formation of protostellar discs under the influence of magnetic fields (e.g. Allen et al., 2003; Matsumoto & Tomisaka, 2004; Machida et al., 2005; Banerjee & Pudritz, 2006, 2007; Price & Bate, 2007; Hennebelle & Fromang, 2008; Hennebelle & Teyssier, 2008; Hennebelle & Ciardi, 2009; Duffin & Pudritz, 2009; Commerçon et al., 2010; Peters et al., 2011, but see also Chapter 6 of this work). A main result of these simulations was that for magnetic field strengths comparable to observations, i.e. a mass-to-flux ratio  $\mu \lesssim 5$  (e.g. Falgarone et al., 2008; Girart et al., 2009; Beuther et al., 2010) no rotationally supported discs were formed. As discussed in Section 6.2.4, strong magnetic braking is responsible for the removal of angular momentum, which is why this problem is also called the "magnetic braking catastrophe". The results of these numerical simulations conflict with observations, which show that well-defined discs are present already in the earliest stages of protostellar evolution. In these observations well-defined protostellar discs were found around both high-mass (e.g. Fuller et al., 2001; Shepherd et al., 2001; Chini et al., 2004; Fernández-López et al., 2011; Preibisch et al., 2011, see also Cesaroni et al. (2007) for a recent review) and low-mass protostellar objects (e.g. Jørgensen et al., 2009; Enoch et al., 2009, 2011). Moreover, a comparison of the spectral energy distribution of young stellar objects in different evolutionary stages, i.e. in the Class 0 and Class I stage, shows that the disc masses do not change significantly from Class 0 to Class I objects (Jørgensen et al., 2009). This indicates that well-defined, rotationally supported protostellar discs frequently observed around later Class I objects (see e.g. Williams & Cieza, 2011, for a recent review) should also be present in the earlier Class 0 stage where direct observations are much more difficult due to extinction by the surrounding gas. It is also well-known that out-

flows are one of the first observable signatures of star formation. As shown in Chapter 7, well-collimated outflows frequently observed around low- and high-mass stars (see Beuther & Shepherd, 2005; Arce et al., 2007, for recent reviews) are coupled to the existence of well-defined, Keplerian discs. This is another strong indication that protostellar discs should already form in the earliest stage of star formation. To summarise, it seems that there exists some conflict between numerical simulations predicting the suppression of protostellar disc formation and observations indicating the presence of protostellar discs in the earliest stages of star formation already.

In recent years there have been some attempts to circumvent the "magnetic braking catastrophe" by incorporating non-ideal MHD effects into numerical simulations. The inclusion of ambipolar diffusion (Mellon & Li, 2009; Duffin & Pudritz, 2009), however, fails to produce Keplerian discs in the earliest evolutionary stages. Considering the effect of Ohmic dissipation, Dapp & Basu (2010) and Dapp et al. (2012) find only very small ( $\sim 10$  solar radii) Keplerian discs forming in the Class 0 stage. The authors expect the discs to grow to observed sizes of 10 – 100 AU during the subsequent evolution towards a Class I / II object. Krasnopolsky et al. (2010) showed that only if an unusually high ohmic resistivity is used Keplerian discs can form in the very beginning. Furthermore, also the combination of ambipolar diffusion and Ohmic dissipation does not yield the desired effect of Keplerian disc formation (Li et al., 2011).

However, recently two mechanisms solving the problem of "catastrophic magnetic braking" were proposed. Including the Hall effect Krasnopolsky et al. (2011) showed that Keplerian discs can indeed form in typically magnetised cloud cores. However, in this case the formation of rotationally supported discs is not a consequence of a reduced magnetic braking efficiency but rather due to the spin-up of the disc due to the Hall effect. Another mechanism to circumvent the "magnetic braking catastrophe" is turbulent reconnection as proposed by Santos-Lima et al. (2012). The authors argue that due to reconnection of magnetic field lines – aided by turbulent motions – the magnetic flux in the disc is lowered, which in turn reduces the magnetic braking efficiency and thus allows for the formation of Keplerian discs.

In this chapter we remedy a shortcoming of the simulations presented in the two previous chapters of this work and of the papers referred to in the beginning of this section, namely their lack of turbulent motions. We present results from a number of simulations investigating the possible role of turbulence in reducing the magnetic braking efficiency and allowing for the formation of protostellar discs. In Section 8.2 we briefly recapitulate the simulation setup, focussing on the changes made to the setup in the previous simulations. In Section 8.3 the simulation results are presented focussing on the formation of protostellar discs. A detailed discussion of the results including a comparison to other numerical work will be presented in Section 8.4 before we summarise our results in Section 8.5.

## 8.2. Initial conditions and numerical methods

We now shortly recapitulate the basic simulation setup. As the starting point of our simulations we have chosen the runs 2.6-4 and 5.2-4 (see Table 5.1). The cloud cores in these simulations have a mass of  $100 M_{\odot}$ , are 0.25 pc in size and embedded in a 0.75 pc-sized cubic simulation box of low-density gas ( $4.2 \cdot 10^{-21} \text{ g cm}^{-3}$ ). The density in the core declines as  $\rho \propto r^{-1.5}$  having a maximum of  $2.3 \cdot 10^{-17} \text{ g cm}^{-3}$  in the centre<sup>1</sup>. The core is rotating rigidly around the  $z$ -axis and is threaded by a magnetic field in the  $z$ -direction declining radially outwards with  $R^{-0.75}$ . We have chosen a ratio of the initial rotational energy to the gravitational energy of  $\beta_{\text{rot}} = 0.04$  as this corresponds well to typically observed values of molecular cloud cores (Goodman et al., 1993; Pirogov et al., 2003; Csengeri et al., 2011). Two different magnetic field strengths are chosen so that the mass-to-flux ratio  $\mu$  (Eq. 3.21) is equal to 2.6 and 5.2, respectively, which is in agreement with observational results (Falgarone et al., 2008; Girart et al., 2009; Beuther et al., 2010; Crutcher et al., 2010). Moreover, this is the most interesting range since here magnetic braking is very efficient and thus prevents the formation of Keplerian discs.

So far the setup is identical to the simulations presented before. We now superimpose a supersonic turbulent velocity field on the initial uniform rotation. The turbulence field consists of velocity fluctuations  $\Delta v(k)$  where the distribution of kinetic energy stored in the velocity fluctuations with a wave number  $k$  is described by the power spectrum

$$E(k) \propto k^{-5/3}. \quad (8.1)$$

This power-law relation with an exponent  $p = -5/3$  is characteristic for fully developed, incompressible turbulence (Kolmogorov, 1941). The modes consist of a natural mixing of solenoidal (divergence free:  $\nabla \cdot \mathbf{v} = 0$ ) and compressive modes (curl free:  $\nabla \times \mathbf{v} = 0$ ) with a ratio of 2:1. This ratio can easily be understood as there are two degrees of freedom for transversal modes and only one for longitudinal modes. The wavelength of the largest mode is chosen such that it approximately corresponds to the diameter of the core, i.e. 0.25 pc. The amount of turbulent kinetic energy in the cores is set equal to the rotational energy, i.e.  $\beta_{\text{turb}} = 0.04$ , corresponding to a turbulent rms-Mach number of  $\sim 2.5$ . This agrees reasonably well with observations of massive cloud cores, which usually report significantly broadened line widths pointing to supersonic turbulent motions (e.g. Caselli & Myers, 1995; Di Francesco et al., 2001; Sadavoy et al., 2012, but see also the seminal review on interstellar turbulence by Elmegreen & Scalo (2004)). Here we note that outside the core the turbulent velocity field is set to zero as this region is not of interest for us and has negligible dynamical influence on the core and hence also on the simulation results.

As pointed out by Girichidis et al. (2011) the realisation of the random turbulence field can have a significant impact on the results, in particular with regard to fragmentation properties. In order to check whether our results are affected by the random turbulent realisation, we performed three simulations with different turbulence seeds but otherwise

---

<sup>1</sup>We remind the reader that we cut off the  $r^{-1.5}$ -profile at a radius of 0.0125 pc in order to avoid unphysically high densities in the centre of the core.

Run	$\mu$	$\beta_{\text{rot}}$	$\beta_{\text{turb}}$	turbulence seed	p
2.6-4-A	2.6	0.04	0.04	A	-5/3
2.6-4-B	2.6	0.04	0.04	B	-5/3
2.6-4-C	2.6	0.04	0.04	C	-5/3
2.6-4-poly	2.6	0.04	0.04	A	-5/3
2.6-4-A-b	2.6	0.04	0.04	A	-2
2.6-0-A	2.6	0	0.04	A	-5/3
5.2-4-A	5.2	0.04	0.04	A	-5/3
2.6-4	2.6	0.04	0	–	–

**Table 8.1.:** Initial conditions of the performed turbulence simulations including run 2.6-4 without turbulence.

identical initial conditions (runs 2.6-4-A, 2.6-4-B and 2.6-4-C in Table 8.1). The simulation 5.2-4-A with the weaker magnetic field ( $\mu = 5.2$ ) was performed with the identical turbulence seed A already used for run 2.6-4-A. Observations of molecular cloud cores frequently reveal a power-law exponent  $p$  of the power spectrum  $E(k)$  around -2 (Larson, 1981; Heyer & Brunt, 2004), which corresponds to pressureless Burgers turbulence. We therefore also performed a simulation with a power-law exponent of -2 for the turbulence seed A. Furthermore, we repeated the simulation with  $\mu = 2.6$ ,  $p = -5/3$  and turbulence seed A with a different cooling routine. In this cooling routine the temperature is directly coupled to the particle density  $n$  via a polytropic index as follows:

$$T \propto n^{(\gamma-1)} \text{ with } \begin{cases} \gamma = 1 & \text{for } n < 10^9 \text{ cm}^{-3} \\ \gamma = 1.1 & \text{for } 10^9 < n < 10^{11} \text{ cm}^{-3} \\ \gamma = 1.3 & \text{for } 10^{11} < n < 10^{16} \text{ cm}^{-3}. \end{cases} \quad (8.2)$$

Finally, we performed a simulation without any overall rotation but only a turbulent velocity field. With the simulations given above we are able to test to what extent our findings depend on the initial conditions as well as on the applied cooling routine. All simulations performed are listed in Table 8.1.

The applied (standard) cooling routine takes into account dust cooling, molecular line cooling and the effects of optically thick gas (see Banerjee et al., 2006, and Section 5.1.2 for details). The maximum spatial resolution used in the simulations is

$$dx = 1.2 \text{ AU} \quad (8.3)$$

and therefore a factor of 4 higher than in the previous simulations without turbulence. This allows for a detailed analysis of the disc structures down to scales  $\lesssim 10$  AU. In the turbulence simulations we introduce sink particles above a density threshold of

$$\rho_{\text{crit}} = 1.14 \cdot 10^{-10} \text{ g cm}^{-3}. \quad (8.4)$$

The sink particles have an accretion radius of 3.1 AU, a factor of about 2.6 larger than the smallest cell size. As a refinement criterion we only use the Jeans criterion but not the

second derivative criterion (see Section 5.1.1 for details) as otherwise the entire cloud core would be refined due to small density perturbations induced by the turbulent motions, which would make the simulations extremely costly. The Jeans criterion guarantees that the Jeans length is resolved everywhere with at least 8 grid cells. We note that in particular for magnetohydrodynamical turbulence simulations it has been suggested to use an even higher resolution (Federrath et al., 2011). However, due to computational cost reasons this could not be accomplished here.

In Section 5.2 we introduced an artificial density threshold in order to limit the Alfvén velocity  $v_A$  and prevent the hydrodynamical timestep to drop to prohibitively small values. The density threshold was applied in a geometrically well-defined region around the centre of the simulation domain. As in the turbulence runs sink particles do not necessarily form in the centre, this criterion is useless. We therefore modified the criterion for the density threshold as follows: The density threshold of  $1 \cdot 10^{-15} \text{ g cm}^{-3}$  will be applied only on the two highest AMR refinement levels and only in those cells in which the hydrodynamical timestep, approximately calculated as

$$dt = dx/v_A, \quad (8.5)$$

falls below  $3 \cdot 10^6$  s. This allows for a reasonable timestep without adding a significant amount of mass to the simulation domain.

### 8.3. Results

In total we have performed 7 simulations with varying initial conditions. For reasons of clarity we do not present the results of all runs in detail but focus on four fiducial runs namely 2.6-4-A, 2.6-4-B, 2.6-0-A and 2.6-4-A-b. With these simulations we can demonstrate how the results depend on the initial realisation of the turbulence field (runs 2.6-4-A and 2.6-4-B), the exponent of the turbulence spectrum (run 2.6-4-A-b) and the fact whether an overall rotation is present or not (run 2.6-0-A). We emphasise that concerning disc formation the results of the runs 2.6-4-C, 2.6-4-A-p and 5.2-4-A are qualitatively very similar to the four other runs. Hence, we are confident that the main findings do not depend on the randomly chosen, initial turbulence field nor on the used cooling function nor do they change if a slightly weaker initial magnetic field is used. We again emphasise that we solely focus on the process of disc formation and leave other points like fragmentation and accretion behaviour for future work.

Since we are interested in the properties and the evolution of protostellar discs, we restrict our consideration to the time after the first sink particle has formed ( $t_0$ ). Depending on the simulation, this happens after roughly 15 – 20 kyr. At this point large-scale filaments have developed, in which the discs form (for fragmentation and disc formation in massive cores without magnetic fields see Banerjee & Pudritz, 2006; Girichidis et al., 2011). From this point on we run the simulations for further 15 kyr (except run 2.6-0-A which, for computational cost reasons, has been followed for 12.5 kyr only). In order to determine global disc properties like mass, centre-of-mass, and the angular momentum

vector, we only consider gas with densities larger than  $5 \cdot 10^{-13} \text{ g cm}^{-3}$  around a sink particle. By visual inspection of the density isocontours and variation of this threshold we found this value to be reasonable. Furthermore, it roughly corresponds to the threshold where the gas gets optically thick (see Section 5.1.2). With respect to the centre-of-mass and the orientation of the disc we now can calculate the rotation velocity  $v_\phi$  and the radial infall velocity  $v_{\text{rad}}$  for each grid cell in the disc, i.e. with a density above the threshold of  $5 \cdot 10^{-13} \text{ g cm}^{-3}$ . Making use of a density threshold has the advantage that gas from the outflow cavity above and below the disc is excluded in this consideration. For the outer regions where no gas with densities larger than  $5 \cdot 10^{-13} \text{ g cm}^{-3}$  is found, we adopt a simple geometrical criterion considering all the gas within a height of 20 AU above/below the midplane defined by the disc. The radius where this geometrical criterion becomes necessary is usually of the order of 50 – 100 AU depending on the actual simulation. Hence, we are able to analyse the velocity structure outside the disc as well. In order to get an impression of the scatter of the different velocity components, we do not azimuthally average the values of  $v_\phi$  and  $v_{\text{rad}}$ .

In Fig. 8.1 we show the radial dependence of  $v_\phi$  and  $v_{\text{rad}}$  15 kyr after the formation of the first sink particle for all cells in the disc formed first in each of the runs 2.6-4-A, 2.6-4-B, 2.6-0-A and 2.6-4-A-b. To get an impression of whether the discs are rotationally supported or not, we also plot the Keplerian velocity  $v_{\text{kep}} = \left(\frac{GM_r}{r}\right)^{1/2}$ , where  $G$  is the gravitational constant and  $M_r$  the mass of all sink particles and gas within a sphere of radius  $r$  around the disc centre. As can be seen,  $v_\phi$  is close to  $v_{\text{kep}}$  out to a radius of  $\sim 50$  AU or even more with a scatter of about 50% in each direction as indicated by the dotted lines. This is a remarkable result since for previous simulations of low- and high-mass cores with mass-to-flux ratios  $\mu < 10$  only sub-Keplerian discs were found (e.g. Allen et al., 2003; Price & Bate, 2007; Mellon & Li, 2008; Hennebelle & Fromang, 2008; Duffin & Pudritz, 2009, and Chapter 6 of this work).

We note that, although all runs contain more than one sink particle, only the disc around the first sink formed has a considerable size of  $\sim 50$  AU or more. This disc usually contains several sinks. Some of the remaining sinks do not have an associated disc at all. This can be attributed to the ejection from an already existing disc due to many-body interactions with nearby sinks. Therefore these ejected sinks have a high relative speed with respect to the surrounding gas, which hampers the build-up of a disc. Furthermore, some of the sinks without any large ( $\gtrsim 50$  AU) disc have been created only shortly before the end of the simulation so that their discs are not yet well developed. However, we emphasise that also these very young discs reveal Keplerian velocity profiles, but to a radius of a few 10 AU only.

We note that in parts the angular momentum vectors of the discs are well off the  $z$ -axis. For example, in run 2.6-4-B the disc orientation is almost perpendicular to the overall rotation over the entire 15 kyr (see Fig. 8.2) and also for run 2.6-4-C initially the angular momentum of the disc is well off the  $z$ -axis and approaches the  $z$ -axis only at the end of the simulation. This demonstrates that the local angular momentum associated with the turbulent motions strongly affects the formation of the discs. This is even more clearly demonstrated by the formation of a disc in run 2.6-0-A, where no overall rotation

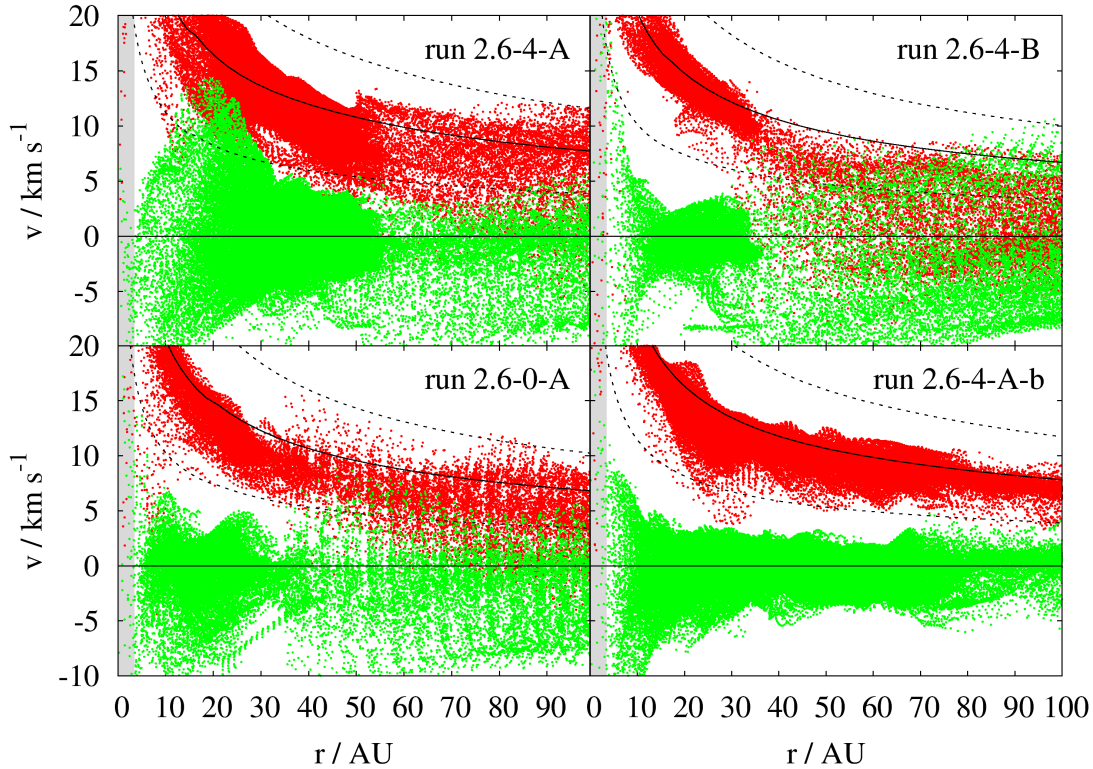


**Figure 8.1.:** Radial dependence of the rotation (red) and radial velocity (green) for the disc formed first in each of the runs 2.6-4-A, 2.6-4-B, 2.6-0-A and 2.6-4-A-b. The black solid line shows the Keplerian velocity  $v_{\text{kep}}$ , the dotted lines 50% and 150% of  $v_{\text{kep}}$ . The regions below 4 AU are affected by resolution effects, therefore they are shaded grey to guide the reader’s eye.

is present. We note that the orientation of the discs varies only slowly over time as the large-scale structure in which they reside does not change much during the time considered ( $\sim 15$  kyr). Furthermore, the discs presented here have masses of the order of  $0.1 M_{\odot}$  and drive molecular outflows. However, due to the turbulent surroundings of the discs with velocities comparable to the outflow velocity it is hard to track the outflow by means of the velocity structure alone. Hence, it is hard to estimate a reliable mass of the outflows driven by the discs, which is why we will not follow this topic further in this work.

Furthermore, since in all discs shown in Fig. 8.1  $v_{\phi}$  scatters around  $v_{\text{kep}}$ , this indicates that this result is neither an incidental consequence of the specific turbulence seed nor of the power-spectrum exponent (run 2.6-4-A-b). Moreover, also changing the thermodynamical behaviour of the gas using a polytropic equation of state (run 2.6-4-poly) or removing the overall core rotation (2.6-0-A) does not change the result qualitatively. For all discs we find that  $v_{\text{rad}}$  scatters around zero and is almost always smaller than  $v_{\phi}$  and significantly smaller than the free-fall velocity  $v_{\text{ff}} = \sqrt{2}v_{\text{kep}}$ . This is in strong contrast to the disc in run 2.6-4, which has the same initial setup as the runs presented here except

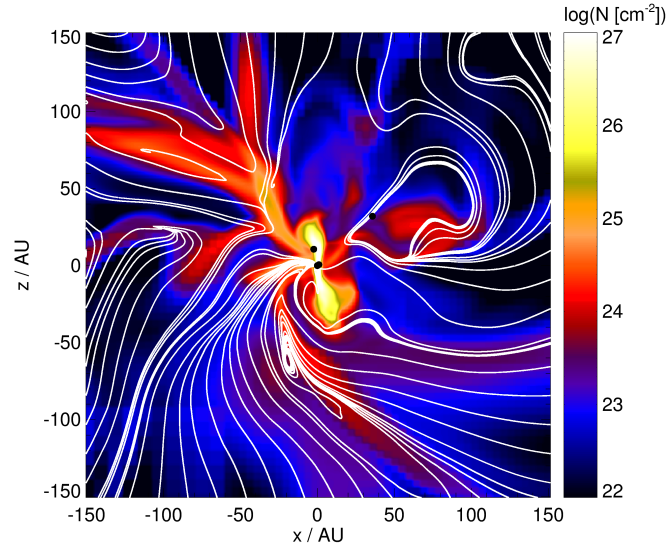


**Figure 8.2.:** Edge-on view of the disc formed first in run 2.6-4-B. The column density is overplotted with the magnetic field lines (white) and the sink particles (black dots). The disc angular momentum pointing into the  $x$ -direction is well off from the global angular momentum (pointing into the  $z$ -direction) and the magnetic field structure is highly disordered.

the initial turbulence field. The disc was found to be strongly sub-Keplerian with  $v_{\text{rad}}$  close to  $v_{\text{ff}}$ . The difference becomes particularly clear when comparing the top-on view of the discs formed first in the runs 2.6-4-A, 2.6-4-B, 2.6-0-A and 2.6-4-A-b (Fig. 8.3) with that of highly magnetised runs without turbulent motions (compare right panel of Fig. 6.4). The discs have a relatively well-defined outer boundary around a column density of  $\sim 3 \cdot 10^{24} \text{ cm}^{-2}$ . The edge of the disc roughly corresponds to the radius where the volume density in the disc drops below a value of  $5 \cdot 10^{-13} \text{ g cm}^{-3}$ . From the top left panel of Fig. 8.3 it can also be inferred that the reason for the relative large values of  $v_{\text{rad}}$  seen in run 2.6-4-A around 20 AU (top left panel of Fig. 8.1) are due to a secondary sink particle at this position.

Why, even in the case of such strongly magnetised cores, are Keplerian discs formed? The suppression of Keplerian disc formation in previous studies without turbulence is due to the very efficient magnetic braking (Mouschovias & Paleologou, 1980), which removes angular momentum from the midplane at a very high rate (see Section 6.2.4 and in particular Fig. 6.10). Hence, in the turbulence runs presented here the magnetic braking efficiency has to be reduced significantly. Two possible mechanisms which could accomplish this have been discussed recently in literature. The first mechanism is the loss of magnetic flux in the disc and in its surroundings. Secondly, it was shown that a misalignment of the magnetic field and the angular momentum vector of the disc also reduces the magnetic braking efficiency (Hennebelle & Ciardi, 2009; Ciardi & Hennebelle, 2010;

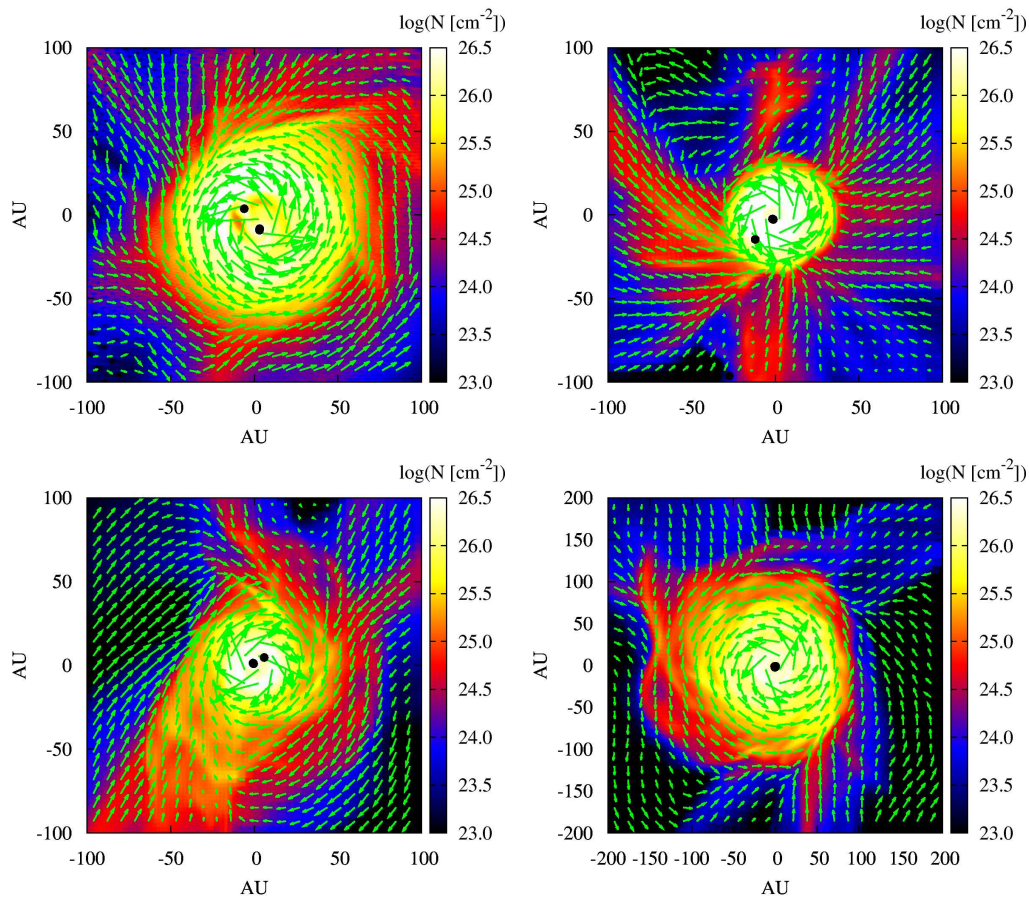


**Figure 8.3.:** Column density in logarithmic scaling for the top-on view of the four discs formed first in the runs 2.6-4-A, 2.6-4-B, 2.6-0-A and 2.6-4-A-b (from top left to bottom right). Additionally, the velocity field (green vectors) and the projected position of the sink particles (black dots) are shown. Note the different scale in the bottom right panel. The appearance of the discs differs significantly from that of highly magnetised non-turbulent runs (compare right panel of Fig. 6.4).

Joos et al., 2012). In the following we try to work out the reason why in our simulations with initial turbulence Keplerian discs are formed.

In a first step we try to estimate the dynamical importance of the magnetic field for the gas dynamics. In Chapter 6 we have shown that the magnetic field starts to play an important role in the dynamical evolution of the gas as soon as the mass-to-flux ratio drops below a value of  $\sim 10$ , resulting in the suppression of Keplerian disc formation. For this reason we firstly calculate the mass-to-flux ratio in a sphere with a radius of 500 AU around the centre of each disc. For this purpose we calculate the volume-weighted, mean magnetic field  $|\langle \mathbf{B} \rangle|$  as well as the mass  $M$  of the gas in the sphere. With these quantities

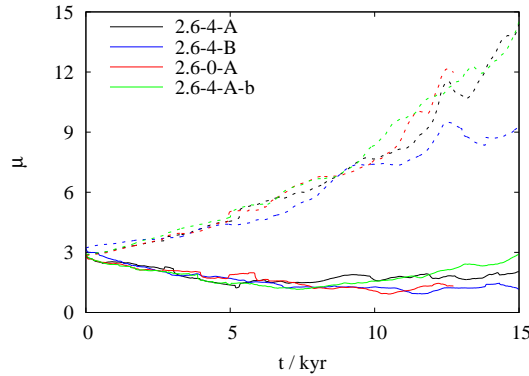


**Figure 8.4.:** Mass-to-flux ratio  $\mu$  in spheres with a radius of 500 AU around the centre-of-mass of the same four discs as in Fig. 8.1 taking into account the gas mass only (solid lines) and the sum of gas and sink particle masses (dashed lines).

the average mass-to-flux ratio in the sphere is defined as

$$\mu = \frac{M}{\pi r^2 |\langle \mathbf{B} \rangle|} / \frac{0.13}{\sqrt{G}}. \quad (8.6)$$

We plot the time evolution of  $\mu$  in Fig. 8.4 for the same four discs as in Fig. 8.1, i.e. the discs formed first in each of the runs 2.6-4-A, 2.6-4-B, 2.6-0-A and 2.6-4-A-b. When taking into account only the mass of the gas in the sphere (solid lines),  $\mu$  varies around a mean of 2 – 3, which is in rough agreement with the overall value of 2.6. Furthermore, for the four discs considered  $\mu$  stays well below the critical value of  $\sim 10$  for which in both low- and high-mass protostellar cases the formation of Keplerian discs is suppressed (see Chapter 6). Hence, from our previous results and those of other authors one would expect that no Keplerian discs should build up, which obviously is not the case.

In Fig. 8.5 we plot the scaling of the magnetic field with the density. For this purpose the mean magnetic field strength in density bins of equal width in log-space is calculated. For reasons of clarity we only plot the results for run 2.6-4-A for different times but note that the results of the other runs are qualitatively very similar. As can be seen, the observed scaling  $B \propto \rho^{0.5}$  is very similar to that of the non-turbulent run 2.6-4 (green line). There seems to be a moderate build-up of magnetic energy between  $10^{-15}$  and  $10^{-11}$  g cm $^{-3}$ . The overall shape, however, does not change significantly. At late times the magnetic field strength at densities above  $10^{-11}$  g cm $^{-3}$  does not grow anymore, a result also observed in the other simulations. This could point to a flux loss at densities larger than  $10^{-11}$  g cm $^{-3}$ . However, this density is by far higher than the density in the surroundings of the disc indicating that in the surroundings the magnetic field is reasonably well coupled to the gas. This seems to contradict the findings of Santos-Lima et al. (2012), who propose that in the disc and its surroundings turbulent reconnection occurs, which lowers the magnetic flux and thus the magnetic braking efficiency. However, further comparison to their work is not possible as the authors do not consider the scaling of the magnetic field.

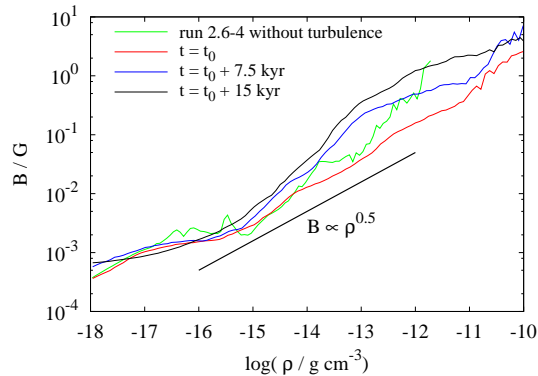


**Figure 8.5.:** Scaling of the magnetic field for different times in run 2.6-4-A as well as in the non-turbulent run 2.6-4.

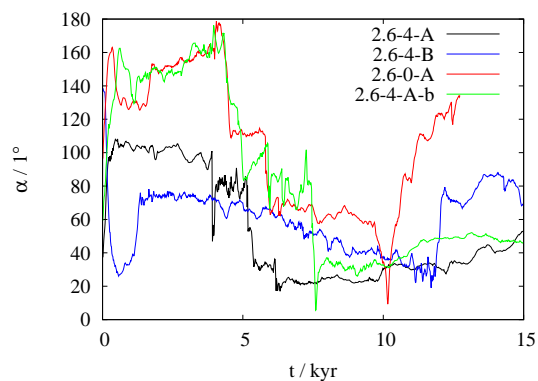


**Figure 8.6.:** Inclination of the mean magnetic field  $\langle \mathbf{B} \rangle$  to the angular momentum vector of the disc in spheres with a radius of 500 AU around the centre-of-mass for the same four discs as in Fig. 8.1.

Another way of reducing the magnetic braking efficiency was investigated by Hennebelle & Ciardi (2009), Ciardi & Hennebelle (2010) and Joos et al. (2012). These authors found that even for a small misalignment of the overall magnetic field and the rotation axis Keplerian discs can form. As we consider a turbulent flow, it is very likely that the magnetic field and the rotation axis are misaligned. In Fig. 8.6 we plot the angle  $\alpha$  between the disc angular momentum vector and  $\langle \mathbf{B} \rangle$  in the spheres around the four fiducial discs. The angle  $\alpha$  is significantly larger than  $0^\circ$ , which supports the picture of a reduced magnetic braking efficiency due to a misalignment of the magnetic field and the rotation axis. However, when considering the magnetic field line structure around the disc in run 2.6-4-B in an edge-on view (Fig. 8.2), one can see that calculating an average magnetic field vector is a very crude approximation. As can be seen, the magnetic field structure is highly disordered and approximating this structure by a mean magnetic field is at least questionable. Also around the other discs the field

structure is found to be highly disordered. Hence, beside  $\alpha$  also the value of  $\mu$  calculated in Eq. 8.6 should be taken with caution. We note that the turbulent motions responsible for the highly disordered magnetic field also explain the large variations in  $\alpha$  seen in Fig. 8.6. Due to the velocity fluctuations the magnetic field in the surroundings of the discs changes relatively fast. This causes the large variations in the inclination of  $\langle \mathbf{B} \rangle$  with respect to the disc angular momentum vector, whose direction varies rather moderately over time.

The highly disordered magnetic field indicates a third reason why the magnetic braking efficiency is strongly reduced. Considering Fig. 8.3 it can be seen that in the surroundings of each disc the velocity field is highly turbulent with no signs of a coherent rotation structure. Therefore, no toroidal magnetic field component (with respect to the coordinate system of the disc) can be built up. But as the angular momentum is mainly extracted by toroidal Alfvénic waves, it is not surprising that the magnetic braking efficiency is strongly reduced in the environment of the disc despite a low mass-to-flux ratio (compare Fig. 8.4). Moreover, the disordered magnetic field structure itself impedes the coupling of the fast rotating gas in the inner parts to slowly rotating gas in the outer parts. Such a kind of field configuration with a long magnetic lever arm (compare Fig. 6.8) connecting the inner and outer parts would even more increase the efficiency of magnetic braking. To summarise, the magnetic braking efficiency is reduced due to the lack of a proper toroidal magnetic field component and the highly disordered magnetic field structure in the disc environment.

Despite the lack of a coherent rotation structure, locally the inwards angular momentum transport can remain high due to *local* shear flows driving large angular momentum fluxes. Such accretion flows, which deviate from a perfectly radial inflow and therefore carry large amounts of angular momentum, can be seen in Fig. 8.3. We also note that such a non-coherent flow cannot be slowed down by the magnetic field as efficiently as it would be the case for large-scale, coherent rotational motions. This can be seen in our previous simulations (Chapter 6) without initial turbulence where the angular momentum is removed almost completely *before* the gas hits the disc. Hence, it is the shear flow generated by turbulent motions that provides the required angular momentum to build up Keplerian discs.

To quantify the above described picture, we calculate the torques of the gas  $\tau_{\text{gas}}$  (Eq. 6.4) and the magnetic field  $\tau_{\text{mag}}$  (Eq. 6.5) in cylinders of variable radii and a total height of 40 AU<sup>2</sup> around the centre-of-mass of each disc. The symmetry axis of the cylinders is determined by the angular momentum vector of the corresponding disc. In Fig. 8.7 we plot the ratio of  $\tau_{\text{gas}}$  to  $\tau_{\text{mag}}$  for the first disc in each of the runs 2.6-4-A, 2.6-4-B, 2.6-0-A and 2.6-4-A-b and the disc in run 2.6-4 without turbulence. For the turbulence runs  $\tau_{\text{gas}}$  exceeds  $\tau_{\text{mag}}$  on average by at least a factor of a few, i.e. angular momentum is transported inwards at a higher rate than it is extracted by the magnetic field. This is also observed for the discs in the other runs not shown here. We briefly note that the gravitational torques not shown here are generally even smaller than  $\tau_{\text{mag}}$  and

---

<sup>2</sup>This height is found to be reasonable by visually inspecting the discs in edge-on view. Furthermore, a variation of this value does not qualitatively change the overall picture.

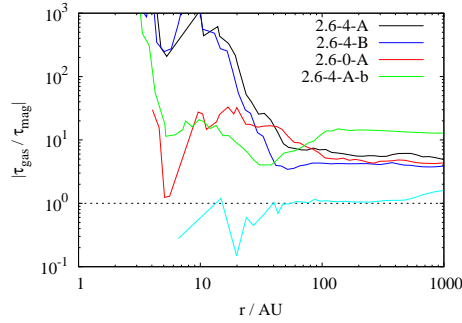


**Figure 8.7.:** Ratio of  $\tau_{\text{gas}}$  to  $\tau_{\text{mag}}$  for the same four discs as in Fig. 8.1 (same colours as in Fig. 8.4) and for the disc in run 2.6-4 without turbulence (light blue line).

are thus dynamically even less important. Hence, for the turbulence runs there is a net transport of angular momentum inwards resulting in the observed build-up of Keplerian discs. In contrast, for the non-turbulent run  $\tau_{\text{gas}}$  is almost perfectly balanced by  $\tau_{\text{mag}}$ , which prevents the formation of rotationally supported discs.

This result fits in the picture described above where the magnetic braking efficiency is reduced due to the disordered magnetic field and the presence of local shear flows instead of a coherent rotation structure. To summarise, it seems that the turbulent disc environment is the reason for the build-up of a Keplerian disc.

## 8.4. Discussion

### 8.4.1. Dependence on the initial conditions

Of particular interest was the question how different initial turbulence fields might influence the formation of protostellar discs. From the three runs 2.6-4-A, 2.6-4-B and 2.6-4-C with a Kolomogorov type turbulence spectrum it can be seen that the actual realisation of the turbulence field has only little influence on the size and velocity structure of the discs (see Fig. 8.1 and 8.3). Furthermore, also different power-law exponents of the turbulence spectrum seem not to affect the results significantly. This behaviour is in agreement with recent results of Bate (2009) and Walch et al. (2012) showing that varying the power-law exponent has only little influence on certain properties of star formation like e.g. protostellar mass distributions. However, as Walch et al. (2012) pointed out, the largest wavelength used in the turbulence spectrum can significantly influence the results as this mode carries the largest amount of kinetic energy. Hence, in our case it would be interesting to see what happens if we reduce the largest turbulence mode, which currently roughly corresponds to the diameter of the core, to a significantly smaller scale. Furthermore, as shown by Girichidis et al. (2011), the fragmentation properties critically depend on the density profile of the core. Hence, it would be of interest to perform simulations with a more flattened profile, which would be more susceptible to fragmentation. However, due to computational cost reasons the effect of enhanced fragmentation and of

the variation of the size of the largest turbulence mode could not be tested during the course of this work.

#### 8.4.2. Mass-to-flux ratio

In Section 8.3 we have considered the mean mass-to-flux ratio in spheres of 500 AU around the discs only taking into account the mass of the gas. The reason for this approach was the possibility to compare the results to those of Chapter 6 and thus to estimate the importance of the magnetic field for the gas dynamics. However, when including the mass of the sink particles in the mass  $M$  in Eq. 8.6, the value of  $\mu$  at the end of each run is larger by a factor of  $\sim 5$ , i.e.  $\mu \simeq 10 - 15$  (see dashed lines in Fig. 8.4). Hence, there occurs a real magnetic flux loss in the spheres and one could argue that this flux loss would be enough to allow for Keplerian disc formation as now  $\mu$  is in the range where Keplerian discs have been found. However, we argue that to properly estimate the importance of the magnetic field for the gas dynamics, it is more insightful to take into account the mass of the gas alone. The reason for this is that magnetic braking directly affects the rotation of the gas only and not that of already existing sink particles. Moreover, the increase of  $\mu$  due to the inclusion of the sink particles (compared to the value of  $\mu$  calculated with the gas mass only) is not constant but increases in time since shortly after the formation of the sink particle the gas mass in the sphere dominates over the sink mass. Hence, in the beginning ( $t \lesssim 10$  kyr), which is the actual phase during that the discs are formed, even the mass-to-flux ratio including the sink particle mass is clearly *below* 10 indicating that the magnetic field should be strong enough to efficiently remove angular momentum and to prevent Keplerian discs from forming. Since this is not the case, the flux loss alone cannot explain the formation of the Keplerian discs.

We emphasise that in the case of initial turbulence the value of the mass-to-flux ratio has to be taken with caution. One reason is that accretion onto the disc along the magnetic field lines increases the mass-to-flux ratio when measuring it in a fixed (not comoving) volume. Furthermore, the highly disordered structure of the magnetic field in the vicinity of the discs (see Fig. 8.2 for an example) complicates the interpretation of the mass-to-flux ratio, which originally was derived for a well-ordered, purely poloidal magnetic field (Mouschovias & Spitzer, 1976). However, we tried to estimate the mass-to-flux ratio in a different way: Calculating the magnetic flux through the surface of a cylinder with diameter and height of 1000 AU and comparing the flux to its mass, we find a mass-to-flux ratio similar to that found in Fig. 8.4 differing by a few 10% only. Hence, the estimate of  $\mu$  done in Section 8.3 seems to be rather robust and is only little influenced by the highly disordered magnetic field line structure, but most likely by mass accretion along the field lines.

#### 8.4.3. The reduced magnetic braking efficiency

Recently Santos-Lima et al. (2012) have reported the formation of Keplerian discs in turbulent, strongly magnetised low-mass cores. The authors attribute this to the effect of turbulent reconnection (Lazarian & Vishniac, 1999) lowering the magnetic flux in

the centre. Analysing the scaling of the magnetic field with the density, we find that the observed relation  $B \propto \rho^{0.5}$  is very similar to the non-turbulent case and more or less constant over time indicating a good coupling between the magnetic field and the gas. However, as pointed out before, some magnetic flux loss becomes apparent when taking into account the sink particle masses in the calculation of  $\mu$ . This flux loss is even more pronounced when going to smaller scales of the order of the disc radius, i.e.  $\sim 100$  AU. This is reflected by a mass-to-flux ratio on these scales significantly larger than 10 (including the sink particle mass), which cannot be explained by an artificial increase of  $\mu$  due to accretion along magnetic field lines alone. Hence, on these scales clearly some magnetic flux loss has occurred. Therefore, it could be argued that turbulent reconnection is happening on these scales. Also from Fig. 8.5 some flux loss is apparent at densities above  $\sim 10^{-11}$  g cm $^{-3}$ . Typical scales associated with this density are of the order of 30 – 40 AU. However, on these scales ( $\lesssim 100$  AU) where the magnetic flux loss becomes clearly apparent the velocity structure seems to be relatively well-ordered (Fig. 8.3), which makes turbulent reconnection unlikely to happen. Hence, we rather attribute the flux loss to numerical diffusion.

One could now argue that the diffusion of the magnetic field on the disc scale is responsible for the build-up of the Keplerian discs. Then, however, the question arises why in the non-turbulent case magnetic diffusion is less efficient. This can be explained by a simple, heuristic picture: The increased magnetic flux loss – compared to the non-turbulent run – is a direct consequence of the increased timescale for the gas infall compared to the diffusion timescale. This in turn means that the radial infall velocity has to be decreased compared to the non-turbulent run. This decrease of the radial infall velocity, however, requires the existence of a rotationally supported structure with infall velocities already close to zero (compare Fig. 8.1). Hence, before magnetic diffusion can become efficient at all, there must be enough angular momentum available to build up a Keplerian disc. This in turn requires the magnetic braking efficiency to be reduced on larger scales ( $\gtrsim 100$  AU), which – as we have shown – can be attributed to the disordered magnetic field structure and the local shear flows around the discs. With other words, the magnetic diffusion/flux loss on the scales of the disc is not the reason for the build-up of a Keplerian disc but rather its consequence. Nevertheless, by means of the small-scales flux loss magnetic diffusion certainly helps to keep the disc in a rotationally supported state.

The large misalignment of the magnetic field of the spheres and the angular momentum of the discs of up to  $90^\circ$  (see Fig. 8.6) also might weaken the effect of magnetic braking as suggested by Hennebelle & Ciardi (2009), Ciardi & Hennebelle (2010) and Joos et al. (2012). In their work, however, only uniformly rotating spheres with a well-ordered magnetic field were considered, which is clearly not the case here (see Fig. 8.2 and 8.3). Therefore, it is hard to tell to what extent in our case the misalignment affects the magnetic braking efficiency. Moreover, it seems that the simulations of the authors mentioned before more or less represent a special case of the situation observed here namely a somehow disordered (in their case misaligned) magnetic field and/or the missing of a coherent rotation structure in the vicinity of the disc.

We note that recently Hennebelle et al. (2011) and Commerçon et al. (2011) also performed simulations of high-mass turbulent cloud cores where they found large-scale outflows. Since these outflows require the existence of well-defined protostellar discs, their work clearly supports our simulation results. However, as these authors do not explicitly consider the properties of their discs, a further comparison to their work is not possible. Nevertheless, their and our results indicate that one should detach from the classical picture of magnetic braking for a coherently rotating structure threaded by a well-ordered magnetic field. As we have shown, such a structure does not occur under realistic conditions – at least in the case of massive star formation with highly supersonic turbulent motions.

To summarise, two different aspects play a role in the formation of the discs. On large scales ( $\gtrsim 100$  AU) magnetic braking is reduced due to a disordered magnetic field and the missing of a proper toroidal field component. Simultaneously, the angular momentum flux remains high due to local shear flows around the discs transporting mass and angular momentum inwards. On small scales ( $\lesssim 100$  AU) magnetic diffusion sets in, significantly increasing the mass-to-flux ratio. This, however, can only happen if the infall velocity is reduced due to an already existing Keplerian disc.

#### **8.4.4. Early vs. late stage disc formation**

Recently, Krasnopolsky et al. (2011) have proposed that including the Hall effect can result in the formation of large-scale Keplerian discs. They claim, however, that a Hall coefficient about one order of magnitude larger than expected under realistic conditions would be required. Furthermore, in this case the spin-up of the disc is not due to a reduced magnetic braking efficiency but due to the Hall-induced magnetic torque, which depends on the direction of the magnetic field. This is demonstrated by the fact that Krasnopolsky et al. (2011) find counterrotating discs, i.e. discs which rotate in the opposite direction as the surrounding core when the field direction is flipped. Recently it was also shown that Ohmic dissipation fails to produce Keplerian discs larger than roughly 10 solar radii in the earliest evolutionary stage (Dapp & Basu, 2010; Dapp et al., 2012), unless a strongly enhanced resistivity is used (Krasnopolsky et al., 2010). Furthermore, also the inclusion of ambipolar diffusion does not help to form Keplerian discs (Mellon & Li, 2009; Duffin & Pudritz, 2009). Hence, it seems that all three non-ideal MHD effects cannot account for the formation of Keplerian discs. However, as we have shown, already for the ideal MHD limit Keplerian discs can form in strongly magnetised cores when turbulent motions are included. Therefore, it seems that non-ideal MHD effects or turbulent reconnection are not necessarily required to avoid the “magnetic braking catastrophe”.

Based on their simulations, the authors mentioned in the paragraph before suggest that well-defined, Keplerian discs build up during the evolution of the central object from the Class 0 to the Class I stage and are not present from the very beginning. Indeed, earlier observations of individual Class 0 sources found cases where no well-defined, Keplerian discs were detected (e.g. Belloche et al., 2002). These observations support the picture of a successive build-up of discs during the evolution towards the Class I stage,

which would alleviate the magnetic braking problem. These findings seem to contradict our results presented here. However, comparing more recent observations of spectral energy distributions (SEDs) of a sample of Class 0 sources with detailed radiative transfer models suggests that the majority of the objects harbours well-defined protostellar discs forming in the earliest stages (Jørgensen et al., 2009; Enoch et al., 2009, 2011). Furthermore, Jørgensen et al. (2009) do not find significant differences between the disc masses in Class 0 and Class I objects. This might indicate that also other properties like kinematics of Class 0 stage discs are similar to that of Class I stage discs, which are in general observed to be rotationally supported (for an overview see section 4.3.3 in Williams & Cieza, 2011, and references therein). However, as the aforementioned observations usually do not provide a clear visual identification of the discs, one has to be careful when interpreting these results. Indeed, there are some recent observations which suggest that there are no well-defined discs around Class 0 objects (Maury et al., 2010). We note that the aforementioned observations mainly refer to low- and intermediate-mass protostars. For high-mass protostellar objects the observation of protostellar discs is even more challenging due to the stronger extinction of radiation by the large amount of surrounding gas. Nevertheless, there are observations of well-defined, Keplerian discs with typical sizes of a few 100 AU around massive protostellar objects (Fuller et al., 2001; Shepherd et al., 2001; Chini et al., 2004; Fernández-López et al., 2011; Preibisch et al., 2011, but see also the review of Cesaroni et al. (2007)) although also these observations, just like those mentioned before, often refer to the later, somewhat more evolved Class I phase.

To summarise, one has to state that the question of whether protostellar discs form already in the earliest (Class 0) stage as proposed in this work or by a successive build-up towards the Class I stage remains highly debated. For this question to be answered, high-resolution observations have to be performed, e.g. with the newly designed Atacama Large Millimeter/submillimeter Array (ALMA). Nevertheless, our work clearly shows that in massive star forming regions under realistic conditions, i.e. when including supersonic turbulent motions, early type, rotationally supported protostellar discs can indeed form.

## 8.5. Conclusion

We have performed collapse simulations of strongly magnetised ( $\mu = 2.6, 5.2$ ),  $100 M_{\odot}$  cloud cores. A turbulent velocity field was superimposed on the uniform core rotation. We find that after an initial collapse phase of  $\sim 15$  kyr discs with typical masses of  $\sim 0.1 M_{\odot}$  form. The discs have radii of 50 – 100 AU and rotate with Keplerian velocities – a result in strong contrast to previous simulations of strongly magnetised cores containing no initial turbulence. By performing several simulations we showed that our findings do neither depend on the random realisation of the turbulence field nor the exponent of the turbulence spectrum nor the adopted cooling routine. We also showed that Keplerian discs can be formed even if no overall core rotation is present.

We suggest that the main reason for Keplerian disc formation is the turbulent surroundings of the disc. As there is no coherent rotation structure on scales of several 100 AU, the generation of a toroidal magnetic field is suppressed therefore lowering the magnetic braking efficiency already *before* the gas hits the disc. Furthermore, we find that the magnetic field is highly disordered in the surroundings of the discs, which also reduces the magnetic braking efficiency. At the same time there is a net inwards angular momentum transport by the gas due to local shear flows carrying large amounts of angular momentum.

On scales of the disc itself ( $\leq 100$  AU) significant magnetic flux loss is observable. This enhanced flux loss might be the consequence of numerical diffusion, which is more efficient than in the non-turbulent runs due to the lower infall velocities in the already existing Keplerian disc. We again emphasise that this requires a reduced magnetic braking efficiency already at larger scales so that enough angular momentum is available on scales of 100 AU to build up the disc. Furthermore, we suggest that the reduced magnetic braking efficiency due to an inclination between the magnetic field lines and the rotation axis as observed recently (Hennebelle & Ciardi, 2009; Ciardi & Hennebelle, 2010; Joos et al., 2012) is a special case of a strongly disordered magnetic field as observed in our simulations.

To summarise, our work strongly suggests that the “magnetic braking catastrophe” as reported in numerous papers is more or less a consequence of the highly idealised initial conditions neglecting turbulent motions. A turbulent velocity field in the surroundings of the disc and a disordered magnetic field structure, as obtained with more realistic initial conditions, is enough to allow for the formation of Keplerian discs. Other effects like turbulent reconnection or non-ideal MHD effects seem to act only on scales of the already existing discs. Hence, turbulence alone provides a natural and at the same time very simple mechanism to solve the “magnetic braking catastrophe” problem.

In future work we plan to extend our analysis to an even wider parameter space, in particular allowing for different initial core masses and turbulence strengths. Hence, we will be able to test whether the mechanism explored in this chapter also applies to the entire range of initial conditions typical for star formation. This will be particularly interesting for the case of low-mass protostellar cores, where usually only subsonic turbulence is observed and thus the velocity perturbations – the main driver of the formation of Keplerian discs – are significantly smaller.

## 9. Summary and Outlook

### 9.1. Summary

In this work I have studied the influence of magnetic fields on various aspects of the formation process of massive stars focussing on the earliest stage of protostellar evolution. This was done by means of a number of large-scale numerical simulations of collapsing molecular cloud cores. The cores had a mass of  $100 M_{\odot}$ , were threaded by a magnetic field along the  $z$ -axis varying in strength from simulation to simulation, were rotating with different rotation frequencies around the  $z$ -axis, and partly had a superimposed turbulent velocity field.

#### 9.1.1. Disc formation and protostellar accretion rates

In Chapter 6 I focussed on the effect of magnetic fields and rotation on protostellar accretion rates and on the formation and properties of protostellar discs. Turbulence was not included in these simulations – studying its influence was postponed to Chapter 8. For the non-turbulent simulations I showed that, despite the fact that the initial conditions – regarding the magnetic and rotational energy – cover more than two orders of magnitude in parameter space, the protostellar accretion rates are remarkably constant varying only by a factor of  $\sim 3$ . I attribute this fact to two competing effects of the magnetic field simultaneously counteracting and enhancing accretion.

Another important result of this work is the fact that for non-turbulent cloud cores the formation of Keplerian discs is suppressed for an initial mass-to-flux ratio smaller than 10, i.e. for strong magnetic fields. In these cases I find that sub-Keplerian discs with strong infall motions form. This is in good agreement with numerical work on low-mass star formation by other authors finding a similar critical mass-to-flux ratio of  $\mu = 5 - 10$  below which Keplerian disc formation is suppressed. However, this result seems to conflict with observational results as observations usually show that typical star forming regions have mass-to-flux ratios which are only slightly supercritical, i.e.  $\mu \lesssim 5$ , and that well-defined Keplerian discs are present in a very early protostellar phase already. In contrast, my simulations of strongly magnetised, non-turbulent massive cloud cores as well as related work on low-mass star formation of other authors suggest that there should be no such discs in the earliest phase of star formation. This apparent contradiction between numerical work for both low- and – as shown here – high-mass star formation on the one hand and observational results on the other hand has led to the formulation of the so-called “magnetic braking catastrophe”. This problem has been investigated intensively over the last decade and at first sight also my work seemed to confirm the existence of this problem.

### 9.1.2. Outflow formation

In Chapter 7 of this work I expanded the analysis of the simulations presented in Chapter 6 now focussing on the formation of outflows and the influence of the initial conditions on outflow properties. Firstly, by generalising the magnetohydrodynamical wind theory I derived an analytical criterion from the equations of magnetohydrodynamics with which I can analyse the driving mechanism of outflows. In contrast to the already existing criterion, with this new criterion I can examine the outflows well off from the disc as well as situations with sub-Keplerian disc rotation as observed in a number of my simulations.

Considering the morphology of the outflows in the simulations I find significant differences. Both, well-collimated, fast outflows and slowly expanding, sphere-like outflows are found, where the former are observed for weak initial magnetic fields and fast core rotation and the latter for strong magnetic fields ( $\mu < 10$ ). When relating the outflow morphology to the velocity structure of the underlying protostellar disc that drives the outflow, I showed that for the formation of well-collimated, fast outflows Keplerian discs are required. Applying the newly derived wind criterion, I could show that all outflows observed in the simulations are launched centrifugally from the discs with varying contribution to the driving from the toroidal magnetic field, which is particularly important at greater heights and larger radii. Furthermore, I demonstrated that analysing the field line structure or the toroidal magnetic field strength as often done in literature is not sufficient to unambiguously determine the launching mechanism of the outflow. I also showed that the morphological differences of the outflows are mainly due to the varying strength of the hoop stress responsible for outflow collimation.

I also introduced an evolutionary scenario in which the slow, sphere-like outflows represent a transient feature in the earliest stage of protostellar evolution which might recollapse again to the disc or will be overtaken by a fast, well-collimated jet developing somewhat later.

### 9.1.3. Turbulent disc formation

From the work in the past decade on low-mass star formation and from this work on high-mass star formation it has become clear that there is indeed a problem in forming Keplerian discs in quiescent, i.e. non-turbulent cloud cores. As protostellar discs and their associated outflows represent keystones in our current picture of star formation, the incapability of numerical simulations to produce such discs presents a severe problem in current research. However, in particular the simulations of massive cores studied in Chapter 6 and 7 lack the presence of turbulent motions frequently observed in massive star forming regions. Hence, the aim of Chapter 8 was to remedy this shortcoming and to study the influence of turbulence on the formation of protostellar discs.

By including a supersonic turbulence field in simulations of a strongly magnetised core for which previously no Keplerian disc was observed, I now find that Keplerian discs are formed. This result remains unaltered when changing the initial turbulence field or even when completely removing the overall core rotation. I showed that in the surroundings of the Keplerian discs the magnetic field is highly disordered, which prevents an effi-

cient coupling of the inner, fast rotating disc to the outer, slowly rotating environment so that the magnetic braking efficiency is reduced significantly. Moreover, the lack of a coherently rotating structure in the surroundings of the disc hampers the build-up of a toroidal magnetic field thus also reducing the effect of magnetic braking. As simultaneously local shear flows created by the turbulent motions provide a high amount of angular momentum, this results in the formation of Keplerian discs. This mechanism of a turbulence-induced formation of Keplerian discs explored in this work presents a powerful way to circumvent the “magnetic braking catastrophe”.

To summarise, I showed that the presumable magnetic braking problem, which I already discussed in the beginning of this work, is solved in the end in a very natural manner, simply by including turbulent motions.

## 9.2. Outlook

### 9.2.1. Turbulent disc formation for a wider mass range

The turbulence-mediated disc formation process discovered in this work is most likely the most important aspect of this thesis. However, so far this mechanism is tested only for a fixed core mass of  $100 M_{\odot}$  and a fixed turbulence strength. As this mechanism represents an important aspect of the star formation theory, i.e. it allows for the formation of well-defined, Keplerian discs at a very early stage already, it is of great importance to expand this study to a wider range of initial conditions. Here, in particular the initial mass of the core is of great interest as stars form in cores with masses ranging from a few solar masses up to a few  $1000 M_{\odot}$ . As usually the turbulence strength varies with the size and hence the mass of prestellar cores, a variation of the core mass would be particularly interesting for low-mass cores. Here the turbulence is in general observed to be subsonic. Hence, the velocity fluctuations, which are the main driver of the formation of Keplerian discs as shown in this work, are much weaker and it will be of interest to see whether in this case turbulence can still aid the formation of Keplerian discs or not.

### 9.2.2. Protostellar outflows in turbulent cores

So far I have not considered the outflows driven from the discs in the turbulent cores. In this context it will be of interest to determine global outflow properties like mass or momentum and to see whether the analytical outflow criterion derived in this work is also applicable for such a turbulent environment. Moreover, since the turbulent simulations represent the actual initial conditions of massive star formation much better than the non-turbulent simulations, it would be interesting to compare the outflow properties of the simulations to that of observations.

Furthermore, outflow structures observed in massive star forming regions are often much more complex and less well-ordered than those in low-mass star forming regions. Hence, it is worthwhile to test whether outflows in the turbulence simulations can reproduce this particular structure of massive outflows. In this context, in particular the post-processing of the data with a radiation transfer code would be desirable to produce

synthetic observations which could directly be compared to observational results. This is of particular importance due to the availability of new data with ever higher resolution provided by modern telescopes like e.g. the Atacama Large Millimeter/submillimeter Array.

### 9.2.3. Subgrid models for protostellar feedback

A problem with the direct comparison of the simulation data presented here to observational data is the fact that observations of massive star forming regions usually refer to protostellar ages of a few  $10^4 - 10^5$  yr. Despite the remarkably long integration times in my simulations of up to 15 kyr after the formation of the first sink particle, such timescales are up to one order of magnitude longer than what is obtained in this work. This leads to the requirement of performing simulations over much longer physical timescales. However, due to the very high spatial resolution used in the simulations this would create enormous computational costs requiring several million CPU-hours per simulation. A natural way out of this dilemma would be to use a coarser resolution. However, this in turn might affect the formation of protostellar discs and thus also the self-consistent generation of outflows. If due to computational time limitations the resolution is relatively coarse, probably no proper discs and associated outflows can be formed anymore whereas for higher resolution they would be formed. This problem can be circumvented by coupling a subgrid outflow model to the sink particles routine. This subgrid model would model the ejection of gas from the protostellar disc due to an outflow. With such an outflow subgrid model and a coarser spatial resolution it would be possible to follow the simulations over a longer physical timescale while keeping the computational costs on an acceptable level.

At later evolutionary phases also feedback from the radiation emitted by the protostars will become important. By heating up the gas in the core, the radiation changes the fragmentation properties of the core itself as well as of the protostellar discs. Furthermore, by exerting a radiation pressure on the infalling gas also the accretion behaviour might change. In this context it would be of particular interest to see how efficiently an outflow can channel the radiation along the polar directions. Hence, on a long term view it would also be desirable to include the possibility to handle radiation transfer in FLASH.

# A. Appendix

## A.1. A resolution study for run 26-4

Here we present a resolution study for run 26-4 (see Table 5.1 for the initial conditions) by comparing this simulation with two more runs with identical initial conditions but a maximum spatial resolution varied by a factor of 4 in either direction. The initial resolution of the two other runs is identical to that in run 26-4, i.e. in the beginning the mesh in the core has a spacing of 302 AU. We list the runs and their corresponding parameters in Table A.1. The critical value of the density above which sink particles are created is adapted in accordance with the resolution. For all runs performed the refinement criterion applied guarantees that the disc region is resolved on the highest level used. In particular, we focus in this analysis on accretion properties and radial profiles of different quantities in the disc. Due to computational cost reasons caused by the higher spatial resolution run 26-4-H is followed for 2000 yr only. Hence, we compare the results of the three runs at this time.

First, we consider radial profiles of the density, temperature, and velocity in the disc. The quantities in each run are averaged azimuthally and vertically in the disc with a height of 47 AU above and below the midplane. The accretion shock occurring at  $\sim 150$  AU in the density profile (top left panel of Fig. A.1) is clearly resolved in the runs 26-4-H and 26-4. In run 26-4-L, however, the shock is somewhat smoothed out due to the limited resolution. Hence, a resolution of 4.7 AU seems required to properly resolve the accretion shock. Within the accretion shock, however, the density increases with resolution. We attribute this to the fact that the vertical structure of the disc is not fully resolved at least in the runs 26-4 and 26-4-L. Here in large parts the vertical disc height is represented by a few grid cells only (compare Fig. 6.8). Therefore, to fully resolve the vertical disc structure, a higher resolution, probably even above that in run 26-4-H, would be needed, which is currently not feasible.

Run	$dx$ (AU)	$\rho_{\text{crit}}$ ( $10^{-12}$ g cm $^{-3}$ )	$t_0$ (kyr)	$M_{\text{sink}}$ ( $M_{\odot}$ )
26-4-L	18.9	0.0657	15.1	1.42
26-4	4.7	1.78	15.2	1.05
26-4-H	1.2	114	15.3	1.03

**Table A.1.:** Performed simulations for the resolution study with maximum spatial resolution, threshold density for sink particle creation, formation time of the first sink particle and total accreted mass after 2000 yr.

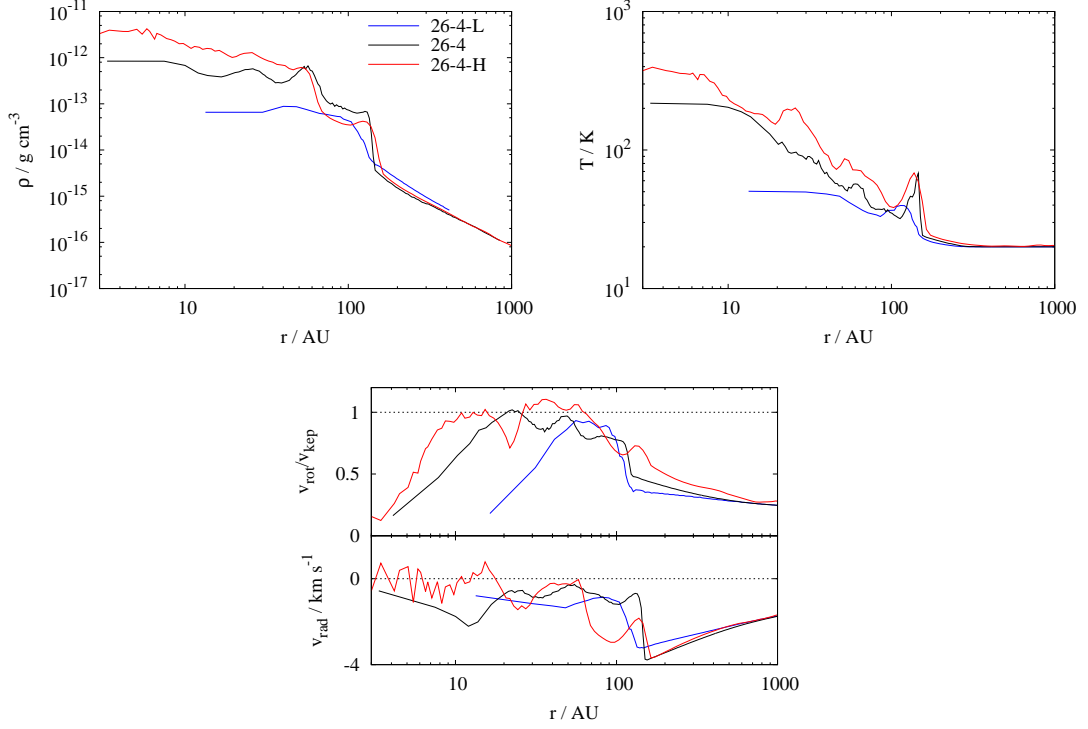


**Figure A.1.:** Radial profiles of density (top left), temperature (top right), and velocity structure (bottom) after 2000 yr for the runs 26-4-L, 26-4 and 26-4-H with a maximum spatial resolution of  $dx = 18.9$  AU, 4.7 AU and 1.2 AU, respectively. The accretion shock seen in the density and temperature is not well resolved for run 26-4-L.

A similar result holds for the temperature profiles as well (top right panel of Fig. A.1). The temperature jump at the accretion shock seems to be reasonably well resolved in run 26-4 whereas in run 26-4-L it is smoothed out markedly. The higher the final resolution the higher are the temperatures within the accretion shock. This is due to the strong coupling of temperature and density above  $10^{-13}$  g cm $^{-3}$ , where the gas gets optically thick resulting in higher temperatures at higher gas densities. Different densities and temperatures in the disc will also influence the susceptibility of the disc for fragmentation. In general, fragmentation is delayed with lower spatial resolution due to the lower densities in the disc. Whereas for run 26-4-L further fragmentation of the disc occurs not until 6900 yr after the formation of the first sink particle, for run 26-4 and 26-4-H the disc starts to fragment already after 2600 yr and 1500 yr, respectively.

Next, we analyse the velocity structure in the disc (see bottom panel of Fig. A.1). In run 26-4-L no Keplerian disc has built up yet. However, we mention that in its further evolution the rotation reaches Keplerian velocities as well. In run 26-4 the rotation is already Keplerian up to a radius of  $\sim 60$  AU in good agreement with run 26-4-H. Furthermore, the comparison between both runs shows that in run 26-4 the decline in  $v_{\text{rot}}/v_{\text{kep}}$  at 20 AU is most likely a resolution effect as in run 26-4-H this decline occurs

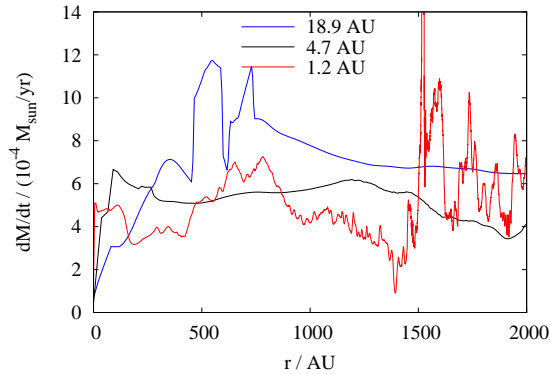


**Figure A.2.:** Total accretion rate for the first 2000 yr in the runs 26-4-L, 26-4 and 26-4-H. The lower the resolution the higher are the mean accretion rates (respectively the totally accreted masses in Table A.1) although there is a clear convergence towards higher resolution.

at a roughly three times smaller radius of  $\sim 8$  AU. This supports the statement made in Section 6.2.2 that the inner 10 AU in runs with a resolution of 4.7 AU are strongly affected by numerical resolution. The radial velocities of all three runs agree qualitatively reasonably well at radii larger 10 AU despite some minor quantitative details. Hence, we conclude that regarding the velocity structure in the midplane run 26-4 is reasonably well converged at radii larger than 10 AU, i.e. as soon as the radial distance is resolved with more than a few grid cells.

In Fig. A.2 we show the time evolution of the total accretion rate for the three runs considered. In run 26-4-H two more sink particles are created after roughly 1500 yr, which cause the large variations in the accretion rate. In general, however, the accretion rates of the three runs are of the same order of magnitude. It can also be inferred from Table A.1 that the total accreted mass and accordingly the mean accretion rate decreases with increasing spatial resolution. The accretion rate of run 26-4-L is higher than that of run 26-4 by about 35%. We therefore conclude that regarding accretion properties run 26-4-L is not yet fully converged. The difference in accreted mass between run 26-4-H and run 26-4, however, is of the order of 2% only and thus significantly lower than the difference between run 26-4-L and run 26-4. Hence, there is a clear convergence of the accretion rates with increasing resolution and we conclude that a resolution of 4.7 AU is sufficiently high to properly describe the accretion properties of the protostars. From the formation time  $t_0$  listed in Table A.1 it can also be inferred that  $t_0$  increases with spatial resolution. This behaviour is expected as for higher resolution sink particles are created at higher densities and thus later times during the collapse. However, the relative time differences are of the order of 1% only and can therefore be considered as negligible.

In summary, one can see that a resolution of 4.7 AU is sufficiently high to properly follow protostellar accretion rates, resolve the accretion shock at the edge of the disc, and correctly display the velocity structure in the disc down to radii of about 10 – 15 AU. In contrast, run 26-4-L with a resolution of 18.9 AU reveals significant differences from run 26-4-H showing that is not yet converged. However, also run 26-4 seems to be not fully

converged regarding to the density and temperature structure in the disc. We attribute this partly to the poor spatial resolution of the vertical disc structure. Hence, a higher resolution, probably even above the one used in run 26-4-H, would be necessary to reach convergence regarding this point. However, due to significantly higher computational costs this has not been feasible so far wherefore a spatial resolution of 4.7 AU is used throughout Chapter 6 and 7. This particular choice was also motivated physically as we want to resolve the first core. As the first core builds up as soon as the gas starts to get optically thick, which happens around  $10^{-13}$  g cm<sup>-3</sup> (see Section 5.1.2), the Jeans length at densities above this threshold has to be resolved, which requires a resolution of a few AU.

# Acknowledgements

Mein größter Dank gilt meinen Betreuern Robi Banerjee und Ralf Klessen, die mich während meiner Doktorandenzeit fortwährend unterstützt haben. Die vielen Diskussionen in dieser Zeit boten mir stets neue Impulse und Motivation für meine Arbeit und haben mir einen umfassenderen Einblick in das Thema der Sternentstehung ermöglicht. Auch möchte ich mich bei beiden für die Möglichkeit und Unterstützung bedanken, einen Teil meiner Doktorandenzeit in Kanada zu absolvieren.

Ich möchte mich auch bei Christian Fendt für die Diskussionen im Rahmen der Betreuungskomitee-Treffen bedanken, die mir vor allem bei der Verständnis der Jet-Theorie von großer Hilfe waren. Zudem möchte ich ihm auch als IMPRS-Verantwortlicher danken sowie der HGSP für deren finanzielle Unterstützung meines Kanadaaufenthalts.

Mein weiterer Dank gilt meinen Kollegen in Heidelberg. Hier möchte ich besonders Philipp Girichidis danken für seine Unterstützung, was programmiertechnische und astrophysikalische Probleme angeht, vor allem aber auch für das großartige und freundschaftliche Arbeitsklima in unserem Büro. Des Weiteren danke meinen zeitweiligen Bürokollegen Christoph Federrath, Lukas Konstandin und Erik Bertram für das sehr angenehme Arbeitsklima sowie für die zahlreichen Diskussionen über sink-Teilchen und interstellare Turbulenz. Ich möchte mich hiermit auch bei allen anderen Kollegen am ITA für das stets sehr angenehme Arbeitsklima und die vielen interessanten Diskussionen bedanken.

Mein ganz spezieller Dank gilt Ralph Pudritz an der McMaster Universität in Hamilton, der mir meinen Aufenthalt in Kanada maßgeblich ermöglicht hat und mich dort während des halben Jahres betreut und unterstützt hat. Sein Wissen über die Jet-Theorie hat viel zum Gelingen der Arbeit beigetragen. An dieser Stelle möchte ich auch meinen Kollegen in Hamilton danken, vor allem Mikhail Klassen, Dennis Duffin, Kim Figueira, Leo van Nierop und Mischa Thesberg für ihre freundschaftliche Unterstützung, die meinen Aufenthalt zu einem vollen Erfolg gemacht hat.

Ich möchte mich auch bei meinen Kollegen Lars Buntmeyer, Adam Dybulla und Bastian Körtgen in Hamburg für die gute Aufnahme an der Sternwarte, die vielen und hilfreichen physikalischen Diskussionen sowie das sehr angenehme Arbeitsklima bedanken.

Am meisten möchte ich mich schließlich noch bei meinen Eltern bedanken, die mich während meiner Doktorarbeit und auch während meines Studium immer tatkräftig unterstützt haben. Ohne sie wäre diese Arbeit in dieser Form sicherlich nicht möglich gewesen.



# Bibliography

- Allen, A., Li, Z., & Shu, F. H. 2003, *ApJ*, 599, 363
- Andre, P., Ward-Thompson, D., & Barsony, M. 2000, Protostars and Planets IV, 59
- Appl, S. & Camenzind, M. 1992, *A&A*, 256, 354
- Arce, H. G. & Goodman, A. A. 2001, *ApJ*, 554, 132
- Arce, H. G., Shepherd, D., Gueth, F., Lee, C., Bachiller, R., Rosen, A., & Beuther, H. 2007, Protostars and Planets V, 245
- Artymowicz, P. & Lubow, S. H. 1996, *ApJ*, 467, L77+
- Bachiller, R. 1996, *ARA&A*, 34, 111
- Banerjee, R., Klessen, R. S., & Fendt, C. 2007, *ApJ*, 668, 1028
- Banerjee, R. & Pudritz, R. E. 2006, *ApJ*, 641, 949
- . 2007, *ApJ*, 660, 479
- Banerjee, R., Pudritz, R. E., & Anderson, D. W. 2006, *MNRAS*, 373, 1091
- Banerjee, R., Pudritz, R. E., & Holmes, L. 2004, *MNRAS*, 355, 248
- Baraffe, I. & Chabrier, G. 2010, *A&A*, 521, A44+
- Bastian, N., Covey, K. R., & Meyer, M. R. 2010, *ARA&A*, 48, 339
- Bate, M. R. 2009, *MNRAS*, 397, 232
- Bate, M. R. & Bonnell, I. A. 1997, *MNRAS*, 285, 33
- Baumgardt, H. & Klessen, R. S. 2011, *MNRAS*, 413, 1810
- Beck, R. 2012, *Space Sci. Rev.*, 166, 215
- Belloche, A., André, P., Despois, D., & Blindler, S. 2002, *A&A*, 393, 927
- Beltrán, M. T., Cesaroni, R., Codella, C., Testi, L., Furuya, R. S., & Olmi, L. 2006, *Nature*, 443, 427
- Beltrán, M. T., Cesaroni, R., Zhang, Q., Galván-Madrid, R., Beuther, H., Fallscheer, C., Neri, R., & Codella, C. 2011, *A&A*, 532, A91+

- Bergin, E. A. & Tafalla, M. 2007, *ARA&A*, 45, 339
- Beuther, H., Churchwell, E. B., McKee, C. F., & Tan, J. C. 2007, *Protostars and Planets V*, 165
- Beuther, H., Schilke, P., & Gueth, F. 2004, *ApJ*, 608, 330
- Beuther, H., Schilke, P., Gueth, F., McCaughrean, M., Andersen, M., Sridharan, T. K., & Menten, K. M. 2002a, *A&A*, 387, 931
- Beuther, H., Schilke, P., Menten, K. M., Motte, F., Sridharan, T. K., & Wyrowski, F. 2002b, *ApJ*, 566, 945
- Beuther, H., Schilke, P., Sridharan, T. K., Menten, K. M., Walmsley, C. M., & Wyrowski, F. 2002c, *A&A*, 383, 892
- Beuther, H., Schilke, P., & Stanke, T. 2003, *A&A*, 408, 601
- Beuther, H. & Shepherd, D. 2005, in *Cores to Clusters: Star Formation with Next Generation Telescopes*, ed. M. S. N. Kumar, M. Tafalla, & P. Caselli, 105–119
- Beuther, H. & Sridharan, T. K. 2007, *ApJ*, 668, 348
- Beuther, H., Tackenberg, J., Linz, H., Henning, T., Krause, O., Ragan, S., Nielbock, M., Launhardt, R., Schmiedeke, A., Schuller, F., Carlhoff, P., Nguyen-Luong, Q., & Sakai, T. 2012, *A&A*, 538, A11
- Beuther, H., Vlemmings, W. H. T., Rao, R., & van der Tak, F. F. S. 2010, *ApJ*, 724, L113
- Blandford, R. D. & Payne, D. G. 1982, *MNRAS*, 199, 883
- Bonnell, I. A., Bate, M. R., Clarke, C. J., & Pringle, J. E. 1997, *MNRAS*, 285, 201
- . 2001, *MNRAS*, 323, 785
- Bonnell, I. A., Bate, M. R., & Zinnecker, H. 1998, *MNRAS*, 298, 93
- Bouchut, F., Klingenberg, C., & Waagan, K. 2007, *Numerische Mathematik*, 108, 7, 10.1007/s00211-007-0108-8
- . 2010, *Numerische Mathematik*, 115, 647, 10.1007/s00211-010-0289-4
- Brandenburg, A. & Zweibel, E. G. 1994, *ApJ*, 427, L91
- Cabrit, S., Raga, A., & Gueth, F. 1997, in *IAU Symposium, Vol. 182, Herbig-Haro Flows and the Birth of Stars*, ed. B. Reipurth & C. Bertout, 163–180
- Caselli, P. & Myers, P. C. 1995, *ApJ*, 446, 665

- 
- Cesaroni, R., Galli, D., Lodato, G., Walmsley, C. M., & Zhang, Q. 2007, *Protostars and Planets V*, 197
- Chabrier, G. 2005, in *Astrophysics and Space Science Library*, Vol. 327, *The Initial Mass Function 50 Years Later*, ed. E. Corbelli, F. Palla, & H. Zinnecker, 41
- Chandrasekhar, S. 1956, *ApJ*, 124, 232
- Chandrasekhar, S. & Fermi, E. 1953, *ApJ*, 118, 113
- Chini, R., Hoffmeister, V., Kimeswenger, S., Nielbock, M., Nürnberger, D., Schmidtbreick, L., & Sterzik, M. 2004, *Nature*, 429, 155
- Ciardi, A. & Hennebelle, P. 2010, *MNRAS*, 409, L39
- Clark, P. C., Klessen, R. S., & Bonnell, I. A. 2007, *MNRAS*, 379, 57
- Commerçon, B., Hennebelle, P., Audit, E., Chabrier, G., & Teyssier, R. 2010, *A&A*, 510, L3
- Commerçon, B., Hennebelle, P., & Henning, T. 2011, *ApJ*, 742, L9
- Crutcher, R. M. 1999, *ApJ*, 520, 706
- Crutcher, R. M., Wandelt, B., Heiles, C., Falgarone, E., & Troland, T. H. 2010, *ApJ*, 725, 466
- Csengeri, T., Bontemps, S., Schneider, N., Motte, F., & Dib, S. 2011, *A&A*, 527, A135
- Cunningham, A. J., Klein, R. I., Krumholz, M. R., & McKee, C. F. 2011, *ApJ*, 740, 107
- Curran, R. L. & Chrysostomou, A. 2007, *MNRAS*, 382, 699
- Dapp, W. B. & Basu, S. 2010, *A&A*, 521, L56+
- Dapp, W. B., Basu, S., & Kunz, M. W. 2012, *A&A*, 541, A35
- Di Francesco, J., Myers, P. C., Wilner, D. J., Ohashi, N., & Mardones, D. 2001, *ApJ*, 562, 770
- Dobbs, C. L., Bonnell, I. A., & Clark, P. C. 2005, *MNRAS*, 360, 2
- Duffin, D. F. & Pudritz, R. E. 2009, *ApJ*, 706, L46
- Duffin, D. F., Pudritz, R. E., Seifried, D., Banerjee, R., & Klessen, R. S. 2012, in prep.
- Duquennoy, A. & Mayor, M. 1991, *A&A*, 248, 485
- Egan, M. P., Shipman, R. F., Price, S. D., Carey, S. J., Clark, F. O., & Cohen, M. 1998, *ApJ*, 494, L199

- Elmegreen, B. G. & Scalo, J. 2004, *ARA&A*, 42, 211
- Enoch, M. L., Corder, S., Duchêne, G., Bock, D. C., Bolatto, A. D., Culverhouse, T. L., Kwon, W., Lamb, J. W., Leitch, E. M., Marrone, D. P., Muchovej, S. J., Pérez, L. M., Scott, S. L., Teuben, P. J., Wright, M. C. H., & Zauderer, B. A. 2011, *ApJS*, 195, 21
- Enoch, M. L., Corder, S., Dunham, M. M., & Duchêne, G. 2009, *ApJ*, 707, 103
- Falgarone, E., Troland, T. H., Crutcher, R. M., & Paubert, G. 2008, *A&A*, 487, 247
- Federrath, C., Banerjee, R., Clark, P. C., & Klessen, R. S. 2010, *ApJ*, 713, 269
- Federrath, C., Sur, S., Schleicher, D. R. G., Banerjee, R., & Klessen, R. S. 2011, *ApJ*, 731, 62
- Fernández-López, M., Girart, J. M., Curiel, S., Gómez, Y., Ho, P. T. P., & Patel, N. 2011, *AJ*, 142, 97
- Fontani, F., Caselli, P., Zhang, Q., Brand, J., Busquet, G., & Palau, A. 2012, *A&A*, 541, A32
- Frisch, U. 1995, Turbulence. The legacy of A. N. Kolmogorov.
- Fryxell, B., Olson, K., Ricker, P., Timmes, F. X., Zingale, M., Lamb, D. Q., MacNeice, P., Rosner, R., Truran, J. W., & Tufo, H. 2000, *ApJS*, 131, 273
- Fuller, G. A., Zijlstra, A. A., & Williams, S. J. 2001, *ApJ*, 555, L125
- Girart, J. M., Beltrán, M. T., Zhang, Q., Rao, R., & Estalella, R. 2009, *Science*, 324, 1408
- Girichidis, P., Federrath, C., Banerjee, R., & Klessen, R. S. 2011, *MNRAS*, 413, 2741
- . 2012, *MNRAS*, 420, 613
- Goldreich, P. & Lynden-Bell, D. 1965, *MNRAS*, 130, 125
- Goldsmith, P. F. 2001, *ApJ*, 557, 736
- Goodman, A. A., Benson, P. J., Fuller, G. A., & Myers, P. C. 1993, *ApJ*, 406, 528
- Grasso, D. & Rubinstein, H. R. 2001, *Phys. Rep.*, 348, 163
- Heiles, C. & Crutcher, R. 2005, in *Lecture Notes in Physics*, Berlin Springer Verlag, Vol. 664, *Cosmic Magnetic Fields*, ed. R. Wielebinski & R. Beck, 137
- Heiles, C. & Troland, T. H. 2005, *ApJ*, 624, 773
- Hennebelle, P. & Ciardi, A. 2009, *A&A*, 506, L29

- 
- Hennebelle, P., Commerçon, B., Joos, M., Klessen, R. S., Krumholz, M., Tan, J. C., & Teyssier, R. 2011, *A&A*, 528, A72+
- Hennebelle, P. & Fromang, S. 2008, *A&A*, 477, 9
- Hennebelle, P. & Teyssier, R. 2008, *A&A*, 477, 25
- Heyer, M. H. & Brunt, C. M. 2004, *ApJ*, 615, L45
- Hirota, T., Bushimata, T., Choi, Y. K., Honma, M., Imai, H., Iwadate, K., Jike, T., Kamenō, S., Kameya, O., Kamohara, R., Kan-Ya, Y., Kawaguchi, N., Kijima, M., Kim, M. K., Kobayashi, H., Kuji, S., Kurayama, T., Manabe, S., Maruyama, K., Matsui, M., Matsumoto, N., Miyaji, T., Nagayama, T., Nakagawa, A., Nakamura, K., Oh, C. S., Omodaka, T., Oyama, T., Sakai, S., Sasao, T., Sato, K., Sato, M., Shibata, K. M., Shintani, M., Tamura, Y., Tsushima, M., & Yamashita, K. 2007, *PASJ*, 59, 897
- Hosking, J. G. & Whitworth, A. P. 2004, *MNRAS*, 347, 1001
- Joos, M., Hennebelle, P., & Ciardi, A. 2012, *A&A*, 543, A128
- Jørgensen, J. K., van Dishoeck, E. F., Visser, R., Bourke, T. L., Wilner, D. J., Lommen, D., Hogerheijde, M. R., & Myers, P. C. 2009, *A&A*, 507, 861
- Kahn, F. D. 1974, *A&A*, 37, 149
- Kim, W. & Ostriker, E. C. 2001, *ApJ*, 559, 70
- Kirk, J. M., Ward-Thompson, D., & Crutcher, R. M. 2006, *MNRAS*, 369, 1445
- Klaassen, P. D., Wilson, C. D., Keto, E. R., Zhang, Q., Galván-Madrid, R., & Liu, H.-Y. B. 2011, *A&A*, 530, A53+
- Klein, R. I., Inutsuka, S.-I., Padoan, P., & Tomisaka, K. 2007, *Protostars and Planets V*, 99
- Klessen, R. S. 2001, *ApJ*, 550, L77
- Koch, P. M., Tang, Y.-W., & Ho, P. T. P. 2012, *ApJ*, 747, 79
- Kolmogorov, A. 1941, *Akademiia Nauk SSSR Doklady*, 30, 301
- Krasnopolsky, R., Li, Z.-Y., & Shang, H. 2010, *ApJ*, 716, 1541
- . 2011, *ApJ*, 733, 54
- Kratter, K. M., Matzner, C. D., Krumholz, M. R., & Klein, R. I. 2010, *ApJ*, 708, 1585
- Kroupa, P. 2001, *MNRAS*, 322, 231
- Krumholz, M. R., Cunningham, A. J., Klein, R. I., & McKee, C. F. 2010, *ApJ*, 713, 1120

- Krumholz, M. R., Klein, R. I., & McKee, C. F. 2007, *ApJ*, 656, 959
- Krumholz, M. R., Klein, R. I., McKee, C. F., Offner, S. S. R., & Cunningham, A. J. 2009, *Science*, 323, 754
- Krumholz, M. R., McKee, C. F., & Klein, R. I. 2005, *ApJ*, 618, L33
- Kuiper, R., Klahr, H., Beuther, H., & Henning, T. 2010, *ApJ*, 722, 1556
- . 2011, *ApJ*, 732, 20
- Lada, C. J. & Fich, M. 1996, *ApJ*, 459, 638
- Lai, S.-P., Crutcher, R. M., Girart, J. M., & Rao, R. 2001, *ApJ*, 561, 864
- Larson, R. B. 1969, *MNRAS*, 145, 271
- . 1981, *MNRAS*, 194, 809
- Lazarian, A. & Vishniac, E. T. 1999, *ApJ*, 517, 700
- Li, Z.-Y., Krasnopolsky, R., & Shang, H. 2011, *ApJ*, 738, 180
- Lynden-Bell, D. 1996, *MNRAS*, 279, 389
- . 2003, *MNRAS*, 341, 1360
- Mac Low, M.-M. & Klessen, R. S. 2004, *Reviews of Modern Physics*, 76, 125
- Machida, M. N., Inutsuka, S.-i., & Matsumoto, T. 2008, *ApJ*, 676, 1088
- Machida, M. N., Inutsuka, S.-I., & Matsumoto, T. 2011, *PASJ*, 63, 555
- Machida, M. N., Matsumoto, T., Hanawa, T., & Tomisaka, K. 2005, *MNRAS*, 362, 382
- Mason, B. D., Gies, D. R., Hartkopf, W. I., Bagnuolo, Jr., W. G., ten Brummelaar, T., & McAlister, H. A. 1998, *AJ*, 115, 821
- Matsumoto, T. & Tomisaka, K. 2004, *ApJ*, 616, 266
- Maury, A. J., André, P., Hennebelle, P., Motte, F., Stamatellos, D., Bate, M., Belloche, A., Duchêne, G., & Whitworth, A. 2010, *A&A*, 512, A40
- McKee, C. F. & Ostriker, E. C. 2007, *ARA&A*, 45, 565
- McKee, C. F. & Tan, J. C. 2002, *Nature*, 416, 59
- . 2003, *ApJ*, 585, 850
- Mellon, R. R. & Li, Z. 2008, *ApJ*, 681, 1356
- . 2009, *ApJ*, 698, 922

- 
- Mestel, L. 1961, *MNRAS*, 122, 473
- Michel, F. C. 1969, *ApJ*, 158, 727
- Miettinen, O. 2012a, *A&A*, 540, A104
- . 2012b, *A&A*, 542, A101
- Miller, G. E. & Scalo, J. M. 1979, *ApJS*, 41, 513
- Moeckel, N. & Bally, J. 2007, *ApJ*, 656, 275
- Mouschovias, T. C. & Paleologou, E. V. 1979, *ApJ*, 230, 204
- . 1980, *ApJ*, 237, 877
- Mouschovias, T. C. & Spitzer, Jr., L. 1976, *ApJ*, 210, 326
- Nakamura, F. & Li, Z.-Y. 2007, *ApJ*, 662, 395
- Nakano, T., Nishi, R., & Umebayashi, T. 2002, *ApJ*, 573, 199
- Neufeld, D. A. & Kaufman, M. J. 1993, *ApJ*, 418, 263
- Neufeld, D. A., Lepp, S., & Melnick, G. J. 1995, *ApJS*, 100, 132
- Olson, K. M., MacNeice, P., Fryxell, B., Ricker, P., Timmes, F. X., & Zingale, M. 1999, in *Bulletin of the American Astronomical Society*, Vol. 31, American Astronomical Society Meeting Abstracts, 1430
- Ouyed, R., Clarke, D. A., & Pudritz, R. E. 2003, *ApJ*, 582, 292
- Padmanabhan, P. 2000, *Theoretical astrophysics. Vol.1: Astrophysical processes*
- Padoan, P., Nordlund, Å., Rögnvaldsson, Ö. E., & Goodman, A. 2001, in *Astronomical Society of the Pacific Conference Series*, Vol. 243, *From Darkness to Light: Origin and Evolution of Young Stellar Clusters*, ed. T. Montmerle & P. André, 279–+
- Pelletier, G. & Pudritz, R. E. 1992, *ApJ*, 394, 117
- Peretto, N. & Fuller, G. A. 2010, *ApJ*, 723, 555
- Peters, T., Banerjee, R., Klessen, R. S., & Mac Low, M. 2011, *ApJ*, 729, 72
- Peters, T., Banerjee, R., Klessen, R. S., Mac Low, M., Galván-Madrid, R., & Keto, E. R. 2010a, *ApJ*, 711, 1017
- Peters, T., Klessen, R. S., Mac Low, M., & Banerjee, R. 2010b, *ApJ*, 725, 134
- Pinsonneault, M. H. & Stanek, K. Z. 2006, *ApJ*, 639, L67

- Pirogov, L., Zinchenko, I., Caselli, P., Johansson, L. E. B., & Myers, P. C. 2003, *A&A*, 405, 639
- Pirogov, L. E. 2009, *Astronomy Reports*, 53, 1127
- Preibisch, T., Ratzka, T., Gehring, T., Ohlendorf, H., Zinnecker, H., King, R. R., McCaughrean, M. J., & Lewis, J. R. 2011, *A&A*, 530, A40
- Price, D. J. & Bate, M. R. 2007, *MNRAS*, 377, 77
- Price, D. J., Tricco, T. S., & Bate, M. R. 2012, *MNRAS*, L435
- Pudritz, R. E. & Norman, C. A. 1986, *ApJ*, 301, 571
- Rathborne, J. M., Jackson, J. M., & Simon, R. 2006, *ApJ*, 641, 389
- Ray, T. P. 1981, *MNRAS*, 196, 195
- Ren, J. Z., Liu, T., Wu, Y., & Li, L. 2011, *MNRAS*, 415, L49
- Richer, J. S., Shepherd, D. S., Cabrit, S., Bachiller, R., & Churchwell, E. 2000, *Protostars and Planets IV*, 867
- Ridge, N. A. & Moore, T. J. T. 2001, *A&A*, 378, 495
- Robitaille, T. P. & Whitney, B. A. 2010, *ApJ*, 710, L11
- Sadavoy, S. I., di Francesco, J., André, P., Pezzuto, S., Bernard, J.-P., Bontemps, S., Bressert, E., Chitsazzadeh, S., Fallscheer, C., Hennemann, M., Hill, T., Martin, P., Motte, F., Nguyen Luong, Q., Peretto, N., Reid, M., Schneider, N., Testi, L., White, G. J., & Wilson, C. 2012, *A&A*, 540, A10
- Salpeter, E. E. 1955, *ApJ*, 121, 161
- Santos-Lima, R., de Gouveia Dal Pino, E. M., & Lazarian, A. 2012, *ApJ*, 747, 21
- Schmeja, S. & Klessen, R. S. 2004, *A&A*, 419, 405
- Schneider, N., Csengeri, T., Hennemann, M., Motte, F., Didelon, P., Federrath, C., Bontemps, S., Di Francesco, J., Arzoumanian, D., Minier, V., André, P., Hill, T., Zavagno, A., Nguyen-Luong, Q., Attard, M., Bernard, J.-P., Elia, D., Fallscheer, C., Griffin, M., Kirk, J., Klessen, R., Könyves, V., Martin, P., Men'shchikov, A., Palmeirim, P., Peretto, N., Pestalozzi, M., Russeil, D., Sadavoy, S., Soubie, T., Testi, L., Tremblin, P., Ward-Thompson, D., & White, G. 2012, *A&A*, 540, L11
- Seifried, D., Banerjee, R., Klessen, R. S., Duffin, D., & Pudritz, R. E. 2011, *MNRAS*, 417, 1054
- Seifried, D., Banerjee, R., Pudritz, R. E., & Klessen, R. S. 2012a, *MNRAS*, 423, L40

- Seifried, D., Pudritz, R. E., Banerjee, R., Duffin, D., & Klessen, R. S. 2012b, *MNRAS*, 422, 347
- Semenov, D., Henning, T., Helling, C., Ilgner, M., & Sedlmayr, E. 2003, *A&A*, 410, 611
- Shepherd, D. S., Claussen, M. J., & Kurtz, S. E. 2001, *Science*, 292, 1513
- Shi, H., Zhao, J.-H., & Han, J. L. 2010, *ApJ*, 718, L181
- Shu, F. H. 1992, *The physics of astrophysics. Volume II: Gas dynamics.*
- Shu, F. H., Najita, J. R., Shang, H., & Li, Z.-Y. 2000, *Protostars and Planets IV*, 789
- Sollins, P. K., Hunter, T. R., Battat, J., Beuther, H., Ho, P. T. P., Lim, J., Liu, S. Y., Ohashi, N., Sridharan, T. K., Su, Y. N., Zhao, J.-H., & Zhang, Q. 2004, *ApJ*, 616, L35
- Solomon, P. M., Rivolo, A. R., Barrett, J., & Yahil, A. 1987, *ApJ*, 319, 730
- Spitzer, L. 1968, *Diffuse matter in space*
- Spruit, H. C. 1996, in *NATO ASIC Proc. 477: Evolutionary Processes in Binary Stars*, ed. R. A. M. J. Wijers, M. B. Davies, & C. A. Tout, 249–286
- Sridharan, T. K., Beuther, H., Saito, M., Wyrowski, F., & Schilke, P. 2005, *ApJ*, 634, L57
- Staff, J. E., Niebergal, B. P., Ouyed, R., Pudritz, R. E., & Cai, K. 2010, *ApJ*, 722, 1325
- Surcis, G., Vlemmings, W. H. T., Curiel, S., Hutawarakorn Kramer, B., Torrelles, J. M., & Sarma, A. P. 2011, *A&A*, 527, A48+
- Tackenberg, J., Beuther, H., Henning, T., Schuller, F., Wienen, M., Motte, F., Wyrowski, F., Bontemps, S., Bronfman, L., Menten, K., Testi, L., & Lefloch, B. 2012, *A&A*, 540, A113
- Tang, Y.-W., Ho, P. T. P., Koch, P. M., Girart, J. M., Lai, S.-P., & Rao, R. 2009, *ApJ*, 700, 251
- Testi, L. & Sargent, A. I. 1998, *ApJ*, 508, L91
- Tilley, D. A. & Pudritz, R. E. 2007, *MNRAS*, 382, 73
- Tomida, K., Tomisaka, K., Matsumoto, T., Ohsuga, K., Machida, M. N., & Saigo, K. 2010, *ApJ*, 714, L58
- Tomisaka, K. 1998, *ApJ*, 502, L163+
- . 2002, *ApJ*, 575, 306
- Toomre, A. 1964, *ApJ*, 139, 1217

- Torrelles, J. M., Patel, N. A., Anglada, G., Gómez, J. F., Ho, P. T. P., Lara, L., Alberdi, A., Cantó, J., Curiel, S., Garay, G., & Rodríguez, L. F. 2003, *ApJ*, 598, L115
- Truelove, J. K., Klein, R. I., McKee, C. F., Holliman, II, J. H., Howell, L. H., & Greenough, J. A. 1997, *ApJ*, 489, L179
- Vaidya, B., Fendt, C., Beuther, H., & Porth, O. 2011, *ApJ*, 742, 56
- Waagan, K. 2009, *Journal of Computational Physics*, 228, 8609
- Waagan, K., Federrath, C., & Klingenberg, C. 2011, *Journal of Computational Physics*, 230, 3331
- Walch, S., Whitworth, A. P., & Girichidis, P. 2012, *MNRAS*, 419, 760
- Wang, Y., Beuther, H., Bik, A., Vasyunina, T., Jiang, Z., Puga, E., Linz, H., Rodón, J. A., Henning, T., & Tamura, M. 2011, *A&A*, 527, A32+
- Ward-Thompson, D., André, P., Crutcher, R., Johnstone, D., Onishi, T., & Wilson, C. 2007, *Protostars and Planets V*, 33
- Widrow, L. M. 2002, *Reviews of Modern Physics*, 74, 775
- Wilcock, L. A., Kirk, J. M., Stamatellos, D., Ward-Thompson, D., Whitworth, A., Battersby, C., Brunt, C., Fuller, G. A., Griffin, M., Molinari, S., Martin, P., Mottram, J. C., Peretto, N., Plume, R., Smith, H. A., & Thompson, M. A. 2011, *A&A*, 526, A159
- Wilking, B. A., Gagné, M., & Allen, L. E. 2008, *Star Formation in the  $\rho$  Ophiuchi Molecular Cloud*, ed. B. Reipurth, 351
- Williams, J. P., Blitz, L., & McKee, C. F. 2000, *Protostars and Planets IV*, 97
- Williams, J. P. & Cieza, L. A. 2011, *ARA&A*, 49, 67
- Wolfire, M. G. & Cassinelli, J. P. 1987, *ApJ*, 319, 850
- Wu, Y., Wei, Y., Zhao, M., Shi, Y., Yu, W., Qin, S., & Huang, M. 2004, *A&A*, 426, 503
- Wuchterl, G. & Klessen, R. S. 2001, *ApJ*, 560, L185
- Yorke, H. W. & Sonnhalter, C. 2002, *ApJ*, 569, 846
- Zhang, Q., Hunter, T. R., Brand, J., Sridharan, T. K., Cesaroni, R., Molinari, S., Wang, J., & Kramer, M. 2005, *ApJ*, 625, 864
- Zhang, Q., Wang, Y., Pillai, T., & Rathborne, J. 2009, *ApJ*, 696, 268
- Zhao, B., Li, Z.-Y., Nakamura, F., Krasnopolsky, R., & Shang, H. 2011, *ApJ*, 742, 10
- Zinnecker, H. & Yorke, H. W. 2007, *ARA&A*, 45, 481